MODELING AND SIMULATION OF TIME-DEPENDENT INELASTIC SOFT TISSUE BEHAVIOR

A Dissertation
Presented to
The Academic Faculty

by

Caitlin Martin

In Partial Fulfillment
of the Requirements for the Degree
Doctor of Philosophy in the
Department of Biomedical Engineering

Georgia Institute of Technology

December 2015

MODELING AND SIMULATION OF TIME-DEPENDENT INELASTIC SOFT TISSUE BEHAVIOR

Approved by:

Dr. Wei Sun, Advisor
Department of Biomedical Engineering
Georgia Institute of Technology

Dr. John Elefteriades
School of Medicine
Yale University

Dr. Ajit Yoganathan
Department of Biomedical Engineering
Georgia Institute of Technology

Dr. Muralidhar Padala
School of Medicine
Emory University

Dr. Gang Bao
Department of Mechanical Engineering
Georgia Institute of Technology

Date Approved: August 11, 2015

ACKNOWLEDGEMENTS

First and foremost, I would like to express my deepest gratitude to my advisor, Dr. Wei Sun, for initially encouraging me to pursue a PhD and serving as a mentor to me throughout the years. I would also like to thank him for giving me the opportunity to work on many interesting topics which has allowed me to expand my technical skill set. I would like to thank my thesis committee members, Dr. John Elefteriades, Dr. Ajit Yoganathan, Dr. Gang Bao, and Dr. Muralidhar Padala for their mentorship and support. I would also like to thank Dr. John Elefteriades in addition to Dr. James Duncan for serving as co-advisors on my NIH pre-doctoral fellowship. I must also acknowledge our collaborators, Dr. Charles Primiano and Dr. Raymond McKay, for providing invaluable clinical insight, and my NIH F31 HL112632 pre-doctoral fellowship.

I would like to thank current members and alumni of the Tissue Mechanics Laboratory, especially Dr. Thuy Pham, Dr. Haofei Liu, Dr. Kewei Li, Dr. Qian Wang, and Dr. Eric Sirois for their technical support and guidance on my thesis work. I would also like to thank Huijuan Xu and Katelyn Clark for their assistance in collecting the experimental data, as well as Alexander Werne and Jackson Hair for their assistance in creating computational models associated with this work. I would also like to thank them and other lab members and undergraduate students I have worked with over the years from the University of Connecticut and Georgia Tech, particularly, Andres Caballero, Dr. Wenbin Mao, Kyle Murdock, Andrea Mandragouras, Joseph Calderan, Joseph Mummert,

and Keping Zuo, for making the Tissue Mechanics Laboratory such an enjoyable place to work. Lastly, I would like to thank my family and friends for their unwavering support.

TABLE OF CONTENTS

ACKNOWLEDGEMENTS iii

LIST OF TABLES viii

LIST OF FIGURES x

SUMMARY xxi

INTRODUCTION 1

1.1 Soft collagenous tissue structure and function 1

1.2 Soft collagenous tissue derived medical devices 4

1.3 Time-dependent soft collagenous tissue property changes 6

1.4 Characterization of soft collagenous tissue mechanical properties 8

1.4.1 Characterization of instantaneous soft tissue mechanical properties 9

1.4.2 Characterization of irreversible time-dependent soft collagenous tissue properties 15

1.5 Constitutive modeling of soft collagenous tissue mechanical responses 20

1.5.1 Modeling of hyperelastic soft collagenous tissue properties 21

1.5.2 Modeling of inelastic time-dependent soft collagenous tissue properties 26

1.6 Computational modeling of soft collagenous tissues 29

1.6.1 Computational modeling of elastic soft collagenous tissues 29

1.6.2 Computational modeling of irreversible soft collagenous tissue property changes 30

1.7 Motivation of this study 32

1.7.1 Soft tissue aging and fatigue processes are not well understood 32

1.7.2 There is a lack of suitable constitutive frameworks in the literature 33

1.7.3 Objectives of this study 34

1.7.4 Innovation and significance of this study 36

THEORETICAL AND COMPUTATIONAL FRAMEWORK FOR MODELING TIME-DEPENDENT IRREVERSIBLE SOFT TISSUE PROPERTY CHANGES 38

2.1 Introduction 39

2.1.1 Clinical significance 39

2.1.2 Theoretical frameworks for modeling time-dependent irreversible soft tissue property changes 39

2.1.3 Computational modeling of irreversible soft tissue property changes 44

2.1.4 Motivation of this study 45

2.1.5 Overview of this study 47

2.2 Theoretical framework 47

2.2.1 Initial state tissue properties 47

2.2.2 Selection of strain-energy function 48

2.2.3 Inclusion of internal variables 50

2.2.4 Damage evolution 51

2.2.5 Cycles-to-failure 55

2.2.6 Stress-softening 58

2.2.7 Permanent set 60

2.2.8 Incorporation of the permanent set in the material response 66

2.2.9 Tissue response with irreversible time-dependent effects 68

2.2.10 Parametric study of model parameters 70

2.2.11 Calibration of time-dependent inelastic material parameters 72

2.3 Computational framework 74

2.3.1 Overview of user-material subroutine algorithm 75

2.3.2 Stress-softening and permanent set update procedure 76

2.3.3 Stress and material Jacobian tensor definitions. 77

2.3.4 Numerical considerations for constitutive model parameters 82

2.3.5 User material subroutine verification 86
2.3.6 Example uniaxial tissue fatigue simulation 94
2.4 Discussion 97
2.4.1 Theoretical framework for modeling time-dependent inelastic tissue properties 97
2.4.2 Computational framework for modeling time-dependent inelastic tissue properties 99
2.4.3 Limitations 100
2.5 Conclusions 101
MODELING OF HUMAN ASCENDING AORTA AGING 102
3.1 Introduction 103
3.1.1 Ascending aorta structure and function 103
3.1.2 Age-related ascending aorta property changes 104
3.1.3 Experimental characterization of age-dependent human ascending aorta properties 106
3.1.4 Modeling of age-related changes in blood vessels 109
3.1.5 Computational studies of the human ascending aorta 111
3.1.6 Motivation of this study 112
3.2 Methods 112
3.2.1 Overview of study design 112
3.2.2 Characterization of age-dependent in vivo human AA characteristics 114
3.2.3 Characterization of age-dependent in vitro human AA tissue response 119
3.2.4 Constitutive modeling of human AA aging response 122
3.2.5 Computational modeling of human AA aging 132
3.3 Results 140
3.3.1 In vivo human AA structural characteristics 140

3.3.2 In vitro human AA tissue characteristics 145
3.3.3 Constitutive modeling of human AA aging 149
3.3.4 Initial human AA inflation 153
3.3.5 Effect of aging on the human AA structural properties 154
3.3.6 Effect of aging on the human AA wall stress 159
3.4 Discussion 161
3.4.1 Age-related AA structural property changes 161
3.4.2 Age-related AA tissue property changes 163
3.4.3 Constitutive modeling of human AA aging response 164
3.4.4 Computational modeling of human AA aging 165
3.4.5 Limitations 167
3.5 Conclusions 169
MODELING OF BIOPROSTHETIC HEART VALVE FATIGUE DAMAGE 172
4.1 Introduction 173
4.1.1 Heart valve structure and function 173
4.1.2 Heart valve disease 175
4.1.3 Clinical management of heart valve disease 175
4.1.4 Limited durability of bioprosthetic heart valves 177
4.1.5 Valve durability analyses 180
4.1.6 Experimental characterization of heart valve biomaterial fatigue properties 181
4.1.7 Computational studies on bioprosthetic heart valves 184
4.1.8 Motivation of this study 185
4.2 Methods 187
4.2.1 Overview of study design 187
4.2.2 Constitutive modeling of GLBP tissues 188

4.2.3 Computational modeling of bioprosthetic heart valve fatigue 196
4.3 Results 205
4.3.1 Constitutive modeling of GLBP uniaxial fatigue response 205
4.3.2 Effect of cyclic loading on BHV function 209
4.3.3 Leaflet property parametric study 210
4.3.4 Stent property parametric study 216
4.3.5 Comparison study of SAV and TAV leaflet fatigue 219
4.3.6 Parametric study of TAV underexpansion 221
4.4 Discussion 225
4.4.1 Constitutive modeling of GLBP fatigue response 225
4.4.2 Effect of cyclic loading on SAV function 226
4.4.3 Effect of leaflet properties on SAV durability 226
4.4.4 Effect of stent properties on SAV durability 228
4.4.5 Effect of leaflet coaptation on SAV durability 229
4.4.6 Effect of including distinct matrix and fiber descriptions 230
4.4.7 Computational fatigue analysis of surgical bioprosthetic valves 231
4.4.8 Comparison of SAV and TAV leaflet fatigue damage 232
4.4.9 Effect of TAV underexpansion on durability 233
4.4.10 Limitations of this study 236
4.5 Conclusions 237
CONCLUSIONS 240
5.1 Summary 240
5.2 Clinical relevance 242
5.3 Future directions 243
5.3.1 Refinement of the time-dependent inelastic theoretical framework 243

5.3.2 Advances in the computational modeling of soft tissue aging and fatigue effects 246

5.3.3 Evaluation of ascending aorta aneurysm rupture risk over time 249

5.3.4 Experimental characterization of bioprosthetic heart valve tissue fatigue response 252

5.3.5 Computational based design optimization of bioprosthetic heart valves 253

5.4 Conclusions 254

APPENDIX A – BIOMECHANICAL CHARACTERIZATION OF ASCENDING AORTIC ANEURYSM WITH CONCOMITANT BICUSPID AORTIC VALVE AND BOVINE AORTIC ARCH 255

A.1 INTRODUCTION 255

A.2 MATERIALS AND METHODS 257

A.2.1 Clinical data and aortic specimens 257

A.2.2 Mechanical Tests 258

A.3 RESULTS 262

A.4 DISCUSSION 272

A.4.1 Tissue properties of AsAA 272

A.4.2 Bicuspid aortic valve effect 273

A.5 CONCLUSION 278

APPENDIX B – PREDICTIVE BIOMECHANICAL ANALYSIS OF ASCENDING AORTIC ANEURYSM RUPTURE POTENTIAL 279

B.1 Introduction 279

B.2 METHODS 280

B.2.1 Patient Selection 280

B.2.2 Biomechanical Testing 281

B.2.3 Predictive Modeling 283

B.2.4 Data and Statistical Analysis 288

B.3 RESULTS 289
B.3.1 Predictive analysis 289
B.3.2 Statistical Analysis 293
B.4 DISCUSSION 294
B.4.1 Rupture characteristics of AsAA 294
B.4.2 Bicuspid aortic valve effect 297
B.4.3 Bovine aortic arch effect 298
B.4.4 Clinical indications of rupture potential 298
B.4.5 Limitations 299
B.5 Conclusions 300
REFERENCES 302

LIST OF TABLES

Table 2-1 Fung model parameters for a representative soft tissue. 53

Table 2-2 Modified-Holzapfel model parameters for a typical soft tissue..... 54

Table 2-3 Time-dependent inelastic model parameters used to illustrate the permanents sets predicted by Eq. (2.27) as a function of the peak principle Green strains. 62

Table 2-4 Time-dependent inelastic model parameters used to illustrate the matrix and fiber permanent sets predicted by Eqs. (2.30) and (2.31) as a function of the peak principle Green strains. 65

Table 2-5 Material parameters used in user-material subroutine verification test 1. 87

Table 2-6 Material parameters used in user-material subroutine verification test 2. 90

Table 2-7 Material parameters used in user-material subroutine verification test 3. 92

Table 2-8 Material parameters used in the uniaxial fatigue simulation. 95

Table 3-1 Patient characteristics for age-dependent *in vivo* AA property study..... 115

Table 3-2 Human AA biaxial test specimen characteristics..... 120

Table 3-3 Fung model coefficients for human AA for different age groups 150

Table 3-4 Human AA aging model parameters..... 151

Table 3-5 Comparison of estimated human AA permanent set (PS) with aging with the FE predicted PS with aging in the circumferential (Circ) and longitudinal (Long) directions. 152

Table 4-1 Fung model parameters for CEP valve leaflets adapted from Sun [85]. 189

Table 4-2 Modified-Holzapfel model parameters for CEP valve leaflets. 205

Table 4-3 GLBP fatigue parameters for use with the Fung strain energy function. 206

Table 4-4 GLBP fatigue parameters for use with the modified-Holzapfel strain energy function. 207

Table A-1 Summary of patients' information. 263

Table A-2 Comparison of stiffness at 60 kPa tension between hypertensive and normotensive patients among AsAA, BAV and BAA patient groups.... 268

Table B-1 Summary of patients' characteristics. 281

Table B-2 Fung coefficients for the mean 1:0.5 biaxial test response for the three patient groups. 290

Table B-3 Yield and rupture criteria defined for 50 patients. 292

Table B-4 Correlation between yield/rupture risk and patient clinical characteristics 294

LIST OF FIGURES

Figure 1.1 Scanning electron microscopy image of a cross-sectional cut of a porcine mitral chordae tendinaea adapted from Liao [2] illustrating the collagen fibril crimp structure. 1

Figure 1.2 Typical soft tissue stress-strain response showing high compliance at low stresses (I) when the collagen fibers are highly crimped, gradual stiffening as the collagen fibers begin to bear load (II), and high stiffness at high stresses (III) when the collagen fibers have been completely straightened. 3

Figure 1.3 Examples of chemically-treated tissue based medical devices. a) Repair of stenotic pulmonary arteries with a glutaraldehyde-treated bovine pericardium patch adapted from [8]. b) Tracheal tumor removal and repair with a chemically-treated pericardial patch adapted from [9]. b) The Freestyle valve from Medtronic fabricated from a glutaraldehyde-treated porcine aortic valve for the treatment of aortic stenosis or regurgitation adapted from [10]. 5

Figure 1.4 Mean stress-strain responses of native and glutaraldehyde (Glut) treated porcine aortic valve leaflets under equi-biaxial tension adapted from [11]. The difference between the responses of the leaflets treated under 0 mmHg and 4 mmHg pressure demonstrate how the state of collagen fiber crimp during fixation can influence the mechanical response. 6

Figure 1.5 Mechanical behavior of a collagen tissue under uniaxial tension and schematic of the collagen structure at low (Region I), moderate (Region II), and failure range (Region III) stresses [6]. 7

Figure 1.6 a) The biaxial testing system with an actual testing setup, showing the camera, the two load cells, the two signal conditioners and the four motors. b) A close-up of a representative specimen submerged in an appropriate physiologic solution, marked with four black graphite particles (optical markers for strain measurement) and attached to the device via four hooks at each side. 13

Figure 1.7 *In vivo* second harmonic imaging of rat the patellar tendon over uniaxial fatigue cycling from Fung et al. [57]. Progressive damage and disruption to the collagen structure is shown from (a) the un-fatigued to the (b) low, (c) moderate, and (d) high fatigued states. 20

Figure 1.8 The engineering stress versus stretch ratio of pig skin under a) uniaxial compression and b) uniaxial tension at different strain rates adapted from [78]. Note that the Mooney-Rivlin model cannot capture the stiffening portion of the response, and the Ogden model with one set of parameters

cannot capture the different material responses in perpendicular directions. 23

Figure 1.9 Fung and Ogden model fits of glutaraldehyde-treated bovine pericardium equi-biaxial responses adopted from [85]. Note that the Ogden model cannot capture the shear response or anisotropy of the tissue. 24

Figure 1.10 Cyclic uniaxial tension tests of human carotid artery in the circumferential and axial directions: a) experimental data, and b) constitutive model prediction adapted from Balzani et al. [104]. 28

Figure 1.11 Normalized mass, density, and volume in a abdominal aortic aneurysm at t=10 years adapted from [130]. 32

Figure 2.1 Contour plot of the equivalent strain versus the principal Green strains.. 53

Figure 2.2 Representative equivalent strain contours for the a) matrix and b) fiber components defined by Eqs. (2.11) and (2.13) respectively. 54

Figure 2.3 Illustration of the effects of (a) α and (b) β on the number of cycles to failure. 56

Figure 2.4 Illustration of the effects of (a) α and (b) β on the degree of stress softening. 59

Figure 2.5 Contour plot of the anisotropic permanent set versus the principal Green strains. 62

Figure 2.6 Representative permanent set contours for the a) matrix and b) fiber components as a function of the peak principal strains. 66

Figure 2.7 Illustration of the effects of β on the tissue stress-strain response over cycling with a) $\beta = 0.27$, b) $\beta = 0.5$, c) $\beta = 3$, and d) $\beta = 10$..... 71

Figure 2.8 Illustration of the effects of the permanent set on the stress-strain response over continued cycling with a) $\mathrm{Dpsmaxn} = 0$, b) $\mathrm{Dpsmaxn} = 0.1$, c) $\mathrm{Dpsmaxn} = 0.2$, and $\mathrm{Dpsmaxn} = 0.3$. 72

Figure 2.9 Schematic of stress tensor and material Jacobian tensor update procedure at each time increment in ABAQUS UMAT. 76

Figure 2.10 Projections of the Fung strain energy function potential contour plots in the a) E_{11}-E_{22}, b) E_{11}-E_{12} and c) E_{22}-E_{12} planes without convexity condition imposed; the projections of the strain energy function potential contour plots in the d) E_{11}-E_{22}, e) E_{11}-E_{12} and f) E_{22}-E_{12} planes with convexity condition imposed adapted from [145]. 85

Figure 2.11 Multi-element model used in UMAT verification tests. The arrows illustrate how the uniaxial displacement was applied to the model, and the red-dotted square indicates the 4 central elements from which the simulation results were extracted. 88

Figure 2.12 Analytical and FE predicted SPKS vs. Green Strain responses over 30 simulated cycles of uniaxial loading to a peak strain 0.16 showing very good agreement. 89

Figure 2.13 Analytical and FE predicted SPKS vs. Green Strain responses over 30 simulated cycles of uniaxial loading to a peak strain 0.2 using brick elements showing very good agreement. 91

Figure 2.14 Analytical and FE predicted SPKS vs. Green Strain responses over 30 simulated cycles of uniaxial loading to a peak strain 0.55 using brick elements showing good agreement. 93

Figure 2.15 Analytical and FE predicted SPKS vs. Green Strain responses over 30 simulated cycles of uniaxial loading to a peak strain 0.55 using plane-stress elements showing very good agreement. 93

Figure 2.16 Contour plots of $\boldsymbol{Ds}$ in the matrix (top) and fiber family 1 (bottom) at the 10N state shown on the 0-stress fatigued geometry. The red-dashed squares outline the 0-state tissue model geometry. Note tissue elongation in the loading direction and narrowing in the cross-loading direction 96

Figure 2.17 The FE predicted equi-biaxial responses of each sample at the 0N and 10N states. Note that the complete reversal of the tissue anisotropy in the $\theta = 0°$ sample, and the creation of a preffered direction in the $\theta = 45°$ samples. 97

Figure 3.1 Diagram of the aorta. Note that the AA is the portion of the aorta between the aortic valve and the aortic arch [160]. 104

Figure 3.2 Representative images of the thoracic in a (A) younger and (B) older patient, showing increased curvature in the arch of the older patient, adapted from [178]. 105

Figure 3.3 Circumferential (a) and longitudinal (b) peak equi-biaxial strain values plotted against age and location adapted from [205]. Note the dramatic decrease in AA compliance in both directions between the 31-60 years and >61 year age groups. 109

Figure 3.4 Overview of the computational human AA aging study design. 113

Figure 3.5 a) A cross-sectional image of the aortic valve and b) the same image with the 3D aortic root geometry (shown in pink) projected into the y-plane. c) A long axis view of the reconstructed aortic root geometry with the same

cross-section from b and c shown in the x-z plane. d) Aortic root geometry overlaid for each phase, with each color representing a different phase and a dashed line indicating the cross-sectional measurement plane. e) The aortic root geometries after bisection at the measurement plane. f) A close-up of the measurement plane where the circumference measurements were made and g) the measurement plane during a single phase with points along the surface that were used to create a spline curve around the circumference. 118

Figure 3.6 Flow-chart of AA aging model parameter fitting procedure 122

Figure 3.7 Determination of $\lambda 11_{sys}$ from extrapolated 1:0.5 protocol biaxial test response 127

Figure 3.8 Uniaxial test specimen FE model in the a) un-deformed and b) deformed configurations. Contours of the Cauchy stress in the loading direction are shown on the deformed configuration. 129

Figure 3.9 Uniaxial failure test data for human AA samples. 129

Figure 3.10 a) Segmented AA surface geometry overlaid with 3D CT data in Avizo software for a representative patient. b) Patient 1 AA FE mesh (green) overlaid with original segmented surface geometry (purple). 133

Figure 3.11 AA FE models used in the mesh sensitivity analysis. The mesh in a) is constructed with elements ~0.5 mm x 0.5 mm, the mesh in b) is constructed with elements ~1 mm x 1 mm, and the mesh in c) is constructed with elements ~2 mm x 2 mm. 134

Figure 3.12 Systolic AA max Principal stress contours predicted by FE for the mesh with a) ~0.5 mm x 0.5 mm size elements, b) ~1 mm x 1 mm size elements, and c) ~2 mm x 2 mm size elements. 134

Figure 3.13 Normalized AA peak stress predicted in by FE versus the number of elements used in the model, with data labels indicating the average element size. 135

Figure 3.14 Determination of the systolic stretches in the circumferential and axial directions from the extrapolated biaxial response. 136

Figure 3.15 A schematic of the local cylindrical coordinate system definition based on the AA centerline (yellow dots). The black dotted lines illustrate how the aortic geometry was divided into segments to determine the centerline. 137

Figure 3.16 The final un-pressurized AA mesh overlaid with the original systolic mesh for patient 1. 138

Figure 3.17 Raw a) peak circumferential AA strain, b) mean diameter, c) systolic wall tension, and d) pressure-strain modulus data plotted versus age with linear regression lines..... 141

Figure 3.18 a) The mean systolic circumferential strain for each patient age group with standard deviation bars. b) Physiological pressure versus ascending aorta diameter for the 3 age groups, where the low pressure points represent the diastolic condition, the high pressure points represent the systolic condition, and the middle pressure point was taken from an intermediate phase, plotted as a mean with bi-directional standard error bars. 143

Figure 3.19 *In vivo* tension versus strain responses of the 3 age groups with lower points representing the diastolic condition, the upper points representing the systolic condition, and the middle points representing an intermediate phase, plotted as the mean value with bi-directional standard deviation bars. 144

Figure 3.20 Comparison of the mean pressure-strain modulus value between (a) patients in each of the 3 age groups, and (b) normotensive and hypertensive patients, each plotted with standard deviation bars. 145

Figure 3.21 Representative images of the Left-Coronary Sinus (LCS), Right-Coronary Sinus (RCS) and Non-Coronary Sinus (NCS) of a human aortic root adopted from [33]. Asterisks indicate locations of calcium deposition in the lumen layer of the aortic wall. [1mm sub-division for all images]... 146

Figure 3.22 Human AA equi-biaxial response in the circumferential and longitudinal directions for age groups a) and b) 50-59 years, c) and d) 80-89 years, and e) and f) 90-99 years. 147

Figure 3.23 Mean human AA equi-biaxial responses for the 50-59 years, 80-89 years, and 90-99 years age groups in the a) circumferential and b) longitudinal directions plotted with standard error bars..... 148

Figure 3.24 Representative AA tissue histological sections for a) 6-9 month old porcine model and b) 82 year old human stained with VVG stain. Collagen is rendered pink, elastin black, and smooth muscle brown. Note that the collagen and elastin fiber waviness in the porcine tissue is absent in the aged human sample. 149

Figure 3.25 Estimated human AA pressure versus diameter response from the unpressurized state to the 200 mmHg pressurized state. The age-dependent *in vivo* diastolic and systolic diameters and pressures are also plotted as a reference. 150

Figure 3.26 Overlay of the stress-free single-element FE model geometry at the 50 year, 80 year, and 90 year states, showing increased planar (circumferential and longitudinal) dimensions with age. 152

Figure 3.27 Comparison between the experimental and FE predicted human AA response with aging in the a) circumferential and b) longitudinal directions showing good agreement. Note all data is referenced to the current configuration. 152

Figure 3.28 Overlay of the FE deformed AA geometry under systolic pressurization and the original systolic AA surface geometry segmented from the CT data showing good correspondence. 153

Figure 3.29 Overlay of the FE deformed AA geometry at end diastole at the 50 year (red) and 80 year (blue) states for a) patient 1 and b) patient 2, showing at the aorta has significantly dilated and elongated and the curvature has increased over the course of the simulation. 155

Figure 3.30 FE predicted aorta wall circumferential (CIRC) and axial permanent set distributions for patient 1 showing larger axial permanent sets at each age. 155

Figure 3.31 FE predicted aorta wall circumferential (CIRC) and axial permanent set distributions for patient 2. 156

Figure 3.32 FE predicted and *in vivo* measured AA diameter at a) end diastole and b) peak systole for each age. 157

Figure 3.33 FE predicted and *in vivo* measured AA a) physiological circumferential strain and b) pressure-strain modulus. 158

Figure 3.34 FE predicted ascending aorta distensibility from age 50 years to 80 years. 159

Figure 3.35 FE predicted aorta wall max principal stress distributions for patient 1 (top) and patient 2 (bottom) showing increased stress throughout the vessel from 50 years to 80 years, and the development of new stress concentrations indicated by the arrows at 80 years. 160

Figure 3.36 FE predicted ascending aorta peak max principal stress from age 50 years to 80 years. 160

Figure 4.1 Photographs of the structure of a human excised aortic root showing (a) the entire circumference of the annulus comprised of fibrous and muscular regions and the coapting aortic leaflets, non-coronary (NCL), left-coronary (LCL) and right-coronary (RCL) leaflets; (b) the same aortic root with the ascending aorta (AA), right- (RCA) and left- (LCA) coronary arteries, non-coronary sinus of Valsalva (SOV), sinotubular junction (STJ) and trigone regions. (c) The illustration of the mitral valve anatomical structures and (d) the photograph of a human excised mitral valve showing the mitral annulus, anterior (AML) and posterior (PML) leaflets, fibrous region, chordae tendineae (chords) and papillary muscles (PMs). 174

Figure 4.2 Explanted Ionescu-Shiley BHVs from Lawford (Lawford, Black et al. 1987) displaying (a) leaflet sagging and damage near the commissure and (b) leaflet tearing along the suture attachments. 178

Figure 4.3 Histological sections of porcine BHV leaflet specimens showing progressive delamination with increasing levels of bending fatigue adapted from Mirnajafi et al. [303]. 184

Figure 4.4 Overview of the computational fatigue analysis of bioprosthetic heart valves study design. 188

Figure 4.5 Equi-biaxial response for each leaflet property: a) L1, b) L2, and c) L3, in the radial and circumferential directions..... 189

Figure 4.6 Fatigue induced (a) stiffening in the loading direction and (b) permanent set of GLBP specimens subjected to uniaxial stretch cycles adapted from Sun et al. [105]. 191

Figure 4.7 Fatigue-induced property changes in the loading direction referenced to the a) current, fatigued state, and b) initial, un-fatigued state for a representative sample adapted from Sun et al. (Sun, Sacks et al. 2004). 191

Figure 4.8 (a) Equi-biaxial response of GLBP specimen at the un-fatigued state [105]. (b) Contour plot of equivalent strain with $\psi\text{min} = 4.67\text{kNm}$ and $\psi\text{max} = 4.32\text{x}105\text{kNm}$ marking the damage evolution region. 192

Figure 4.9 Uniaxial failure test data for 5 GLBP specimens with a mean failure strain of approximately 0.45 corresponding to $\psi\text{max} = 4.32\text{x}105\text{kNm}$..... 193

Figure 4.10 SAV finite element model constructed from shell elements in the pressurized state overlapped with the initial un-deformed geometry. 197

Figure 4.11 Diagram of the leaflet material orientations and the fiber orientations drawn on the 2D leaflet schematic. 197

Figure 4.12 Overlay plots of the un-deformed and deformed SAV FE models using brick elements in the a) open position and b) closed position. 198

Figure 4.13 Overlay plots of the un-deformed and deformed TAV FE models in the nominal configuration in the a) open position and b) closed position. ... 199

Figure 4.14 Contour plots of the max principal stress and max logarithmic strain for each valve in the open and closed configurations at the 0N state. In each valve the leaflet stresses and strains were higher in the closed position with peak values located at the commissures (red) and minimum values at the nadir (blue). All contour plots are shown on the aortic side of the leaflet deformed geometry at peak pressurization. 201

Figure 4.15 Contour plots of the peak equivalent strain, fiber and matrix damage in the SAV leaflets due to cyclic opening and closing and cyclic closing only at the 9N state, showing slightly higher peak equivalent strains due to cyclic opening and closing at the free edge, but nearly identical fiber and matrix damage patterns. 202

Figure 4.16 a) The 3 mm UE TAV FE model after inward radial displacement of the stent-attachment line overlaid with the nominal TAV model under minimum pressure. b) A failed explanted 26 mm Sapien XT TAV implanted in a 27 mm Carpentier-Edwards SAV (adapted from [268]). 205

Figure 4.17 GLBP L2 equi-biaxial response from Sun [85] (open circles), with the modified-Holzapfel model fit (black lines), and the contributions from the matrix (blue lines) and fibers (red lines) to the overall response..... 206

Figure 4.18 Schematic of the initial model geometry and loading conditions on the left and specimen at the stress-free state after simulated fatigue with a contour plot of the damage on the right. The red solid line represents the damage zone and the red dotted line represents the un-fatigued geometry..... 208

Figure 4.19 The uniaxial stress-strain response under load control of the simulated specimen compared to the actual specimen at the 0 state and the $30x10^6$ state. 209

Figure 4.20 Overlaid L1 valve leaflet geometry in the fully pressurized state after 0N cycles of fatigue (gray) and 30N cycles of fatigue (blue). a) (Front view) sagging of the leaflet free edge at the 30N state and b) (side view) increased curvature in the leaflet at the 30N state which is particularly pronounced in the belly region. The L1 leaflet max principal stress distribution on the aortic side of the leaflet at the c) 0N and d) 30N states. The arrows indicate the peak stress location..... 210

Figure 4.21 Contour plots of the a) max principal stress at the un-fatigued and fully loaded state and b) the 9N state fatigue damage on the aortic side of the leaflet for each valve of the leaflet property parametric study. 212

Figure 4.22 The effect of leaflet material properties on the peak leaflet a) maximum principal stress and b) equivalent strain. c) The normalized fatigue life of each valve compared to the L2 valve..... 214

Figure 4.23 Contour plots of the a) max principal stress at the un-fatigued (0N) and fully loaded state and b) the 20N state fatigue damage on the aortic side of the leaflet for each valve of the leaflet thickness parametric study. 214

Figure 4.24 The effect of the leaflet thickness on the peak L2 leaflet a) maximum principal stress and b) equivalent strain observed during valve closure at each cycle. The normalized fatigue life of each of the valves with altered leaflet thickness compared to the nominal L2 valve..... 215

Figure 4.25 The effect of the stent elastic modulus on the degree of stent-tip deflection for the L1 valve. 216

Figure 4.26 Contour plots of the a) max principal stress at the un-fatigued and fully loaded state and b) the 20N state fatigue damage on the aortic side of the leaflet for each valve of the stent property parametric study. 218

Figure 4.27 The effect of the stent elastic modulus on the peak L1 leaflet a) maximum principal stress and c) equivalent strain observed during valve closure at each cycle. The effect of the stent elastic modulus on the peak L2 leaflet b) maximum principal stress and e) equivalent strain observed during valve closure at each cycle. The normalized fatigue life of each of the e) L1 and f) L2 leaflet property valves with altered stent properties compared to the corresponding nominal valves. 219

Figure 4.28 The peak a) max principal strain and b) equivalent strain observed in the leaflets for each case and cycle. 221

Figure 4.29 a) Contour plots of the peak equivalent strain, max principal stress, and max principal strain of the TAV at the 9N state and the SAV at the 23N showing similar patterns and peak values. b) Contour plots of the peak equivalent strain, max principal stress, and max principal strain of the SAV at failure (28N state). 221

Figure 4.30 Leaflet coaptation upon full closure in the a) nominal, and b) 1 mm, c) 2 mm, and d) 3 mm stent diameter reduction cases overlaid with a circle of the original stent diameter (gray). 222

Figure 4.31 a) The percent area of leaflet coaptation, b) the MBR of the leaflet free edge and radial mid-line versus the degree of underexpansion at the 0N state. 223

Figure 4.32 Peak a) tensile and b) compressive stress for each valve at the 0N state in different regions of the leaflet: 1) along commissures, 2) belly, and 3) nadir. 224

Figure 4.33 The peak equivalent strain observed in the leaflets for each case and cycle. 225

Figure 4.34 Contour plots of the peak equivalent strain and the matrix and fiber damage at the 4N cycle fatigued state for each case. 225

Figure 5.1 Representative patient-specific AsAA FE results. a) Patient 1 results, representing essentially no risk, showing rupture on the outer curvature at a pressure of $14xPsys$. b) Patient 2 results, representing low risk, showing rupture on the anterior side at a pressure of $6xPsys$. c) Patient 3 results, representing moderate risk, showing rupture on the outer curvature at a pressure of $3xPsys$. d) Patient 4 results, representing high risk, showing

rupture on the inner curvature at a pressure of $1xPsys$. The black arrows indicate the rupture location..... 252

Figure A.1 Illustration of a representative testing sample and its orientation with respect to the excising region of the ascending aortic aneurysm. C – circumferential, L – longitudinal. 258

Figure A.2 (a) Diameter and thickness relationship of ASAA, BAV and BAA patient groups, the BAV group showed a strong correlation (p = 0.02); (b) a consistent trend of increasing thickness and ASI with increasing age in all groups, the ASAA group showed a near significant correlation between thickness and age (p = 0.052). 263

Figure A.3 Mean and standard error equibiaxial stress-strain responses of ASAA, BAV and BAA patient groups in the circumferential (CIRC) and longitudinal (LONG) directions..... 264

Figure A.4 **(**a) The relationship between age and areal strain at 60 and 120 kPa for AsAA, BAV and BAA patient groups, and (b) a significant negative correlation between ultimate tensile strain and age was observed in the circumferential (CIRC) direction of BAV samples and longitudinal (LONG) direction of BAA samples. 265

Figure A.5 Comparison of the mean circumferential (CIRC) and longitudinal (LONG) stiffnesses at (a) low (60 kPa) and (b) high (120 kPa) membrane tensions between ASAA, BAV and BAA patient groups; (c) mean extensibility and (d) mean degree of anisotropy (DA) of ASAA, BAV and BAA tissue samples at low and high membrane tensions. (*****) indicates a statistical significance with $p < 0.05$, (******) indicates a highly statistical significance with $p < 0.001$. Data presented as mean and standard deviation. 266

Figure A.6 **(**a) The relationship between age and areal strain at 60 and 120 kPa for AsAA, BAV and BAA patient groups, and (b) a significant negative correlation between ultimate tensile strain and age was observed in the circumferential (CIRC) direction of BAV samples and longitudinal (LONG) direction of BAA samples. 267

Figure A.7 (a) A circumferential cross section of the aortic wall from a 58-year-old patient with AsAA only. Note the changes in the elastic lamella including collapsed lamella (yellow arrows) and fragmentation of elastic fibers (white arrow). Image was stained with Verhoeff Van-Gieson stain. (b) Evidence of focal loss of SMC cells through loss of cell nuclei (asterisks) in the media layer from an 80-year-old AsAA only patient. (c) A cross section of the aortic wall from a 56-year-old patient with BAV and aortic stenosis. There are evidences of mucoid accumulation in between the elastic lamella (yellow arrow) throughout the media layer and the

disorientation of the smooth muscle cells (double-head arrow). Image was stained with Movat pentachrome. (Bar = 200μm) 270

Figure A.8 A circumferential cross section through the thickness of aortic walls from (a) a 52-year-old AsAA patient (b) a 61-year-old BAV patient and (c) a 75-year-old BAA patient. Severe damages of the elastic lamella and intima thickening due to fibrosis were observed in these images. Image was stained with Verhoeff Van-Gieson stain. (Bar = 200μm). 271

Figure A.9 (a) The percentiles of intima, media and adventitial layers in the AsAA (n = 10), BAV (n = 10) and BAA (n = 9) patient groups, (b) the percentiles of elastin, collagen and SMCs and ground substances in the media layer of each patient group. 272

Figure B.1 (a) $\tau 11$ vs. $\tau 22$ plot, (b) $\tau 11$ vs. E11 plot, and (c) $\tau 22$ vs. E22 plot with all biaxial test protocols. 282

Figure B.2 Uniaxial failure test in the (a) circumferential and (b) longitudinal directions for a selected patient with blue and red asterisks corresponding to the yield and ultimate Cauchy tension values respectively. 283

Figure B.3 (a) Extrapolated biaxial test data with raw test data represented by open circles and the biaxial test data generated by the extrapolation method represented by the lines. The circumferential strain,$E11_{sys}$, at the systolic blood pressure is determined from the extrapolated biaxial data. (b) Extrapolated data with dotted lines to indicate the yield criteria (blue markers) and rupture criteria (green markers). Only the yield strains are indicated on the figure for clarity. In this case, the sample yields in the circumferential direction. 288

Figure B.4 The average aneurysm pressure versus diameter response response for each patient group shown with standard error bars (for clarity). 291

Figure B.5 The mean predicted (a) diameter and (b) blood pressure at yield (red) and rupture (gray). 291

Figure B.6 (a) Yield risk quantified as D_{sys}/D_y and rupture risk as D_{sys}/D_f vs. the pressure-strain modulus, shows strong correlation. (b) Yield risk as P_{sys}/P_y (gray) and rupture risk as P_{sys}/P_f (black) for patients with a pressure-strain modulus less than 100kPa compared to those with a pressure-strain modulus greater than or equal to 100kPa. 294

Figure B.7 (a) AsAA6 biaxial test specimen with the (b) intimal surface and (c) adventitial surface on top, and representative histological slice through the aortic wall with Verhoeff-VanGieson stain rendering elastin purple-black and collagen pink-purple. 297

SUMMARY

Over long periods of time, soft collagenous tissues undergo irreversible microstructural changes including elastin degradation and collagen fiber un-crimping owing in part to the natural aging process and mechanical fatigue damage. These changes are accelerated in tissue-derived medical devices which lack regenerative repair abilities, and have deleterious effects on physiological function. Methods to predict collagenous tissue property changes in response to various factors could facilitate the design of durable tissue-based devices and the development of enhanced diagnostic and preventative treatment methods. However, most of the biomechanics work on soft collagenous tissues reported in the literature thus far, whether experimental, theoretical, or computational, is confined to static, instantaneous tissue property characterization. As such, only the recoverable or *elastic* behavior of tissue is considered, although from a thermodynamics stand point, permanent changes in tissue structure and material properties represent dissipative, *inelastic* effects. Thus, the objective of this dissertation was to develop a theoretical and computational framework to describe the time-dependent inelastic behavior of soft tissues such that the effects of mechanical fatigue damage and aging in soft tissues could be accurately modeled. The framework was implemented in a finite element solver and applied to investigate the effects of aging on the human ascending aorta, and the effects of leaflet fatigue damage in bioprosthetic heart valves. The results from these studies may offer scientific rationale for the design of improved devices and diagnostic methods.

1 INTRODUCTION

1.1 Soft collagenous tissue structure and function

Soft collagenous tissues such as: skin, blood vessels, tendons, and ligaments, are largely comprised of compliant elastin bundled with wavy stiff collagen fibers embedded in a ground substance of proteoglycans and glycosaminoglycans. Collagen has a strongly hierarchical structure: small tropocollagen molecules link together with covalent bonds to form fibrils, which in turn give rise to fibers and fiber bundles. The collagen fibrils are wavy or crimped in structure at the un-strained state with a periodicity between 10 and 100μm, depending on the particular type of tissue [1]. The characteristic collagen crimp behavior is illustrated in the scanning electron microscopy image of a porcine mitral chordae tendinae in Figure 1.1.

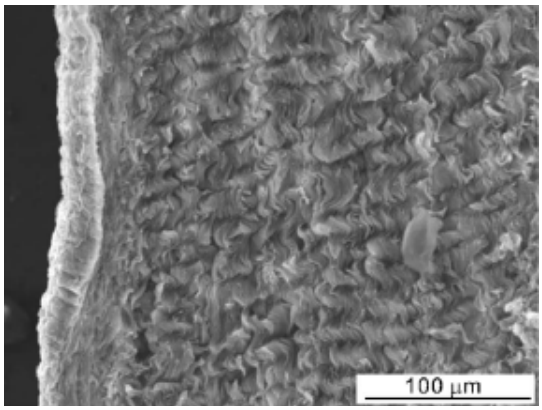

Figure 1.1 Scanning electron microscopy image of a cross-sectional cut of a porcine mitral chordae tendinaea adapted from Liao [2] illustrating the collagen fibril crimp structure.

The ground substance is a viscous gel mainly composed of an electrolytic water solution containing positively charged sodium ions and highly negatively charged

proteoglycans. Proteoglycans are long molecular structures developing along hyaluronic acid. Aggregans, other proteins, are also laterally attached to the hyaluronic acid axis, and are structured around their own axis in which threads of amino acids, namely, glycosaminoglycans are attached. Proteoglycans [3, 4] and fibril [5] associated collagen comprise the interfibrillar bonds adjoining fibrils into fibers and play a role in the mechanical coupling of fibrils [6].

This unique structure gives rise to the highly complex mechanical behavior of soft tissues. The mechanical behavior of tissue is determined by the properties and quantities of each of these components. Because the collagen fibers are much stiffer than the matrix materials, collagen dominates the tensile tissue response. Furthermore, the specific orientation of collagen fibers creates the characteristic anisotropy of the tissue. However, due to the high length to thickness ratio of the collagen fibers, they do not play a significant role in the compressive tissue response. The compressive tissue response is instead dominated by the matrix or ground substance [6].

Due to the initial crimped configuration of the collagen fibrils, the tensile behavior of collagen fibers and collagenous tissues is highly nonlinear. A typical soft tissue tensile stress-strain response is shown in Figure 1.2. It can be seen that the tissue is highly extensible at low loads while the collagen fibers are still crimped and highly stiff at higher loads as the collagen fibers are recruited to bear load. The collagen fibers, once straightened, are essentially inextensible. The mechanical response of a straightened collagen fibril is approximately linear with an elastic modulus of 400 MPa [1]. Therefore, the collagen fibers provide mechanical strength to maintain form whilst

allowing flexibility between various organs of the body. The collagen crimp also acts as a shock absorber.

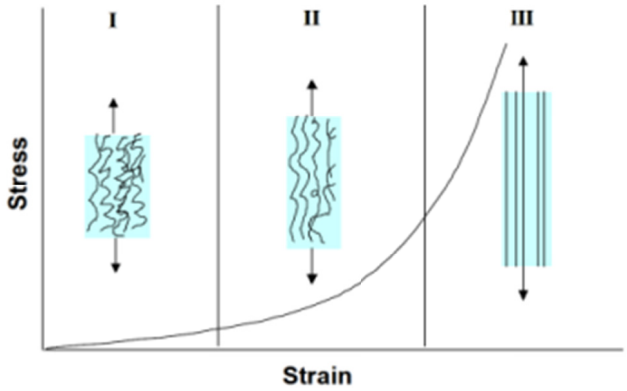

Figure 1.2 Typical soft tissue stress-strain response showing high compliance at low stresses (I) when the collagen fibers are highly crimped, gradual stiffening as the collagen fibers begin to bear load (II), and high stiffness at high stresses (III) when the collagen fibers have been completely straightened.

Under compressive loads, two primary phenomena occur: 1) the ground substance undergoes fluid fluxes within the solid skeleton, and the space between the glycosaminoglycans is reduced [6]. Therefore, tissue compressive stiffness is determined by the incompressible behavior of the ground substance, its capacity to move within the fibrous network, and the electrostatic interaction between the glycosaminoglycans. The electrostatic interaction phenomena are strongly influenced by the concentration of positive sodium ions. The movement of liquid phases within the porous solid structures of the tissue is a time-dependent phenomenon; thus, the compressive stiffness of tissue is loading rate dependent, with lower strain rates resulting in reduced stiffness. Accordingly, the ground substance dominates the viscoelastic response of soft tissues.

These mechanical property intricacies are important for normal physiological function. Specific tissue types are naturally structured to optimize their specific

functionality. For instance, the randomly orientated fibers of the skin permit considerable extension of the tissue until the fibers themselves are loaded. While the fibers of tendons are aligned in parallel and therefore loaded instantly, permitting maximum transfer of the energy of muscle contraction to the skeleton. The cornea provides an example of well-ordered fibers in precise layers at a defined angle to each other thereby allowing the transmission of light [7].

1.2 Soft collagenous tissue derived medical devices

The purpose of most medical devices is to restore normal physiological function, and because soft tissue structure is essential for proper function, medical devices intended to replace diseased or dysfunctional soft tissue should replicate the mechanical behavior of normal healthy tissue. Traditional man-made materials are typically not ideal in this regard. Creating durable scaffold constructs which can replicate the behavior of soft tissues with novel polymeric materials, electro-spinning, and 3D printing techniques is an active area of research.

The mechanical properties of soft collagenous tissues are difficult to replicate, thus, soft collagenous tissue grafts are still used in a broad spectrum of medical applications such as cardiovascular grafting as well as ligament, tendon, cartilage, sclera and hernia repair and replacement. Three types of tissue grafts are used: autografts, which come from the same patient, allografts, which come from another patient, and xenografts which come from animals. The use of autografts eliminates the risk of immunogenicity associated with allografts and xenografts, but requires the patient to undergo additional surgery to harvest the autograft and often results in donor site morbidity. The availability of human tissues in the form of allografts is limited; however,

animal (e.g., porcine and bovine) tissues for xenografts are abundant. These animal tissues need to be thoroughly sterilized via chemical processing and/or low-dose irradiation in order to be suitable for implantation into human patients. Moreover, chemical processing agents, such as glutaraldehyde, are typically used to increase the mechanical stability of xenografts. Figure 1.3 illustrates several examples of chemically-treated xenograft tissue-based medical devices including pericardial patches to replace soft tissues ranging from the pulmonary artery (Figure 1.3a) to the trachea (Figure 1.3b), and a porcine aortic valve to replace a diseased aortic valve (Figure 1.3c).

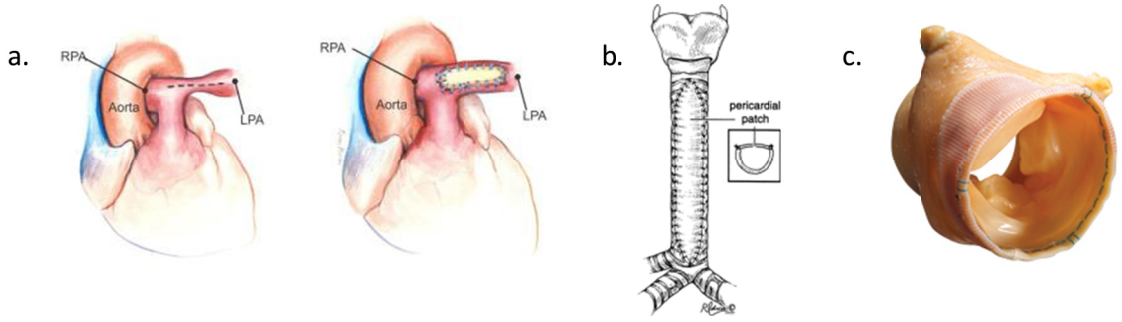

Figure 1.3 Examples of chemically-treated tissue based medical devices. a) Repair of stenotic pulmonary arteries with a glutaraldehyde-treated bovine pericardium patch adapted from [8]. b) Tracheal tumor removal and repair with a chemically-treated pericardial patch adapted from [9]. b) The Freestyle valve from Medtronic fabricated from a glutaraldehyde-treated porcine aortic valve for the treatment of aortic stenosis or regurgitation adapted from [10].

The chemical treatment process creates cross-links between the collagen fibers to preserve the integrity. The creation of cross-links will impact the tissue mechanical properties. Billiar and Sacks [11] have shown that glutraldehyde-treated porcine aortic valve leaflets used to construct bioprosthetic valves are stiffer than native leaflets in both the circumferential and radial directions, and this effect is exacerbated when the tissue is loaded during the fixation process indicating that the state of the collagen fiber crimp is important for preserving the tissue extensibility (Figure 1.4). Still, the chemically-treated

tissue is a good approximation of the native tissue with significant extensibility and similar nonlinear and anisotropic stress-strain behavior.

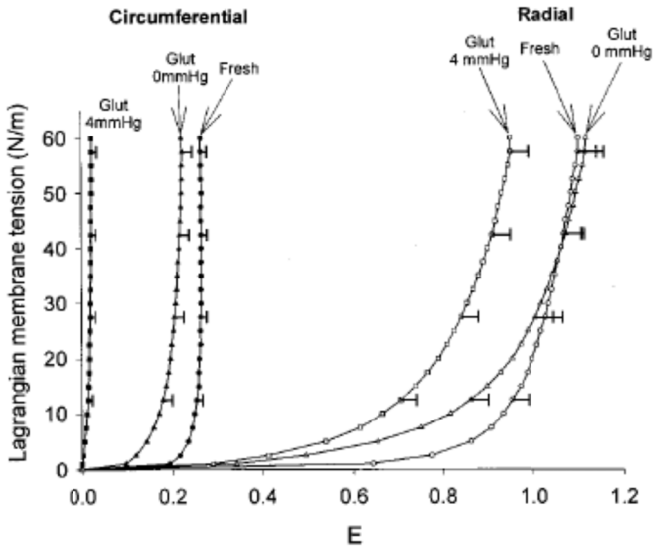

Figure 1.4 Mean stress-strain responses of native and glutaraldehyde (Glut) treated porcine aortic valve leaflets under equi-biaxial tension adapted from [11]. The difference between the responses of the leaflets treated under 0 mmHg and 4 mmHg pressure demonstrate how the state of collagen fiber crimp during fixation can influence the mechanical response.

1.3 Time-dependent soft collagenous tissue property changes

It is well known that soft tissue intrinsic material properties change over time. These changes can be brought on by mechanical loading, the natural aging process, and disease progression. Similar to artificial materials, when the strain exceeds a specific limit the mechanical properties of soft tissues degrade due to fatigue damage [12]. The collagen fibrils and interfibrillar bonds progressively break down, and the material stiffness decreases until the tissue fails as shown in Figure 1.5 [6]. Soft tissues including: skin, brain, arteries [13], venous and vaginal tissue [14-16], and atherosclerotic plaque [17] exhibit softening and unrecoverable strains (permanent set) over time owing in part

to fatigue damage of the non-living components of the tissue [18] and the aging process of the living components. Elastin fibers degrade and become fragmented which leads to irreversible un-crimping of the collagen fibers due to aging. As the collagen fibers begin to straighten the tissue will exhibit an unrecoverable permanent set. The loss of collagen fiber crimp also reduces the fiber recruitment strain, making the tissue stiffer. Thus, the "toe region" characteristic of the soft tissue stress-strain response is essentially eliminated over time [7], and the mechanical function is inevitably compromised. These time-dependent, fatigue-induced changes limit the durability of non-viable tissue-derived implants and scaffolds. For instance, while glutaraldehyde-treated bovine tendon (**GLBT**) has been used as an alternative material to human allografts for tendon and ligament repair, with some clinical success [19], GLBT grafts have been associated with implant ruptures [20, 21]. Fatigue-induced changes are also thought to play an important role in the pathogenesis of native tissues.

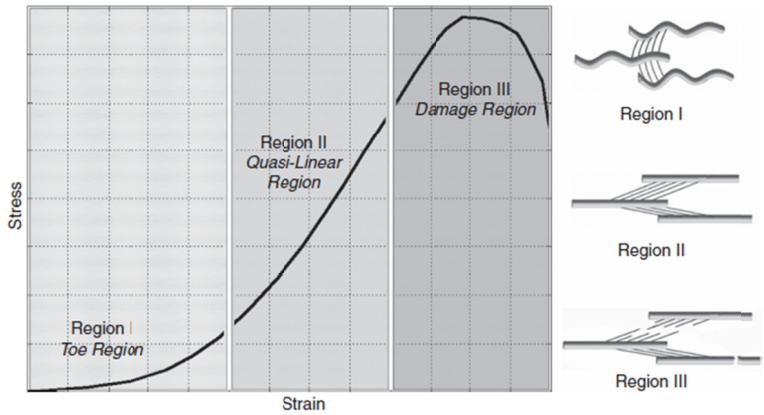

Figure 1.5 Mechanical behavior of a collagen tissue under uniaxial tension and schematic of the collagen structure at low (Region I), moderate (Region II), and failure range (Region III) stresses [6].

The aging process causes the rate of collagen metabolism to decrease, affecting the tissue capacity for self-repair [22]. In rat tissues, by the age of 24 months, the

collagen synthesis rate is decreased 10X compared to that at 1 month. Collagen degradation, on the other hand, increases with maturation. Thus, the majority of the newly synthesized collagen in old rats appears to be destined for degradation [22]. Aging also initiates modifications in collagen fibril diameter distribution and an increase in the crimping angle, which globally increase the tissue tensile stiffness, lower tissue flexibility and toughness, lower failure strain and energy, and decrease the shock-absorbing ability [6]. These aging phenomena are always deleterious to the optimal mechanical functioning of the tissue [6]. For example, age-related changes to the tendons are believed to be one of the causes of the functional decrease in the musculoskeletal systems in the elderly [23]. Aging is the largest known risk factor for most human diseases [24-27], particularly in the development of cardiovascular diseases [28], which represents the primary cause of morbidity and mortality in the elderly [29, 30]. An understanding of the physiological mechanisms involved in the natural aging process of soft tissues is critical for the development of novel prevention, diagnosis and treatment approaches to delay the onset of the debilitating consequences of aging, while an in depth understanding of the fatigue damage process in soft tissues would facilitate the development of methods to mitigate fatigue induced property changes.

1.4 Characterization of soft collagenous tissue mechanical properties

By characterizing the mechanical properties of soft tissues we can better understand physiological function in healthy and pathological conditions. The current state-of-the-art tissue mechanical property testing methods are largely confined to instantaneous characterization methods (i.e. not considering the effects of aging and mechanical fatigue). For instance, uniaxial and biaxial tension tests are commonly used

to characterize the planar material properties of soft tissues, and pressure inflation tests are used to quantify the overall structural response of whole tissues. These testing methods and the data that can be obtained from each are summarized in the following sections.

1.4.1 Characterization of instantaneous soft tissue mechanical properties

Because the collagen fibers are oriented in roughly planar sheets through the tissue thickness, soft collagenous tissues are often assumed to behave like thin membranes. Thus, the mechanical properties of soft tissues are often measured using biaxial or uniaxial planar testing techniques. Planar biaxial testing has become the preferred method for measuring the mechanical properties of soft collagenous tissues. Through biaxial testing the tissue anisotropy and mechanical coupling between the material axes can be measured under multiple different loading protocols spanning the *in vivo* physiological range. This yields a wealth of testing data for constitutive modeling purposes. Uniaxial testing is the most common experimental method for determining the elastic modulus of traditional engineering materials. While anisotropy and mechanical coupling cannot be measured, uniaxial testing is still often used to test the mechanical properties of soft collagenous tissues. It is a relatively simpler experiment than the planar biaxial test and does not require the specialized equipment of a biaxial test. Uniaxial testing is the preferred method to biaxial testing to measure the failure properties of soft tissues.

1.4.1.1 Planar biaxial mechanical testing

A typical biaxial test device and set-up is shown in Figure 1.6. Biaxial experiments are generally performed on a square piece of planar soft tissue, with

dimensions of about 10-25 mm. The specimen is mounted to the biaxial device in trampoline-like fashion using thin threads, which allows the edges to expand freely in the lateral direction. Testing is generally performed with the specimen completely immersed in phosphate buffered normal saline (pH 7.4) at room or body (37 °C) temperature. The central target region must be sufficiently small and located away from the outer edges to avoid the tethering effects. In the central target region the stress and strain field is generally considered homogeneous. Markers are affixed to the tissue surface in this central region for optical strain measurements. The loads applied to the tissue along each axis are continuously measured by the load cells.

The following is a brief summary of how the tissue stress-strain response is calculated from the biaxial test data [31]. Consider deformation of membrane tissues under a biaxial stress state, including non-zero in-plane shear stresses. For this case, let Ω_0 and Ω be the (fixed) reference and deformed configurations of the continuous body, respectively. Consider the general mapping $\chi: \Omega_0 \rightarrow \boldsymbol{R}^3$, which transforms a material point $\boldsymbol{X} \in \Omega_0$ to a position $\boldsymbol{x} = \chi(\boldsymbol{X}) \in \Omega$ in the deformed configuration. For planar homogeneous deformations that occur during a biaxial test, this mapping reduces to

$$x_1 = \lambda_1 X_1 + \kappa_1 X_2, \qquad x_2 = \lambda_2 X_2 + \kappa_2 X_1, \quad x_3 = \lambda_3 X_3 \tag{1.1}$$

where $\lambda_i, i = 1, 2, 3$ are the axial stretch ratios and $\kappa_i, i = 1, 2, 3$ are measures of the in-plane shear. These stretch ratios are components of the deformation gradient tensor, $\boldsymbol{F}$. For the deformations in Eq. (1.1), $\boldsymbol{F}$ is given by

$$\mathbf{F} = \mathrm{Grad}(\mathbf{x}) = \begin{bmatrix} \frac{\partial x_1}{\partial X_1} & \frac{\partial x_1}{\partial X_2} & \frac{\partial x_1}{\partial X_3} \\ \frac{\partial x_2}{\partial X_1} & \frac{\partial x_2}{\partial X_2} & \frac{\partial x_2}{\partial X_3} \\ \frac{\partial x_3}{\partial X_1} & \frac{\partial x_3}{\partial X_2} & \frac{\partial x_3}{\partial X_3} \end{bmatrix} = \begin{bmatrix} \lambda_1 & \kappa_1 & 0 \\ \kappa_2 & \lambda_2 & 0 \\ 0 & 0 & \lambda_3 \end{bmatrix} \tag{1.2}$$

where the out-of-plane stretch $\lambda_3 = h/H$ is the ratio of the deformed (h) to the undeformed thickness (H) of specimen. $\boldsymbol{F}$ is a critical mathematical quantity since it completely describes the deformation state. Since soft tissues are composed primarily of water and have negligible permeability [32], they can be considered incompressible so that

$$J = \det(\boldsymbol{F}) = 1. \tag{1.3}$$

From $\boldsymbol{F}$ the right Cauchy-Green deformation tensor, $\boldsymbol{C}$ is defined as

$$\boldsymbol{C} = \boldsymbol{F}^T\boldsymbol{F}, \tag{1.4}$$

from which the components of the in-plane Green-Lagrange strain tensor, $\boldsymbol{E}$, is given by

$$\boldsymbol{E} = \frac{1}{2}(\boldsymbol{C} - \boldsymbol{I}), \tag{1.5}$$

where $\boldsymbol{I}$ is the second order identity tensor. $\boldsymbol{E}$ is the most common finite strain measure in the soft tissue literature due to the simplicity of the constitutive formulations. The components of $\boldsymbol{F}$ are determined optically to avoid any mechanical interference with the specimen.

As mentioned above, biaxial testing of biological tissues is performed using thin specimens (no more than ~3 mm, usually <1 mm) and acted on by only in-plane loads. A state of plane stress is thus assumed so that the components $\sigma_i, i = 1, 2, 3$ of the Cauchy

stress $\boldsymbol{\sigma}$ (force/deformed area) are 0. During actual experiments one can directly measure only the initial specimen dimensions, so that the Lagrangian stresses $\boldsymbol{P}$ (force/unit original cross-sectional area) are used for convenience. The components of $\boldsymbol{P}$ are computed from the measured axial forces $\boldsymbol{L}$ using

$$P_{11} = \frac{L_1}{Hw_2}, \quad P_{22} = \frac{L_2}{Hw_1}, \tag{1.6}$$

where $w_i, i = 1, 2$ are the planar specimen dimensions. Since experimentally applied loads are normal to the edges, $P_{12} = P_{21} = 0$. The Second Piola-Kirchhoff stress tensor $\boldsymbol{S}$ is the most commonly utilized stress tensor for soft tissue constitutive theories, and is determined using

$$\boldsymbol{S} = \boldsymbol{P}\boldsymbol{F}^{-1}. \tag{1.7}$$

The Cauchy stress tensor, $\boldsymbol{\sigma}$, is determined using

$$\boldsymbol{\sigma} = J^{-1}\boldsymbol{P}\boldsymbol{F}^{T}, \tag{1.8}$$

which in component form is given by (with $P_{12} = P_{21} = 0$):

$$\sigma_{11} = \lambda_1 P_{11}, \quad \sigma_{22} = \lambda_2 P_{22}, \quad \sigma_{12} = \kappa_1 P_{22}, \quad \sigma_{21} = \kappa_2 P_{11}. \tag{1.9}$$

In the case where there is negligible shear strain (i.e. $E_{12} \approx 0$), the normal components of the two stress tensors are related by:

$$S_{11} = \frac{P_{11}}{\lambda_1}, \quad S_{22} = \frac{P_{22}}{\lambda_2} \tag{1.10}$$

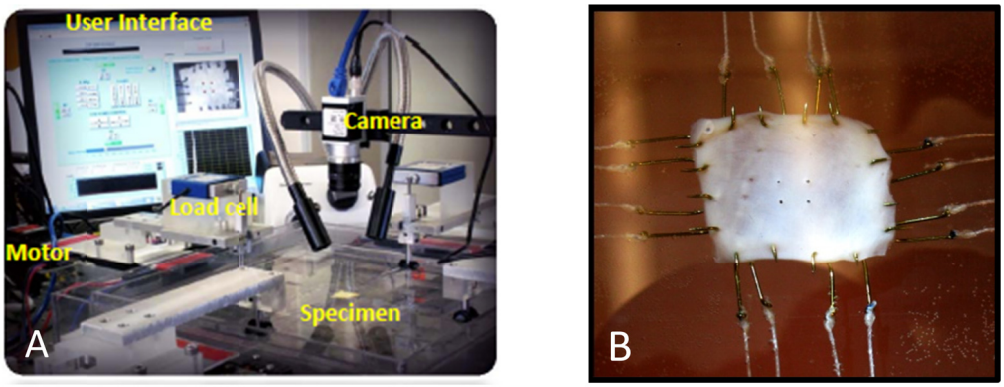

Figure 1.6 a) The biaxial testing system with an actual testing setup, showing the camera, the two load cells, the two signal conditioners and the four motors. b) A close-up of a representative specimen submerged in an appropriate physiologic solution, marked with four black graphite particles (optical markers for strain measurement) and attached to the device via four hooks at each side.

1.4.1.2 Uniaxial tensile testing

In a uniaxial tension test, a strip or dog-bone shape tissue specimen is mounted between two grips and stretched in one direction. The load applied to the tissue is continuously measured by a load cell as in the biaxial test. The tissue stretch is generally measured from the initial specimen length, l_0, and the displacement of the grips, Δl, as

$$\lambda = \frac{l_0 + \Delta l}{l_0}. \tag{1.11}$$

However, recently, researchers have begun using optical markers in the center of the specimen and camera marker tracking techniques to measure the tissue stretch, similar to in the planar biaxial test, which is more accurate. Typically the tissue stretch is only measured along the loading axis. Thus, several assumptions must be made in order to calculate $\boldsymbol{F}$. First, the tissue is typically assumed to be incompressible, which requires that

$$\lambda_1\lambda_2\lambda_3 = 1. \tag{1.12}$$

Here λ_1 represents the tissue stretch in the loading direction, the stretch in the cross-loading directions are assumed to be equal, $\lambda_2 = \lambda_3$, and the shear is assumed to be negligible, $\kappa_1 = \kappa_2 = 0$, thus, the deformation gradient can be obtained as

$$\mathbf{F} = \mathrm{Grad}(\mathbf{F}) = \begin{bmatrix} \frac{\partial x_1}{\partial X_1} & \frac{\partial x_1}{\partial X_2} & \frac{\partial x_1}{\partial X_3} \\ \frac{\partial x_2}{\partial X_1} & \frac{\partial x_2}{\partial X_2} & \frac{\partial x_2}{\partial X_3} \\ \frac{\partial x_3}{\partial X_1} & \frac{\partial x_3}{\partial X_2} & \frac{\partial x_3}{\partial X_3} \end{bmatrix} = \begin{bmatrix} \lambda_1 & 0 & 0 \\ 0 & \lambda_1^{-1} & 0 \\ 0 & 0 & \lambda_1^{-1} \end{bmatrix}. \tag{1.13}$$

The Kirchhoff stress acting on the tissue, P_{11}, is thus given by Eq. (1.6), with $P_{22} = 0$. The Second Piola Kirchhoff and Cauchy stress tensors are then obtained by Eqs. (1.7) and (1.8).

1.4.1.3 Tissue inflation testing

Others have adopted tissue inflation tests to quantify the overall structural response of whole tissues such as blood vessels [33] and urinary bladder [34]. Testing is generally performed with the specimen completely immersed in phosphate buffered normal saline (pH 7.4) at room or body (37 °C) temperature as in the biaxial test. The tissue is deformed via an applied pressure which is recorded throughout the duration of the test. Typically, the tissue deformation is measured from the displacement of small markers or speckle pattern applied to the surface of the tissue using a video-marker tracking or digital image correlation method similar to the approach used for biaxial testing. Because the test is performed on a 3D tissue structure rather than a roughly planar sample as in uniaxial or biaxial tension tests, two CCD cameras are needed to measure the 3D deformation. The tissue response can then be obtained in terms of the

pressure versus the deformation or strain. Alternatively, the entire vessel diameter is measured in terms of the applied pressure. The marker approach allows for regional structural property characterization [33].

1.4.2 Characterization of irreversible time-dependent soft collagenous tissue properties

There have been few studies on the experimental characterization of soft tissue long-term time-dependent property changes, which is probably a result of the many associated challenges. The experimental methods are time consuming and often involve complex testing instruments. Most groups rely on *in vitro* experiments to study soft tissue damage and aging, but *in vivo* methods are emerging, thanks to noninvasive imaging modalities. *In vitro* experiments are simpler to perform than *in vivo* studies, however, do not always reflect the true *in vivo* mechanical environment. These experimental studies, which are primarily focused on the fatigue damage response of soft tissues such as tendons and ligaments, are summarized in the proceeding sections and also in Martin and Sun 2015 [35].

1.4.2.1 Ex vivo tissue fatigue testing

1.4.2.1.1 Isolated tissue material fatigue testing

In an attempt to characterize the specific effects of tensile, compressive, and flexural stresses on soft tissue material properties, several groups have taken an isolated material fatigue test approach. Uniaxial fatigue loading experiments are often adopted due to the relative simplicity of this approach. Uniaxial fatigue experiments can be categorized into 2 groups: load control experiments, where specimens are cycled to a peak load and the progressive increase in tissue extension is monitored, and displacement

control experiments, where specimens are cycled to a peak displacement and the reduction in the peak load is monitored. Load control experiments are attractive because the specimens can be cycled to failure and thus be used to determine a typical stress vs. cycle (S-N) curve for the material; however, these experiments can be very difficult to control particularly for extensible soft tissues. Displacement control experiments typically do not result in specimen failure, but they are much easier to control. In these experiments the progression of fatigue is determined through comparison of the tissue properties before and after fatigue.

Tendons and ligaments comprised mainly of axially aligned collagen fibers experience primarily tensile stresses *in vivo*, thus fatigue studies of these tissues have been primarily limited to uniaxial tension. Through uniaxial fatigue testing, Schectman and Bader [36] observed a decrease in ultimate tensile strength from approximately 100MPa to 49.1MPa for human Extensor digitorum longus tendons post fatigue. Likewise, Wang et al [37] showed a reduction in the failure strength of wallaby tail tendons after cyclic loading. In Provenzano et al. [38] a uniaxial stretch of 5.14% was identified as the threshold to induce damage in the rat medial collateral ligament (MCL). This damage was realized by changes in the tissue stress-strain curve, namely, elongation of the toe region and reduction of the stiffness and ultimate stress [38]. MCL cellular damage was observed at strains below the structural damage threshold, which they postulate may trigger the natural healing process *in vivo* [38]. This hypothesis is supported by the finding of Ker et al. [39] that high-stressed tendons *in vivo* have superior fatigue properties to low-stressed tendons suggesting stress-mediated remodeling of the tissue. Fung et al. [40] also showed that at even low levels of fatigue, before mechanical

property changes are evident, collagen fibers which are normally parallel and uniform in the rat patellar tendon become kinked. At increasing levels of fatigue, the tissue matrix became severely disrupted with poor fiber alignment and widening of the interfiber space [40]. Zec et al. [41] observed significant permanent sets induced in the fatigued rabbit ligament suggesting plastic deformation of the collagen fibers. It is important to note that these fatigue phenomena in tendons and ligaments are distinct from the creep rupture that occurs after prolonged application of a constant stress [37, 42]. Furthermore, the tendon and ligament life cycles predicted from *in vitro* test results are typically unreasonably low due to the absence of any healing mechanisms or possibly other experimental factors [43].

Several groups have conducted *ex vivo* fatigue studies on viable tissue specimens in an effort to determine the relationships between mechanical and biological effects. Banes et al. [44] showed that fatigue loading stimulated deoxyribonucleic acid and collagen synthesis in the avian tendon. Contrarily, Devkota et al. [45] observed a significant increase in collagenase activity in addition to rising levels of inflammatory mediator prostaglandin E_2 (**PGE_2**) over cycling, and hypothesized that PGE_2 was a key factor in the degradation of the ECM [45]. There is evidence that collagenase [46] and inflammatory mediator [47] activity in cyclically loaded tendons may be strain dependent. Increased apoptosis has also been observed in cyclically loaded tendons [45, 48]. Experimental results between groups are not entirely consistent. Much work still remains to be done to correlate mechanical and biological fatigue effects.

These studies demonstrated that under cyclic tension, collagenous tissues exhibit stiffening and permanent set particularly along the loading direction. The permanent set

phenomena has been hypothesized to occur as a result of the following mechanisms: 1) slippage of the collagen networks, 2) hydrolysis of the intermolecular cross-links, 3) or rupture of the glutaraldehyde cross-links in fixed tissues thus allowing for permanent deformation or un-crimping of the collagen networks [49]. Cyclic bending fatigue may lead to collagen fiber distortion and increased flexural stiffness. There is also evidence that mechanical fatigue induces cellular changes in the tissue although the precise effects remain unclear. The main limitation of isolated material tests is that the *in vivo* mechanical environment may not be accurately reproduced, thus the soft tissue fatigue damage mechanisms identified in these experiments may not reflect the *in vivo* mechanisms.

1.4.2.2 In vivo tissue fatigue analysis

The ultimate goal of all tissue fatigue studies is to determine the *in vivo* fatigue response. *In vivo* studies have more clinical relevance. For instance, the results from *in vivo* experiments by Thornton and Bailey [50, 51] demonstrated that the healing ligament is more susceptible to injury under cyclic loads than under static creep loads, which has important implications for the treatment and rehabilitation of ligament injuries. For this reason, many groups have adopted small animal *in vivo* models for studying tendon and ligament fatigue damage. Soslowsky et al. [52], Scott et al. [53] and Millar et al. [54] have used *in vivo* running rat models to study supraspinatus tendon fatigue. Reductions in the tissue extensibility and tensile strength as well as increased cellularity and disruption of the collagen fiber structure were observed following cyclic loading [52]. Results suggested that insulin-like growth factor 1 (**IGF-1**) [53] and pro-inflammatory cytokines [54] may play a role in tendinopathy. Huang et al. [55] and Glazebrook et al.

[56] used similar running rat models to study fatigue of the Achilles tendon. Achilles tendon gross structure was similar for exercised and control rats [55, 56], but collagen disorganization was observed histologically in exercised animals [56]. Fung et al. [57] developed an *in vivo* model which was adopted in several studies to characterize the mechanical and structural changes to the patellar tendon induced by cyclic loading in rats [57-60] and mice [61]. The tendon mechanical properties were measured through controlled uniaxial testing and the fibrous structure was assessed through non-invasive second harmonic generation. Figure 1.7 from Fung et al. [57] shows progressive damage and disruption to the collagen network with increasing levels of fatigue [57, 58, 61]. Analysis of mRNA expression showed modest changes in collagen I, III, and V at early and mid-stage fatigue life and greater changes for late fatigue life [57], which are consistent with pathologic features of human tendon degeneration. Others have adopted the rabbit *in vivo* model [62-64]. Tendon micro-tears have been observed early in fatigue life [64], but surprisingly, gene expression levels in exercised and control rabbits were similar [63].

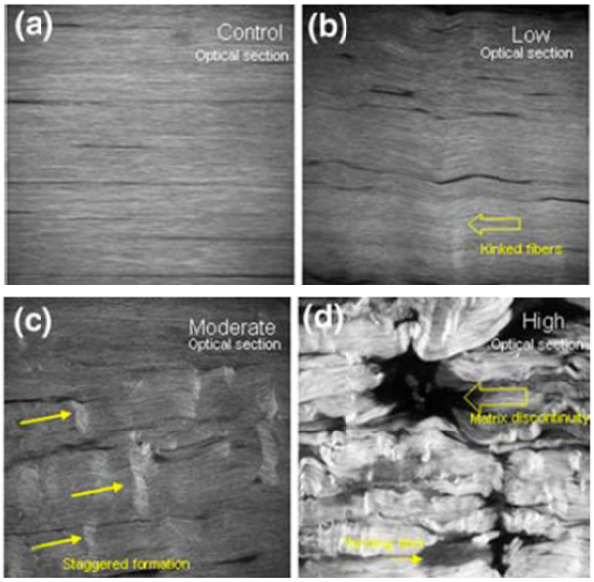

Figure 1.7 *In vivo* second harmonic imaging of rat the patellar tendon over uniaxial fatigue cycling from Fung et al. [57]. Progressive damage and disruption to the collagen structure is shown from (a) the un-fatigued to the (b) low, (c) moderate, and (d) high fatigued states.

1.5 Constitutive modeling of soft collagenous tissue mechanical responses

Early attempts to simulate soft tissue behavior utilized the linear elastic material model, following the generalized Hooke's law [65, 66]

$$\sigma_{ij} = C_{ijkl}\epsilon_{kl} \tag{1.14}$$

where σ_{ij} is the stress tensor, ϵ_{kl} is the strain tensor, and C_{ijkl} is the fourth order elasticity tensor. Linear elastic models are appropriate when the stress-strain relationship is indeed linear, and are typically restricted to relatively small deformations. Linear elastic material properties were chosen for various reasons [67-69], but mainly to simplify the simulation process in order to achieve numerical convergence in finite element (FE) simulation solutions. Over the physiological range of pressures, cardiovascular tissues have been shown to exhibit a relatively linear stress-strain relationship [70]. However, for a FE simulation of tissue deformation from the

undeformed state to a deformed state, the material response is clearly nonlinear and the use of nonlinear material models is essential for any realistic soft tissue simulations. Thus, soft tissues are often assumed to be nonlinear hyperelastic materials.

1.5.1 Modeling of hyperelastic soft collagenous tissue properties

Soft tissues exhibit pronounced mechanical anisotropy, highly nonlinear stress-strain relationships, large deformations, viscoelasticity, and strong mechanical coupling. Thus, simple material models are not suitable for soft tissue applications. In this way, tissue behaves as a hyperelastic material, and the tissue stress-strain response can be derived from a strain energy density function, W. The Second Piola Kirchhoff stress tensor, $\boldsymbol{S}$, can thereby be obtained by

$$\mathbf{S} = \frac{\partial \mathrm{W}}{\partial \boldsymbol{E}}. \tag{1.15}$$

1.5.1.1 Mooney-Rivlin model

Variants of the Mooney-Rivlin strain energy function are commonly used in computational modeling of the aorta [71-77]. The strain energy function for an incompressible Mooney-Rivlin material is given by

$$\mathrm{W} = \mathrm{C}_1(\bar{\mathrm{I}}_1 - 3) + \mathrm{C}_2(\bar{\mathrm{I}}_2 - 3) \tag{1.16}$$

where C_1 and C_2 are material constants and $\bar{I}_1$ and $\bar{I}_2$ are the first and second invariants of the right Cauchy-Green deformation tensor, $\boldsymbol{C}$, given by

$$\bar{I}_1 = tr(\boldsymbol{C}), \tag{1.17}$$

$$\bar{I}_2 = \frac{1}{2}[(tr(\boldsymbol{C}))^2 - tr(\boldsymbol{C^2})]. \tag{1.18}$$

Note that the incompressible Neo-Hookean model, which is also commonly used for soft tissue applications, is a specialization of Eq. (1.16) where $C_2 = 0$. The use of the Mooney-Rivlin model may be suitable for modeling nearly isotropic soft tissue responses under small strains (<20%). The model cannot capture the rapid stiffening effect of soft tissues at large strains.

1.5.1.2 Ogden model

The isotropic and incompressible Ogden model is given in terms of the principal stretches, $\lambda_i, i = 1, 2, 3$, as

$$W = \sum_{p=1}^{N} \frac{\mu_p}{\alpha_p}\left(\lambda_1^{\alpha_p} + \lambda_2^{\alpha_p} + \lambda_3^{\alpha_p} - 3\right) \tag{1.19}$$

where μ_p and α_p are material constants and N is the order. The Ogden model is superior to the Mooney-Rivlin model for modeling isotropic tissue responses to higher strains as shown in Figure 1.8 [78]. Accordingly, the Ogden model is often used to model soft tissue responses under uniaxial tension [79]. However, an anisotropic model is necessary for accurately modeling tissue responses under multi-axial loading conditions.

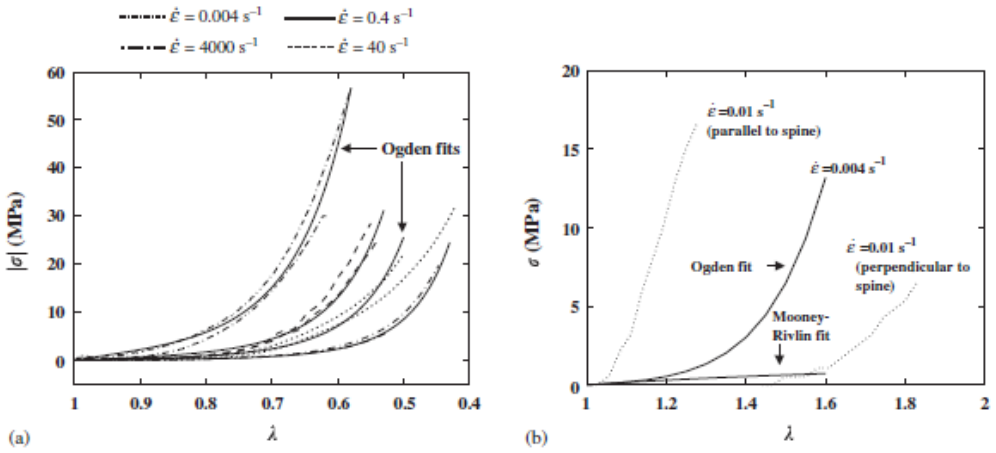

Figure 1.8 The engineering stress versus stretch ratio of pig skin under a) uniaxial compression and b) uniaxial tension at different strain rates adapted from [78]. Note that the Mooney-Rivlin model cannot capture the stiffening portion of the response, and the Ogden model with one set of parameters cannot capture the different material responses in perpendicular directions.

1.5.1.3 Fung-elastic model

The Green-strain based exponential model proposed by Fung [32] is probably the most commonly used hyperelastic model for characterizing the mechanical response of soft tissues [32, 80]. As shown in Figure 1.9, the Fung model can describe the anisotropic biaxial behavior of soft tissues unlike the Ogden model. A two-dimensional Fung-type strain energy function can be expressed as:

$$W = \frac{c}{2}(e^{Q} - 1) \tag{1.20}$$

$$Q = A_1E_{11}^2 + A_2E_{22}^2 + 2A_3E_{11}E_{22} + A_4E_{12}^2 + 2A_5E_{11}E_{12} + 2A_6E_{22}E_{12}$$

where c and A_{1-6} are material constants. Note that Eq. (1.20) has other variants that could be easily treated as a subset or expansion of this model [81]. Eq. (1.20) is often used to model planar biaxial mechanical responses of soft tissues [82] and should be implemented with plane stress elements, such as shell or membrane elements. One problem with Eq. (1.20) is that the transverse shear stiffness (**TSS**) in the 13 and 23

directions are undetermined due to the lack of transmural response definitions in this model. Thus, the TSS is typically assumed. Sun et al. [81] have shown that for FE simulations of bioprosthetic valve closure the valve peak stress is insensitive to changes in TSS values. However, in cases where the tissue bending response is critical such as in valve opening simulations, the use of Eq. (1.20) may give inaccurate results. The 3D Fung model has not been widely used to model soft tissue functions; however, Labrosse et al. [83, 84] has successfully utilized a 3D Fung model in simulation of native aortic valve deformation. Another limitation of the Fung model is that it is phenomenological in formulation. Therefore, there are no descriptions of the tissue structural components and the tissue structure-function relationships are difficult to interpret.

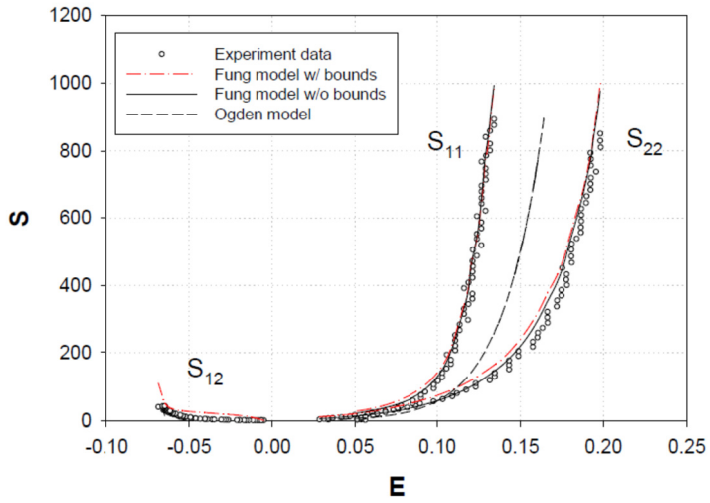

Figure 1.9 Fung and Ogden model fits of glutaraldehyde-treated bovine pericardium equi-biaxial responses adopted from [85]. Note that the Ogden model cannot capture the shear response or anisotropy of the tissue.

1.5.1.4 Strain invariant-based fiber-reinforced hyperelastic model

Soft collagenous tissues are often treated as fiber-reinforced composites because they are comprised of stiff collagen fibers embedded in a compliant matrix. Weiss et al.

[86] and Holzapfel [87] presented a computational framework to implement strain invariant-based models that can accommodate the effects of one or two families of elastic fibers. To use this class of models, soft tissues are typically assumed to be composed of a matrix material with one or more families of embedded fibers, each with a preferred direction. Accordingly, the overall strain energy is decomposed into distinct matrix and fiber contributions by

$$\mathrm{W} = \mathrm{W_m} + \mathrm{W_f} + \mathrm{W_{vol}} \tag{1.21}$$

where W_m and W_f are the isochoric contributions of the matrix and fibers respectively, and W_{vol} is the volumetric strain energy. The deviatoric strain invariant, $\bar{I}_1$, is used to describe the matrix material, and $\bar{I}_{4_i}$ given by

$$\bar{I}_{4_i} = \mathbf{m}_{0_\mathrm{i}} \cdot \boldsymbol{C}\mathbf{m}_{0_\mathrm{i}}, \tag{1.22}$$

is used to describe the properties of the fiber families. Here $\mathbf{m}_{0_\mathrm{i}} \otimes \mathbf{m}_{0_\mathrm{i}}$ denotes the preferred direction of fiber family i.

One example of such models proposed by Holzapfel et al. [87] can be expressed as

$$\mathrm{W_m} = \mathrm{C_{10}}(\bar{\mathrm{I}}_1 - 3), \tag{1.23}$$

$$\mathrm{W_{f_i}} = \frac{\mathrm{k_1}}{2\mathrm{k_2}} \sum_{\mathrm{i}=1}^{2} \left[\exp\left\{ \mathrm{k_2}\left[\kappa \bar{\mathrm{I}}_1 + (1 - 3\kappa)\bar{\mathrm{I}}_{4_\mathrm{i}} - 1 \right]^2 \right\} - 1 \right], \qquad \mathrm{i} = 1,2$$

$$\mathrm{W_{vol}} = \frac{1}{\mathrm{D}}(\mathrm{J} - 1)^2,$$

where C_{10}, k_1, k_2, D are material constants and J is the determinant of the deformation gradient. It can be seen that the matrix response follows the Neo-Hookean form, and D

enforces near incompressibility with small values, i.e. on the order of $1e^{-6}$. For this model, two planar and symmetric fiber families are assumed, thus the preferred fiber family orientations are defined as

$$\mathbf{M}_{\mathrm{i}} = \mathbf{m}_{0_{\mathrm{i}}} \otimes \mathbf{m}_{0_{\mathrm{i}}} \text{ with } \mathbf{m}_{0_1} = [\cos\theta, \sin\theta, 0] \text{ and } \mathbf{m}_{0_2} = [\cos\theta, -\sin\theta, 0], \qquad (1.24)$$

where θ is the angle between the first material axis and the preferred fiber direction moving counter-clockwise. The dispersion parameter, κ, is used to describe the degree of fiber alignment, where $\kappa = 0$ indicates a perfectly aligned fiber family, and $\kappa = \frac{1}{3}$ indicates a completely randomly oriented fiber family.

There are several variations of the model that have been applied to heart valve simulations. Prot et al. [88] implemented the Holzapfel material model into the analysis of healthy and pathological human mitral valves. Similarly, in the study by Stevanella et al. [89], the mitral valve dynamics were simulated where leaflet properties were characterized through a transversely isotropic model proposed by May-Newman and Yin [90], while the same material model was used by Conti et al. [91] and Auricchio et al. [92] to simulate aortic valve biomechanics.

1.5.2 Modeling of inelastic time-dependent soft collagenous tissue properties

There has been less progress in the modeling of the inelastic time-dependent behavior of soft tissue properties. Most groups only consider the quasi-static, elastic tissue response. The time-dependent soft tissue constitutive laws in the literature primarily fall under one of three categories: 1) soft tissue viscoelasticity, which deals with the time-dependent, but recoverable soft tissue property effects; 2) soft tissue damage modeling, which describes the degradation of tissue property due to excessive

mechanical loading; and 3) growth and remodeling frameworks which can describe tissue growth and remodeling over time due to biological and mechanical stimuli. Viscoelastic models have been extensively studied in the literature [13, 87, 93-96]. However, because the characterization of viscoelasticity requires the entire history of deformation in order to take into account its rate dependency [97], it may be impractical to include viscoelasticity when modeling the long-term effects of aging and fatigue damage in biological tissues. The progress on irreversible time-dependent tissue property modeling is discussed in the following sections.

1.5.2.1 Soft tissue damage modeling

In 1987, Simo [98] introduced the concept of a fully three-dimensional finite-strain viscoelastic damage model, based on irreversible thermodynamics with internal variables, as an extension of classical damage mechanics theory. This pioneering work served as the basis for several soft tissue damage models [99-104]. More recent models have been developed to apply both the stress-softening and permanent set effects of damaged soft tissue [102, 104]. Constitutive modeling results of the human carotid artery under cyclic uniaxial tension from Balzani et al. [104] are illustrated in Figure 1.10. Note that this framework as well as others [99-104] can be utilized to model damage phenomena induced by cyclic stretching with increasing magnitude. However, damage in these models is dependent only upon the strain history and not on the number of loading cycles. Under this assumption a tissue specimen subjected to cyclic displacement-control loading will only incur damage during the first cycle given the elastic limits of the tissue are exceeded. However, uniaxial tension fatigue experiments [105] show that the structural and mechanical properties of chemically-treated tissue are

altered at the low fatigue state ($30x10^6$ loading cycles) and continue to change between low and moderate fatigue state ($65x10^6$ cycles) under displacement control loading. This limits the applicability of such models to study long-term tissue property changes due to fatigue damage and aging when the loading conditions are relatively constant throughout life. The inclusion of a continuous damage mechanism is necessary [101, 106]. However, the continuous damage mechanism proposed in the literature by Miehe [139] is very computationally expensive: calculation requires integrating the strain energy at every time interval, and is thus impractical for studying the damage accrued over long periods of time.

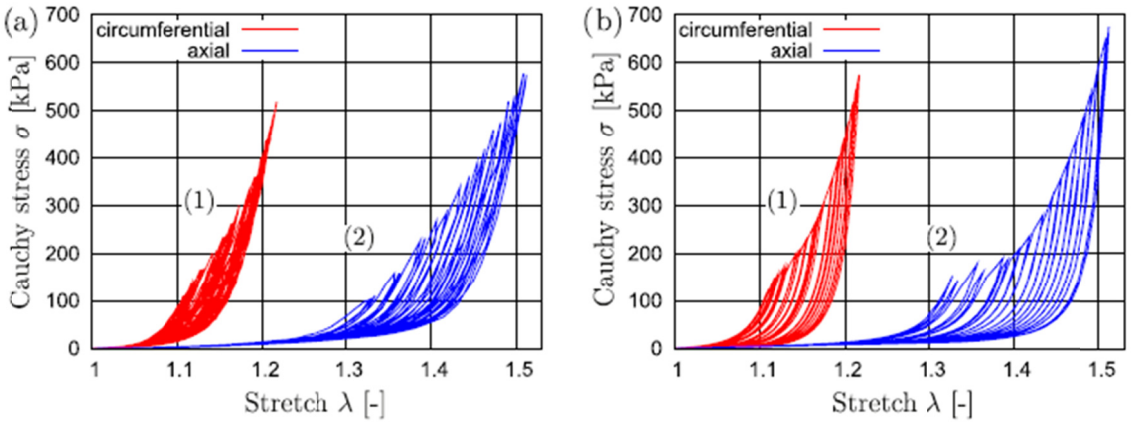

Figure 1.10 Cyclic uniaxial tension tests of human carotid artery in the circumferential and axial directions: a) experimental data, and b) constitutive model prediction adapted from Balzani et al. [104].

1.5.2.2 Tissue growth and remodeling

There are also several groups working on modeling arterial growth and remodeling (**G&R**) [107-115]. These frameworks account for multi-scale arterial property changes in response to time, mechanical loading, and biological stimuli. Most G&R models use the mixed formulation where the tissue properties are the result of the

summation of the quantity and mechanical properties of each constituent, i.e. collagen, elastin, smooth muscle. An advantage of G&R models is that they can be used to elucidate tissue adaptation mechanisms. For instance, the G&R model parameters can be perturbed to capture a known change in the tissue structure and mechanical properties due to aging, and because these parameters have physical interpretations, tissue microstructural changes can be determined. For instance, the work of Valentin, Humphrey, and Holzapfel [115] suggests that the loss of elastin and smooth muscle cells play a key role in the loss of functionality in the aging aorta. However, no evolution equation for elastin or smooth muscle was proposed [115]; thus, age-related changes to the tissue could not be predicted. It is also difficult to obtain the necessary experimental data to calibrate these models.

1.6 Computational modeling of soft collagenous tissues

Constitutive models can be used to determine the stress and strain resulting from a known load acting a particular material with a known initial geometry. For instance, for the planar biaxial test set-up described in section 1.4.1.1, it is relatively straight-forward to calculate the stress-strain response in the center of the specimen where the strain field is homogeneous. However, to determine the stress and strain distributions across the whole specimen including around the attachments where the loads are applied; numerical methods are necessary [93]. Using numerical approaches, complex conditions that may be difficult to replicate physically or describe analytically can be simulated.

1.6.1 Computational modeling of elastic soft collagenous tissues

Computational methods such as the finite element (**FE**) method has been very important in the field of biomechanics, because they make it feasible to consider complex

anatomical geometries and loading conditions in biomedical applications. Structural FE can provide a full and detailed quantitative stress and strain analysis of regions of interest, while computational fluid dynamics can provide a quantitative description of the flow characteristics. Fully-coupled fluid-structure interaction methods are also emerging to more comprehensively model biomechanics particularly for cardiovascular applications.

Early studies employing FE to investigate human aortic valve (**AV**) function began in the 1970s [65, 116, 117]. The valve leaflet geometry data were obtained from photogrammetric analysis of moulds made from human AVs. Thin shell FE models were generated to perform linear elastic stress analysis [65]. Recent advances in non-invasive clinical imaging modalities such as echocardiography (**Echo**), magnetic resonance imaging (**MRI**), and computed tomographic imaging (**CT**), now make it possible to reconstruct 3D patient-specific anatomical models. Many groups are now using patient-specific computational models for a wide range of biomechanics applications including: aorta [72, 76] and aortic aneurysm [71, 73, 118] inflation to assess wall stress, and transcatheter aortic valve replacement [79, 119-123] to evaluate success of the procedure.

1.6.2 Computational modeling of irreversible soft collagenous tissue property changes

Computational simulations utilizing tissue fatigue damage and aging constitutive models calibrated from experimental tests could be extremely useful for studying tissue fatigue and aging in a wide array of applications, yet little has been accomplished in this area.

1.6.2.1 Computational modeling of tissue damage

Several researchers have demonstrated the suitability of continuum damage models to capture the damage and failure responses of tissue through numerical and single-element FE simulations. Ehret and Itskov [14] presented numerical simulations of the softening effect of mouse skin under cyclic uniaxial tension, while Li and Robertson [101] and Maher et al. [124] simulated arterial damage. Li and Robertson [101] also simulated elastin damage and failure in arterial strips subjected to cyclic loading, where a residual strain was observed upon elastin damage due to the collagen recruitment mechanism. Maher et al. [124] simulated softening and permanent set in arterial tissue in a single-element model. Others have adopted more physiologically relevant multi-element simulations of whole tissues to investigate soft tissue damage [99, 100, 103, 125-128]; however, in each case, only one loading cycle was considered.

1.6.2.2 Computational modeling of tissue growth and remodeling

G&R formulations are quite complex which can make them difficult to implement in FE formulations. Most computational growth and remodeling works are thus limited by the use of unrealistic, simplified geometries [110-115]. However, it is well known that the true anatomy plays a critical role in vessel mechanics, thus there is a need for more patient-specific computational models [129]. A more complex computational model is presented by Erickson et al. [130] for the abdominal aortic aneurysm (**AAA**) shown in Figure 1.11. Elastin degradation was prescribed to the model and a volumetric growth and remodeling method was used to investigate changes in the AAA mass, density, and volume over the course years (Figure 1.11). Yet, this also represents an idealistic AAA geometry.

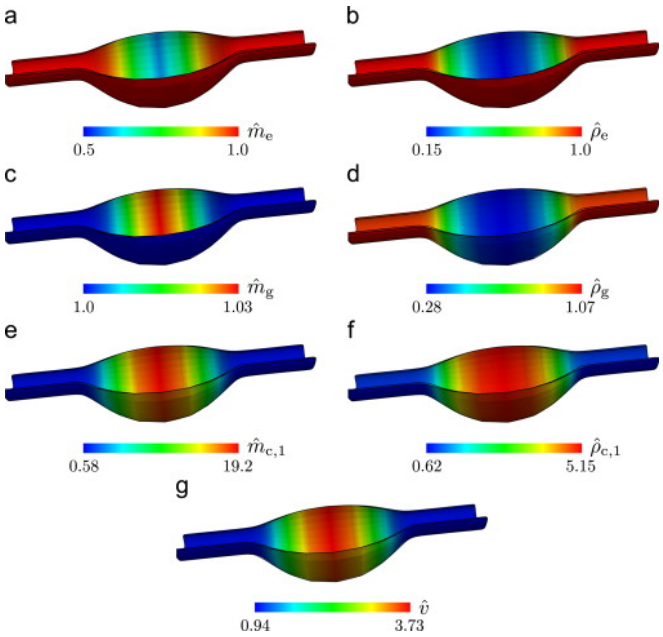

Figure 1.11 Normalized mass, density, and volume in a abdominal aortic aneurysm at t=10 years adapted from [130].

1.7 Motivation of this study

1.7.1 Soft tissue aging and fatigue processes are not well understood

Our existing knowledge of age-related soft tissue property changes is largely based on mean *in vivo* measurements for patient populations stratified by age. However, soft tissue properties, anatomies, *in vivo* loading conditions, and biological factors can vary greatly among patients. Consequently, the roles of mechanical and environmental factors on the progression of permanent tissue property changes are not well understood.

From the work that has been done to study fatigue damage in soft collagenous tissues, it is clear that there are significant and complex changes to the tissue mechanical properties and structure resulting from fatigue. However, the precise relationships between loading modalities, frequency and duration on these fatigue-induced changes

have not been established. Furthermore, the existing data are predominately limited to uniaxial fatigue tests which may not represent physiological loading conditions.

Tissue fatigue and aging constitutive models that can be calibrated from simple, isolated experiments, such as cyclic uniaxial loading, and then implemented in FE could be used to simulate irreversible soft tissue property changes under more complex and physiologically relevant loading conditions. Such models could be beneficial for assessing a patient's risk of developing disease and experiencing tissue degeneration or rupture, and may facilitate the design of durable tissue-based devices and the development of improved diagnostic and disease prevention strategies. An advantage of simulation-based fatigue analysis is that well-controlled parametric studies can be performed to determine the precise effects of different loading, geometry, or design factors.

1.7.2 There is a lack of suitable constitutive frameworks in the literature

Most studies on soft tissue biomechanics reported in the literature thus far, whether experimental, theoretical, or computational, are largely confined to static, instantaneous tissue property characterization. As such, only the recoverable or *elastic* behavior of tissue is considered. From a thermodynamics stand point, permanent changes in tissue structure and material properties represent dissipative, *irreversible*, *inelastic* effects; thus, much of the existing quasi-static work is unsuitable for describing these changes.

There has been very little theoretical work on irreversible soft tissue property changes over time. These phenomena are distinct from tissue hysteresis or viscoelasticity

which represent time-dependent, but recoverable, soft tissue property changes. Many researchers have used growth and remodeling frameworks to investigate tissue adaptation to mechanical and biological stimuli, but these frameworks typically cannot describe the degradation of tissue-derived medical devices with the absence of healing mechanisms over time. Traditional continuum damage mechanics theories have been used to model tissue damage and degradation, but most do not consider geometrical changes, or permanent set, that occur in conjunction with damage. Furthermore, in these studies, tissue damage evolution is only considered when the peak strain throughout the loading history has been exceeded. Under this assumption, a tissue specimen subjected to strain-controlled loading cycles would only incur damage on the first cycle, and experiments have shown that this is not the case [105]. Tissue damage accumulates with cycling, and may become significant over long periods of time. Accordingly, the existing theoretical frameworks are not suitable for modeling the progression of irreversible soft tissue property changes in response to fatigue and aging where the loading conditions are relatively constant.

1.7.3 Objectives of this study

The objective of this study was to develop a theoretical and computational framework to describe the time-dependent inelastic behavior of soft tissues such that the effects of natural aging and mechanical fatigue damage on soft tissues can be accurately modeled. To this end, the following specific aims were proposed:

Aim 1: Develop a theoretical finite thermoelastic framework with internal variables to describe irreversible soft tissue property changes. A phenomenological theoretical framework was developed to describe the time-dependent dissipative property

changes of soft tissues including the accumulation of stress-softening and permanent set. Soft tissue was treated as a nonlinear hyperelastic material, and irreversible property changes were modeled with the inclusion of internal variables following thermodynamic principles. This process involved:

- Determination of the internal variables needed to describe fatigue and aging phenomena in soft tissues
- Determination of the evolution functions for these internal variables
- Development of a constitutive relation to incorporate the internal variables into the stress-strain response

Aim 2: Develop a computational framework to model the finite inelastic behavior of soft tissue. The theoretical framework developed in Aim 1 was particularized for numerical realization. The resulting computational framework was implemented in ABAQUS FE software via a user material subroutine and validated against experimental data. This aim involved:

- Development of an algorithm to update the tissue material response as a function of the number of loading cycles and loading magnitude over the course of an FE simulation
- Verification of the user material subroutine coding in single- and multi-element FE models against analytical solutions
- Incorporation of the constitutive models in simple FE simulations to validate that the time-dependent irreversible tissue behavior can be accurately predicted

Aim 3: Investigate irreversible soft tissue property changes in biomedical applications. Irreversible soft tissue property changes were investigated for two biomedical applications using the computational framework developed in Aim 2. First, tissue property changes with natural aging were modeled for the human ascending aorta (**AA**). Then, the effects of purely mechanical fatigue damage were investigated in bioprosthetic heart valves (**BHV**). This aim involved:

- Characterization of the age-related structural and mechanical property changes of the human AA
- Constitutive modeling of time-dependent inelastic material responses of human AA and glutaraldehyde-treated bovine pericardium (**GLBP**) tissue
- Incorporation of the constitutive models for human AA aging and GLBP fatigue damage in physiologically relevant FE models
- Finite element simulations of human AA aging and GLBP-BHV fatigue damage

1.7.4 Innovation and significance of this study

In this thesis, a theoretical and computational framework for modeling irreversible changes in soft tissue was developed to address a fundamental gap in our understanding of the effects of fatigue and aging on soft tissue properties. The developed computational framework represents a significant enhancement over traditional static FE analyses, because under fatigue and aging conditions, both the tissue geometries and material properties will change, thus, the magnitude and distribution of stress will change. Consequently the location of the initial peak stress identified in a static analysis may not correlate to the ultimate tissue damage and failure regions. The theoretical and

computational fatigue and aging framework developed in this study can be used to predict tissue geometry changes and failure risk over time. Through parametric FE fatigue and aging studies the influence of various factors on the progression of tissue damage may be elucidated, which will improve understanding of these processes, and may facilitate the design of durable tissue-based devices and improved diagnostic and disease prevention methods.

2 THEORETICAL AND COMPUTATIONAL FRAMEWORK FOR MODELING TIME-DEPENDENT IRREVERSIBLE SOFT TISSUE PROPERTY CHANGES

In the previous chapter, we discussed that fatigue damage and natural aging can cause elastin fragmentation and collagen fiber un-crimping in soft collagenous tissues. These phenomena represent time-dependent irreversible effects which may limit the durability of tissue-derived implants, and play a role in the pathogenesis of native tissues. A computational platform to study the effects of soft tissue fatigue and aging effects may improve understanding of these processes and ultimately may facilitate durable tissue-derived device design and improved diagnostic and disease prevention strategies. However, little has been accomplished in the area of constitutive modeling of time-dependent irreversible soft tissue property changes. Thus, in this chapter, a novel theoretical and computational framework to describe time-dependent irreversible phenomena associated with soft tissue fatigue damage and aging is presented. The developed framework is consistent with thermodynamic principles and includes mechanisms for the stress-softening and permanent set observed in fatigued and aged tissues. The theoretical framework was particularized for the finite element (**FE**) method and implemented in ABAQUS commercial FE solver via user material subroutines. The accuracy of the subroutine coding was verified in single- and multi-element simulations, and the ability of the model to describe soft tissue fatigue behavior was demonstrated in uniaxial fatigue simulations. Some of the results of this chapter are published in [35, 131-133].

2.1 Introduction

2.1.1 Clinical significance

Soft tissues undergo irreversible mechanical property changes over time such as stiffening and dilation. These changes occur as a result of natural aging and cyclic loading, but may be accelerated due to elevated mechanical loading and/or the onset and progression of disease. A better understanding of this process is critical for identifying patients at risk of developing disease and experiencing tissue degeneration or rupture, and may facilitate the development of improved diagnostic and disease prevention strategies. A computational platform will be a useful and inexpensive tool to quickly study the effects of soft tissue fatigue and aging. Computational simulations provide for highly controlled and quantitative analyses to study the distinct effects of various loading conditions and design features on tissue durability, and are thus, advantageous over complex fatigue experiments. However, there are a limited number of the necessary constitutive models for describing the fatigue damage process in soft biological tissues.

2.1.2 Theoretical frameworks for modeling time-dependent irreversible soft tissue property changes

While recoverable time-dependent tissue property changes, i.e. viscoelasticity, have been studied, there are few studies on the irreversible tissue property changes brought on by mechanical fatigue, aging, and disease. Most of these works can be classified into one of two groups: soft tissue damage modeling or growth and remodeling (**G&R**) modeling. Most G&R frameworks are based on the hypothesis that G&R occurs to restore stress equilibrium. Thus, these frameworks can be used to investigate the effects of a perturbation in the stress environment; however they typically cannot predict

the change in stress environment that occurs due to fatigue and aging effects: in this case a degradation or damage term is necessary. Natali et al. [6] and Buckley et al. [134] have shown that a damage-based framework can also qualitatively describe age-related soft tissue property changes; however, they do not provide specific evolution equations based on age. Modeling of tissue damage in the literature has been focused on capturing the stress-softening and permanent set phenomena of tissue subjected to supra-physiological loads.

2.1.2.1 Stress softening

As a tissue becomes damaged, the stiffness will degrade and become "softer" much like rubber materials: this phenomenon is referred to as "stress softening". Note that the softening effect is the reduction of the peak stress required to produce a given stretch in the material with respect to the un-fatigued state. Tissue stiffening in response to fatigue is often observed when referencing the post-fatigued state when the permanent set stretches are not included in the overall deformation calculation. When permanent set is included in the analysis, tissues exhibit stress softening. Early soft tissue damage models only accounted for tissue stress softening. Most of which were based on the pioneering work of Simo [98]. In 1987, Simo [98] introduced the concept of a fully three-dimensional finite-strain viscoelastic damage model, based on irreversible thermodynamics with internal variables. According to Simo's work [98], a material is initially characterized by a stored energy (strain energy), W. Damage initiates a departure of free energy, thus for the purpose of soft tissue damage constitutive modeling, a strain energy reduction factor, also known as the stress softening or damage term, D, is incorporated into the strain energy function,

$$W = (1 - D)W_0, \tag{2.1}$$

where $W_0$is the initial stored energy of the tissue. The softening term evolves from 0 at the undamaged state to 1 at complete tissue failure as a function of the maximum equivalent strain [98]. The equivalent strain, Ξ_t, is defined as a scalar measure of the stored energy at time, *t*, given by

$$\Xi_t(\mathbf{E}(t)) := \sqrt{2W^0(\mathbf{E}(t))}, \tag{2.2}$$

where $\boldsymbol{E}(t)$ is the Green strain tensor at time $t \in [0, T]$. Tissue damage is evaluated when the equivalent strain at time *t* equals the maximum equivalent strain observed throughout the strain history. If the maximum equivalent strain exceeds the damage threshold for the particular material or tissue, damage is initiated. The degree of damage is a function of the maximum equivalent strain.

Many different damage evolution equations have been proposed. Early tissue damage models including those by Arnoux et al. [135] and Hokanson and Yazdani's [136], were typically restricted to isotropic damage. However, the damage response of soft tissue is highly dependent on the material orientations [137] and the direction of applied loads. Anisotropy in the stress softening response is particularly important for describing tissue damage under compression or bending, when the stress may be low because the fiber constituents are not bearing load, yet the matrix components are experiencing large deformations.

A common approach to implement anisotropy in the tissue softening is by defining distinct damage criteria for the fibrous and matrix components [13, 99-101, 126, 138, 139]. Typically for fiber reinforced composite materials, such as collagenous

tissues, the strain energy function is split into fiber and matrix responses. The strain energy function is now given by

$$\mathrm{W} = \mathrm{W}_{\mathrm{vol}} + (1 - \mathrm{D}_{\mathrm{m}})\mathrm{W}_{\mathrm{m}}^{0} + (1 - \mathrm{D}_{\mathrm{f}})\mathrm{W}_{f}^{0} \tag{2.3}$$

where W_{vol}, $\mathrm{W}_{\mathrm{m}}^{0}$ and W_{f}^{0} are the volumetric, matrix, and fiber contributions to the strain energy respectively, and D_m and D_f are the softening terms corresponding to the matrix and fiber components respectively. Damage in soft tissue is assumed to be independent of hydrostatic pressure, hence there is no softening term associated with the volumetric response.

The decomposition of the strain energy function, allows for independent definitions of the equivalent strain and thus damage, for the matrix and fiber constituents. Natali et al. [140, 141] and Balzani et al. [125] used this approach but considered only damage to the fibrous components for tendon and arterial applications respectively. For added generality, Rodriguez et al. [100] introduced a damage model that incorporated both fiber and matrix damages of fibrous soft tissue. Isotropic matrix damage was defined using the standard continuum damage framework by Simo [98], but fiber damage was considered to be a stochastic process related to the length and distribution of the collagen fibers [100]. Later, Calvo et al. [99], Peña et al. [13], and Peña and Calvo [126] proposed similar damage models for fibrous tissue taking a continuum approach. Li and Robertson [101] took a multi-mechanism approach for modeling tissue damage by incorporating mechanical and enzymatic degradation of elastin, as well as the recruitment of collagen fibers. Peña and Doblare [139] have also adopted Dorfmann and Ogden's [142] pseudo-elastic approach to describe the softening of vena cava tissue because this

approach is more appropriate for describing the unloading response of tissues compared to other continuum damage models.

2.1.2.2 Permanent set

More recent tissue damage models have also included descriptions for the unrecoverable strains or tissue permanent set in addition to stress softening [14-17, 94, 128, 131, 143]. Several different methodologies have been adopted to describe tissue permanent set. Gasser and Holzapfel [94] presented an elastoplastic constitutive model to capture permanent deformations in damaged biological fiber-reinforced composites. They postulate that the primary mechanism of permanent set in biological tissues is the rupture of proteoglycan bridges between adjacent collagen fibrils which allows for relative sliding of the fibrils and plastic deformation of the matrix material in the direction of the fibers, thus they include a permanent set mechanism only in the fiber direction. The works by Ehret and Itskov [14] and Peña 2011 [16] include tissue permanent set descriptions through the evolution of internal variables. While Francsechini et al. [15] and Maher et al. [17, 124] used Dorfmann and Ogden's [142] theory of pseudo-elasticity to describe the permanent set of brain and arterial tissue respectively. Maher et al. [124] presented a tissue damage constitutive model with distinct softening and permanent set definitions in the matrix and fibers, while many other tissue damage models only considered permanent set in the fibrous components [16, 94]. Maher and Early [144] found that the artery undergoes more significant permanent deformations in the radial direction, thus supporting the inclusion of a non-collagenous matrix permanent set definition. Briefly, damage effects by the pseudo-elasticity theory [142] are enforced through an additive split of the isochoric stress tensor

into the stress softened portion and the inelastic portion. The isochoric stress, S_{isch}, with softening and permanent set is then given by

$$\mathrm{S_{isch}} = (1 - \mathrm{D})\mathrm{S_0} - \mathrm{S_{IN}}, \tag{2.4}$$

where S_0 is the undamaged stress tensor and S_{IN} is the inelastic stress. The magnitudes of the inelastic stresses are dependent on the maximum strain invariant values throughout loading, and thus the permanent sets evolve similar to the softening term, only when the maximum strain is exceeded [124].

2.1.3 Computational modeling of irreversible soft tissue property changes

Several groups have presented physiologically relevant multi-element simulations of whole tissues to investigate soft tissue damage using the tissue damage frameworks discussed in section 2.1.2. Balzani et al. [125] simulated damage to 2D arterial segments due to overstretching while incorporating the artery residual stresses at the unloaded state. Rodriguez et al. [100] simulated tissue damage under tensile torsion in a multi-element FE model; however, damage was only considered in the fibers. Both Calvo et al. [99] and Peña et al. [126] simulated damage to the MCL under tension. The FE models of the human MCL were generated from magnetic resonance imaging (MRI) scans. The tissue mechanical and failure properties in Peña et al. [126] were adopted from experimental failure testing data for the rabbit MCL presented by Woo et al. [127]. Calvo et al. [99] also investigated arterial damage due to balloon angioplasty and clamping. Alastrué et al. [103] implemented the continuum damage model by Calvo et al. [99] and the stochastic damage model by Rodriguez et al. [100] to determine the effect of different methodologies on the predicted damage patterns. The damage patterns in both cases were similar, but the stochastic model predicted more evenly distributed

damage compared to the highly localized damage surrounding areas of large stress gradients predicted by the continuum model [103]. Gasser [128] simulated the effects of supraphysiological pressures in AAA FE models reconstructed from computed tomography-angiography (CTA) images. Areas of localized damage and permanent deformations were identified [128], and demonstrated the promise for computational tissue damage modeling to be used for aneurysm rupture risk assessment.

2.1.4 Motivation of this study

One major limitation of much of the existing modeling work on soft tissue fatigue is the lack of a cycle or time factor in the damage evolution equation. In the literature [13, 16, 98-100, 124-126, 135, 139], the maximum value of $\Xi_t(\boldsymbol{E}(t))$ over the past history up to the current time T was often used to evaluate damage evolution:

$$\Xi_t^{\max} := \max_{0\le t\le T} \sqrt{2W^0(\mathbf{E}(t))}, \tag{2.5}$$

where Ξ_t and Ξ_t^{max} define a damage surface, φ_d, in the strain space given by

$$\varphi_d(\mathbf{E}(t), \Xi_t^{\max}) := \Xi_t(\mathbf{E}) - \Xi_t^{\max} = 0. \tag{2.6}$$

A non-increasing damage criterion in the strain space was defined by the condition $\varphi_d < 0$. However, it should be noted that such damage surface is not suitable for fatigue damage evolution because even if $\Xi_t(\boldsymbol{E})$ is smaller than Ξ_t^{max}, fatigue damage could still occur over continued cycling. For instance, according to Eq. (2.6) a tissue specimen subjected to cyclic displacement-control loading cycles would only incur damage during the first cycle. However, uniaxial tension fatigue experiments [105] show that the structural and mechanical properties of GLBP tissue are altered at the low fatigue state ($30\text{x}10^6$ loading cycles) and continue to change between low and moderate fatigue

states ($65x10^6$ cycles) under displacement control loading. The traditional tissue damage models can only be utilized to model damage induced by cyclic stretching with increasing magnitude. This limits the applicability of such models to study long-term fatigue damage when the loading conditions are relatively constant throughout fatigue life. At normal physiological stress levels, a tissue should not become damaged under a single cycle of loading. Thus, these works are only relevant for studying acute injury due to supraphysiological loads, and not damage related to fatigue or natural aging. The inclusion of a continuous damage mechanism is necessary [101, 106].

Very few groups include a time or cycle dependent soft tissue damage mechanism. A continuous damage evolution parameter based on the accumulated equivalent strain has been presented in the literature [101, 106], where the accumulated equivalent strain, Ξ_t^{acc}, is given as:

$$\Xi_t^{acc}(t) = \int_0^t \left| d\sqrt{2W^0(\mathbf{E}(s))}/ds \right| ds. \tag{2.7}$$

The Ξ_t^{acc} term allows for fatigue damage evolution; however, this approach is computationally expensive for long-term applications.

Furthermore, most constitutive modeling efforts have been focused on just the characterization of experimental data. There is much less studies on the feasibility of using these models in complex computational applications. A computational platform to analyze the effects of fatigue and aging would be a useful and inexpensive tool to quickly study the effects of time and loading. Computational simulations provide for highly controlled and quantitative analyses to study the distinct effects of various loading conditions and design features on tissue durability, and are thus, advantageous over

complex fatigue experiments. The lack of time-dependent computational studies for soft tissues is partly because the time-dependent material models that have been proposed are not typically available in commercial FE codes and because they are often very complex, they can be difficult to implement in commercial codes. Another challenge is the inherent numerical instability and convergence issues associated with many of the nonlinear soft tissue constitutive frameworks.

2.1.5 Overview of this study

In this chapter, a theoretical finite thermoelastic framework with internal variables was developed to describe the accumulation of irreversible soft tissue property changes due to fatigue and aging. The developed theoretical framework was specialized for the FE method and implemented in ABAQUS software via a user-material subroutine. Such computational framework will permit simulation of soft tissue fatigue and aging effects in physiologically relevant conditions which may be difficult to recreate physically. The advantage of using a commercial FE code is that the code has been thoroughly tested and verified for general applications, allowing the user to create models with essentially any geometry, contact conditions, etc. The subroutine coding was verified in single- and multi-element simulations, and applicability of the model to describe soft tissue fatigue effects was demonstrated in uniaxial fatigue simulations.

2.2 Theoretical framework

2.2.1 Initial state tissue properties

Let Ω_0 and Ω be the fixed reference and deformed configurations of a continuous body respectively. We consider the general mapping $\boldsymbol{\chi}: \Omega_0 \rightarrow \boldsymbol{R}^3$, which transforms a

material point $\boldsymbol{X} \in \Omega_0$ to a position $\boldsymbol{x} = \boldsymbol{\chi}(\boldsymbol{X}, t) \in \Omega$ in the deformed configuration at time t. Assuming that the stress at any point in the body Ω_0 depends only on the deformation surrounding that point, from Eq. (1.2), the deformation gradient, $\boldsymbol{F}$, at time t can be written as

$$\mathbf{F}(\mathbf{X}, \mathrm{t}) = \frac{\partial \boldsymbol{\chi}(\mathbf{X}, \mathrm{t})}{\partial \mathbf{X}} \ . \tag{2.8}$$

The Green strain tensor, $\boldsymbol{E}$, can then be defined as a function of $\boldsymbol{F}(\boldsymbol{X}, t)$ from Eqs. (1.4) and (1.5).

$$\mathbf{E}(\boldsymbol{X}, t) = \tfrac{1}{2}(\mathbf{F}^{\mathrm{T}}\mathbf{F} - 1). \tag{2.9}$$

Soft tissues are often assumed to be nearly incompressible ($\det \boldsymbol{F} \approx 1$), anisotropic, nonlinear, hyperelastic material [145] and the un-fatigued strain energy, W^0, can be expressed as a function of $\boldsymbol{E}$. Thus, the in-plane second Piola Kirchhoff stress at the un-fatigued state ($\boldsymbol{S}^0$) can be computed by Eq. (1.15).

2.2.2 Selection of strain-energy function

The theoretical framework described in the proceeding sections is valid for any strain energy function. For soft tissues an appropriate strain energy function should be nonlinear and anisotropic. Therefore, in this study, both the Fung-type strain energy function Eq. (1.20) [32] and two modifications of the Holzapfel structural-based strain energy function Eq. (1.23) [87] were used to describe the tissue initial strain energy (at $t = 0$). The main limitation of the Fung model is that it is purely phenomenological, thus, the individual contributions of the different tissue constituents cannot be elucidated. The modified-Holzapfel model has distinct descriptions of for the matrix and fiber

responses. This structurally-motivated approach to modeling can provide insight into the structure-function relationships of the individual tissue constituents. However, in practice, it is difficult to determine the unique material and time-dependent properties of the matrix and fibers; thus, the parameters are typically determined through curve-fitting, making the model phenomenological as well.

2.2.2.1 *Modified-Holzapfel model*

From Eq. (1.21), the modified-Holzapfel structural-based initial strain energy function is given by

$$\mathrm{W}^0 = \mathrm{W}_\mathrm{m}^0(\bar{\mathbf{C}}) + \mathrm{W}_\mathrm{f}^0(\bar{\mathbf{C}}, \mathrm{M}) + \mathrm{W}_\mathrm{vol}(\mathbf{C}), \tag{2.10}$$

where W_m^0 and W_f^0 represent the initial strain energy for the matrix and fiber components respectively, and W_{vol} is the volumetric strain energy. The definitions for the matrix and fiber strain energies were modified from Eq. (1.23). Two versions of W_m^0 were used:

$$\mathrm{W}_\mathrm{m}^0(\bar{\mathbf{C}}) = \mathrm{c}_1\{\exp[\mathrm{c}_2(\bar{\mathrm{I}}_1 - 3)] - 1\}, \text{and} \tag{2.11}$$

$$\mathrm{W}_\mathrm{m}^0(\bar{\mathbf{C}}) = \mathrm{c}_1\{\exp[\mathrm{c}_2(\bar{\mathrm{I}}_1 - 3)] - 1\} + \left(\frac{I_{1_m}-3}{c_3}\right)\left(\frac{\bar{I}_1-3}{I_{1_m}-3}\right)^{c_3}, \tag{2.12}$$

where $c_{1,2}$ are the matrix parameters at low strains ($\bar{\mathbf{I}}_1 < I_1^m$), I_1^m represents the $\bar{I}_1$ value at which the tissue response rapidly stiffening, and $c_3$is the matrix parameter controlling the stiffness at high strains ($\bar{\mathbf{I}}_1 \geq I_1^m$). The fiber strain energies are given by:

$$\mathrm{W}_{\mathrm{f_i}}^0(\bar{\mathbf{C}}, \mathbf{M_i}) = \begin{cases} \frac{\mathrm{k}_1}{2\mathrm{k}_2}\left[\exp\left\{\mathrm{k}_2\left(\bar{\mathrm{I}}_\mathrm{j} - 1\right)^2\right\} - 1\right] & if\ \bar{\mathrm{I}}_\mathrm{j} \geq 1 \\ 0 & if\ \bar{\mathrm{I}}_\mathrm{j} < 1 \end{cases}, \qquad \mathrm{i} = 1{,}2,\ \ \mathrm{j} = 4{,}6, \tag{2.13}$$

where $\bar{\boldsymbol{C}}$ is the deviatoric right Cauchy-Green tensor and $k_{1,2}$ are the fiber parameters. The fiber orientation is defined by Eq. (1.24) and the W_vol is defined by Eq. (1.23). Note

that the contribution of the fibers is zero under compression ($\bar{I}_j < 1$), because under compression, the response of the tissue is given by the bulk modulus of the ground matrix, whereas the collagen fibers have negligible effects [6].

2.2.3 Inclusion of internal variables

Soft tissue properties are typically defined in terms of the strain energy, W, where the tissue response is a function of the deformation gradient, $\boldsymbol{F}$, only. However, this formulation neglects the effects of temperature, viscoelasticity, and inelasticity. To fully characterize the thermodynamic state of tissue, the energy function, now referred to as the Helmholtz free-energy rather than just the strain energy, is given by [146]:

$$\mathrm{W} = \mathrm{W}(\mathbf{F}, \Theta, \zeta_1, \dots, \zeta_\mathrm{m}) \tag{2.14}$$

where Θ is the absolute temperature, and $\zeta_\alpha, \alpha = 1, \dots, m$ are additional internal variables representing the thermoviscoelastic and inelastic contributions to the material response.

For the purpose of modeling fatigue and aging in cardiovascular tissues, temperature effects on the free-energy are ignored because the *in vivo* temperature is constant (36.8 ºC). Viscoelastic effects are also ignored, because cardiovascular tissues are cyclically loaded at a relatively constant rate *in vivo* in response to the pumping of the heart, and the hysteresis effect of tissue has been shown to diminish over continued cycling [93]. Thus, for cardiovascular tissues, the free-energy is defined in terms of $\boldsymbol{F}$ and two internal variables: a stress-softening parameter, D_s, and a permanent set parameter, $\boldsymbol{D_{ps}}$. The free-energy function can be expressed as:

$$\mathrm{W} = \mathrm{W}(\mathbf{E}, \mathrm{D_s}, \mathbf{D_{ps}}). \tag{2.15}$$

At the un-fatigued state, both $\mathrm{D_s}$ and $\mathrm{D_{ps}}$ are inactive, i.e. $\mathrm{D_s} = 0$ and $\mathbf{D_{ps}} = 0$, thus W is only a function of $\boldsymbol{E}$,

$$\mathrm{W}(\mathbf{E}, 0,0) = \mathrm{W}^0(\mathbf{E}). \tag{2.16}$$

The parameters $\mathrm{D_s}$ and $\mathbf{D_{ps}}$ become active with the onset of fatigue damage induced by cyclic loading and the inclusion of these terms provides a means of changing the form of the strain energy function, which is no longer elastic. The fatigued strain energy function can be expressed as:

$$\mathrm{W}\big(\mathbf{E}, \mathrm{D_s}, \mathbf{D_{ps}}\big). = (1 - \mathrm{D_s})\mathrm{W}^0(\mathbf{E}) + \mathrm{W_{ps}}(\mathbf{E}, \mathrm{D_s}, \mathbf{D_{ps}}), \tag{2.17}$$

where W_{ps} is the dissipated strain energy due to the permanent set and $D_s W^0$ represents the dissipated energy due to the softening effect alone. This form of the energy function is similar to the pseudo-elastic energy function proposed by Dorfmann and Ogden [142] to describe inelastic mechanical behavior of particle-filled elastomers.

2.2.4 Damage evolution

In order to establish the law of tissue fatigue damage evolution, we first start with the equivalent strain Ξ_t [98], Eq. (2.2), a scalar quantity proportional to the strain energy at time t. Here it is assumed that material damage is related to the maximum distortional energy, independent of hydrostatic pressure [98].

Remark 2.1*:* The equivalent strain is analogous to the von Mises stress often used as a damage criterion in traditional engineering materials, in that it is a scalar term, and the contours can define the damage zone of the material in terms of the deformation. The

equivalent strain contours for a representative soft tissue are shown in Figure 2.1 using the Fung model parameters given in Table 2-1.

Since the primary focus of this study is long-term tissue property changes due to natural aging and fatigue damage after millions of cycles of loading, the damage criteria were only evaluated at the peak of each sinusoidal loading cycle to reduce computational time. Therefore, we introduce a peak equivalent strain which is updated after each loading cycle and is equal to the max equivalent strain experienced during the loading portion of that cycle, given explicitly by:

$$\Xi_{\mathrm{n}}^{\mathrm{peak}} = \max_{\mathrm{t}\in\left[\frac{\mathrm{n}}{\mathrm{f}},\frac{\mathrm{n+1}}{\mathrm{f}}\right]} \sqrt{2\mathrm{W}^{0}(\mathbf{E}(\mathrm{t}))} \quad , \quad \mathrm{n} = 0, 1, 2, 3, \cdots, \mathrm{n}_{\mathrm{tot}}, \tag{2.18}$$

where f is the frequency and n is the number of loading cycles up to a maximum number, n_{tot}.

Remark 2.2*:* In the literature [16, 98-100, 103], the maximum value of $\Xi_t(\boldsymbol{E}(t))$ over the past history up to the current time T was used to evaluate damage evolution (Eq.(2.5)), and the damage surface in the strain space was defined by Eq. (2.6). Based on these studies [16, 98-100, 103], a non-increasing damage criterion in the strain space was defined by the condition $\varphi_d < 0$. However, it should be noted that such damage surface is not suitable for fatigue damage evolution because even if $\Xi_t(\boldsymbol{E})$ is smaller than Ξ_t^{max}, fatigue damage could still occur over continued cycling.

Remark 2.3: A continuous damage evolution parameter based on the accumulated equivalent strain has been presented in the literature [101, 106] . The Ξ_t^{acc} term (Eq. (2.7)), allows for fatigue damage evolution; however, this approach is computationally expensive for long-term applications.

Table 2-1 Fung model parameters for a representative soft tissue.

$c\ (kPa)$	A_1	A_2	A_3	A_4	A_5	A_6
1.00	56.19	175.0	-18.02	50.90	-9.67	0.17

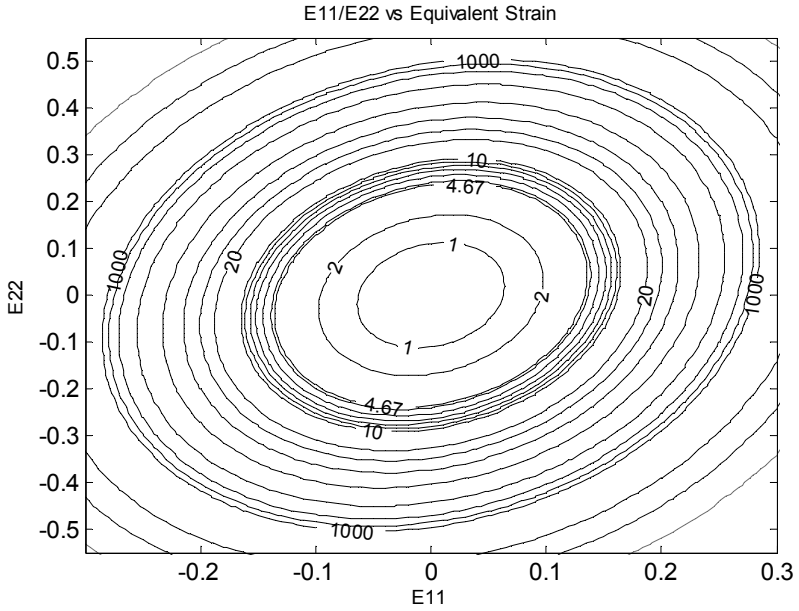

Figure 2.1 Contour plot of the equivalent strain versus the principal Green strains.

2.2.4.1 Peak equivalent strain defined by component

When using a structurally motivated strain energy function divided into distinct contributions from different tissue constituents as in the modified-Holzapfel model, Eq. (2.10), the peak equivalent strain can also be defined in terms of each of the constituents. For Eq. (2.10) the peak equivalent strain for the matrix and fiber constituents are

$$\Xi_{n_m}^{peak} = \max_{t\in\left[\frac{n}{f'}\frac{n+1}{f}\right]} \sqrt{2W_m^0(\mathbf{E}(t))} \ , \ n = 0, 1, 2, 3, \cdots, n_{tot}, \text{ and} \tag{2.19}$$

$$\Xi_{n_f}^{peak} = \max_{t\in\left[\frac{n}{f'}\frac{n+1}{f}\right]} \sqrt{2W_f^0(\mathbf{E}(t))} \ , \ n = 0, 1, 2, 3, \cdots, n_{tot}, \tag{2.20}$$

respectively. The matrix and fiber equivalent strain contours for a representative soft tissue are illustrated in Figure 2.2 using the modified-Holzapfel model (Eqs. (2.11) and (2.13)), and the model parameters given in Table 2-2. Note that the fiber equivalent

strain in Figure 2.2b is unidirectional. Because the fibers are oriented at $\theta = 90°$, the fiber equivalent strain has non-zero values only when the strain in the fiber direction (E_{22}) is positive.

Table 2-2 Modified-Holzapfel model parameters for a typical soft tissue.

$c_1\ (kPa)$	c_2	$k_1\ (kPa)$	k_2	$\theta\ (°)$
1.0	22.67	18.15	147.67	90.0

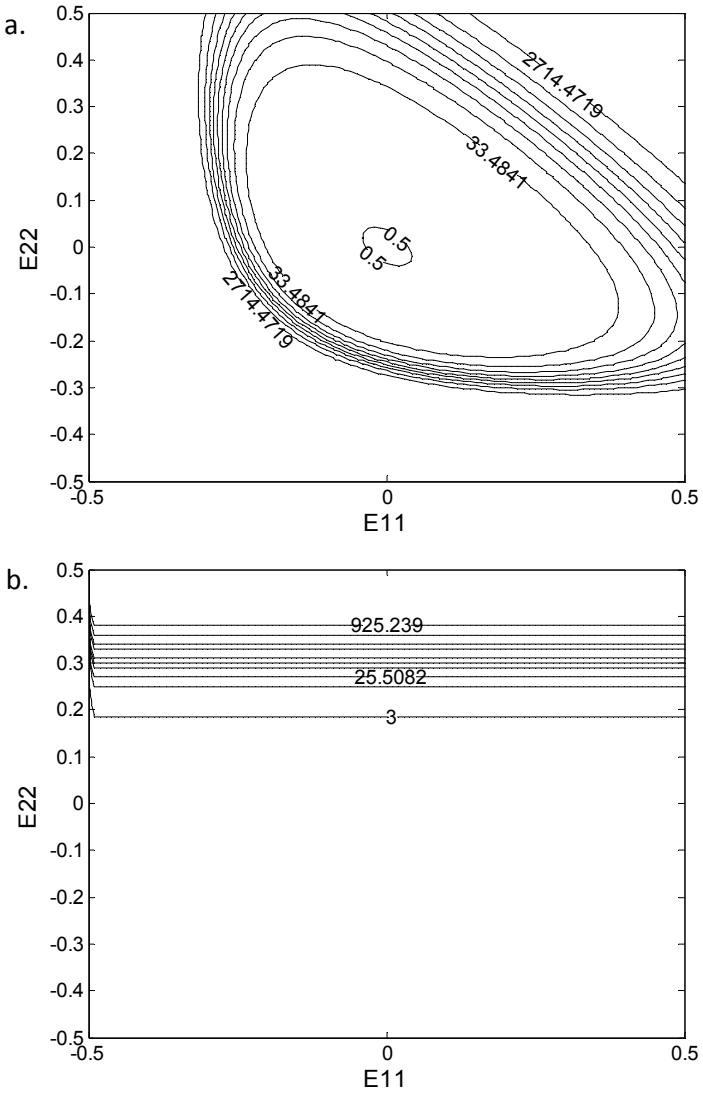

Figure 2.2 Representative equivalent strain contours for the a) matrix and b) fiber components defined by Eqs. (2.11) and (2.13) respectively.

2.2.5 Cycles-to-failure

Two parameters, ψ_{min} and ψ_{max}, are introduced to define the boundaries of the fatigue damage evolution zone. A specimen cyclically loaded to an equivalent strain of ψ_{max} will fail instantaneously during the first loading cycle. A specimen loaded to an equivalent strain of ψ_{min}will be able to endure a maximum number, n_{max}, of loading cycles before complete failure. Therefore, ψ_{min} represents the minimum equivalent strain to elicit the accumulation of fatigue damage, while ψ_{max} represents the tissue maximum equivalent strain limit. Herein, we propose that the number of cycles until failure (n_{tot}) is given by the following equation:

$$n_{tot}\left(\Xi_n^{peak}\right) \tag{2.21}$$

$$= \begin{cases} \infty & if\ \ \Xi_n^{peak} < \psi_{min} \\ \dfrac{\beta(n_{max}-1)}{\Xi_n^{peak} - \psi_{min} + \beta}\left(\dfrac{1 - exp^{\alpha\left(1-\frac{\Xi_n^{peak}}{\psi_{max}}\right)}}{1 - exp^{\alpha\left(1-\frac{\psi_{min}}{\psi_{max}}\right)}}\right) + 1 & if\ \psi_{min} \le \Xi_n^{peak} \le \psi_{max}, \\ 1 & if\ \ \Xi_n^{peak} > \psi_{max} \end{cases}$$

where α and β are material constants governing the amount of damage incurred by a single cycle at Ξ_n^{peak}. These parameters are intrinsic of a material and should be measured from tissue fatigue tests conducted at different Ξ_n^{peak} values. The inclusion of fitted parameters α and β allow the model to capture a wide range of fatigued tissue responses. The effects of varying α and β in Eq. (2.21) on the number of cycles to failure, n_{tot}, are illustrated in Figure 2.3. Increasing α decreases the number of cycles-to-failure, particularly at high Ξ_n^{peak} values, while increasing β increases the number of cycles-to-failure, particularly at low Ξ_n^{peak} values.

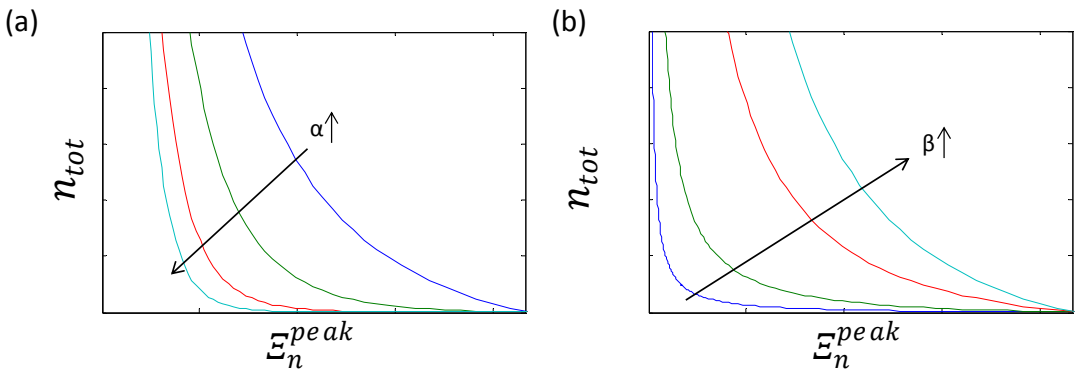

Figure 2.3 Illustration of the effects of (a) α and (b) β on the number of cycles to failure.

Remark 2.4: The cycles-to-failure curve proposed is analogous to the S-N (stress versus cycle) curve used to express the fatigue properties of traditional engineering materials. An equivalent-strain based formulation was employed to facilitate model calibration through displacement-controlled fatigue experiments where Ξ_n^{peak} is held relatively constant throughout loading. The n_{tot} function can be determined from a series of fatigue-to-failure experiments under different Ξ_n^{peak} values.

2.2.5.1 Cycles-to-failure defined by component

The cycle-to-failure equation can also be defined by component when the peak equivalent strain is defined by component. For Eq. (2.10) the cycles-to-failure for the matrix and fiber components are

$$\mathrm{n}_{\mathrm{tot}_\mathrm{m}}\left(\Xi_{\mathrm{n_m}}^{\mathrm{peak}}\right)$$

$$= \begin{cases} \infty & if\ \ \Xi_{\mathrm{n_m}}^{\mathrm{peak}} < \psi_{min_m} \\ \dfrac{\beta_m\left(n_{max_m}-1\right)}{\Xi_{\mathrm{n_m}}^{\mathrm{peak}} - \psi_{min_m} + \beta_m}\left(\dfrac{1-exp^{\alpha_m\left(1-\frac{\Xi_{\mathrm{n_m}}^{\mathrm{peak}}}{\psi_{max_m}}\right)}}{1-exp^{\alpha_m\left(1-\frac{\psi_{min_m}}{\psi_{max_m}}\right)}}\right)+1 & if \Xi_{\mathrm{n_m}}^{\mathrm{peak}} \le \Xi_{\mathrm{n_m}}^{\mathrm{peak}} \le \psi_{max_m}, \\ 1 & if\ \ \Xi_{\mathrm{n_m}}^{\mathrm{peak}} > \psi_{max_m} \end{cases} \tag{2.22}$$

and

$$\mathrm{n}_{\mathrm{tot}_\mathrm{f}}\left(\Xi_{\mathrm{n_f}}^{\mathrm{peak}}\right)$$

$$= \begin{cases} \infty & if\ \ \Xi_{\mathrm{n_f}}^{\mathrm{peak}} < \psi_{min_f} \\ \dfrac{\beta_f\left(n_{max_f}-1\right)}{\Xi_{\mathrm{n_f}}^{\mathrm{peak}} - \psi_{min_f} + \beta_f}\left(\dfrac{1-exp^{\alpha_f\left(1-\frac{\Xi_{\mathrm{n_f}}^{\mathrm{peak}}}{\psi_{max_f}}\right)}}{1-exp^{\alpha_f\left(1-\frac{\psi_{min_f}}{\psi_{max_f}}\right)}}\right)+1 & if\ \Xi_{\mathrm{n_f}}^{\mathrm{peak}} \le \Xi_{\mathrm{n_f}}^{\mathrm{peak}} \le \psi_{max_f}, \\ 1 & if\ \ \Xi_{\mathrm{n_f}}^{\mathrm{peak}} > \psi_{max_f} \end{cases} \tag{2.23}$$

respectively. Note that the damage zone defined by ψ_{min} and ψ_{max} and the material parameters α and β, can be defined distinctly for the matrix and fibers to more accurately model the soft tissue fatigue damage response.

Remark 2.5: Typically the fibrous components of soft tissues are naturally oriented in the direction of peak stress; thus, the equivalent strain may be higher in the fibers than in the matrix. However, this does not necessarily mean that the fibers will become more damaged than the matrix components. The minimum equivalent strain to induce damage

to the fibers is likely higher than that of the matrix. Indeed, elastin degradation with aging is well-documented, but the collagen fibers largely remain intact, albeit straightened out. Defining the cycles-to-failure by component provides a mechanism to characterize the enhanced durability of the fibers versus the matrix despite being under higher loading.

2.2.6 Stress-softening

The stress softening caused by cyclic fatigue damage is considered to be a function of both the equivalent strain and the number of loading cycles. For tissue long-term aging and fatigue applications, since we are interested in the accumulation of damage over millions of cycles, we assume that at a given equivalent strain, an equal amount of damage is accumulated during each loading cycle, representing a linear accumulation of damage over millions of cycles. Therefore, the total amount of damage due to stress softening, D_s, after *n* tensile loading cycles is given by

$$D_s\left(\Xi_n^{peak}\right) = \begin{cases} 0 & \text{if } \Xi_n^{peak} < \psi_{min} \\ \sum_{n=0}^{n} \frac{1}{n_{tot}} & \text{if } \psi_{min} \le \Xi_n^{peak} \le \psi_{max}. \\ 1 & \text{if } \Xi_n^{peak} > \psi_{max} \end{cases} \tag{2.24}$$

It can be seen that an increase in α results in greater damage due to stress softening at low Ξ_n^{peak} values (Figure 2.4a), whereas an increase in β has the converse effect (Figure 2.4b). The degree of stress softening is more sensitive to changes in β at low Ξ_n^{peak} values, but more sensitive to changes in α at high Ξ_n^{peak} values.

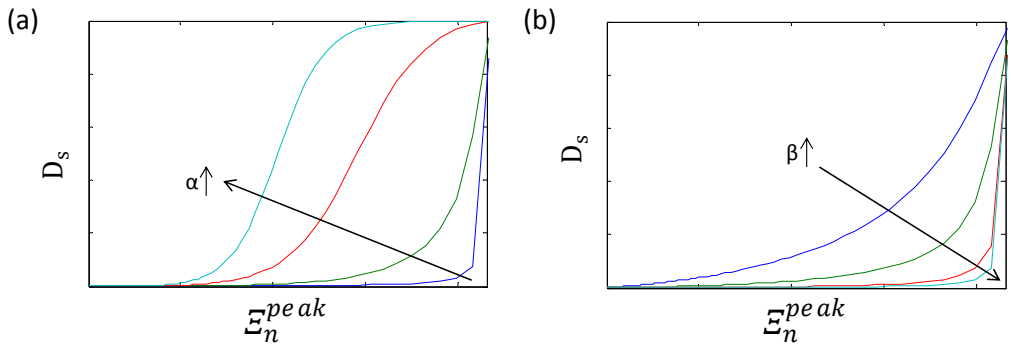

Figure 2.4 Illustration of the effects of (a) α and (b) β on the degree of stress softening.

Remark 2.6: Because there is a limited amount of experimental data showing the accumulation of damage over continued cycling, a linear accumulation of damage was assumed. However, Eq. (2.24) could be easily modified by introducing a nonlinear, time-dependent accumulation of damage, provided that experimental fatigue data are available at different time points for quantifying such nonlinear accumulations of damage.

Remark 2.7: *In vivo* valve and vessel tissues are deformed under pressure loading (i.e., a load-control condition); therefore, the Ξ_n^{peak} value will change (e.g. increase) from cycle to cycle as the tissue softens, thus, the n_{tot} will decrease each cycle, representing accelerated fatigue damage compared to the displacement-control loading condition. This means that even with using a linear D_s evolution function, the D_s predicted under load-control conditions will be nonlinear.

2.2.6.1 Stress softening defined by component

Similarly, the stress softening to the matrix and fiber components are given by

$$D_{s_m}\left(\Xi_{n_m}^{peak}\right) = \begin{cases} 0 & \text{if } \Xi_{n_m}^{peak} < \psi_{min_m} \\ \sum_{n=0}^{n} \frac{1}{n_{tot_m}} & \text{if } \psi_{min_m} \leq \Xi_{n_m}^{peak} \leq \psi_{max_m}, \\ 1 & \text{if } \Xi_{n_m}^{peak} > \psi_{max_m} \end{cases} \tag{2.25}$$

and

$$D_{s_f}\left(\Xi_{n_f}^{peak}\right) = \begin{cases} 0 & \text{if } \Xi_{n_f}^{peak} < \psi_{min_f} \\ \sum_{n=0}^{n} \frac{1}{n_{tot_f}} & \text{if } \psi_{min_f} \leq \Xi_{n_f}^{peak} \leq \psi_{max_f}, \\ 1 & \text{if } \Xi_{n_f}^{peak} > \psi_{max_f} \end{cases} \tag{2.26}$$

respectively.

2.2.7 Permanent set

Tissue damage is associated with irreversible tissue elasticity loss. Therefore, when the elastic limits of the tissue are exceeded, a permanent set is exhibited upon unloading. The magnitude of the permanent set, $\boldsymbol{D_{ps}}$, is related to the degree of softening in the tissue and thus is also a function of Ξ_n^{peak}. The permanent set is also related to the peak strain applied to the tissue. For instance, under the cyclic uniaxial tension loading condition, a tissue specimen will permanently elongate in the direction of loading and narrow in the cross-loading directions. The magnitude of the permanent set will increase with the applied peak strain, but cannot exceed the peak strains applied. Because different areas of the tissue may be experiencing different loading conditions, the permanent set definition should be independent of the loading condition.

The permanent set upon complete tissue failure, $\boldsymbol{D_{psmax}}$, can be measured experimentally by quantifying the change in the specimen geometry before and after

fatigue loading. For planar tissues, $\boldsymbol{D_{ps}}$ has components of D_{ps11}, D_{ps22}, and D_{ps12}. For long-term fatigue applications, we assume that at a given equivalent strain, an equal amount of permanent set is accumulated during each loading cycle, representing a linear accumulation of permanent set over millions of cycles.

2.2.7.1 <u>*Peak principal strain approach*</u>

One simple form for the permanent set, $D_{ps_{ij}}$, is given by:

$$\mathrm{D_{ps_{ij}}}\left(\Xi_{\mathrm{n}}^{\mathrm{peak}}\right)=\begin{cases}0 & \text{if } \Xi_{\mathrm{n}}^{\mathrm{peak}}<\psi_{\mathrm{min}}\\ \displaystyle\sum_{\mathrm{n=1}}^{\mathrm{n}}\frac{1}{\mathrm{n_{tot}}}\mathrm{D_{psmax}^{n}}\frac{\mathrm{E_{n_{ij}}^{peak}}}{\mathrm{E_{n}^{max}}} & \text{if } \psi_{\mathrm{min}}\le\Xi_{\mathrm{n}}^{\mathrm{peak}}\le\psi_{\mathrm{max}}\\ \mathrm{D_{psmax}^{n}} & \text{if } \Xi_{\mathrm{n}}^{\mathrm{peak}}>\psi_{\mathrm{max}}\end{cases}. \tag{2.27}$$

Here, the permanent set is scaled by the peak Green strain ratio, $\frac{E_{n_{ij}}^{peak}}{E_n^{max}}$, to enforce anisotropy in the permanent set, where $E_{n_{ij}}^{peak}$ is the Green strain at $\Xi_t = \Xi_n^{peak}$ in direction *ij*, and $E_n^{max} = max\left\{E_{n_{ij}}^{peak}\right\}$. The D_{psmax}^n refers to the maximum permanent set Green strain associated with uniaxial tensile failure along the *kl* direction ($D_{psmax_{kl}}$), where the *kl* direction corresponds to that of E_n^{max}, i.e. $kl = \arg max\left\{E_{n_{ij}}^{peak}\right\}$. Under this modified formulation, we assume that the permanent set is most significant in the direction of the maximum peak strain and that the permanent set in the other directions is proportional to the ratio of peak strains. The representative contour plots in Figure 2.5 show the permanent sets predicted by Eq. (2.27) with the Fung model parameters in Table 2-2 and the time-dependent inelastic model parameters given in Table 2-3 as a function of the peak principle Green strains.

Table 2-3 Time-dependent inelastic model parameters used to illustrate the permanents sets predicted by Eq. (2.27) as a function of the peak principle Green strains.

Inelastic model material parameters						
$\psi_{min}\left(\frac{\sqrt{kN}}{m}\right)$	$\psi_{max}\left(\frac{\sqrt{kN}}{m}\right)$	n_{max}	α	β	$D_{psmax_{11}}$	$D_{psmax_{22}}$
2.0	10,000	1,000	1.00	0.1	0.1	0.1

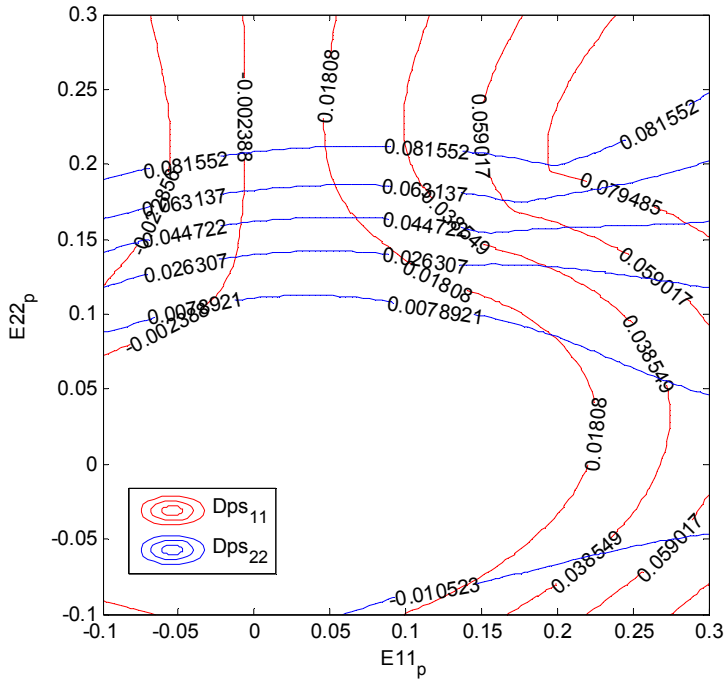

Figure 2.5 Contour plot of the anisotropic permanent set versus the principal Green strains.

Remark 2.8: The permanent set as defined in Eq. (2.27) is analogous to the plastic strain in classical finite strain elastoplasticity theory, where the plastic strain, $\boldsymbol{\varepsilon_P}$, is given by

$$\boldsymbol{\varepsilon_P} = \dot{\lambda}\frac{\partial f}{\partial \boldsymbol{\sigma}}, \tag{2.28}$$

$\dot{\lambda}$ is a loading index and f is a yield function, dependent on the current stress ($\boldsymbol{\sigma}$) state and the previously accumulated plastic strains [147]. For the purpose of this study, the tissue permanent set was considered to be a function of Ξ_n^{peak}, which serves as the yield function, and the peak strains, which reflect the current stress state.

2.2.7.2 Permanent set defined by component

The permanent set can also be defined by component. Two different approaches were explored. The first approach is very similar to that presented in section 2.2.7.1, only the permanent set was only defined for the matrix materials. The permanent set was assumed to be dependent on the matrix damage rather than the fiber damage on account of experimental observations that permanent sets are more significant perpendicular to the preferred fiber orientation in aortic and carotid tissues [144]. Accordingly, the tissue permanent set, D_{ps}, is given by [132]:

$$\mathrm{D}_{\mathrm{ps}_{\mathrm{ij}}}\left(\Xi_{\mathrm{n_m}}^{\mathrm{peak}}\right) \tag{2.29}$$

$$= \begin{cases} 0 & \text{if } \Xi_{\mathrm{n_m}}^{\mathrm{peak}} < \psi_{\mathrm{min_m}} \\ \displaystyle\sum_{\mathrm{n}=1}^{\mathrm{n}} \frac{1}{\mathrm{n}_{\mathrm{tot_m}}} \mathrm{D}_{\mathrm{psmax}}^{\mathrm{n}} \frac{\mathrm{E}_{\mathrm{n_{ij}}}^{\mathrm{peak}}}{\mathrm{E}_{\mathrm{n}}^{\mathrm{max}}} \quad \mathrm{i,j} = 1,2 & \text{if } \psi_{\mathrm{min_m}} \leq \Xi_{\mathrm{n_m}}^{\mathrm{peak}} \leq \psi_{\mathrm{max_m}}. \\ \mathrm{D}_{\mathrm{psmax}}^{\mathrm{n}} & \text{if } \Xi_{\mathrm{n_m}}^{\mathrm{peak}} > \psi_{\mathrm{max_m}} \end{cases}$$

Remark 2.9: Note that although only the matrix cycles-to-failure term, $\frac{1}{n_{tot_m}}$, appears in Eq. (2.29), under the affine deformation assumption considered in this framework, permanent set of the matrix component will also induce permanent set in the fiber direction. While this formulation is simple, it can accommodate anisotropy in the permanent set because the $E_{n_{ij}}^{peak}$ is a function of the stress and stiffness in direction i.

To add flexibility to the permanent set calculation, it can also be defined in terms of the matrix and fiber components distinctly. Accordingly, the matrix contribution to the permanent set is given by

$$D_{ps_{m_{ij}}}\left(\Xi_{n_m}^{peak}\right) \tag{2.30}$$

$$= \begin{cases} 0 & if\ \Xi_{n_m}^{peak} < \psi_{min_m} \\ \sum_{n=1}^{n} \frac{1}{n_{tot_m}} D_{ps_m}^{max} \left(\frac{\mathrm{E}_{\mathrm{n_{ij}}}^{\mathrm{peak}}}{\mathrm{E}_{\mathrm{n}}^{\mathrm{max}}} \right) \quad \mathrm{i,j} = 1,2 & if\ \psi_{min_m} \leq \Xi_{n_m}^{peak} \leq \psi_{max_m} \\ D_{ps_m}^{max} & if\ \Xi_{n_m}^{peak} > \psi_{max_m} \end{cases}.$$

Note that this permanent set definition is identical to Eq. (2.29). Similarly, the fiber contribution to the permanent set is given by

$$D_{ps_f}\left(\Xi_{n_m}^{peak}\right) \tag{2.31}$$

$$= \begin{cases} 0 & if\ \Xi_{n_f}^{peak} < \psi_{min_f} \\ \sum_{n=1}^{n} \frac{1}{n_{tot_f}} D_{ps_f}^{max} \quad i = 1,2,3 & if\ \psi_{min_f} \leq \Xi_{n_f}^{peak} \leq \psi_{max_f} \\ D_{ps_f}^{max} & if\ \Xi_{n_f}^{peak} > \psi_{max_f} \end{cases}.$$

Note that the fiber permanent set contribution is a scalar unlike the matrix contribution which is a tensor. This is because the fibers are assumed to only contribute to the permanent set along the preferred fiber direction. Physically this can be interpreted as the fiber un-crimping process.

The overall tissue permanent set can then be expressed in terms of a deformation gradient, $\boldsymbol{F}_{ps}$, as

$$\boldsymbol{F}_{ps} = \boldsymbol{F}_{ps_m} + D_{ps_f}\boldsymbol{M} - \boldsymbol{F}_{ps_m}\boldsymbol{M} \tag{2.32}$$

where $\boldsymbol{F}_{ps_m}$ is the deformation gradient associated with the matrix contribution to the permanent set, $\boldsymbol{D}_{\boldsymbol{ps_m}}$, calculated from Eqs. (1.4) and (1.5). The tissue permanent set expressed as a Green Strain is then

$$\boldsymbol{D}_{ps} = \frac{1}{2}(\boldsymbol{F}_{ps}^{T}\boldsymbol{F}_{ps} - \boldsymbol{I}). \tag{2.33}$$

The matrix and fiber permanent sets predicted by Eqs. (2.30) and (2.31) respectively for a representative tissue are illustrated in Figure 2.6 using the modified-Holzapfel model parameters in Table 2-2 and the time-dependent inelastic model parameters of Table 2-4. Note that the matrix permanent set contours in the 11 and 22 directions are symmetric, because it is an isotropic material, and the fiber permanent set only occurs in the 22 direction corresponding to the fiber direction.

Table 2-4 Time-dependent inelastic model parameters used to illustrate the matrix and fiber permanent sets predicted by Eqs. (2.30) and (2.31) as a function of the peak principle Green strains.

Inelastic model matrix material parameters					
$\psi_{min_m}\ (\frac{\sqrt{kN}}{m})$	$\psi_{max_m}\ (\frac{\sqrt{kN}}{m})$	n_{max_m}	α_m	β_m	D_{psmax_m}
0.1	1000.0	200.0	1.0	1.0	0.105
Inelastic model fiber material parameters					
$\psi_{min_f}\ (\frac{\sqrt{kN}}{m})$	$\psi_{max_f}\ (\frac{\sqrt{kN}}{m})$	n_{max_f}	α_f	β_f	D_{psmax_f}
0.1	10,000.0	200.0	1.0	0.1	0.105

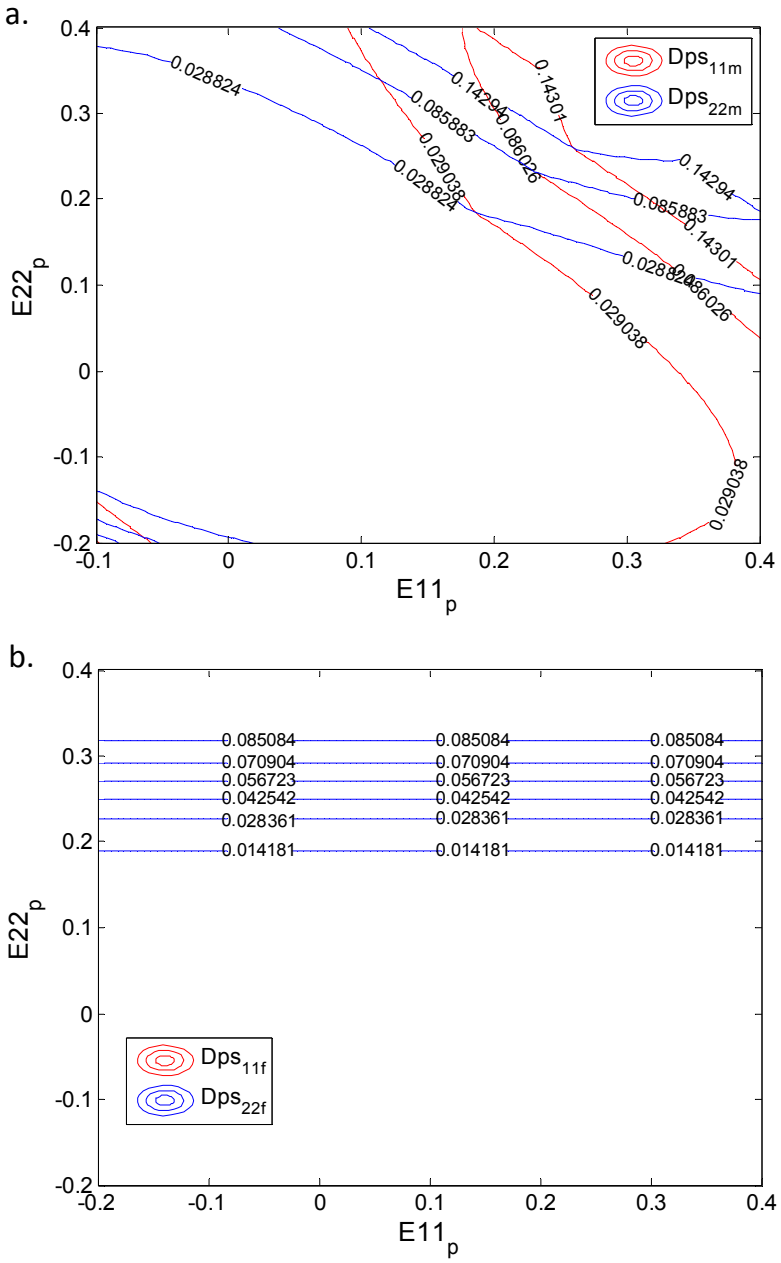

Figure 2.6 Representative permanent set contours for the a) matrix and b) fiber components as a function of the peak principal strains.

2.2.8 Incorporation of the permanent set in the material response

We employ a plastic stress, $\boldsymbol{S_P}$, to enforce the permanent set [131].

$$\mathbf{S_P} = -\frac{\partial(1-\mathrm{D_s})\mathrm{W}^0}{\partial \mathbf{E}}|_{(\mathbf{E}=\mathbf{D_{ps}})}. \tag{2.34}$$

The $\boldsymbol{S_P}$ contribution to the overall tissue response is governed by η in Eq. (2.36), which was modified from Dorfmann and Ogden's η function [142] in order to accommodate for the dissipated equivalent strain associated with the permanent set, Ξ_{ps}, defined by

$$\Xi_{\mathrm{ps}} := \sqrt{2\mathrm{W}^0(\mathbf{E}(\mathrm{t}))}|_{(\mathbf{E}=\mathbf{D_{ps}})}. \tag{2.35}$$

$$\eta = \frac{\Xi_{\mathrm{t}} - \Xi_{\mathrm{ps}}}{\Xi_{\mathrm{n}}^{\mathrm{peak}} - \Xi_{\mathrm{ps}}}, \tag{2.36}$$

It can be seen that the magnitude of $\boldsymbol{S_P}$ depends on the magnitude of the permanent sets. The η term is a function of Ξ_{t} that modulates the transition of $\boldsymbol{S_P}$ from the inactive phase ($\eta = 1$) at peak loading, i.e. $\Xi_t = \Xi_n^{peak}$, to the fully active phase ($\eta = 0$) at the permanent set.

Remark 2.10: Residual strains in [16] are enforced by altering the strain invariants. This would be analogous to implementing the permanent set by shifting the Green strains in this formulation, i.e. $\boldsymbol{E}_n = \boldsymbol{E}^0 + \boldsymbol{D_{ps}}$. This permanent set formulation may be more intuitive, and would be easy to calibrate with experimental data. However, we chose to use a stress formulation to describe the permanent sets to facilitate the implementation into finite element (**FE**) software ABAQUS in which only the stress and stiffness tensors are defined explicitly and the strains approximated.

Remark 2.11: The purpose of the η function is to control the $\boldsymbol{S_p}$ contribution to the tissue response. For this reason, we chose a simple form for η. A more sophisticated functional form may be necessary for the accurate modeling of unloading cycles.

2.2.9 Tissue response with irreversible time-dependent effects

The overall fatigued response expressed as the second Piola-Kirchoff stress, $\boldsymbol{S}$, is given by:

$$\mathbf{S} = (1 - \mathrm{D_s})\frac{\partial \mathrm{W}^0}{\partial \mathbf{E}} + \frac{\partial (1 - \mathrm{D_s})}{\partial \mathbf{E}}\mathrm{W}^0 + \frac{\partial \mathrm{W_{ps}}}{\partial \mathbf{E}} + \frac{\partial \mathrm{W_{ps}}}{\partial \mathrm{D_s}}\frac{\partial \mathrm{D_s}}{\partial \mathbf{E}} + \frac{\partial \mathrm{W_{ps}}}{\partial \mathbf{D_{ps}}} : \frac{\partial \mathbf{D_{ps}}}{\partial \mathbf{E}}. \tag{2.37}$$

It is assumed that $\mathrm{D_s}$ and $\mathbf{D_{ps}}$ are independent of $\boldsymbol{E}$, i.e. $\frac{\partial \mathrm{D_s}}{\partial \mathbf{E}} = \frac{\partial \mathbf{D_{ps}}}{\partial \mathbf{E}} = 0$, which is valid within a loading cycle because both are functions of $\Xi_{\mathrm{n}}^{\mathrm{peak}}$ only and at a given cycle $\Xi_{\mathrm{n}}^{\mathrm{peak}}$ is a constant value. The permanent set contribution is defined implicitly through Eqs. (2.17) and Eqs. (1.24)-(2.2).

$$\frac{\partial \mathrm{W_{ps}}}{\partial \mathbf{E}} = (1 - \eta)\mathbf{S_P}. \tag{2.38}$$

Thus, the second Piola-Kirchhoff stress tensor may be expressed in the following reduced form:

$$\mathbf{S} = (1 - \mathrm{D_s})\frac{\partial \mathrm{W}^0}{\partial \mathbf{E}} + \ (1 - \eta)\mathbf{S_p}. \tag{2.39}$$

Here it can be seen that at peak loading, $\Xi_t = \Xi_n^{peak}$, $\boldsymbol{S}$ is reduced to Eq. (2.40) because $\eta = 1$, and at no load ($\mathbf{E} = \mathbf{D_{ps}}$ and $\eta = 0$) $\mathbf{S}$ is given by Eq. (2.41).

$$\mathbf{S} = (1 - \mathrm{D_s})\frac{\partial \mathrm{W}^0}{\partial \mathbf{E}} \tag{2.40}$$

$$\mathbf{S} = (1 - \mathrm{D_s})\frac{\partial \mathrm{W}^0}{\partial \mathbf{E}} + \ \mathbf{S_P} \tag{2.41}$$

The elasticity tensor in the material description may be expressed in the following form:

$$\mathbb{C}(\mathrm{n}) = \frac{\partial}{\partial \mathbf{E}}\left((1-\mathrm{D_s})\frac{\partial \mathrm{W}^0}{\partial \mathbf{E}} + (1-\eta)\mathbf{S_P}\right). \tag{2.42}$$

Eq. (2.42) can be expanded using the chain rule to

$$\mathbb{C}(\mathrm{n}) = \frac{-\partial \mathrm{D_s}}{\partial \mathbf{E}} : \frac{\partial \mathrm{W}^0}{\partial \mathbf{E}} + (1-\mathrm{D_s})\frac{\partial^2 \mathrm{W}^0}{\partial \mathbf{E}^2} + \frac{-\partial \eta}{\partial \mathbf{E}} : \mathbf{S_P} + (1-\eta)\frac{\partial \mathbf{S_P}}{\partial \mathbf{E}}. \tag{2.43}$$

Again, because D_s and $\boldsymbol{S_P}$ are functions of only Ξ_n^{peak}, both values are constant throughout loading/unloading, these terms do not affect the stiffness matrix. Thus, $\mathbb{C}$ can be reduced to

$$\mathbb{C}(\mathrm{n}) = (1-\mathrm{D_s})\frac{\partial^2 \mathrm{W}^0}{\partial \mathbf{E}^2} - \mathbf{S_P} : \frac{\partial \eta}{\partial \mathbf{E}}, \tag{2.44}$$

where $\frac{\partial \eta}{\partial \mathbf{E}}$ was solved by applying the chain rule as

$$\frac{\partial \eta}{\partial \mathbf{E}} = \frac{\partial \eta}{\partial \Xi_\mathrm{t}} \frac{\partial \Xi_\mathrm{t}}{\partial \mathrm{W}^0} \frac{\partial \mathrm{W}^0}{\partial \mathbf{E}}. \tag{2.45}$$

Combining Eqs. (2.34), (2.44), and (2.45) the stiffness matrix can then be expressed as

$$\mathbb{C}(\mathrm{n}) = (1-\mathrm{D_s})\frac{\partial^2 \mathrm{W}^0}{\partial \mathbf{E}^2} - \mathbf{S_P} : \frac{1}{\Xi_\mathrm{n}^{\mathrm{peak}} - \Xi_{\mathrm{ps}}} \frac{1}{\sqrt{2\mathrm{W}^0}} \frac{\partial^2 \mathrm{W}^0}{\partial \mathbf{E}^2}. \tag{2.46}$$

The damage induced by fatigue is a non-reversible, non-decreasing quantity. Therefore, the following conditions must be satisfied:

$$\frac{\partial \mathrm{D_s}}{\partial \mathrm{t}} \geq 0, \frac{\partial \mathbf{D_{ps}}}{\partial \mathrm{t}} \geq 0. \tag{2.47}$$

These conditions make this model distinct from models to capture the Mullin's effect in rubbers. For the Mullin's effect, $\mathrm{D_s}$ and $\mathbf{D_{ps}}$ become inactive during reloading (even after the material has been damaged) and the material response follows the primary loading curve once the previous maximum strain has been exceeded. Additional damage is only realized when the material is unloaded again. For the purpose of modeling long-

term fatigue damage, damage is only evaluated at the peak of each loading cycle, at which point the stress and stiffness matrices are updated. The unloading curve then reflects the updated fatigue response. Each reloading curve follows the previous unloading curve until damage is reevaluated at the peak load. In this case, the incremental damage over one cycle is very small, and therefore, the loading and subsequent unloading curve may be nearly identical.

2.2.10 Parametric study of model parameters

The effect of the time-dependent inelastic model parameters on the soft tissue response over cycling is demonstrated in the parametric studies in the following sections.

2.2.10.1 Effect of β on the tissue response over cycling

It was shown in Figure 2.3 that α and β control the amount of incremental damage per cycle, where α has a stronger influence at high Ξ_n^{peak} values, and β has a stronger influence at low Ξ_n^{peak} values. Thus, the effect of β on the uniaxial tissue response under physiological range loads was investigated analytically using the Fung model parameters in Table 2-1 and the time-dependent inelastic model parameters in Table 2-3, with β values of 0.27, 0.5, 3, and 5.

The exemplary effects of changing β on the fatigue damage due to both stress softening and permanent sets are illustrated in Figure 2.7. Using these parameters it is clear that the cycle-dependent tissue response is highly sensitive to the β values below 1, where the stress-strain response changes rapidly over continued cycling. The stress-strain response is more stable with β greater than 1.

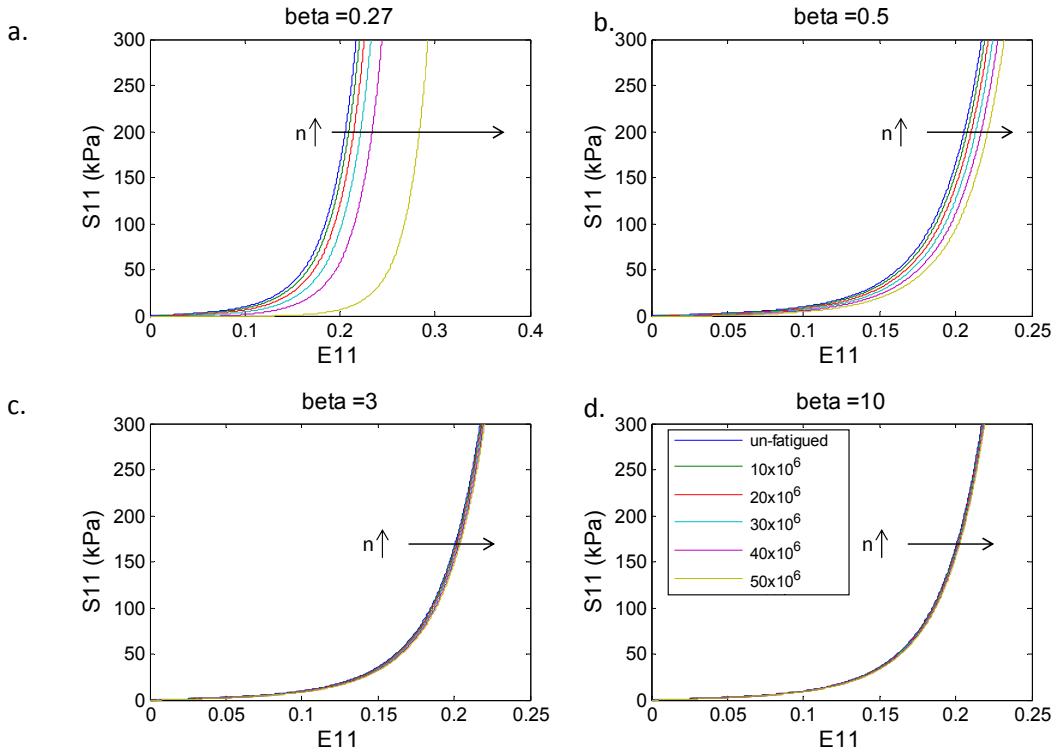

Figure 2.7 Illustration of the effects of β on the tissue stress-strain response over cycling with a) $\beta = 0.27$, b) $\beta = 0.5$, c) $\beta = 3$, and d) $\beta = 10$.

2.2.10.2 *Effect of permanent set on the tissue response over cycling*

The effect of the permanent set on the overall time-dependent tissue response was analytically investigated using the Fung model parameters in Table 2-1 and the time-dependent inelastic model parameters in Table 2-3, with D^{n}_{psmax} values of 0, 0.1, 0.2, and 0.3.

Figure 2.8 shows that when the permanent set at the fatigued state is small, the tissue becomes more compliant over cycling. However, when the permanent set is large, the tissue becomes stiffer with continued cycling. This effect was particularly apparent with $D^{n}_{psmax} = 0.3$ shown in Figure 2.8d at the $50x10^6$ cycle state: the stress-strain

response has become essentially a vertical line. The toe-region of the stress-strain response is lost with large permanent set values.

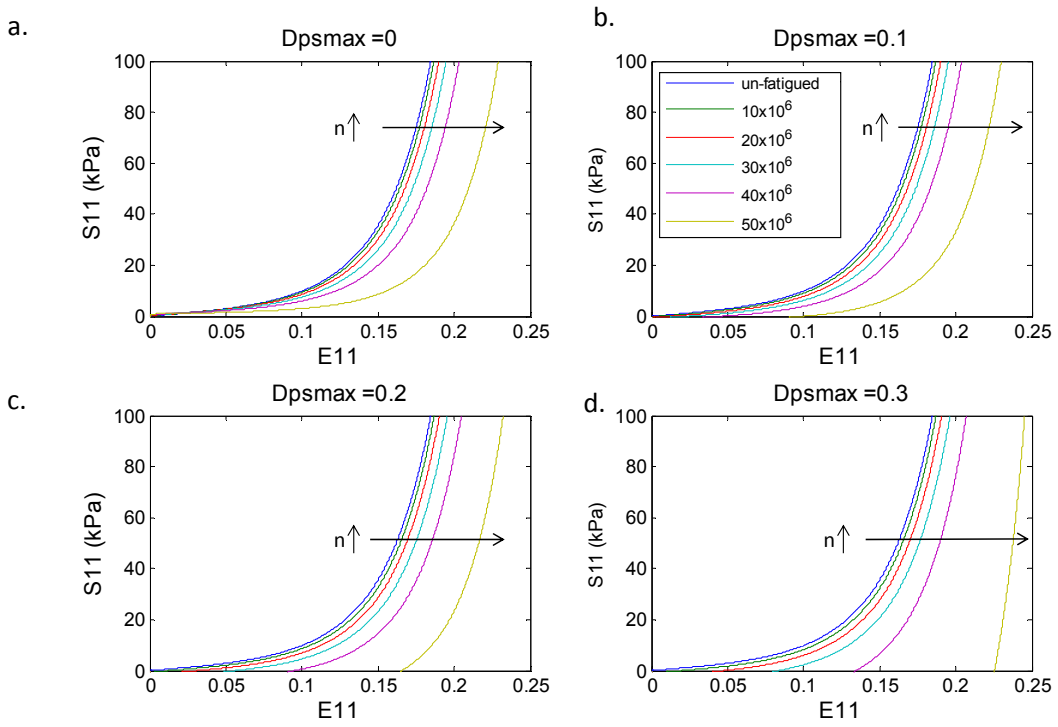

Figure 2.8 Illustration of the effects of the permanent set on the stress-strain response over continued cycling with a) $D^{n}_{psmax} = 0$, b) $D^{n}_{psmax} = 0.1$, c) $D^{n}_{psmax} = 0.2$, and $D^{n}_{psmax} = 0.3$.

2.2.11 Calibration of time-dependent inelastic material parameters

The cycles-to-failure definition, Eq. (2.21), was defined as the number of cycles to failure at a given peak equivalent strain to facilitate model parameter calibration through uniaxial tension cycling. Uniaxial experiments are limited because they do not represent *in vivo* loading conditions. Theoretically, biaxial fatigue testing experiments could be performed to determine the tissue fatigue properties under various loading protocols; however, these types of experiments would be extremely complex. Therefore, the practical study design to determine the time-dependent inelastic model parameters for

a specific tissue is through displacement-controlled uniaxial fatigue experiments. The experiment should be conducted along the preferred fiber orientation and perpendicular to the preferred fiber orientation respectively in order to determine the cycles-to-failure for the fiber and matrix components distinctly.

First, the ψ_{max} parameter, representing the equivalent strain limit of the tissue, can be determined through uniaxial failure tests. The Second Piola Kirchhoff stress versus Green Strain response in the loading direction obtained through uniaxial failure tests by Eqs. (1.4)-(1.7) and (1.11)-(1.13) can be used to numerically calculate the strain energy associated with tissue failure, W_f, by integrating the S vs. E curve from $E = 0$ to $E = E_f$ where E_f is the failure strain. This can be achieved, for instance, by using the Simpson's Trapezoid Rule for numerical integration:

$$W_f = \int_{E=0}^{E=E_f} S dE \approx \frac{1}{2}\sum_{i=1}^{i=N}(E_{i+1} - E_i)\big(S(E_{i+1}) + S(E_i)\big). \tag{2.48}$$

Then ψ_{max} can be calculated by plugging W_f into Eq. (2.2) as

$$\psi_{max} = \sqrt{2W_f}. \tag{2.49}$$

In order to define ψ_{max} separately per component, one option is to test the tissue failure properties both the preferred fiber direction and the cross-fiber direction. The W_f determined from the test data in the preferred fiber direction can be used to calculate ψ_{max_f}, and the W_f in the cross-fiber direction can be used to calculate ψ_{max_m}. Alternatively, techniques to isolate each component such enzymatic degradation of the fibers or matrix could be used. Then the failure properties of each isolated component could be used to determine ψ_{max_f} and ψ_{max_m} respectively. The concern with this route,

is that when one component is removed, the remaining component may be somewhat damaged.

Once the displacement to cause failure in one cycle is known, the displacement should be reduced, and the tissue should be cycled to failure to determine an additional point on the n_{tot} vs. $\Xi_{\mathrm{n}}^{\mathrm{peak}}$ curve. This process should be repeated until a curve similar to that shown in Figure 2.3 can be obtained. The n_{tot} per cycle will get larger each time the displacement ($\Xi_{\mathrm{n}}^{\mathrm{peak}}$) is reduced. In practice, at some point the n_{tot} will become so large, that one can assume that at a single cycle to the corresponding $\Xi_{\mathrm{n}}^{\mathrm{peak}}$ value, the tissue accumulates a negligible amount of damage. Therefore, the n_{max} should be set to this n_{tot} value, and ψ_{min} should be set to the corresponding $\Xi_{\mathrm{n}}^{\mathrm{peak}}$ value. The n_{max} will depend on the application. The α and β parameters can then be obtained through curve fitting of the n_{tot} vs. $\Xi_{\mathrm{n}}^{\mathrm{peak}}$ experimental data.

Alternatively, the tissue properties may be characterized by uniaxial or biaxial tension tests before and after fatigue following experimental protocols presented by Sun et al. [105] and Sellaro et al. [137]. In this case, the time-dependent model parameters α and β would be determined through nonlinear regression in order to fit the tissue response before cycling and at different fatigue states.

2.3 Computational framework

The theoretical framework was implemented in ABAQUS commercial FE software via the user-material subroutine (**UMAT**) utility in ABAQUS Standard.

2.3.1 Overview of user-material subroutine algorithm

The UMAT utility available in ABAQUS Standard makes it possible to define any constitutive model of arbitrary complexity. User-defined material models can be used with any ABAQUS structural element type. During an FE simulation, the estimated deformation gradient at time t, $\boldsymbol{F}_t$, as well as any solution-dependent variables are passed into the UMAT at each material point in the model at each integration point. Within the UMAT the Cauchy stress for large-strain applications and the material jacobian must be explicitly defined in terms of $\boldsymbol{F}_t$ and the solution dependent variables. If the Cauchy stress at that point is within the tolerance of the static equilibrium stress, the solution converges. If the Cauchy stress is not within tolerance, the Newton-Raphson method is used to iteratively update the $\boldsymbol{F}_t$ based on the material jacobian, until convergence is reached.

Because the time-dependent inelastic tissue behavior is dependent on the peak equivalent strain and loading history, these values were stored as solution dependent variables, which were passed into the UMAT to calculate the tissue behavior at each material point in the model. These values were used to evaluate and update the stress-softening and permanent set and could be updated within the UMAT for the next iteration. Thus, they provided a method of passing the results from previous time increments to the current time increment. The subroutine was coded in FORTRAN 77 in accordance with the ABAQUS user manual. A flow chart of the general stress tensor, solution-dependent variables, and material Jacobian tensor update procedure in the ABAQUS UMAT is given in Figure 2.9. The detailed procedure is described in the proceeding sections.

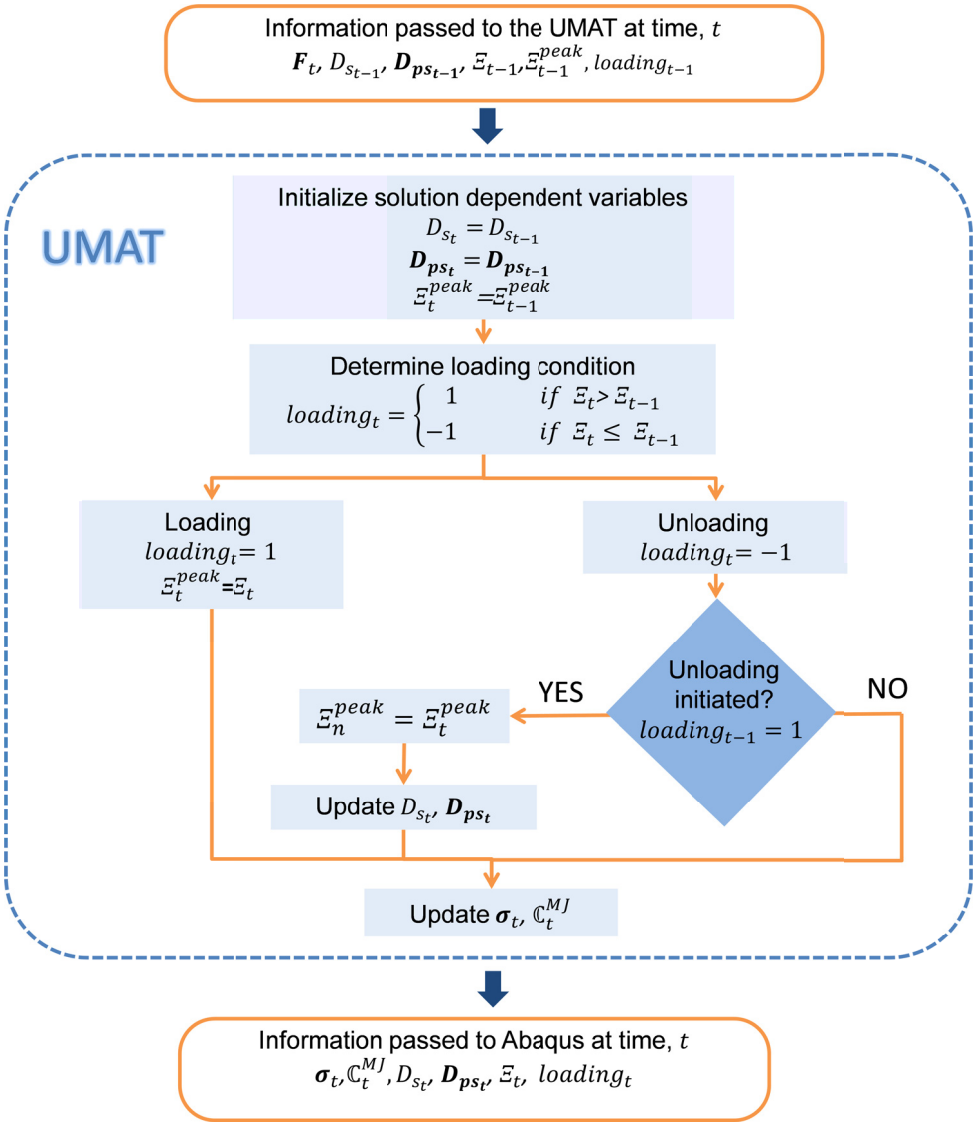

Figure 2.9 Schematic of stress tensor and material Jacobian tensor update procedure at each time increment in ABAQUS UMAT.

2.3.2 Stress-softening and permanent set update procedure

Cycle dependent parameter values including the Ξ_n^{peak}, D_s, and $\boldsymbol{D_{ps}}$ were stored as solution-dependent variables in the UMAT at each time increment. Thus, the values for Ξ_n^{peak}, D_s, and $\boldsymbol{D_{ps}}$ during the previous increment $(t-1)$ were passed into the UMAT at time t, where they were updated. The Ξ_n^{peak} parameter was updated during the loading portion of each cycle to reflect the maximum Ξ_t value during that particular

cycle. At the onset of unloading, D_s, and $\boldsymbol{D_{ps}}$ were updated based on the current Ξ_n^{peak} value. The D_s, and $\boldsymbol{D_{ps}}$ then remained constant through unloading and the successive loading cycle until unloading was initiated again, and these variables were re-updated.

A loading status variable at time t, $loading_t$, was used to determine whether the material point was being loaded or unloaded at time t, where $loading_t = 1$ during loading, and $loading_t = -1$ during unloading. Assuming a constant loading and unloading rate, the loading time equals half of the total cycle time, t_{cyc}. Thus, we have

$$\text{loading}_\text{t} = \begin{cases} 1, & \text{t} \le 0.5t_{cyc} \\ -1 & \text{t} > 0.5t_{cyc} \end{cases}. \tag{2.50}$$

Therefore, the beginning of unloading is when $\text{loading}_\text{t} = -1$ and $\text{loading}_{\text{t}-1} = 1$.

2.3.3 Stress and material Jacobian tensor definitions.

In ABAQUS, the stress tensor must be supplied in the form of the Cauchy stress, $\boldsymbol{\sigma}$, at each time increment, t, which can be calculated from the deformation gradient at time t, $\boldsymbol{F}_t$, and the Second Piola Kirchhoff stress tensor at time t, $\boldsymbol{S}_t$, determined by Eq. (2.39), using the "push forward" operation from Eqs. (1.7) and (1.8):

$$\boldsymbol{\sigma}_\text{t} = \text{J}^{-1}\mathbf{F}_\text{t}\mathbf{S}_\text{t}\mathbf{F}_\text{t}^\text{T}, \tag{2.51}$$

where J is the determinant of $\boldsymbol{F}$. The material Jacobian tensor, $\mathbb{C}^{MJ}$, as defined in ABAQUS is given by

$$\mathbb{C}^{\text{MJ}} = \frac{1}{\text{J}}\mathbb{C}^{\tau\text{J}}, \tag{2.52}$$

where $\mathbb{C}^{\tau J}$ is the tangent modulus tensor for the Jaumann rate of the Kirchhoff stress. In ABAQUS it is not necessary to define $\mathbb{C}^{MJ}$ precisely to obtain an accurate solution; thus

$\mathbb{C}^{MJ}$ was calculated by the "numerical approximation of the tangent moduli method" proposed by Sun et al. [148] which is easier to implement and can be used for any strain energy function. Accordingly, the tangent modulus tensor for the Jaumann rate of the Kirchhoff stress was approximated by

$$\boldsymbol{\tau} = \mathrm{J}\boldsymbol{\sigma}, \tag{2.53}$$

$$\hat{\mathbf{F}}^{(\mathrm{ij})} = \mathbf{F} + \frac{\varepsilon}{2}(\mathrm{e_i} \otimes \mathrm{e_j} + \mathrm{e_j} \otimes \mathrm{e_i}), \tag{2.54}$$

$$\mathbb{C}^{\tau \mathrm{J}(\mathrm{ij})} \approx \frac{1}{\varepsilon}\left[\boldsymbol{\tau}\left(\hat{\mathbf{F}}^{(\mathrm{ij})}\right) - \boldsymbol{\tau}(\mathbf{F})\right], \tag{2.55}$$

where $\boldsymbol{\tau}$ is the Kirchhoff stress, ε is a small perturbation parameter, and $\widehat{\boldsymbol{F}}^{(ij)}$ is the associated perturbed deformation gradient. Thus the approximate $\mathbb{C}^{MJ}$ was calculated at each time increment by

$$\mathbb{C}_{\mathrm{t}}^{\mathrm{MJ}(\mathrm{ij})} \approx \frac{1}{\mathrm{J_t}\varepsilon}\left[\boldsymbol{\tau}\left(\hat{\mathbf{F}}_{\mathrm{t}}^{(\mathrm{ij})}\right) - \boldsymbol{\tau}(\mathbf{F}_{\mathrm{t}})\right]. \tag{2.56}$$

An ε value of $1\mathrm{x}10^{-8}$ was used in all simulations based on the results of [148].

2.3.3.1 Incompressibility constraint

For FE implementation, the tissue incompressibility constraint must be enforced with a Langrangian multiplier or the penalty method where a finite large bulk modulus is used to enforce the incompressibility condition. Different approaches were taken with the Fung and modified-Holzapfel strain energy functions, and use of two-dimensional (2D) and three-dimensional (3D) elements.

2.3.3.1.1 Two-dimensional elements

For use in 2D shell elements, the tissue was assumed to be incompressible as often done due to the high water content and low permeability of soft tissues. The

incompressibility condition requires that $J = 1$, so the Second Piola Kirchhoff stress tensor can be expressed as [149]

$$\mathbf{S} = \mathrm{p}\mathbf{C}^{-1} + (1 - \mathrm{D_s})\frac{\partial \mathrm{W}^0}{\partial \mathbf{E}} + (1 - \eta)\mathbf{S_{ps}}, \tag{2.57}$$

where p is a Lagrangian multiplier to enforce the incompressibility constraint. Because $\boldsymbol{S_{ps}}$ is simply $\boldsymbol{-S}$ evaluated at the permanent set, D_{ps}, $\boldsymbol{S}$ can be expressed as

$$\mathbf{S} = \mathrm{p}\mathbf{C}^{-1} + (1 - \mathrm{D_s})\frac{\partial \mathrm{W}^0}{\partial \mathbf{E}} - (1 - \eta)\left(\mathrm{p}\mathbf{C}^{-1} + (1 - \mathrm{D_s})\frac{\partial \mathrm{W}^0}{\partial \mathbf{E}}|_{(\mathbf{E}=\mathbf{D_{ps}})}\right). \tag{2.58}$$

The deviatoric stress is expressed as

$$\bar{\mathbf{S}} = \mathbf{S} - \frac{1}{3}(\mathbf{S}\colon\mathbf{C})\mathbf{C}^{-1} = \tag{2.59}$$

$$(1 - \mathrm{D_s})\frac{\partial \mathrm{W}^0}{\partial \mathbf{E}} - \frac{1}{3}\left((1 - \mathrm{D_s})\frac{\partial \mathrm{W}^0}{\partial \mathbf{E}}\colon\mathbf{C}\right)\mathbf{C}^{-1} -$$

$$(1 - \eta)\left((1 - \mathrm{D_s})\frac{\partial \mathrm{W}^0}{\partial \mathbf{E}} - \frac{1}{3}\left((1 - \mathrm{D_s})\frac{\partial \mathrm{W}^0}{\partial \mathbf{E}}\colon\mathbf{C}\right)\mathbf{C}^{-1}|_{(\mathbf{E}=\mathbf{D_{ps}})}\right).$$

Thus, Eq. (2.57) can be written in the following form

$$\mathbf{S} = \mathrm{p}\mathbf{C}^{-1} + \bar{\mathbf{S}} = \tag{2.60}$$

$$\mathrm{p}\mathbf{C}^{-1} + (1 - \mathrm{D_s})\frac{\partial \mathrm{W}^0}{\partial \mathbf{E}} - \frac{1}{3}\left((1 - \mathrm{D_s})\frac{\partial \mathrm{W}^0}{\partial \mathbf{E}}\colon\mathbf{C}\right)\mathbf{C}^{-1} -$$

$$(1 - \eta)\left(\mathrm{p}\mathbf{C}^{-1} + (1 - \mathrm{D_s})\frac{\partial \mathrm{W}^0}{\partial \mathbf{E}} - \frac{1}{3}\left((1 - \mathrm{D_s})\frac{\partial \mathrm{W}^0}{\partial \mathbf{E}}\colon\mathbf{C}\right)\mathbf{C}^{-1}|_{(\mathbf{E}=\mathbf{D_{ps}})}\right).$$

For 2D elements the through thickness shear and normal stresses are assumed to be zero; thus, $S_{13} = S_{23} = S_{33} = 0$. Therefore, we have

$$S_{33} = pC_{33}^{-1} - \frac{1}{3}\left((1 - D_s)\frac{\partial W^0}{\partial \mathbf{E}} : \mathbf{C}\right) C_{33}^{-1} \tag{2.61}$$

$$-(1 - \eta)\left(pC_{33}^{-1} - \frac{1}{3}\left((1 - D_s)\frac{\partial W^0}{\partial \mathbf{E}} : \mathbf{C}\right) C_{33}^{-1}|_{(\mathbf{E}=\mathbf{D_{ps}})}\right.$$

For the Fung model Eq. (1.20), $\frac{\partial W^0}{\partial \mathbf{E}} = 0$, and S_{33} reduces to

$$S_{33} = pC_{33}^{-1} - \frac{1}{3}\left((1 - D_s)\frac{\partial W^0}{\partial \mathbf{E}} : \mathbf{C}\right) C_{33}^{-1} \tag{2.62}$$

$$-(1 - \eta)\left(pC_{33}^{-1} - \frac{1}{3}\left((1 - D_s)\frac{\partial W^0}{\partial \mathbf{E}} : \mathbf{C}\right) C_{33}^{-1}|_{(\mathbf{E}=\mathbf{D_{ps}})}\right.$$

At peak loading, $\eta = 1$, and p can be obtained as

$$p = \frac{1}{3}\left((1 - D_s)\frac{\partial W^0}{\partial \mathbf{E}} : \mathbf{C}\right). \tag{2.63}$$

Therefore, Eq. 3.7 is reduced to

$$\mathbf{S} = (1 - D_s)\frac{\partial W^0}{\partial \mathbf{E}} + (1 - \eta)S_{ps} \tag{2.64}$$

which is the same formulation as for a compressible material. For a plane stress state p can be explicitly determined and eliminates the need for using the mixed-formulation proposed by Fung and Tong [149] where p is treated as another independent variable, as well as the penalty method proposed by Holzapfel [87].

For using the modified-Holzapfel model Eqs. (2.11)-(2.13), with shell elements, the volumetric contribution to the strain energy function, W_{vol}, was eliminated, and a similar approach was taken as with the Fung model to enforce the incompressibility constraint. In the case of the modified-Holzapfel model,

$$\frac{\partial \mathrm{W}^0}{\partial \mathrm{E}_{33}} = \frac{\partial \mathrm{W}}{\partial \mathrm{I}_1}\frac{\partial \mathrm{I}_1}{\partial \mathrm{C}_{33}}\frac{\partial \mathrm{C}_{33}}{\partial \mathrm{E}_{33}} = 2\mathrm{W}_1, \tag{2.65}$$

where $W_1 = \frac{\partial \mathrm{W}^0}{\partial I_1}$. Thus, S_{33} can be expressed as

$$\mathrm{S}_{33} = 0 = \mathrm{p}\mathrm{C}_{33}^{-1} + 2\left(1 - \mathrm{D}_{s_m}\right)\mathrm{W}_1 \tag{2.66}$$

$$-\frac{1}{3}\left(\left[\left(1 - \mathrm{D}_{s_m}\right)\frac{\partial \mathrm{W}_m^0}{\partial \mathbf{E}} + \left(1 - \mathrm{D}_{s_{f_k}}\right)\frac{\partial \mathrm{W}_{\mathrm{f}_k}^0}{\partial \mathbf{E}}\right] : \mathbf{C}\right)\mathrm{C}_{33}^{-1} -$$

$$(1 - \eta)\left(\mathrm{p}\mathrm{C}_{33}^{-1} + 2\left(1 - \mathrm{D}_{s_m}\right)\mathrm{W}_1 -\right.$$

$$\left.\frac{1}{3}\left(\left[\left(1 - \mathrm{D}_{s_m}\right)\frac{\partial \mathrm{W}_m^0}{\partial \mathbf{E}} + \left(1 - \mathrm{D}_{s_{f_k}}\right)\frac{\partial \mathrm{W}_{\mathrm{f}_k}^0}{\partial \mathbf{E}}\right] : \mathbf{C}\right)\mathrm{C}_{33}^{-1}|_{(\mathbf{E}=\mathbf{D}_{\mathbf{ps}})}\right.$$

where $k = 1, \ldots, K$ is the number of fiber families. At peak loading, $\eta = 1$, and p can be obtained as

$$\mathrm{p} = -2\left(1 - \mathrm{D}_{s_m}\right)\mathrm{W}_1\mathrm{C}_{33} + \frac{1}{3}\left(\left[\left(1 - \mathrm{D}_{s_m}\right)\frac{\partial \mathrm{W}_m^0}{\partial \mathbf{E}} + \left(1 - \mathrm{D}_{s_{f_k}}\right)\frac{\partial \mathrm{W}_{\mathrm{f}_k}^0}{\partial \mathbf{E}}\right] : \mathbf{C}\right). \tag{2.67}$$

Therefore, Eq. (2.39) can be expressed as

$$\mathbf{S} = \left(1 - \mathrm{D}_{s_m}\right)\frac{\partial \mathrm{W}_m^0}{\partial \mathbf{E}} + \left(1 - \mathrm{D}_{s_{f_k}}\right)\frac{\partial \mathrm{W}_{\mathrm{f}_k}^0}{\partial \mathbf{E}} - 2\left(1 - \mathrm{D}_{s_m}\right)\mathrm{W}_1\mathrm{C}_{33} + \tag{2.68}$$

$$(1 - \eta)\left(\left(1 - \mathrm{D}_{s_m}\right)\frac{\partial \mathrm{W}_m^0}{\partial \mathbf{E}} + \left(1 - \mathrm{D}_{s_{f_k}}\right)\frac{\partial \mathrm{W}_{\mathrm{f}_k}^0}{\partial \mathbf{E}} - 2\left(1 - \mathrm{D}_{s_m}\right)\mathrm{W}_1\mathrm{C}_{33}|_{(\mathbf{E}=\mathbf{D}_{\mathbf{ps}})}\right.$$

2.3.3.1.2 Three-dimensional elements

For the use of the modified-Holzapfel model with 3D brick elements, the penalty method [87] was used to enforce incompressibility. Accordingly, Eq. (2.39) was alternatively expressed as

$$\mathbf{S} = \frac{\partial \mathrm{W}^0_{\mathrm{vol}}}{\partial \mathbf{E}} + (1 - \mathrm{D_m}) \frac{\partial \mathrm{W}^0_m}{\partial \mathbf{E}} + \left(1 - \mathrm{D_{f_k}}\right) \frac{\partial \mathrm{W}^0_{\mathrm{f}_k}}{\partial \mathbf{E}} + (1 - \eta)\mathbf{S_{ps}}. \tag{2.69}$$

and

$$\mathbf{S} = \boldsymbol{S}_{vol} + \bar{\mathbf{S}}, \text{ where } \boldsymbol{S}_{vol} = \frac{\partial \mathrm{W}^0_{\mathrm{vol}}}{\partial \mathbf{E}}. \tag{2.70}$$

The $\bar{\mathbf{S}}$ is given similarly by Eq. (2.59).

2.3.4 Numerical considerations for constitutive model parameters

To ensure convergence and numerical stability of the model, the convexity of the initial strain energy function and a low condition number of the material stiffness matrix was ensured per Sun and Sacks [145]. In most commercial FE codes, the Newton-Raphson method is generally used to evaluate the material stiffness matrix. If the elasiticity tensor, $\mathbb{C}$, given by Eq. (2.46), is positive definite, full rank, and well-conditioned, then numerical solution of the equilibrium equations will be stable and accurate. In our experience, as long as the initial $\mathbb{C}$ is positive definite, full rank, and well-conditioned, the accumulation of stress-softening and permanent set could be simulated. Problems with convergence in some cases arose at $t = 0.5t_{cyc}$ at the highly fatigued state when the material response was updated to reflect the new stress-softening and permanent set due to the jump in the stress value.

2.3.4.1 Convexity of the strain energy function

It can be seen from Eq. (2.42) that the elasticity tensor is the second partial derivative, or Hessian, of the strain energy. It is known that when the Hessian of a function is positive definite, the corresponding function will be convex [150]. Thus, by requiring $\mathbb{C}$ to be positive definite, convexity of the strain energy is enforced. Convexity

of the strain energy physically implies that the projections of the contours of W over the strain space form convex surfaces [87].

For the Fung model, convexity of the strain energy function is not guaranteed. Convexity of the Fung model was ensured following Sun and Sacks [145]. Accordingly, the stiffness matrix can be expressed as

$$\mathbf{D} = \frac{\mathrm{C}}{2}\mathrm{e}^{\mathrm{Q}}\begin{bmatrix} 2\mathrm{A}_1 + \zeta_1^2 & 2\mathrm{A}_3 + \zeta_1\zeta_2 & 2\mathrm{A}_5 + \zeta_1\zeta_3 \\ 2\mathrm{A}_3 + \zeta_1\zeta_2 & 2\mathrm{A}_2 + \zeta_2^2 & 2\mathrm{A}_6 + \zeta_2\zeta_3 \\ 2\mathrm{A}_5 + \zeta_1\zeta_3 & 2\mathrm{A}_6 + \zeta_2\zeta_3 & 2\mathrm{A}_4 + \zeta_3^2 \end{bmatrix} \tag{2.71}$$

where $\zeta_1 = 2A_1E_{11} + 2A_3E_{22} + 2A_5E_{12}$, $\zeta_2 = 2A_2E_{22} + 2A_3E_{11} + 2A_6E_{12}$, $\zeta_3 = 2A_4E_{12} + 2A_5E_{11} + 2A_5E_{11} + 2A_6E_{22}$. In the reference configuration ($E_{11} = E_{12} = E_{22} = 0$) $\boldsymbol{D}$ is reduced to

$$\mathbf{D} = \frac{\mathrm{C}}{2}\begin{bmatrix} 2\mathrm{A}_1 & 2\mathrm{A}_3 & 2\mathrm{A}_5 \\ 2\mathrm{A}_3 & 2\mathrm{A}_2 & 2\mathrm{A}_6 \\ 2\mathrm{A}_5 & 2\mathrm{A}_6 & 2\mathrm{A}_4 \end{bmatrix}. \tag{2.72}$$

Positive definiteness then requires that the determinants associated with all of the upper-left submatrices of $\boldsymbol{D}$ are positive. The following parameter constraints ensure positive definiteness at the reference configuration

$$\mathrm{c} > 0,\ \mathrm{A}_1 > |\mathrm{A}_3|, \mathrm{A}_2 > |\mathrm{A}_3| \text{ and } \mathrm{A}_1\mathrm{A}_2\mathrm{A}_4 + 2\mathrm{A}_3\mathrm{A}_6\mathrm{A}_5 - \mathrm{A}_5^2\mathrm{A}_2 - \mathrm{A}_6^2\mathrm{A}_1 - \mathrm{A}_3^2\mathrm{A}_4 > 0. \tag{2.73}$$

From Eqs. (1.20) and (2.17), at the reference configuration in the fatigued state, the stress-softening term is added to $\boldsymbol{D}$ as

$$\mathbf{D} = \frac{\mathrm{C}}{2}(1 - \mathrm{D_s}) \begin{bmatrix} 2\mathrm{A}_1 & 2\mathrm{A}_3 & 2\mathrm{A}_5 \\ 2\mathrm{A}_3 & 2\mathrm{A}_2 & 2\mathrm{A}_6 \\ 2\mathrm{A}_5 & 2\mathrm{A}_6 & 2\mathrm{A}_4 \end{bmatrix}. \tag{2.74}$$

Because $(1 - D_s)$ term is always positive, the same parameter constraints to ensure convexity at the un-fatigued reference state also ensure convexity at the fatigued reference state.

However, these constraints are not sufficient to guarantee positive definiteness over the entire strain space. The positive definiteness of $\boldsymbol{D}$ must be ensured at every point in the strain space, in order to ensure convexity of W. In practice, it is generally sufficient to evaluate the positive definiteness of $\boldsymbol{D}$ by examining the convexity of the contours of W within the strain space. Representative strain energy contours are plotted over the $E_{11} - E_{22}$, $E_{11} - E_{22}$, and $E_{22} - E_{12}$ planes in Figure 2.10 for the Fung model without the convexity condition imposed (Figure 2.10a-c) and with the convexity condition imposed (Figure 2.10d-f).

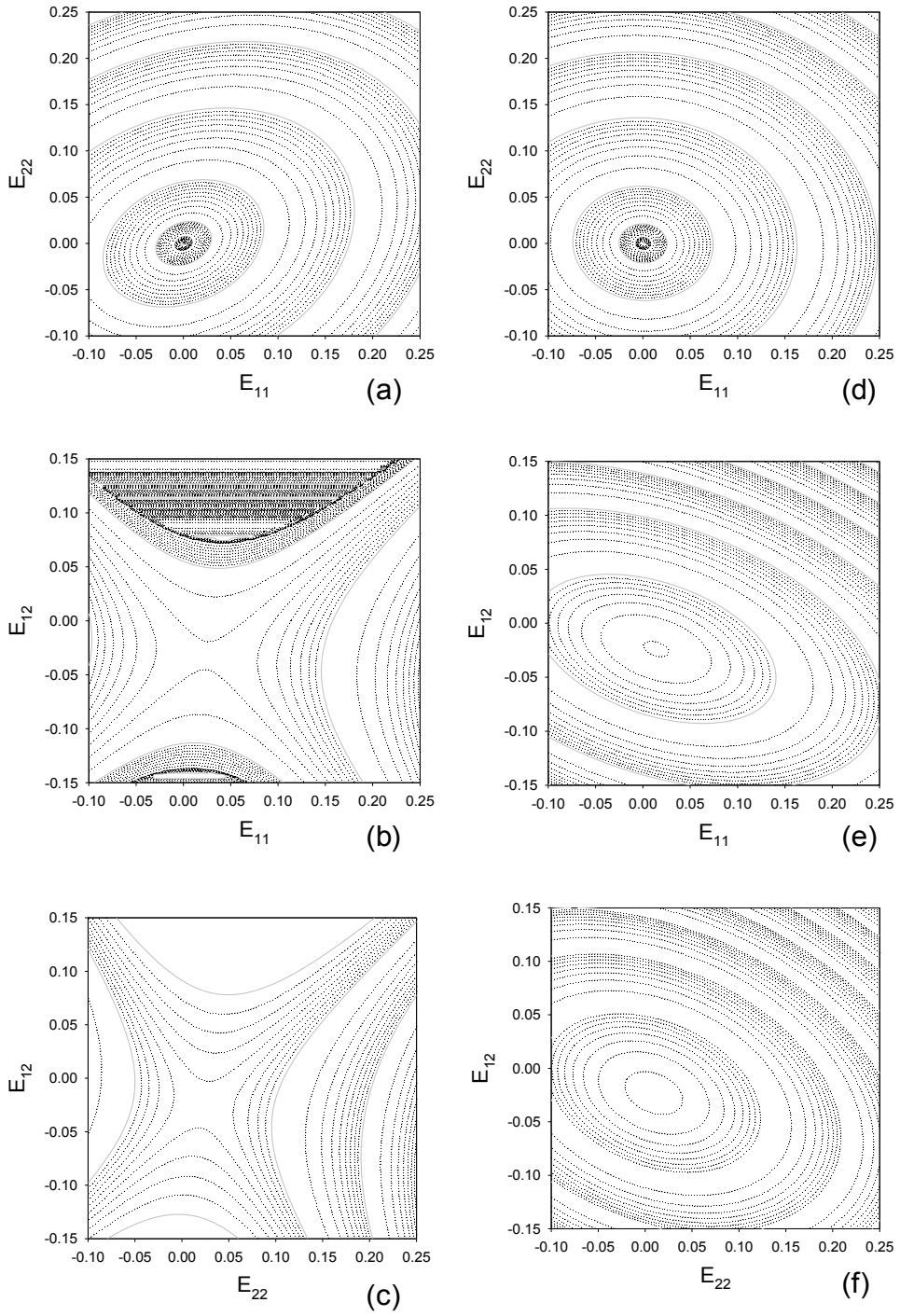

Figure 2.10 Projections of the Fung strain energy function potential contour plots in the a) E_{11}-E_{22}, b) E_{11}-E_{12} and c) E_{22}-E_{12} planes without convexity condition imposed; the projections of the strain energy function potential contour plots in the d) E_{11}-E_{22}, e) E_{11}-E_{12} and f) E_{22}-E_{12} planes with convexity condition imposed adapted from [145].

For the modified-Holzapfel model, convexity of the strain energy function is guaranteed [87]. Therefore, it was not necessary to check each set of material parameters for convexity.

2.3.4.2 Condition number of the stiffness matrix

The condition number is defined as

$$R = \|\boldsymbol{D}\| \cdot \|\boldsymbol{D}^{-1}\| \tag{2.75}$$

where the norm of $\boldsymbol{D}$ is defined as $\|\boldsymbol{D}\| = max_{1\leq j\leq n} \sum_{i=1}^{n} \left|D_{ij}\right|$. Typically, a condition number is ≤ 200 is acceptable for numerical convergence of the Fung model [145].

2.3.5 User material subroutine verification

The user material subroutine was verified in single- and multi-element simulations to ensure that the coding was free from errors and that the stress-softening and permanent set effects could be captured in the simulations.

2.3.5.1 Verification test 1

The time-dependent inelastic model using Eq. (2.24) for the evolution of the stress-softening parameter and Eq. (2.27) for the evolution of the permanent set parameter was coded in an ABAQUS UMAT in conjunction with the Fung-type initial strain energy function Eq. (1.20). The model implementation was verified in single- and multi-element cyclic uniaxial stretch simulations to a peak Green strain of 0.16. Both FE models were constructed with 8-node plane stress (CPS8R) elements in ABAQUS. The initial Fung model parameters and time-dependent inelastic model parameters used in each test are provided in Table 2-5.

Table 2-5 Material parameters used in user-material subroutine verification test 1.

Initial Fung model tissue material parameters						
C (kPa)	A_1	A_2	A_3	A_4	A_5	A_6
1.00	56.19	175.00	-18.02	50.90	-9.67	0.17
Inelastic model material parameters						
$\psi_{min}\left(\frac{\sqrt{kN}}{m}\right)$	$\psi_{max}\left(\frac{\sqrt{kN}}{m}\right)$	n_{max}	α	β	$D_{psmax_{11}}$	$D_{psmax_{22}}$	$D_{psmax_{12}}$
4.67	431,840.00	368.0	1.00	0.58	0.1	0.1	0.05

2.3.5.1.1 Single-element simulation

The single-element model consisted of a single 1 mm x 1 mm x 0.4 mm element. One side of the element was fixed and a peak displacement of 0.149 mm was applied to the opposing side to induce a peak Green strain of 0.16 on the model. The simulation consisted of 30 steps in total. Each step consisted of applying displacement with a sinusoidal loading curve from 0 mm to 0.149 mm and back to 0 mm. The mean Second Piola-Kirchhoff stress (**SPKS**) vs. Green strain response from the 8 integration points was extracted from each step of the simulation results for comparison with the analytical solution.

2.3.5.1.2 Multi-element simulation

The multi-element model, shown in Figure 2.11, was adapted from a previously developed biaxial test specimen model [151]. The model consisted of 400 elements comprising a 25 mm x 25 mm x 0.4 mm square. As in the single-element model, one side of the model was fixed and a peak displacement of 3 mm was applied to the opposing side (Figure 2.11), to induce a peak Green strain of 0.16 to the central 4 elements of the model. Again, each step of the simulation consisted of one loading cycle to the peak uniaxial displacement. The mean SPKS vs. Green strain response from the 4 central

elements were extracted from each step of the simulation for comparison with the analytical and single-element model FE solutions.

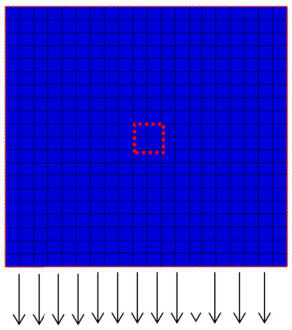

Figure 2.11 Multi-element model used in UMAT verification tests. The arrows illustrate how the uniaxial displacement was applied to the model, and the red-dotted square indicates the 4 central elements from which the simulation results were extracted.

The FE and analytically calculated material responses for every 5th cycle of loading for verification test 1 are illustrated in Figure 2.12. It can be seen that both the single- and multi-element simulation results match the analytical solution, which serves to verify the UMAT coding.

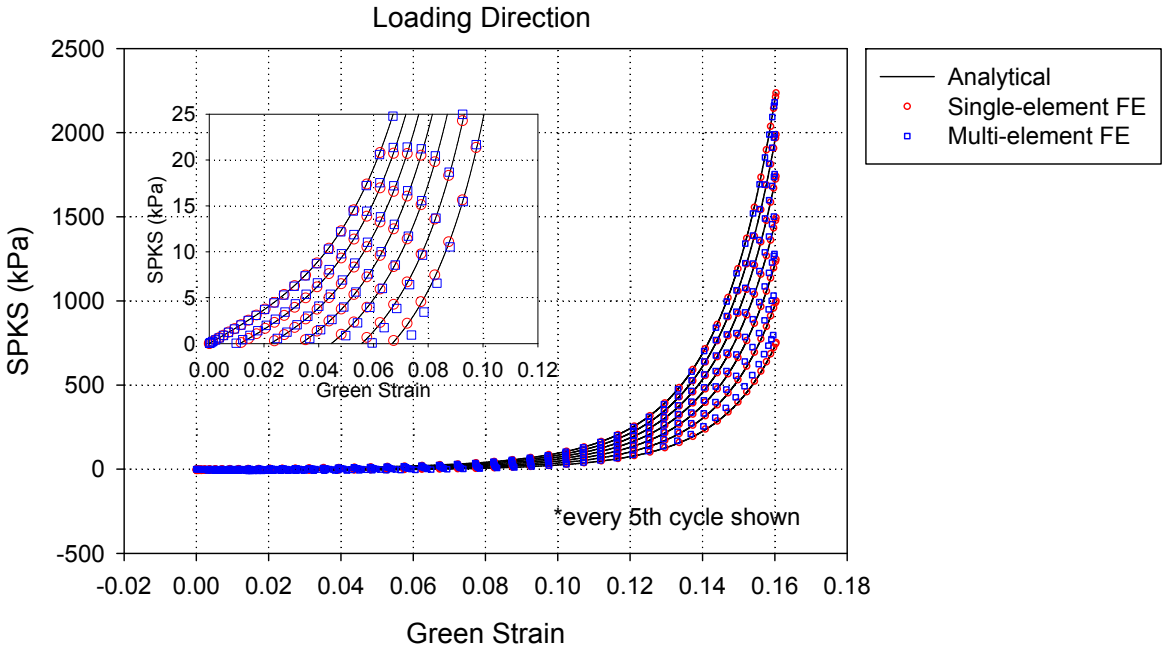

Figure 2.12 Analytical and FE predicted SPKS vs. Green Strain responses over 30 simulated cycles of uniaxial loading to a peak strain 0.16 showing very good agreement.

2.3.5.2 Verification test 2

The time-dependent inelastic model using Eqs. (2.25) and (2.26) for the evolution of the matrix and fiber stress-softening parameters and Eq. (2.29) for the evolution of the permanent set parameter was coded in an ABAQUS UMAT in conjunction with the modified-Holzapfel strain energy function (Eqs. (2.11) and (2.13)). The model implementation was verified in single- and multi-element cyclic uniaxial stretch simulations to a peak Green strain of 0.2. Both FE models were constructed with 8-node continuum brick elements (C3D8H) elements in ABAQUS. The brick element models were created from the plane-stress element models used in verification test 1 by simply extruding the thickness of the 2D elements to 0.4 mm. The initial modified-Holzapfel model parameters and time-dependent inelastic model parameters used in each test are provided in Table 2-6.

Table 2-6 Material parameters used in user-material subroutine verification test 2.

Initial modified-Holzapfel model tissue material parameters					
$c_1\ (kPa)$	c_2	$k_1\ (kPa)$	k_2	θ	D
30.03	3.47	74.50	63.19	43.11	1e-5
Inelastic model matrix material parameters					
$\psi_{min_m}\ (\frac{\sqrt{kN}}{m})$	$\psi_{max_m}\ (\frac{\sqrt{kN}}{m})$	n_{max_m}	α_m	β_m	D_{psmax_m}
4.37	431,840	36.8	1.0	10.0	0.105
Inelastic model fiber material parameters					
$\psi_{min_f}\ (\frac{\sqrt{kN}}{m})$	$\psi_{max_f}\ (\frac{\sqrt{kN}}{m})$	n_{max_f}	α_f	β_f	D_{psmax_f}
4.37	431,840	36.8	1.0	10.0	n/a

The FE and analytically calculated material responses for every 5th cycle of loading for verification test 2 are illustrated in Figure 2.13. It can be seen that both the single- and multi-element simulation results match the analytical solution. The slight deviations between the FE and analytical responses at high stresses are due to the treatment of compressibility. In the analytical solution, the tissue was assumed to be perfectly incompressible; however, in the FE simulations, the tissue was assumed to be slightly compressible. Note that the near incompressibility condition was enforced using the penalty method. These results serve to verify the UMAT coding.

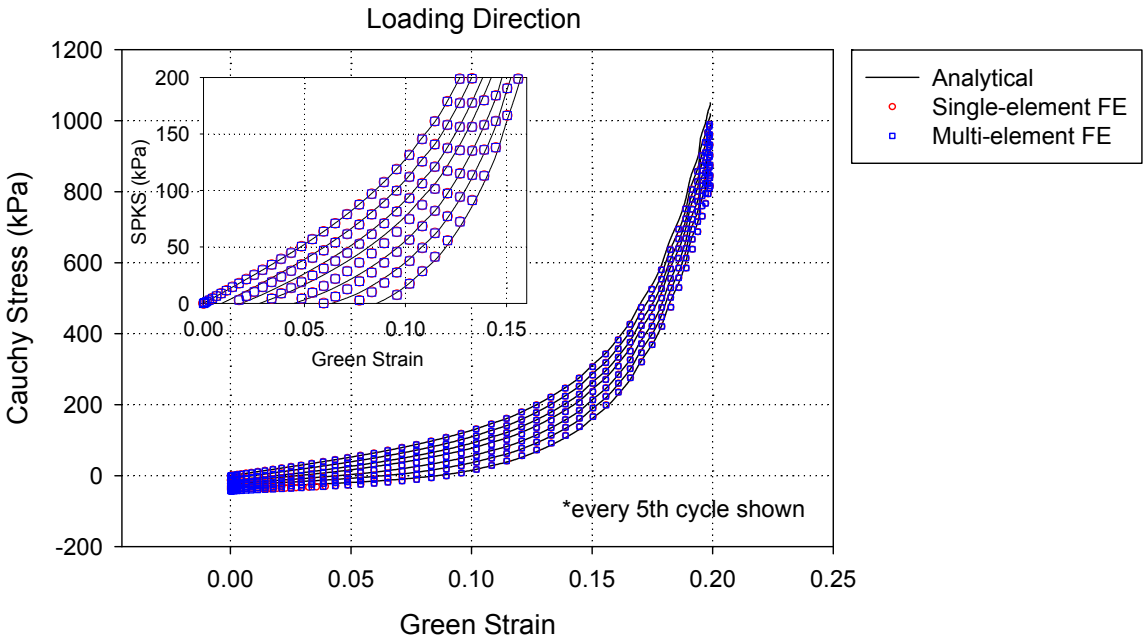

Figure 2.13 Analytical and FE predicted SPKS vs. Green Strain responses over 30 simulated cycles of uniaxial loading to a peak strain 0.2 using brick elements showing very good agreement.

2.3.5.3 Verification test 3

The time-dependent inelastic model using Eqs. (2.25) and (2.26) for the evolution of the matrix and fiber stress-softening parameters and Eqs. (2.30)-(2.33) for the evolution of the permanent set parameter was coded in an ABAQUS UMAT in conjunction with the modified-Holzapfel strain energy function (Eqs. (2.12) and (2.13)). The model implementation was verified in single- and multi-element cyclic uniaxial stretch simulations to a peak Green strain of 0.55. Verification tests were run utilizing the plane-stress element models of verification test 1, and the continuum brick element models of verification test 2. The initial modified-Holzapfel model parameters and time-dependent inelastic model parameters used in each test are provided in Table 2-7.

Table 2-7 Material parameters used in user-material subroutine verification test 3.

Initial modified-Holzapfel model tissue material parameters							
$c_1\ (kPa)$	c_2	c_3	$\bar{\mathrm{I}}_1^m$	$k_1\ (kPa)$	k_2	θ	D
18.55	1.0	7.0	3.8	0.1	1.5	0.0	5e-4
Inelastic model matrix material parameters							
$\psi_{min_m}\ (\frac{\sqrt{kN}}{m})$	$\psi_{max_m}\ (\frac{\sqrt{kN}}{m})$	n_{max_m}	α_m	β_m	D_{psmax_m}		
1.00	50.0	100.0	1.0	20.0	1.6		
Inelastic model fiber material parameters							
$\psi_{min_f}\ (\frac{\sqrt{kN}}{m})$	$\psi_{max_f}\ (\frac{\sqrt{kN}}{m})$	n_{max_f}	α_f	β_f	D_{psmax_f}		
0.50	50.0	100.0	1.0	10.0	0.8		

The FE and analytically calculated material responses for every 5th cycle of loading for verification test 3 using brick elements are illustrated in Figure 2.14. The results using plane-stress elements are shown in Figure 2.15. It can be seen that in both cases the single- and multi-element simulation results match the analytical solution. The slight deviations between the FE results using brick elements and analytical responses at high stresses are again due to the treatment of compressibility (see discussion in section 2.3.5.2). The results using the plane-stress elements shown in Figure 2.15 were generated assuming perfect incompressibility; thus, the FE results more closely match the analytical solution. The good agreement between the FE and analytical results serve to verify the UMAT implementation.

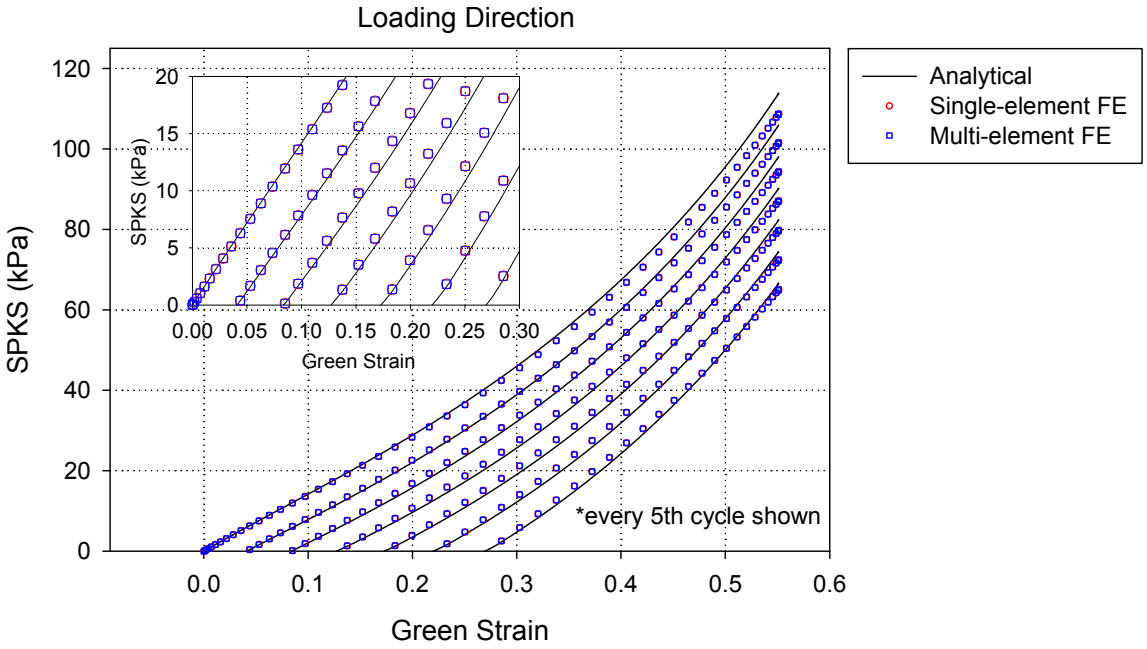

Figure 2.14 Analytical and FE predicted SPKS vs. Green Strain responses over 30 simulated cycles of uniaxial loading to a peak strain 0.55 using brick elements showing good agreement.

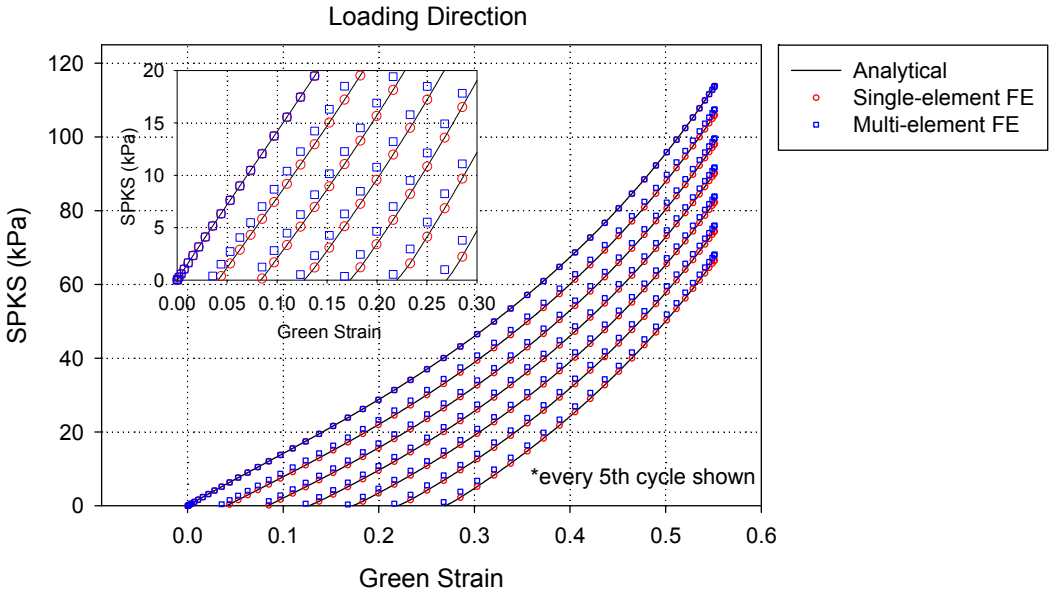

Figure 2.15 Analytical and FE predicted SPKS vs. Green Strain responses over 30 simulated cycles of uniaxial loading to a peak strain 0.55 using plane-stress elements showing very good agreement.

2.3.6 Example uniaxial tissue fatigue simulation

The developed computational framework was used to investigate the effects of cyclic uniaxial tension on a typical soft tissue specimen. The multi-element model used in the simulation is shown in Figure 2.11. The initial tissue properties were defined by the modified-Holzapfel model of Eqs. (2.11) and (2.13), the stress-softening was defined by Eqs. (2.25) and (2.26), and the permanent set was defined by Eqs. (2.30)-(2.33). The material parameters are listed in Table 2-8. In order to investigate the effects of fiber family orientation on the fatigue properties, two additional specimens were assigned the exact same material and fatigue properties: only the fiber orientation was changed to $\theta = 45°$ and $\theta = 90°$. Note that $\theta = 90°$ represents the case where the tissue is loaded in the preferred fiber direction, while $\theta = 0°$ represents the case where the tissue is loaded in the cross-fiber direction. Each simulation consisted of 3 steps: 1) 0-state equi-biaxial tension, 2) uniaxial cycles to a peak stress of 1MPa, and 3) fatigued state equi-biaxial tension. Fatigue damage accumulation was limited to the uniaxial cycling step and was not considered in the top and bottom rows of elements as these represent the tissue clips in experiments. To reduce computational time, each simulated cycle corresponds to $N = 1\text{x}10^6$ cycles in real time. The average SPKS vs. Green Strain response during each step was extracted from the central 16 elements.

Table 2-8 Material parameters used in the uniaxial fatigue simulation.

Initial modified-Holzapfel model tissue material parameters					
$c_1\ (kPa)$	c_2	$k_1\ (kPa)$	k_2	θ	D
1.00	22.67	8.15	47.67	0.00	1e-6
Inelastic model matrix material parameters					
$\psi_{min_m}\ (\frac{\sqrt{kN}}{m})$	$\psi_{max_m}\ (\frac{\sqrt{kN}}{m})$	n_{max_m}	α_m	β_m	D_{psmax_m}
0.50	431,840	360.0	1.0	0.85	0.105
Inelastic model matrix material parameters					
$\psi_{min_f}\ (\frac{\sqrt{kN}}{m})$	$\psi_{max_f}\ (\frac{\sqrt{kN}}{m})$	n_{max_f}	α_f	β_f	D_{psmax_f}
3.0	431,840	500.0	1.0	0.19	0.051

Contour plots of the stress-softening in the matrix and fiber components at the 10N state were compared between the samples. Figure 2.16 shows drastically different fatigue patterns in the samples depending on the fiber orientation. In sample with the fibers oriented at 90° both the fibers and matrix components become slightly damaged. A small amount of permanent set is evident from the tissue elongation in the loading direction. Tissue narrowing in the cross-loading direction was negligible. In the sample oriented with the fibers at 0° there was a higher degree of matrix softening, although there was no softening in the fibers. Elongation in the loading direction and significant tissue narrowing in the cross-loading direction were also evident. In the sample oriented with the fibers at 45° there was significant matrix and fiber softening and permanent sets in both directions.

The simulated equi-biaxial responses at the 0N and 10N states were extracted from the simulation results for comparison. Figure 2.17 shows that the equi-biaxial properties referenced to the current cycle (permanent-set not included) did not change much after fatigue in the $\theta = 90°$ sample, but changed dramatically in the $\theta = 0°$ sample and $\theta = 45°$ sample. The $\theta = 90°$ sample displayed a slightly stiffer response in the

loading direction with little change to the cross-loading direction, which resulted in increased mechanical anisotropy with fatigue. The $\theta = 0°$ specimen became stiffer in the loading direction and much more compliant in the cross-loading direction to completely reverse the mechanical anisotropy in the tissue after fatigue, i.e. the cross-fiber direction became stiffer than the fiber direction. The $\theta = 45°$ specimen was initially isotropic, but became stiffer in the loading direction and more compliant in the cross-loading direction by the 10N state, which induced a preferred direction in the tissue.

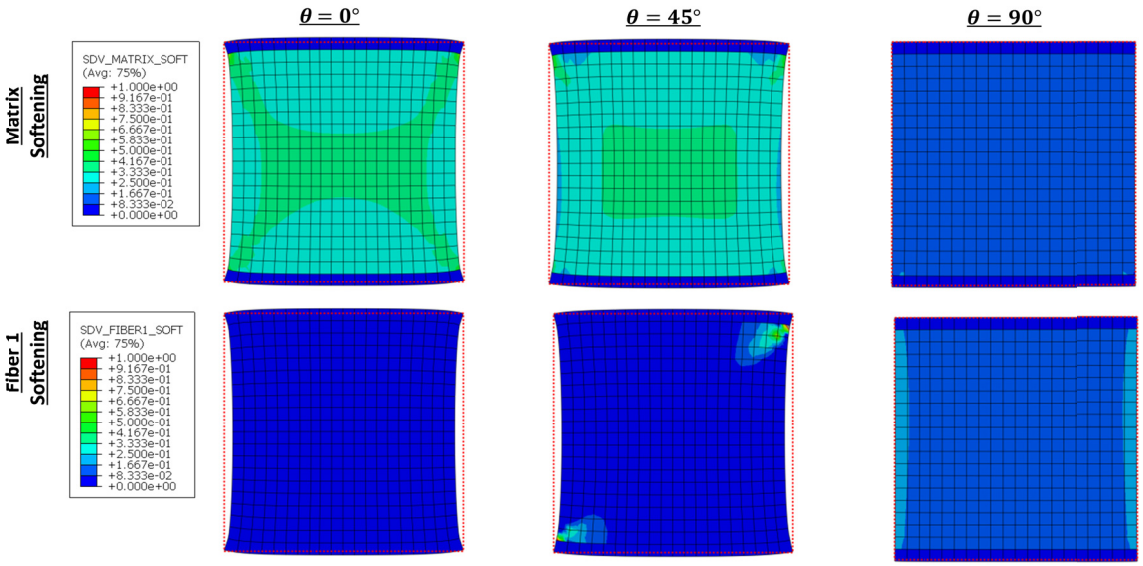

Figure 2.16 Contour plots of $\boldsymbol{D_s}$ in the matrix (top) and fiber family 1 (bottom) at the 10N state shown on the 0-stress fatigued geometry. The red-dashed squares outline the 0-state tissue model geometry. Note tissue elongation in the loading direction and narrowing in the cross-loading direction

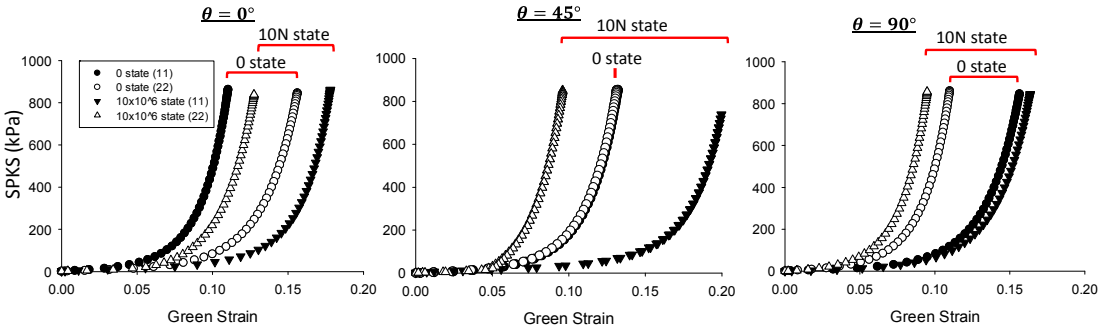

Figure 2.17 The FE predicted equi-biaxial responses of each sample at the 0N and 10N states. Note that the complete reversal of the tissue anisotropy in the $\theta = 0°$ sample, and the creation of a preffered direction in the $\theta = 45°$ samples.

The effect of the collagen fiber orientation on the fatigue response of glutaraldehyde-treated bovine pericardium (**GLBP**) was experimentally investigated by Sellaro *et al*. [137] with a similar experimental protocol as simulated here. Briefly, in their $\theta = 90°$ group, they saw slight stiffening in the fiber direction with little change to the cross-fiber direction, causing increased mechanical anisotropy. This can be explained physically by increased fiber alignment and un-crimping in the fiber direction [105, 137]. In their $\theta = 0°$ group, they saw increased stiffness in the cross-fiber direction and compliance in the fiber direction, causing a reversal of the mechanical anisotropy after fatigue [137], which can be explained by reorientation of the collagen fibers from the cross-loading direction towards the loading direction [137]. The results of the $\theta = 90°$ and $\theta = 0°$ simulations presented here show these same trends, which demonstrate the capability of this model to capture the multi-axial fatigue response of soft tissue.

2.4 Discussion

2.4.1 Theoretical framework for modeling time-dependent inelastic tissue properties

The presented theoretical framework is suitable for modeling time-dependent inelastic tissue property changes due to fatigue and aging which include stress-softening

and permanent set. The model ability to capture a wide range of time-dependent tissue responses was demonstrated through parametric studies of the model parameters. For instance, the damage evolution zone can be defined for a particular material and by changing α and β the rate of damage at different regions of this zone can be changed. Also, by changing the degree of maximum permanent set, the net change in tissue stiffness, from net softening to net stiffening, with continued cyclic can be changed. This allows the model to describe, for instance, the net softening of tendons cyclically loaded to supraphysiological levels [38], and also the net stiffening of blood vessels with age. Therefore, the framework is general and can be applied to describe the inelastic properties of many different tissue types.

The distinguishing characteristic of this approach with respect to that of others [98-101, 103], is that the focus is on long-term fatigue and aging effects. Unlike previous damage models for fiber-reinforced composites [98-101, 103] we considered an incremental accumulation of damage at a set equivalent strain, whereas other models considered an accumulation of damage only when the previous maximum equivalent strain had been exceeded. This approach was also unique to other models that consider damage-induced permanent set [16, 142, 152], because our focus was not to model the hysteresis effect of each unloading cycle, rather the progressive permanent change in specimen geometry due to long-term cyclic loading, and thus the D_s and D_{ps} functions are active during both loading and unloading cycles at the onset of damage. Therefore, the presented framework is not intended for the accurate fitting of each loading and unloading curve, rather a uniform damage accumulation is assumed to model the

transition from a un-fatigued state to a fatigued state with long-term (100+ million) loading cycles.

2.4.2 Computational framework for modeling time-dependent inelastic tissue properties

The developed computational framework for modeling time-dependent inelastic tissue properties can be used to simulate the effects of cyclic loading on tissues under more complex loading conditions and in more complex model geometries, in which there is no analytical solution. Thus, this makes it possible to apply the theoretical framework to a wide variety of applications, for instance, to investigate the effects of tissue fatigue and aging on whole tissues or tissue-derived medical device function under physiological loading.

The ability of the computational framework to capture the fatigue phenomena of GLBP under cyclic uniaxial tension was demonstrated in uniaxial fatigue simulations utilizing FE models similar to the experimental GLBP test specimens in [137]. The model was also able to capture the effect of the fiber orientation on the tissue fatigue response observed experimentally, where cycling the tissue in the cross-fiber direction induced complete reversal of the mechanical anisotropy and cycling the tissue in the fiber direction slightly increased the degree of anisotropy in the tissue [137]. The overall changes in the specimen geometry due to permanent set including elongation in the loading direction and narrowing in the cross-loading direction, were also similar to those observed experimentally [137].

The inclusion of permanent set, which is a novel aspect of this approach, is particularly important for studying the effects of tissue fatigue and aging in

physiologically relevant multi-element models, because a change in the model geometry induced by the permanent set may have unexpected effects on the model stress distribution. For instance, for bioprosthetic heart valve (**BHV**) applications, the inclusion of permanent set allows for investigation of changes to the degree of leaflet coaptation in the fatigued BHV. This is of importance because as the leaflets become stretched out, there may be wrinkling of the leaflets during leaflet coaptation. This leaflet wrinkling and ‘‘pinwheeling’’ may increase the stresses in the leaflets and accelerate the rate of damage [153].

2.4.3 Limitations

Due to limited experimental data, a linear progression of the stress softening and permanent set parameters at a given equivalent strain over cycling was assumed. Both of these values may evolve faster during the initial cycles, thus, Eqs. (2.24)-(2.26) and (2.27)-(2.34) may be modified in the future to accommodate non-linearity. Furthermore, to give the model more flexibility, the functional form of the permanent set should be independent of the loading condition. As presented, the permanent sets in each direction under any applied loads are assumed to be proportional to the D_{psmax} which was measured under the uniaxial loading condition. Again, more experimental data is necessary to determine an appropriate functional form for the permanent set.

The developed framework is also phenomenological and cannot describe microstructural changes in the tissue. Thus, rather than focusing on how soft tissues change on the microstructural level in response to biological and mechanical stimuli, the focus of this study is modeling the degradation of tissue mechanical function. The benefit of a phenomenological model is that it can be more easily implemented in FE

where the effects of fatigue and aging can be simulated in realistic anatomical geometries under physiological loading.

2.5 Conclusions

In this chapter, we presented a novel theoretical framework to describe the time-dependent inelastic behavior of soft tissues in response to mechanical fatigue damage and natural aging. Through parametric analysis of the model parameters, it was shown that the constitutive framework can describe a wide range of time-dependent inelastic material responses including the softening observed in tendons subjected to supraphysiological loads [38], as well the stiffening observed in the aging arteries. Thus, this framework may be applicable for many biomedical applications.

The theoretical framework was implemented in ABAQUS commercial FE code via a UMAT. The accuracy and robustness of the UMAT coding was verified through single- and multi-element simulations. The UMAT was used in an example tissue uniaxial fatigue simulation. The simulation results demonstrated that the computational framework developed in this study can predict realistic tissue fatigue damage patterns and responses including the impact of the fiber orientation. Thus, this framework may facilitate durable tissue-derived device design, and improve understanding of the impacts of aging on soft tissue properties and organ function. The benefits of a computational platform are that it could be used for general applications, i.e. tissue types, anatomies, loading conditions and it permits quantitative and efficient analyses.

3 MODELING OF HUMAN ASCENDING AORTA AGING

In Chapter 2, we developed a theoretical and computational framework to model nonlinear, hyperelastic, time-dependent soft tissue material properties under finite strain. In this chapter and the following chapter, we applied this theoretical and computational framework to model age-dependent aortic tissue property changes in natural human aging, and cycle-dependent tissue property changes in bioprosthetic heart valve devices, respectively. Both applications have significant clinical relevance: aging is the largest risk factor of cardiovascular disease, and durability is one of the primary limiting factors preventing the use of bioprosthetic heart valves across all patient populations.

The aorta is the largest blood vessel in the body and is responsible for delivering blood from the heart to the rest of the body. Therefore, the aorta sees the largest blood pressures in the body, particularly at the ascending aorta (**AA**). The AA has a particularly high degree of elastin which aids in the propulsion of blood; however, the elastin becomes fragmented over long periods of time which causes the AA to dilate and stiffen, reduces functional capacity, and increases the risk of cardiovascular disease. Methods to predict age-related AA tissue and structural property changes and how they will impact physiological function could be used to identify patients at risk and may facilitate timely interventions. Therefore, in this chapter, we first characterized the age-related structural and mechanical property changes of the human AA through *in vivo* and *in vitro* measurements. We then utilized this data, in the development of a constitutive model of human AA aging. The human AA aging constitutive model was implemented in patient-specific AA finite element (**FE**) models, and the effects of aging were

simulated. The FE predicted AA structural property changes were validated against *in vivo* measurements. The simulation results showed that the AA wall stresses increase over time, and this increase becomes significant after many years. Some of the results presented in this chapter are published in [154, 155].

3.1 Introduction

3.1.1 Ascending aorta structure and function

In normal arteries, the extracellular matrix (**ECM**) proteins: collagen, elastin, fibrillin, glycoproteins and proteoglycans produced by smooth muscle cells ensure the stability, resilience and compliance [156, 157]. Collagen and elastin primarily provide the structural integrity of the vessels. Elastin allows the vessels to stretch under pressure and relax once the pressure is removed, while collagen provides strength and protects against over dilation.

The aorta, shown in Figure 3.1, is the largest artery in the body. It is responsible for delivering blood from the heart to the systemic circulation. Therefore, the aorta sees the highest blood pressures in the body, particularly at the proximal end near the heart which is considered the AA. The aorta is normally highly elastic which aids in the propulsion of blood downstream to the systemic vasculature [158]. The AA has a particularly high ratio of elastin to collagen to aid in this capacity [159].

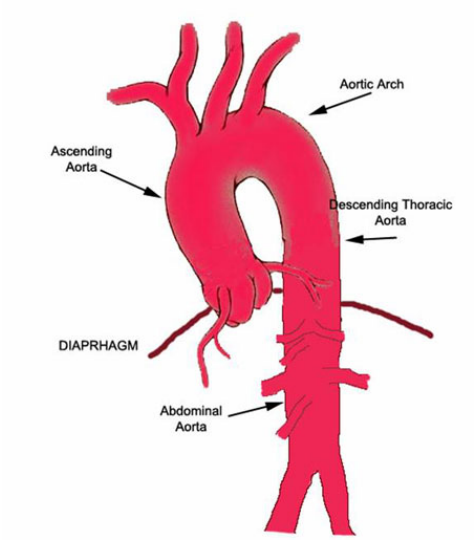

Figure 3.1 Diagram of the aorta. Note that the AA is the portion of the aorta between the aortic valve and the aortic arch [160].

3.1.2 Age-related ascending aorta property changes

The natural aging process initiates increased expression of matrix metalloproteases (**MMP**) and decreased expression of tissue inhibitors of MMPs even in healthy elderly patients. These changes result in a reduction of elastin due to elastin fiber degradation and increased collagen deposition, which are often associated with tissue calcification [24]. There is experimental evidence that the fragmentation of aortic elastin with age is also associated with mechanical fatigue caused by the pulsatile wall strain over the course of a lifetime [18, 161-163]. Elastin fragmentation then leads to the permanent un-crimping of the collagen fibers.

Age-related changes in the architecture and quantity of the ECM components, are the underlying cause of functional changes to the aorta associated with disease and aging [87, 156, 161, 164-172]. These changes are realized on the tissue and organ levels by dilation and loss of extensibility. Aortic dilation, elongation and stiffening with aging are well documented [173-191]. Figure 3.2 shows that aortic elongation over time leads to

an increase in the aortic arch curvature. These changes are clinically relevant because there is growing evidence that arterial dilation and stiffening are both markers and predictors of cardiovascular disease. Impacts of arterial stiffening include: increased systolic pressure, which causes cardiac hypertrophy and increased ventricular oxygen consumption, and increased risk for the development of cardiovascular disease. Arterial stiffening can be exacerbated by diabetes, hypertension or atherosclerosis [24, 192, 193]. Age-related dilation can also lead to aneurysm, dissection, and rupture. By the age of 65 years, 6-9% of patients have an aneurysm [194].

Figure 3.2 Representative images of the thoracic in a (A) younger and (B) older patient, showing increased curvature in the arch of the older patient, adapted from [178].

The distensibility of the proximal AA decreases more significantly with age than other regions of the aorta [195]. The AA is exposed to the largest expansile wall stresses during cardiac contraction thereby increasing the propensity for elastin fiber fragmentation and failure [156, 159, 181]. Because the initial elastin to collagen ratio is higher in the AA than the distal segments of the aorta, fatigue induced elastin degeneration has the potential to cause the greatest loss of distensibility in this segment

[159]. Despite the clinical significance of age-related AA property changes, the mechanisms governing these processes are not well understood.

An understanding of the age-dependent AA mechanics is critical for diagnostic and pre-operative evaluation. Establishing the age-specific AA tissue characteristics will allow for identification of abnormalities aside from changes brought on by aging alone. Such information becomes even more important in the current era, as mechanical evaluation of the diseased aorta is becoming part of clinical practice [196-198].

3.1.3 Experimental characterization of age-dependent human ascending aorta properties

The AA *in vivo* structural properties have been extensively studied using clinical diagnostic means; this data, while useful clinically, provides limited information regarding the tissue nonlinear properties and microstructure for a rigorous engineering analysis. There have been very few studies on the latter.

3.1.3.1 Human ascending aorta in vivo structural properties

Aortic compliance can be assessed relatively simply and non-invasively using carotid-femoral pulse wave velocity (**PWV**) measurements via the current clinical standard [177, 183, 199]. One limitation of this approach is that it is an integrated estimate of the aortic stiffness along the entire length, and thus does not provide information on the regional aortic stiffness [195]. It has been shown that the aorta does not uniformly stiffen, and the observed regional differences are likely important in determining the overall cardiovascular risk [181]. Imaging modalities such as electrocardiogram-gated magnetic resonance imaging (**MRI**), echocardiography, and multi-detector computed tomography (**CT**), are available to assess the regional stiffness.

Prior investigations have assessed the effects of aging on the AA properties using such *in vivo* imaging data [173-191]. The consistent finding in all studies is that the AA is indeed changing over time, with marked dilation (as well as elongation) and stiffening. Measurement accuracy is one of critical issues for the quantification of AA mechanical characteristics. The aorta is not oriented perfectly axial, and measuring the AA diameter from a stack of 2D axial CT scans [173, 186, 191, 200] may yield inaccurate results [201]. Hager *et al.* [175] found that by using strictly axial plane CT images to measure the AA, the AA diameter can be overestimated by as much as 21%. Moreover, the AA diameter measurement distinction needs to be made between different phases of the cardiac cycle. The relative change in aortic cross-sectional area throughout the cardiac cycle may be as high as 50% in young patients [202]. Finally, the sample size should be relatively large [178, 180] and due to the known aortic size difference between male and female [174, 175, 180, 182, 186, 188, 199, 203], a gender-specific quantification of the AA diameter is necessary.

There have been relatively few engineering studies on the quantification of the detailed AA *in vivo* mechanical properties [177, 178, 180, 181, 183, 184, 190, 191]. The AA stiffness was indirectly assessed in 56 patients respectively using MRI. In [180], [181], and [190] the distensibility of the AA was assessed by MRI in 26 (13 male, 13 female), 20, and 224 patients respectively. While, in [191], the AA distensibility was assessed based on diameter measurements made from axial CT slices in 293 patients. In each case, the distensibility was shown to be negatively correlated with age [180, 181, 190, 191]. In [178] the AA cyclic strain was measured in the circumferential and

longitudinal directions in 14 patients from CT data, and in [184] the relative thoracic aortic strain was measured in 4 patients from MRI data.

One limitation of *in vivo* studies is that they provide limited mechanical test data for constitutive modeling purposes. The *in vivo* data only describes the AA behavior under physiological loading, which is a relatively small stress range (from diastolic to systolic pressure) and represents only one loading condition. Furthermore, it is difficult to measure the AA properties in the axial direction from *in vivo* data, thus, most *in vivo* data only includes measurements of the AA mechanical properties, i.e. distensibility, strain, compliance, in the circumferential direction. Yet, the AA like all soft tissues is anisotropic; therefore, accurate modeling of the AA mechanics warrants more rigorous characterization of the tissue properties through multi-axial and multi-loading protocol *in vitro* mechanical tests of dissected tissues.

3.1.3.2 Human ascending aorta in vitro tissue properties

Unfortunately there have been few studies on the *in vitro* characterization of healthy human AA tissues, particularly on the effects of age on the tissue properties due to the limited availability of human AA tissues. Most of the *in vitro* studies on the human aorta biomechanical properties [204-210] have be on tissues collected from patients with arterial diseases such as Marfan syndrome and aneurysm. Li et al. [208] conducted uniaxial tests on AA samples from 6 patients aged from 18 to 30 years old; however, no conclusion could be made regarding age-related changes due to the small sample size (n=6) and age range. Michel et al. [207] measured the structural compliance of AA segments from 24 patients aged from 38-77 years through pressure inflation tests and found that the circumferential and longitudinal stretch ratios decrease with age. Yet,

as with *in vivo* studies, the inflation test provides limited data for modeling purposes. The only reports of human biaxial testing come from Azadani et al. [211] and Haskett et al. [205]. Azadani et al. [211] measured the biaxial properties of the human AA and aortic sinuses in 14 patients aged 47±14 years. They reported a trend of age-related stiffening; however, the age range of patients studied was relatively narrow. Haskett et al. [205] reported the most extensive human AA biaxial test dataset including samples from patients 0-30 years (n=6), 31-60 years (n=9), and >61 years (n=18). The AA peak strain under equi-biaxial tension was dramatically reduced in the older patients particularly those over 61 years as shown in Figure 3.3, and this was also found to be true along the length of the aorta. Still, it is not clear how the AA tissue properties evolve beyond the age of 60 years, when the risk of aortic disease is the highest [194].

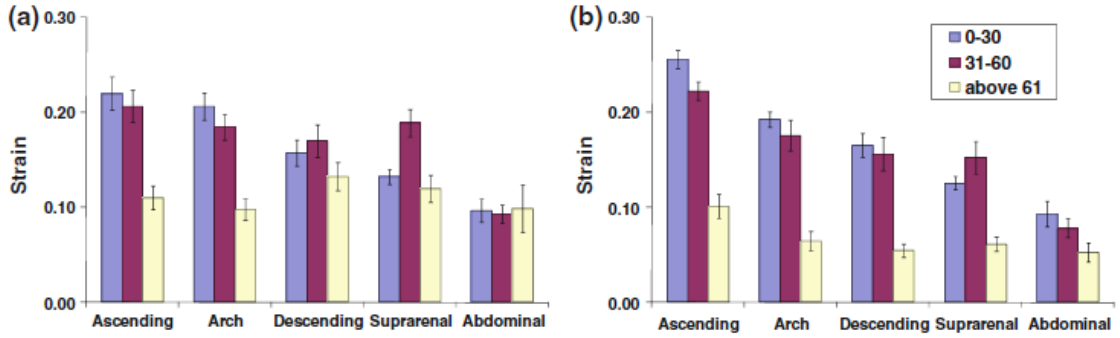

Figure 3.3 Circumferential (a) and longitudinal (b) peak equi-biaxial strain values plotted against age and location adapted from [205]. Note the dramatic decrease in AA compliance in both directions between the 31-60 years and >61 year age groups.

3.1.4 Modeling of age-related changes in blood vessels

Theoretical models can be used to precisely quantify the role of different aging mechanisms and can improve understanding of aging processes. Several groups [212-214] have used structural-based constitutive frameworks to determine the underlying

determinants of age-related changes in arteries. For instance, Spronk et al. [212] used a structural-based constitutive law with descriptions of the elastin, collagen and vascular smooth muscle based on the work of Zulliger et al. [215] to investigate microstructural changes needed to produce the observed functional changes in carotid artery structural properties. Their approach involved fitting the pressure-area response of arterial segments in younger patients, and then assessing which parameters must be changed in the model in order to fit the response of older arterial segments. They found that the changes in the pressure-area response could be described by a reduction in the elastin stiffness and an increase in collagen recruitment. The theoretical results of Valentin, Humphrey, and Holzapfel [115] also suggest that the loss of elastin is a fundamental mechanism of aging. Additionally, their results provided evidence that the loss of vasoactive function plays a critical role in age-related arterial changes [115]. Horny et al. [213] used a similar approach to determine age-related changes in the human abdominal aorta mechanical properties. They found that the extensibility limiting term was most sensitive to aging, indicating that the tissue, as expected, becomes less extensible with age.

These studies provide insight by describing aging mechanisms, but cannot predict the aged tissue response. Constitutive models which incorporate AA microstructural and tissue property changes with aging are needed to predict the effects on organ level functionality. Yet, there are few theoretical works for modeling the aging process. Tsamis et al. [161] proposed a constitutive law combining constrained mixture theory, continuum damage theory, and global growth for modeling stress-induced structure based remodeling of arteries, based on the hypothesis that changes in artery properties and

structure are due to mechanical fatigue damage of elastin, cross-linking of collagen fibers and elastin by advanced glycation end-products, and stress-driven remodeling. They demonstrated that the model could predict age-related changes in arterial dimensions, mass fractions of microstructural components, wall stress, pulsatile strain, and elastin damage consistent with experimental findings.

3.1.5 Computational studies of the human ascending aorta

A limitation of purely constitutive frameworks for modeling arteries is that generally a perfectly cylindrical geometry is assumed [161]. Computational approaches utilizing more realistic anatomical geometries extracted from clinical imaging data are being increasingly adopted to study thoracic aorta biomechanics [71-77]. Through FE and fluid-structure interaction analyses, it has been shown that the locations of peak wall stress correspond to common dissection initiation points just above the sinotubular junction [73, 77] and distal to the left subclavian ostium [73]. The peak wall stress in aneurysms of the aortic arch is correlated to the overall aneurysm size as expected, but also the eccentricity, which may be a factor in the rupture of small aneurysms [71]. Aortic root motion and hypertension have also been shown to significantly increase the wall stress [72]. The main limitations of these studies are the use of simplified, isotropic tissue properties, which do not account for adaptation of the material and structural properties due to aging [71-77] and idealized geometries [74, 75]. In these studies, the peak vessel wall stress was the biomechanical index of interest; however, the accurate AA tissue properties and geometries, which change over time due to underlying microstructural changes brought on by aging [216, 217], disease progression [218], or other factors [219, 220], are necessary for accurate stress prediction. Thus, the

simulation results corresponding to the current patient's age, are only valid for that particular snap-shot in time.

3.1.6 Motivation of this study

Most of what we know about age-related AA property changes is derived from statistical analysis of large population *in vivo* studies. While informative, patient variability rising from genetic and environmental differences makes it difficult to predict age-related changes in particular patients. It is challenging to follow-up patients, particularly healthy patients, for long periods of time to assess these changes. Furthermore, the *in vivo* data that can be collected provide limited information that is generally not region specific.

Therefore, the long-term goal of this study is to apply the constitutive and computational modeling framework of Chapter 2 to specifically describe AA tissue and microstructural property changes with aging, and to predict age-related AA functional changes in a particular patient based on their current AA structural properties assessed through *in vivo* imaging. Such framework could provide quantitative, region-specific, biomechanical assessment of aortic dilation, elongation, and wall stress, and may facilitate disease diagnosis and timely repair.

3.2 Methods

3.2.1 Overview of study design

In this chapter, the age-dependent AA *in vivo* structural characteristics and material properties for healthy humans were quantified through analysis of clinical image data, and *in vitro* mechanical tests, respectively. These *in vivo* and *in vitro* datasets were

then used to develop a constitutive model of AA aging based on the time-dependent inelastic theoretical and computational framework described in Chapter 2. The developed human AA aging constitutive model was then implemented in computational simulations to analyze AA aging under physiological loadings in patient-specific AA FE models. The simulation results including the AA diameter and compliance at different age states were compared to the known age-dependent AA structural properties measured *in vivo* [155] to validate the modeling approach. The resultant computational model was used to assess the effects of aging on the human AA mechanics. The overall study design is illustrated in the flow chart of Figure 3.4. This marks the first study where the FE method was used to investigate age-related changes in human AA mechanics.

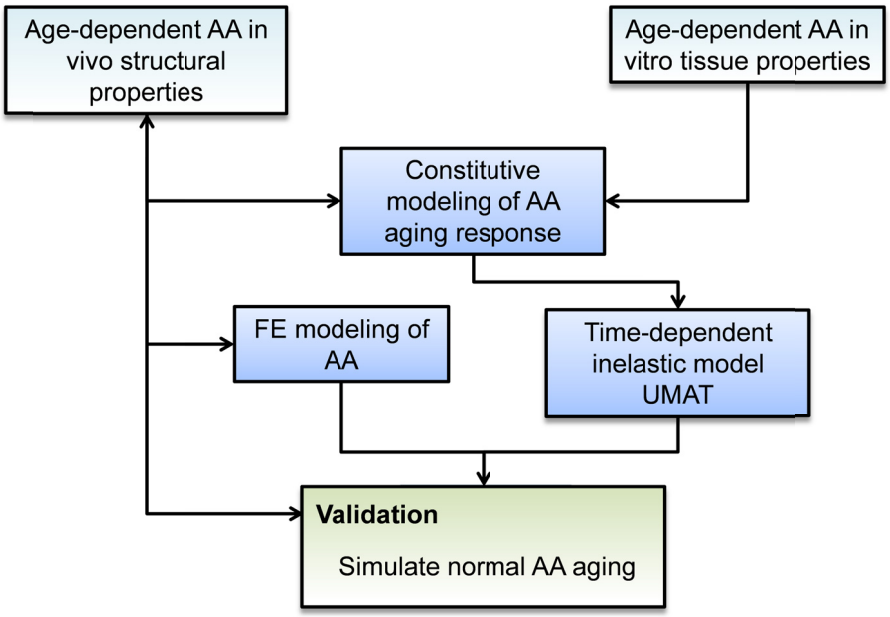

Figure 3.4 Overview of the computational human AA aging study design.

3.2.2 Characterization of age-dependent *in vivo* human AA characteristics

Due to the relatively low spatial resolution of MRI, and the small sample sizes of past CT studies, we quantified the age- and gender-specific *in vivo* mechanical characteristics of the human AA utilizing multiphase clinical CT scans.

3.2.2.1 Patient selection

A total of 45 male patients referred to Hartford Hospital Cardiac Lab for multiphase cardiac CT imaging were studied. The study population was limited to male patients to isolate the effects of aging from possible gender-based differences on the AA properties. All patients underwent CT scans because of suspected coronary artery disease, but presented with no known aortopathies, e.g. aortic dilation, dissection, Marfan syndrome, bicuspid aortic valve, etc. The exam images were retrospectively analyzed in this study. The CT examination was performed on a GE LightSpeed 64-channel volume computed tomography scanner. A collimation of 25-30 × 0.625 mm and a rotation time of 375 ms were used, resulting in a temporal resolution of less than 200 ms between scans (phases). Typically 10 phases can be obtained for each cardiac cycle depending on the heart rate and pitch. There were approximately 100-150 axial CT images with thickness of 0.625 mm, containing the aortic geometry from the aortic valve to the ascending aorta for each phase [221]. Institutional Review Board approval to review these de-identified images was obtained.

Clinical data, including the age, diastolic and systolic blood pressures measured by brachial sphygmomanometer, and known cardiovascular risk factors, were obtained for each of the patients. To study the effect of age, patients were selected from five age groups: 30-39 year olds, 40-49 year olds, 50-59 year olds, 60-69 year olds, and 70-79

year olds. Because the number of younger patients was limited, only 5 patients were analyzed for the 30-39 year old group. All other groups consisted of 10 patients. The patient clinical data is summarized in Table 3-1.

Table 3-1 Patient characteristics for age-dependent *in vivo* AA property study

	Known Cardiovascular Risk Factors							
Patient Group	*Smoker*	*prior MI*	*Diabetes*	*CAD*	*Hyper-cholester-olemia*	*Obesity*	*Family history*	*Hyper-tension*
30-39 years (n=5)	n=1	N/A	N/A	N/A	n=1	N/A	n=1	n=0
40-49 years (n=10)	n=2	N/A	n=1	n=2	n=2	n=1	n=2	n=0
50-59 years (n=10)	N/A	n=1	N/A	n=1	N/A	N/A	N/A	n=3
60-69 years (n=10)	n=2	n=2	n=1	n=1	N/A	N/A	n=2	n=4
70-79 years (n=10)	N/A	n=1	n=1	n=1	n=1	N/A	n=1	n=2
Total (n=45)	n=5	n=4	n=3	n=6	n=4	n=1	n=6	n=9

*MI=myocardial infarction, CAD=coronary artery disease, Family history refers to family history of cardiovascular disease.

3.2.2.2 3D ascending aorta reconstruction

The 3D AA and aortic root geometry was reconstructed for each patient for each of the phases using Avizo 6.3 software (Burlington, MA). Figure 3.5a shows a representative axial CT slice of the aortic valve. The AA and aortic root were segmented semi-automatically in Avizo by adjusting the pixel intensity thresholds to isolate the AA geometry from the neighboring tissues (Figure 3.5b-c).

3.2.2.3 Analysis of in vivo tension and strain state

Following the 3D reconstruction, the AA surface geometry for each phase was then imported into Altair HyperMesh 11.0 (Altair Engineering Inc, MI) for subsequent analysis. Figure 3.5d displays the overlaid AA and aortic root geometry for one representative patient, where each color represents the geometry during a single phase. Cardiac movement was evident from the small displacement of the coronary arteries. The measurement plane was then created in the AA at the level of the right pulmonary artery by bisecting the overlaid geometries from each phase orthogonal to the direction of flow. From Figure 3.5e-f it can be clearly seen that manipulation of the 3D geometries, such as overlapping and dissecting using engineering software, facilitates the accurate measurement of AA dimensions. The AA circumference for each phase was obtained by measuring a closed smooth curve generated from multiple points selected around the AA circumference (Figure 3.5g).

The circumferential aortic strain, ε, was defined as the ratio of the change in aortic circumference with respect to the aortic circumference at end-diastole [178],

$$\varepsilon_i = (C_i - C_{dias})/C_{dias}, \tag{3.1}$$

where C_i is the AA circumference for phase i, while C_{dias} is for diastole. The use of circumference in the strain calculation, rather than diameter, eliminates the assumption of a circular cross-section [178]. The diastolic and systolic blood pressures were obtained for each patient. The CT images corresponding to the intermediate phases were assumed to be taken at equal CT scan time intervals. The AA pressure waveform [222] between peak-systole and end-diastole was assumed to be the same for each patient. The

pressure-strain modulus [223-225], PS_{mod}, was then calculated as a measure of the physiological AA stiffness by,

$$PS_{mod} = (C_{dias}\ (P_{sys} - P_{dias}\ ))/(C_{sys} - C_{dias}\ ), \tag{3.2}$$

where P_{sys} and P_{dias} are the systolic and diastolic pressures. The PS_{mod} is an attractive metric because it can be easily calculated from non-invasive clinical measurements. As in other studies [219, 226-228], we assumed that a small segment of the AA can be treated as a thin-walled cylinder and thus the Laplace equation can be used to assess wall stresses. The Laplace equation,

$$\sigma = (PR)/h, \tag{3.3}$$

expresses the stress, σ, along the circumference of a cylindrical pressure vessel as a function of the luminal pressure, P, the vessel radius, R, and the wall thickness, h. Because the AA wall thickness could not be discerned from the imaging data, the circumferential AA wall tension, t, was calculated for each phase,

$$t_i = (P_i D_i)/2, \tag{3.4}$$

where P_i is the associated pressure and D_i is the AA diameter for phase i determined from the measured circumference

$$D_i = C_i/\pi. \tag{3.5}$$

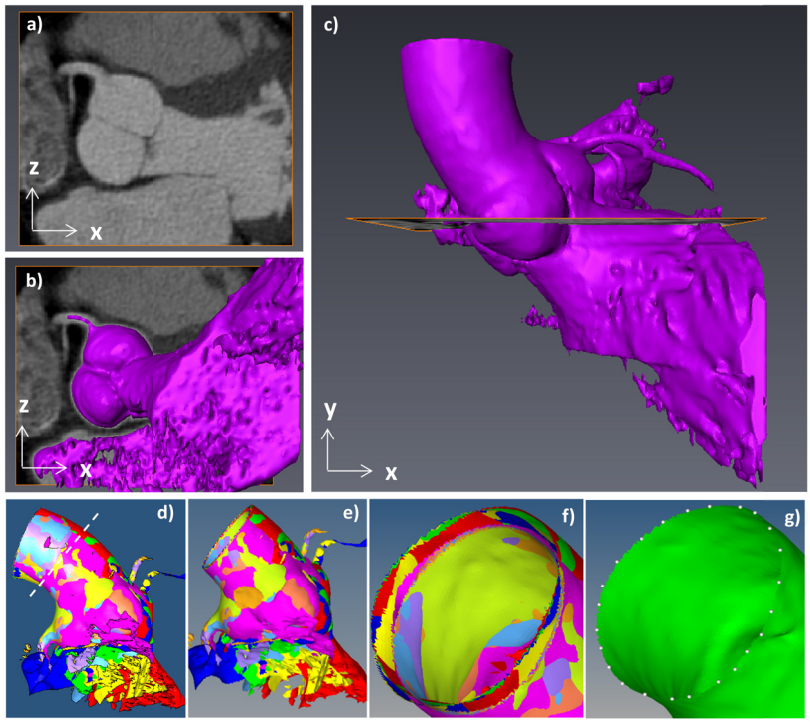

Figure 3.5 a) A cross-sectional image of the aortic valve and b) the same image with the 3D aortic root geometry (shown in pink) projected into the y-plane. c) A long axis view of the reconstructed aortic root geometry with the same cross-section from b and c shown in the x-z plane. d) Aortic root geometry overlaid for each phase, with each color representing a different phase and a dashed line indicating the cross-sectional measurement plane. e) The aortic root geometries after bisection at the measurement plane. f) A close-up of the measurement plane where the circumference measurements were made and g) the measurement plane during a single phase with points along the surface that were used to create a spline curve around the circumference.

3.2.2.4 Statistical analysis

The linear correlation between the AA mechanical characteristics, i.e., pressure, systolic circumferential strain, mean AA diameter, systolic wall tension, and pressure-strain modulus, versus the patient ages were tested using SigmaPlot 11.0 (San Jose, California) via the Pearson Product Moment correlation test. One-way ANOVA and rank-sum tests were used to compare the mean values between age groups using

Minitab16 (State College, PA). In all cases, p-values less than 0.05 were considered to indicate a significant difference between the means. In the proceeding sections, all results are presented as the mean value ± the standard deviation.

3.2.3 Characterization of age-dependent *in vitro* human AA tissue response

3.2.3.1 Human heart characteristics.

Fresh frozen human cadaver hearts (n=12) were obtained from the National Disease Research Interchange (**NDRI**, Philadelphia, PA). The hearts were categorized by patient age into the following three groups: 50-59 years old (n=4, 55±4 years), 80-89 years old (n=4, 84±4 years), and 90-99 years old (n=4, 96±1 years). Each heart was submerged in the 37˚C oxygenated low-sodium, high-potassium solution (in mM: 0.4 KH2PO4; 1.0 MgSO4:7H2O; 28 NaHCO3; 1.5 CaCl2:2H2O; 5.6 Dextrose; 117.5 L-Glutamic acid) for 30 minutes and treated with cryopreservation solution (15% dimethyl sulfoxide) before being stored in a -80°C freezer until mechanical testing could be performed. Studies have shown that cryopreservation does not significantly modify the biomechanical properties of aortic tissue [229]. Human specimen characteristics are presented in Table 3-2. The use of human tissues was approved by the Research Compliance Office of the University of Connecticut for this study.

Table 3-2 Human AA biaxial test specimen characteristics

Heart	**1**	**2**	**3**	**4**	**5**	**6**	**7**	**8**	**9**	**10**	**11**	**12**
Age	51	52	56	59	80	82	87	88	95	95	96	98
Sex	F	F	M	F	F	M	F	F	F	M	F	F
Cause of Death	C	HC	C	IH	unk	AP	unk	Alz	RA	NC	CPA	RA
Primary Disease	C	n	C	n	n	n	PKD	CAD	n	n	n	n
Risk Factors												
Diabetes	n	n	n	n	n	n	n	unk	n	n	n	y
GERD	n	n	n	y	n	n	n	y	n	n	n	n
Pneumonia	n	n	n	n	n	y	n	n	y	n	n	n
Dementia	n	n	n	n	n	n	y	n	n	n	n	n
Atherosclerosis												
Coronary	n	n	n	n	n	n	n	y	n	n	n	n

Alzheimer's = Alz, Asperation Pneumonia=AP, C = cancer, CA = cardiac arrest, CAD = Coronary artery disease, CPA = Chronic pulmonary aspergillosis, GERD = Gastroesophogeal reflux disease, HC = Huntington's Chorea, IC = intracranial hemorrhage, NC = natural causes (old age), RA = respiratory arrest, PKD = Polycystic Kidney Disease, unk=unknown

3.2.3.2 Planar Biaxial Mechanical Testing

Square samples from the AA were excised from each heart to undergo biaxial mechanical testing. The sample dimensions were approximately 20 x 20 mm. Care was taken to align the edges of each specimen along the circumferential and longitudinal directions of the aorta to determine the differences in mechanical properties with respect to anatomical orientation. The thickness of each sample was measured in five places along the center of the specimen with a Mitutoyo rotating thickness gauge (Model 7301) with an accuracy of ± 0.01 mm. Four graphite markers delimiting a square approximately 3 mm x 3 mm in size were glued to the central region of the tissue surface for optical strain measurements.

Biaxial testing was carried out according to the methods presented in section 1.4.1.1 per Sacks and Sun [82]. Briefly, tissue samples were submerged in aqueous

0.09% NaCl solution at room temperature, and stress-controlled test protocols were utilized while the ratio of the normal Lagrangian stress components P_{11}: P_{22} was kept constant with P_{12} = P_{21} = 0. Twenty continuous cycles of preconditioning were performed to reduce tissue hysteresis. Each sample was tested at the maximum load possible without causing tissue damage. At the maximum load, seven consecutive stress protocols were conducted at the following ratios: P_{11} : P_{22} = 0.75:1, 0.5:1, 0.3:1, 1:1, 1:0.75, 1:0.5, and 1:0.3. Tissue samples were assumed to be incompressible and planar.

3.2.3.3 *Histological Analysis.*

The fibrous structure of aged human and porcine AA tissues were examined in both the circumferential and longitudinal directions via histological analysis. Porcine (6-9 months old) tissues were included to serve as a control. Porcine hearts were obtained from Animal Technologies Inc. (Tyler, TX) and treated using the human heart protocol in section 3.2.3.1. Tissue specimens were cryopreserved following the biaxial tests. After thawing, tissues were fixed in formalin for 24 hours prior to the histology process. Each sample was then dehydrated through a process of varied alcohol concentrations, embedded in paraffin, and serially sectioned at 5μm through the thickness. Samples were then mounted on microscope slides and dried. After deparaffinization, slides were stained with the Verhoeff Van-Gieson (**VVG**) stain in order to identify the components of interest: collagen, elastin, and smooth muscle fibers. Digital images of each section were obtained from an Olympus U-TVO.5xC digital camera coupled to an Olympus BX40 light microscope and qualitatively analyzed to compare the relative content and orientation of each component.

3.2.4 Constitutive modeling of human AA aging response

The age-dependent human AA tissue structural and mechanical properties presented in sections 3.2.2 and 3.2.3 were utilized to develop a constitutive model of human AA aging using a combination of analytical and FE methods. The following sub-sections describe in detail how the AA aging model material parameters were determined. The overall process is illustrated in the flowchart of Figure 3.6.

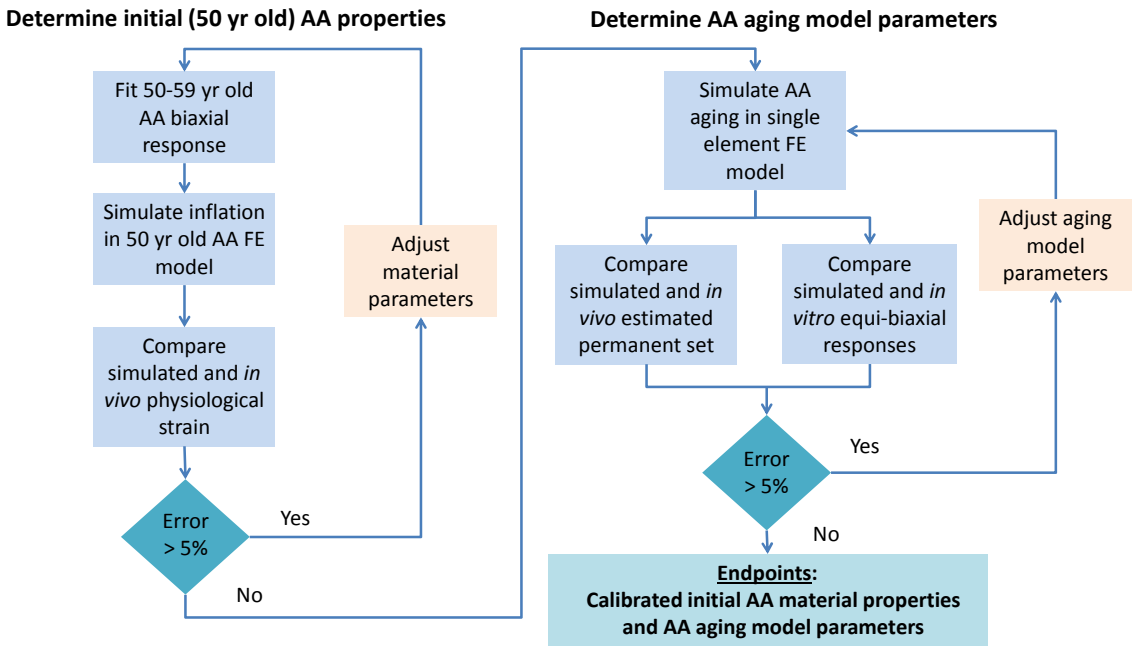

Figure 3.6 Flow-chart of AA aging model parameter fitting procedure

3.2.4.1 Determination of initial AA material parameters

The mean 50-59 year old human AA tissue properties were assumed to be the initial tissue properties for the purpose of this AA aging model. Note that the AA elasticity was dramatically reduced in the patients over 61 years as shown in Figure 3.3. Accordingly, the mean 50-59 year old AA response was fitted with the modified-Holzapfel model of Eqs. (2.12) and (2.13). This form of the matrix strain energy function

was chosen in order to capture the nearly linear 50-59 year old AA stress-strain response at low stress levels as demonstrated in the equi-biaxial responses shown in Figure 3.23, and the rapid stiffening of the response at high stress levels as shown in the uniaxial failure test data in Figure 3.9. The fiber orientation was fixed to $\theta = 0$, corresponding to the circumferential direction due to the experimental observation that the collagen fibers are highly circumferentially aligned in the human AA [205]. The suitability of the initial model parameters was tested by simulating AA inflation to the diastolic and systolic levels in two patient-specific AA FE models generated for patients between the ages of 50 and 59 years and comparing the physiological AA strain predicted from FE with that measured *in vivo* by Eq. (3.1) The FE modeling methods are described in detail later in section 3.2.5. The initial model parameters were adjusted until good agreement was achieved between the model predicted and experimentally measured mean equi-biaxial response and the FE predicted and *in vivo* measured mean physiological strain. An error of ≤5% between the FE and *in vivo* physiological strain measurements was deemed acceptable.

3.2.4.2 Determination of AA aging material parameters

The time-dependent inelastic model was used to describe the transition of the AA material properties from the initial (50-59 year old) to the 80-89 year and 90-99 year old aged states. The evolution of stress-softening was defined by Eqs. (2.25) and (2.26), and the evolution of permanent set was defined by Eqs. (2.30)-(2.33).

3.2.4.2.1 Estimation of human ascending aorta permanent set with age

The human AA permanent set in the circumferential direction with age was estimated by analytically "backing out" the un-pressurized AA diameter for each age and

calculating the change in the un-pressurized diameter. The AA tissue specimens were not in intact tubular form; therefore, the unloaded diameter was unknown and had to be calculated. Utilizing the mean age-dependent AA biaxial responses and *in vivo* structural data, the entire age-dependent AA pressure versus diameter response from 0 mmHg to 200 mmHg was estimated. In order to achieve this, the biaxial responses, which are measured at low stress levels, must be extrapolated to the physiological stress levels, as described in the proceeding sections.

Constitutive modeling of human AA biaxial testing data

The human AA tissue specimens were assumed to be anisotropic, incompressible, nonlinear hyperelastic materials. Therefore, the mean AA biaxial data for each age group was first fitted with the Fung-type model, Eq. (1.20) using a Marquardt-Levenberg non-linear regression algorithm with SYSTAT 13 software (Systat Software, Inc. Chicago, Illinois).

Extrapolation of biaxial testing data

The AA tissue was assumed to be of a closed-end, thin-walled cylinder as in previous studies [219, 226-228]. The assumed cylindrical shape may be valid for the healthy AA, because unlike in descending and abdominal aortic aneurysms, the healthy AA is typically diffuse and relatively homogenous, with no significant intraluminal thrombus [201].

According to the Laplace law, the ratio of the circumferential to longitudinal Cauchy stress in the aortic wall is 1:0.5. Thus,

$$0.5\sigma_{11} = \sigma_{22}, \tag{3.6}$$

where, the subscript "*11*" refers to the circumferential direction, and "*22*" refers to the longitudinal direction. The biaxial test stress response in the material description can be expressed in the spatial description through Eqs. (1.7) and (1.8). Assuming no shear, E_{12}=E_{21}=0, and incompressibility, $\lambda_{11}\lambda_{22}\lambda_{33} = 1$, the Cauchy stress in the circumferential and longitudinal directions can be expressed as

$$\sigma_{11} = F_{11}^2 S_{11},\ \sigma_{22} = F_{22}^2 S_{22}, \tag{3.7}$$

respectively. The Second Piola Kirchhoff stresses can be expressed in terms of the Fung model coefficients as

$$S_{11} = \frac{\partial W}{\partial E_{11}} = \frac{c}{2}(2A_1E_{11} + 2A_3E_{22})e^Q, \tag{3.8}$$

$$S_{22} = \frac{\partial W}{\partial 22} = \frac{c}{2}(2A_2E_{22} + 2A_3E_{11})e^Q.$$

In order to extrapolate the biaxial data, the deformation gradient, $\boldsymbol{F}$, must be incremented in each direction, and the increments of F_{11} and F_{22} are not arbitrary, rather they are dependent on the material properties and the loading conditions. To extrapolate the raw biaxial test data, given that the σ_{11}: σ_{22} ratio is kept at 1:0.5 and F_{11} is incremented, from Eqs. (3.6)-(3.8) we have

$$\frac{1}{2}F_{11}^2[A_1(F_{11}^2 - 1) + A_3(F_{22}^2 - 1)] = F_{22}^2[A_2(F_{22}^2 - 1) + A_3(F_{11}^2 - 1)], \tag{3.9}$$

which can be expanded to

$$\frac{1}{2}[A_1F_{11}^4 - A_1F_{11}^2 + A_3F_{11}^2F_{22}^2 - A_3F_{11}^2] = A_2F_{22}^4 - A_2F_{22}^2 + A_3F_{11}^2F_{22}^2 - A_3F_{22}^2. \tag{3.10}$$

By rearranging Eq. (3.10), we get

$$A_2F_{22}^4 + F_{22}^2\left(\frac{1}{2}A_3F_{11}^2 - A_2 - A_3\right) + \frac{1}{2}[(A_1 + A_3)F_{11}^2 - A_1F_{11}^4] = 0. \quad (3.11)$$

Therefore, F_{22} can be solved in terms of F_{11} and the Fung model coefficients by solving for the roots of the polynominal function in Eq. (3.11). Equation (3.11) was solved numerically using the built-in "fzero" function in Matlab (Natick, MA), and the resulting, real-number, F_{22} value for each F_{11} increment was used in subsequent calculations.

Finally, because the AA wall thickness *in vivo* is unknown, the tissue response was expressed in terms of the tension and the initial tissue thickness H was assumed to be 1. The tension in the material description analogous to $\boldsymbol{S}$ is given by

$$\boldsymbol{T} = H\boldsymbol{S}, \quad (3.12)$$

and the tension in the spatial description is

$$\mathbf{t} = \mathrm{h}\boldsymbol{\sigma}, \quad (3.13)$$

where h is the deformed tissue thickness determined by

$$\mathrm{h} = \mathrm{H}F_{33} = \frac{H}{F_{11}F_{22}}. \quad (3.14)$$

Estimation of age-dependent AA pressure versus diameter response

The circumferential Cauchy wall tension, $t_{11_{sys}}$, at the age-dependent mean systolic blood pressure, p_{sys}, was calculated by the Laplace equation,

$$t_{11_{sys}} = p_{sys}\frac{D_{sys}}{2}, \quad (3.15)$$

where D_{sys} is the mean age-dependent diameter of the AA at p_{sys}, as measured through image analysis. Because the *in vivo* data was only collected for patients 79 years and

below, D_{sys} and p_{sys} for the 80-89 and 90-99 year old groups were estimated based on the linear regression models of Eqs. (3.25) and (3.27). From the extrapolated biaxial data, the circumferential stretch $\lambda_{11_{sys}}$, corresponding to $t_{11_{sys}}$, was determined (see Figure 3.7).

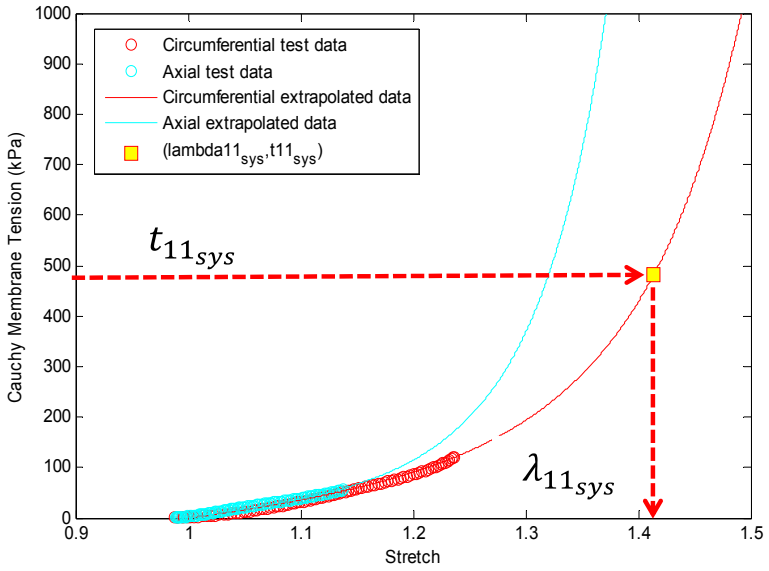

Figure 3.7 Determination of $\lambda_{11_{sys}}$ from extrapolated 1:0.5 protocol biaxial test response.

Since the mean D_{sys} at p_{sys} is known for each age group, the mean AA diameter at the unloaded (0 mmHg) state can then be determined as,

$$D_0 = \frac{D_{sys}}{\lambda_{11_{sys}}}. \tag{3.16}$$

Once D_0 is known, it is possible to generate the entire pressure vs. diameter curve. The diameter, D, at each strain increment is calculated by Eq. (3.17), and is used to calculate the pressure, P, at each strain increment by Eq. (3.18).

$$D = \lambda_{11} D_0 \tag{3.17}$$

$$P = \frac{2t_{11}}{D} \tag{3.18}$$

With the entire pressure versus diameter response, the AA permanent set in the circumferential direction could be approximated as the change in the unloaded AA diameter from the initial (50-59 years) state to the aged states (80-89 years and 90-99 years). The D_{ps} in the circumferential direction for the 80-89 year ($D_{\mathrm{ps}_{80-89}}$) and 90-99 year old ($D_{\mathrm{ps}_{90-99}}$) age groups are given explicitly by

$$D_{\mathrm{ps}_{80-89}} = \frac{1}{2}\left(\left(\frac{D_{0_{80-89}}}{D_{0_{50-59}}}\right)^2 - 1\right),\ D_{\mathrm{ps}_{90-99}} = \frac{1}{2}\left(\left(\frac{D_{0_{90-99}}}{D_{0_{50-59}}}\right)^2 - 1\right), \tag{3.19}$$

where $D_{0_{50-59}}$, $D_{0_{80-89}}$, and $D_{0_{90-99}}$ are the unpressurised AA diameters for the 50-59 year, 80-89 year, and 90-99 year old groups respectively.

3.2.4.2.2 Determination of AA equivalent strain limits

The maximum equivalent strain limits of the AA tissue, ψ_{max_m} and ψ_{max_f}, can be determined from uniaxial failure data in the fiber and cross-fiber directions. However, because there is no uniaxial failure test data available for the 50-59 year old human AA, these values were approximated. Uniaxial tension simulations were conducted using FE with the 50-59 year old AA material parameters determined in section 3.2.4.1. Briefly, the uniaxial test model was in a dog-bone shape (Figure 3.8) and constructed with large-strain continuum brick elements (C3D8H) in ABAQUS. The nodes at one end of the model were fixed in all directions, and the nodes at the opposite end were displaced to stretch the sample. The matrix and fiber equivalent strains calculated through the FE simulations at a stress level of 3.5 MPa, representing the approximate failure level determined through the uniaxial failure tests for older human AA samples (Figure 3.9),

were each approximately 30 $kPa^{1/2}$. Therefore, a value of 50 $kPa^{1/2}$ was assumed for both ψ_{max_m} and ψ_{max_f} as a conservative estimate of the failure equivalent strains.

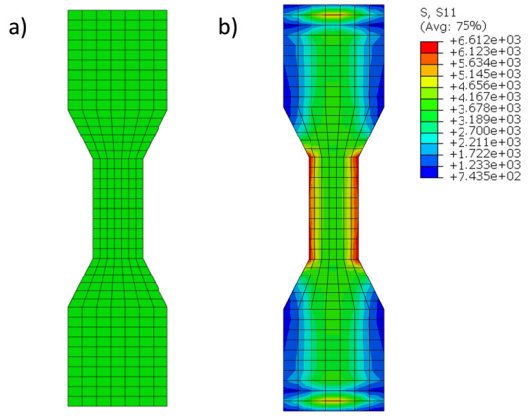

Figure 3.8 Uniaxial test specimen FE model in the a) un-deformed and b) deformed configurations. Contours of the Cauchy stress in the loading direction are shown on the deformed configuration.

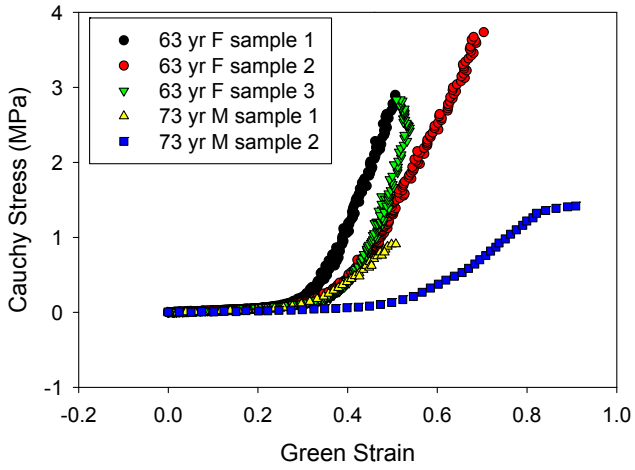

Figure 3.9 Uniaxial failure test data for human AA samples.

The minimum equivalent strain limits of the AA tissue, ψ_{min_m} and ψ_{min_f} are more difficult to determine. It was assumed that over the course of a year (one cycle) some small incremental damage is accumulated in both the matrix and fiber components of the AA. Thus, the ψ_{min_m} and ψ_{min_f} approximately correspond to the peak equivalent

strain levels *in vivo* at the 50 year old state. The *in vivo* peak equivalent strain levels at the 50 year old state were therefore estimated through FE simulation, again using the 50-59 year old AA material parameters determined in section 3.2.4.1, and a single large-strain continuum brick element model (C3D8H). The *in vivo* circumferential and longitudinal stress levels for the 50 year old state were determined from the linear regression model in Figure 3.17c for the systolic tension in the circumferential direction, $t_{11_{sys}}$. A deformed tissue thickness of 2 mm was assumed per [226] to calculate the systolic circumferential stress, $\sigma_{11_{sys}}$, from $t_{11_{sys}}$ and Eq. (3.13), and the stress in the longitudinal direction, $\sigma_{22_{sys}}$, was then obtained from the law of Laplace Eq. (3.6). The single-element model was then deformed by applying the *in vivo* stresses, $\sigma_{11_{sys}}$ and $\sigma_{22_{sys}}$ to the corresponding sides of the model via concentrated nodal forces. The peak matrix and fiber equivalent strains predicted in the model were 6.9 $kPa^{1/2}$ and 0.67 $kPa^{1/2}$ respectively. Thus, ψ_{min_m} and ψ_{min_f} were assumed to be less than or equal to 6.9 $kPa^{1/2}$ and 0.67 $kPa^{1/2}$ respectively. The ψ_{min_m} and ψ_{min_f} were initially set to these values, and were adjusted to better fit the age-dependent AA property data as described in the inverse FE procedure in the proceeding section.

3.2.4.2.3 Inverse finite element method to determine the AA aging model material parameters

To simply the model fitting process the values for $\alpha_m, \alpha_f, n_{max_m}$ and n_{max_f} were assumed. Because the parameter α predominately affects the damage evolution response at large (near failure) $\Xi_{\mathrm{n}}^{\mathrm{peak}}$ values and has a minimal impact on the damage evolution at low values $\Xi_{\mathrm{n}}^{\mathrm{peak}}$, as shown in Figure 2.4, it was assumed to not have a major impact on

age-related AA property changes which accumulate over years at relatively low $\Xi_{\mathrm{n}}^{\mathrm{peak}}$ values. Therefore, α_m and α_f were each set to 1. It was also assumed that the AA will never rupture at normal physiological $\Xi_{\mathrm{n}}^{\mathrm{peak}}$ values, thus, the cycles-to-failure for the matrix and fiber components, n_{max_m} and n_{max_f}, respectively should exceed the normal lifetime. Thus, the AA would only rupture under supra-physiological loads or disease conditions. Accordingly, both n_{max_m} and n_{max_f} were set to 100 cycles, representing 100 years beyond the initial (50 year) state.

The remaining AA aging model parameters (β_m, β_f, $D_{ps_m}^{max}$, and $D_{ps_f}^{max}$) were determined through an inverse FE procedure using the single-element model described in section 3.2.4.2.2 to determine the upper bounds for ψ_{min_m} and ψ_{min_f}. The ψ_{min_m} and ψ_{min_f} values were also adjusted in order to fit the human AA property data. The simulation consisted of five steps: 1) equi-biaxial tension at the 50 year (initial) state, 2) 30 cycles of biaxial tension to the age-dependent *in vivo* stress levels, 3) equi-biaxial tension at the 80 year (cycle 30) state, 4) 10 cycles of biaxial tension to the age-dependent *in vivo* stress levels, and 5) equi-biaxial tension at the 90 year (cycle 40) state. Each simulated cycle of biaxial tension was equivalent to 1 year. Age-related AA tissue stress-softening and permanent set were only allowed to evolve in step 2, representing the transition from the 50 year to 80 year states, and step 4, representing the transition from the 80 year to 90 year states. The circumferential and longitudinal *in vivo* stress levels were calculated for cycle 1-40 representing ages 50 years to 90 years as described in sections 3.2.2.3 and 3.2.4.2.1.

The simulated stress-strain responses from steps 1, 3, and 5 were extracted from the simulation results for comparison with the corresponding human AA equi-biaxial data (Figure 3.23). The circumferential permanent set, $D_{ps_{11}}$, was also extracted from the simulation results for comparison with the estimated human AA circumferential permanent set in section 3.2.4.2.1. The aging model parameters were adjusted until there was good correspondence between the FE and experimental data. FE predicted equi-biaxial responses within one standard deviation of the mean experimental equi-biaxial responses, and FE predicted permanent sets within 5% of the experimental permanent sets, were considered sufficient.

3.2.5 Computational modeling of human AA aging

The human AA aging constitutive model developed in section 3.2.4 was utilized in FE simulations of AA aging. Patient-specific AA FE models were reconstructed for two representative patients between the ages of 50 and 59 years for the analysis. Patient 1 was a 54 year old male and patient 2 was a 58 year old male. Both patients were normotensive with no history of cardiovascular disease.

3.2.5.1 Reconstruction of patient-specific systolic AA geometry

The three-dimensional AA surface geometry was reconstructed from the clinical CT data for each patient using Avizo 8.1 software (Burlington, MA). The aorta was segmented semi-automatically in Avizo by adjusting the pixel intensity thresholds to isolate the AA geometry from the neighboring tissues as described in section 3.2.2.2. The surface geometry was exported from Avizo and imported into Altair HyperMesh 12.0 (Altair Engineering Inc., MI) to create shell-element AA FE models containing the AA just distal to the sinotubular junction to the descending aorta (Figure 3.10). The

branching arteries at the arch were removed. The AA FE models were constructed with 4-node quadrilateral shell elements (S4R) approximately 1 mm x 1 mm in size in ABAQUS 6.13 FE software (Simulia, RI). Mesh convergence analysis demonstrated that this element size was adequate for accurate stress predictions.

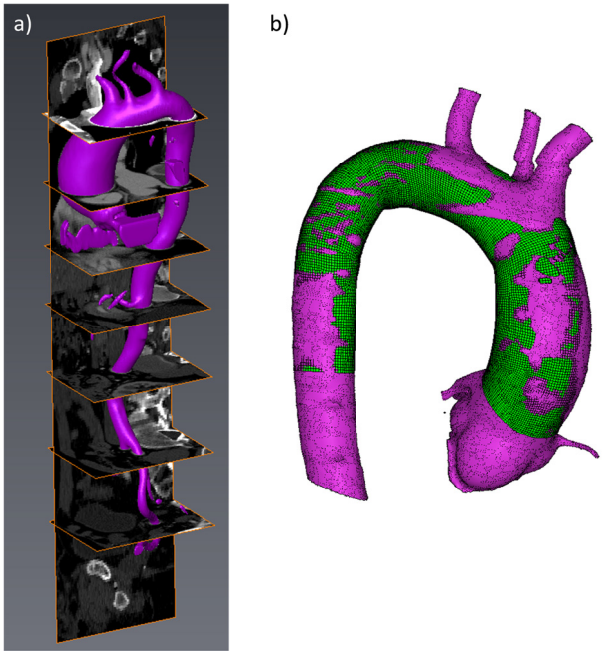

Figure 3.10 a) Segmented AA surface geometry overlaid with 3D CT data in Avizo software for a representative patient. b) Patient 1 AA FE mesh (green) overlaid with original segmented surface geometry (purple).

3.2.5.1.1 Mesh convergence analysis

A mesh convergence study was performed on an aortic FE model featured in Figure 3.11. Three FE meshes were created with average element sizes of: 2 mm x 2 mm (Figure 3.11a), 1 mm x 1 mm (Figure 3.11b), and 0.5 mm x 0.5 mm (Figure 3.11c). Systolic inflation was simulated per the methods described later in section 3.2.5.3 with each mesh. The max principal stress contours at systolic pressure are shown for each mesh in Figure 3.12. The element size did not significantly impact the stress distribution.

However, the peak aortic wall stress increased with decreasing element size from 2 mm x 2 mm to 1 mm x 1 mm, where the peak stress began to plateau (see Figure 3.13). The peak stress in the 1 mm x 1 mm mesh was within 0.5% of the peak stress in the 0.5 mm x 0.5 mm mesh and took approximately 1 hour real-time using 24 CPU cores on a HPC cluster to run vs. the 12 hour run time of the 0.5 mm x 0.5 mm mesh simulation. Therefore, an average element size of 1 mm x 1 mm was selected for all the FE models.

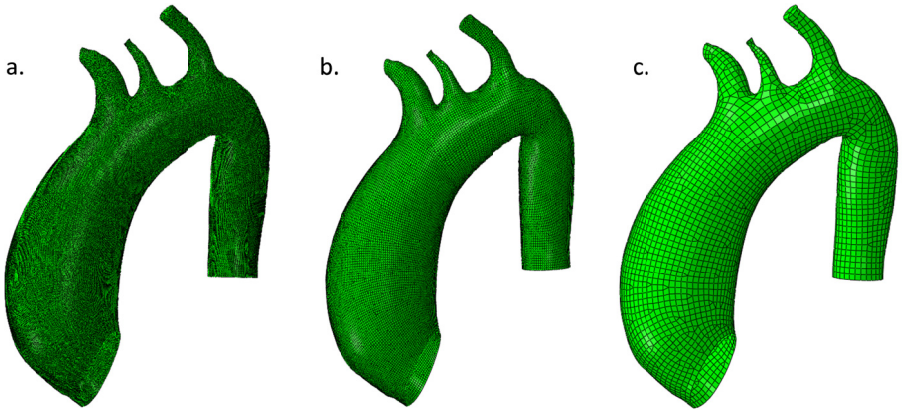

Figure 3.11 AA FE models used in the mesh sensitivity analysis. The mesh in a) is constructed with elements ~0.5 mm x 0.5 mm, the mesh in b) is constructed with elements ~1 mm x 1 mm, and the mesh in c) is constructed with elements ~2 mm x 2 mm.

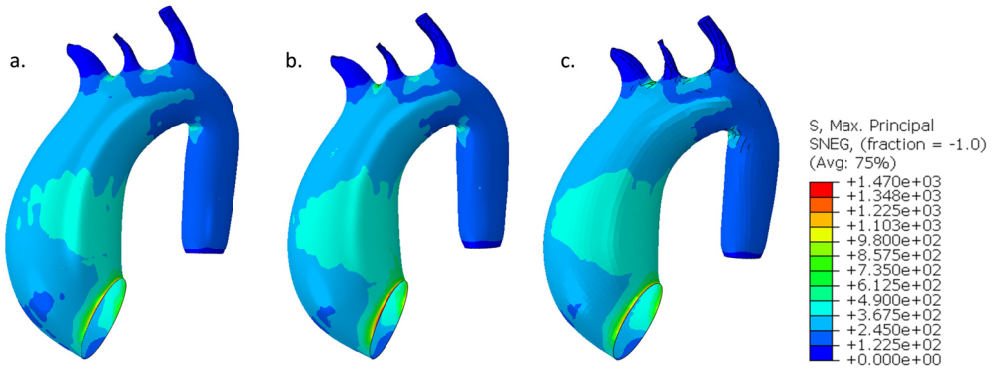

Figure 3.12 Systolic AA max Principal stress contours predicted by FE for the mesh with a) ~0.5 mm x 0.5 mm size elements, b) ~1 mm x 1 mm size elements, and c) ~2 mm x 2 mm size elements.

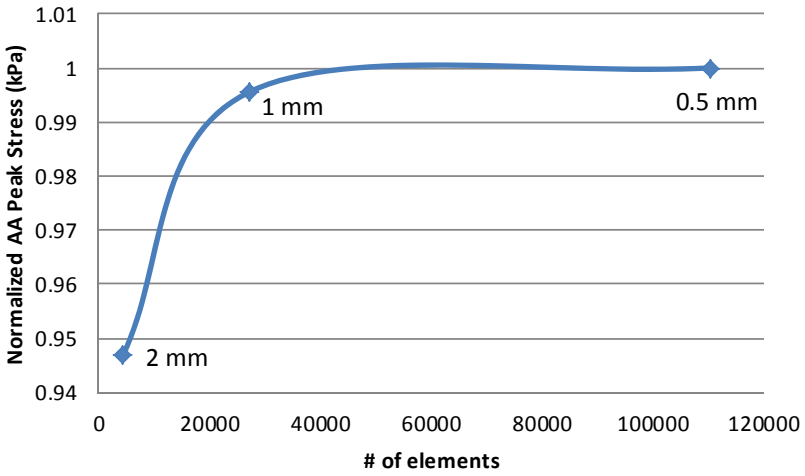

Figure 3.13 Normalized AA peak stress predicted in by FE versus the number of elements used in the model, with data labels indicating the average element size.

3.2.5.2 Reconstruction of un-pressurized AA geometry

3.2.5.2.1 Determine the systolic stretches

The AA FE mesh generated from CT data is in the pressurized condition. The AA pressure at that time was assumed to be equivalent to the systolic cuff pressure obtained for that particular patient. For FE analysis, the initial, un-deformed AA models should be constructed with the AA geometries at the zero-stress, un-pressurized state. Using the AA mesh generated directly from the CT data (i.e. at the pressurized state) for FE analysis would result in unrealistic AA dilation. Thus, in this study, the systolic AA meshes were transformed to obtain the un-pressurized geometry using the following approach. Treating the AA as a thin-walled cylindrical pressure vessel as often done [155, 219, 226-228], the systolic wall tension in the circumferential direction (systolic hoop tension), $t_{11_{sys}}$, is given by the Law of Laplace Eq. (3.15), and the systolic wall tension in the longitudinal direction is given through Eqs. (3.6) and (3.15) as

$$t_{22_{sys}} = p_{sys} \frac{D_{sys}}{4}, \tag{3.20}$$

where $P_{sys}$and D_{sys} are the systolic AA pressure and diameter respectively. Following the method presented in section 3.2.4.2.1 and [155], the AA tissue stress-strain response for the 1:0.5 biaxial tension protocol was then extrapolated to the physiological tension level. The circumferential and axial tissue stretches at the systolic condition, $\lambda_{11_{sys}}$ and $\lambda_{22_{sys}}$ respectively, were then inversely determined (Figure 3.14).

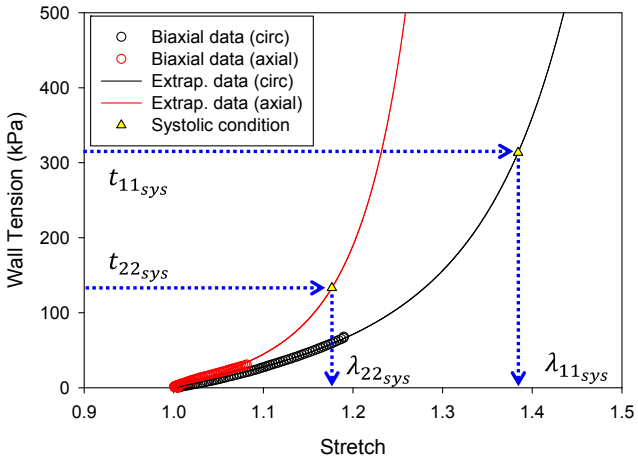

Figure 3.14 Determination of the systolic stretches in the circumferential and axial directions from the extrapolated biaxial response.

3.2.5.2.2 Determine the vessel centerline

The vessel centerline of each AA FE mesh was calculated using a custom Matlab (Mathworks, MA) script. Using the script, each AA mesh was graphically divided into approximately 10 roughly cylindrical segments along the length of the aorta (Figure 3.15). For more tortuous vessels, more segments were used. The center point in each segment was determined using the Matlab built-in unconstrained nonlinear optimization function, "fminunc", to minimize the variance of the array of distances from each node of the mesh within the segment to the center point of the segment. The AA centerline was

then obtained by fitting the center points for all of the segments with a 3D spline curve (Figure 3.15).

The AA centerline was used to define a local cylindrical coordinate system for every point (node) in the systolic AA mesh. The maximum AA diameter at each point along the centerline was calculated in the script by determining the maximum distance between two nodes within the local $r - \theta$ plane.

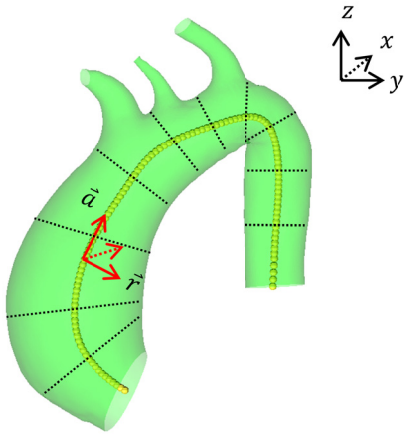

Figure 3.15 A schematic of the local cylindrical coordinate system definition based on the AA centerline (yellow dots). The black dotted lines illustrate how the aortic geometry was divided into segments to determine the centerline.

3.2.5.2.3 Transform the systolic AA mesh

The coordinates for each node in the systolic AA mesh were transformed to obtain the corresponding nodal coordinates in the un-pressurized geometry. To achieve this, each node in the systolic mesh was scaled by $1/\lambda_{11_{sys}}$ and $1/\lambda_{22_{sys}}$ in the circumferential and axial directions respectively as defined by the local cylindrical coordinate system. The resulting shell-element un-pressurized AA mesh was assigned a

uniform thickness equivalent to the mean stress-free tissue thickness measured for the 50-59 year old AA tissue samples during the mechanical test protocol (3.2.3.2).

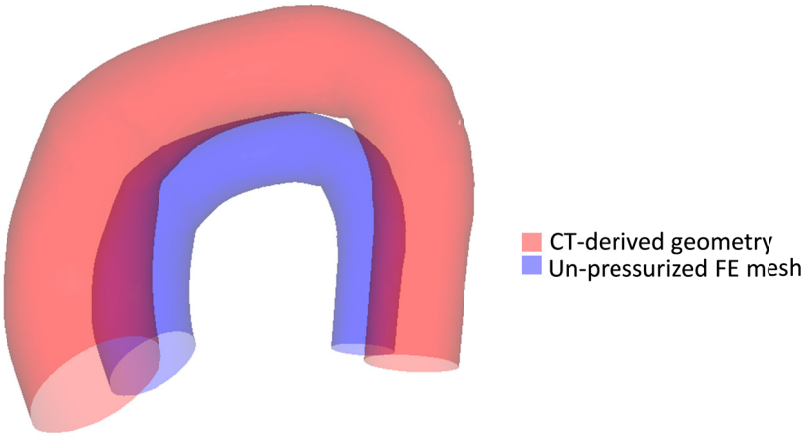

Figure 3.16 The final un-pressurized AA mesh overlaid with the original systolic mesh for patient 1.

3.2.5.3 FE simulation

The resultant un-pressurized AA meshes were used in AA aging simulations in ABAQUS software. The AA tissue properties were defined by the constitutive law and aging parameters determined in section 3.2.4. Local material axes were defined at each element of the model corresponding to the local cylindrical coordinate system determined through the center line analysis (section 3.2.5.2.2).

3.2.5.3.1 Simulation and analysis of AA inflation

Initial AA inflation was simulated in two steps. In step 1, a uniform pressure equal to the 50 year old mean diastolic pressure determined from the linear regression model Eq. (3.24) in section 3.1.3.1 was applied to the luminal surface of the entire vessel model. In step 2, the luminal pressure was increased to the 50 year old mean systolic pressure determined from Eq. (3.25), and then decreased to the 51 year old diastolic

pressure. One simulation step was equivalent to 1 patient year. In each subsequent step, the luminal pressure was ramped from the diastolic pressure to the systolic pressure for the corresponding age, and then decreased to the diastolic pressure for the $age + 1$. A maximum of 40 cycles of pressurization were applied to the model, corresponding to 40 years, from age 50 years to age 90 years.

The AA model deformation was constrained by two boundary conditions. The nodes along the vessel circumference at the proximal end and the distal end were only allowed to deform in the radial direction, as defined by the local cylindrical coordinate system. No other constraints were imposed on the model.

The simulation results were used to measure the AA diameter at diastole, D_{dias}, and systole, D_{sys}, from the deformed AA FE mesh at the corresponding diastolic, P_{dias}, and systolic, P_{sys}, pressure levels for each step. Each diameter measurement represented the distance between the same 2 nodes in the mesh at the maximum diameter level determined from the centerline analysis. These values were also used to calculate the physiological circumferential strain and the pressure-strain modulus by

$$\varepsilon_{phys} = (D_{sys} - D_{dias})/D_{dias}, \text{ and} \tag{3.21}$$

$$PS_{mod} = (D_{dias}\ (P_{sys} - P_{dias}\ ))/(D_{sys} - D_{dias}\ ), \tag{3.22}$$

respectively, for comparison with the corresponding *in vivo* metrics calculated in section 3.2.2. The AA distensibility at systole was calculated by

$$dist_{sys} = \frac{1}{D_{sys}^2} \frac{(D_{sys}^2 - D_{dias}^2)}{P_{sys} - P_{dias}}, \tag{3.23}$$

to facilitate comparison between the simulation results and corresponding *in vivo* measurements in the literature. The peak AA wall max principal stress and permanent sets in the circumferential and longitudinal directions were also extracted from the simulation results for each step of the simulation.

3.3 Results

3.3.1 *In vivo* human AA structural characteristics

3.3.1.1 Analysis of in vivo AA characteristics

Figure 3.17 shows a *significant* negative linear correlation between the peak circumferential strain and patient age (Figure 3.17a), as well as *significant* positive linear correlations between the mean AA diameter, systolic wall tension, and pressure-strain modulus and the patient age (Figure 3.17b-d). The most statistically significant correlation was between strain and age with a p-value of 0.0006. The results of the linear correlation tests are given in Figure 3.17, where *y* is the dependent measured variable and *x* is the patient age. Linear regression analysis was also conducted in order to obtain the diastolic (P_{dias}) and systolic pressures (P_{sys}) versus age relationships, as well as the diastolic (D_{dias}) and systolic diameters (D_{sys}) versus age relationships. They are given by

$$P_{dias} = -0.118age + 85.84, \quad (3.24)$$

$$P_{sys} = 0.166age + 119.09, \quad (3.25)$$

$$D_{dias} = 0.128age + 24.58, \quad (3.26)$$

$$D_{sys} = 0.099age + 28.45, \quad (3.27)$$

respectively.

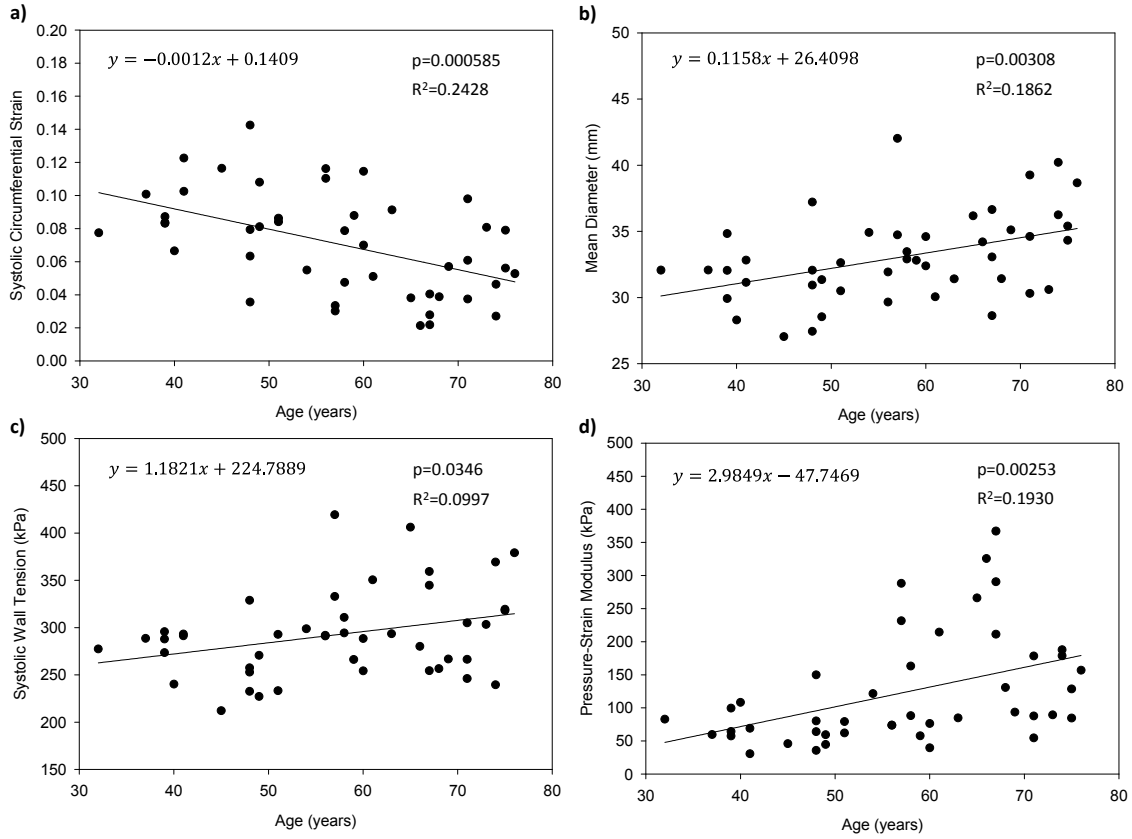

Figure 3.17 Raw a) peak circumferential AA strain, b) mean diameter, c) systolic wall tension, and d) pressure-strain modulus data plotted versus age with linear regression lines.

3.3.1.2 Comparison between age groups

The mean peak strains were significantly higher in the 30-39 and 40-49 groups at 0.088±0.018 and 0.087±0.039, than in the 60-69 group at 0.051±0.026, with p-values of

0.009 and 0.027 respectively, as well as in the 70-79 group at 0.052±0.022, with p-values of 0.003 and 0.018. There was essentially no difference in the peak strain values between the 30-39 and 40-49 groups (p=0.954) or the 60-69 and 70-79 groups (p=0.951). The mean peak strain in the 50-59 group (0.072±0.030) was smaller than those of the 30-39 and 40-49 groups and larger than in the 60-69 and 70-79 groups, although these differences were not significant. For this reason, the original 5 patient age groups were condensed to 3 for the subsequent analysis: 30-49, 50-59, and 60-79 year olds. The mean peak strains were significantly higher in the 30-49 at 0.092±0.03 than in the 60-79 group at 0.056±0.03 with $p < 0.001$ (Figure 3.18a). There was no significant difference between the 30-49 and 50-59 year old groups, or between the 50-59 and 60-79 year old groups; however, the mean peak strain was consistently larger in the younger patients.

The mean diastolic diameter was significantly smaller among the young patients (30-49 years) at 29.9±2.8 mm than the old patients (60-79 years) at 33.2±3.2 mm (p=0.003). The difference between the mean diastolic diameter in young patients compared to that of the middle-aged (50-59 years) patients at 32.4±3.8 mm was approaching statistical significance (p=0.062). There was no difference in the mean diastolic diameters between the middle-aged and old groups (p=0.542). The same trends were observed while comparing the mean systolic diameters between the groups; however the differences between the means were less drastic. The mean systolic diameter of the young patients (32.5±2.5 mm) was smaller than that of the middle-aged patients (34.7±3.2 mm) although not significantly (p=0.067) and of the old patients (35.1±3.3 mm) at statistical significance (p=0.017). Again, there was no difference between the mean systolic diameters of the middle-aged and old groups (p=0.783).

The *in vivo* AA pressure-diameter and tension-strain responses were evaluated for each patient group. Figure 3.18b shows that the pressure-diameter response is clearly shifted to the right with age, indicating larger diameters at each phase. This figure also shows that end-diastolic pressures were lower and peak-systolic pressures were higher for the older patients although not significantly. Moreover, the pressure-diameter response represented the AA structural compliance. The Figure 3.18b demonstrated steeper curves with aging indicating increased stiffness. The mean tension-strain responses for each group in Figure 3.19 show that the tissue modulus increased with age, and suggest that while the diastolic tension remains relatively constant throughout life, the systolic wall tension is higher in the middle-aged (303.0±48.5 kPa) and old (304.9±49.2 kPa) patient groups compared to the young (268.5±31.3 kPa) patient group with p-values of 0.041 and 0.017 respectively.

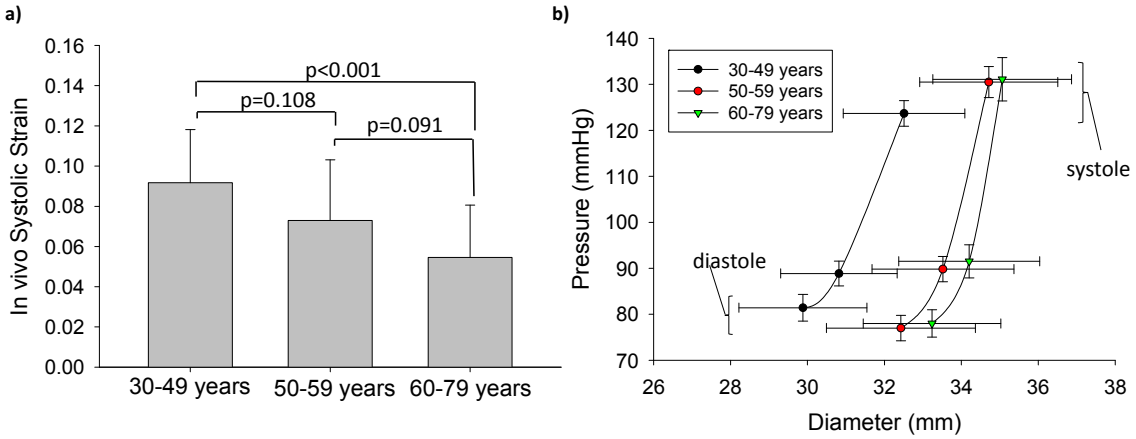

Figure 3.18 a) The mean systolic circumferential strain for each patient age group with standard deviation bars. b) Physiological pressure versus ascending aorta diameter for the 3 age groups, where the low pressure points represent the diastolic condition, the high pressure points represent the systolic condition, and the middle pressure point was taken from an intermediate phase, plotted as a mean with bi-directional standard error bars.

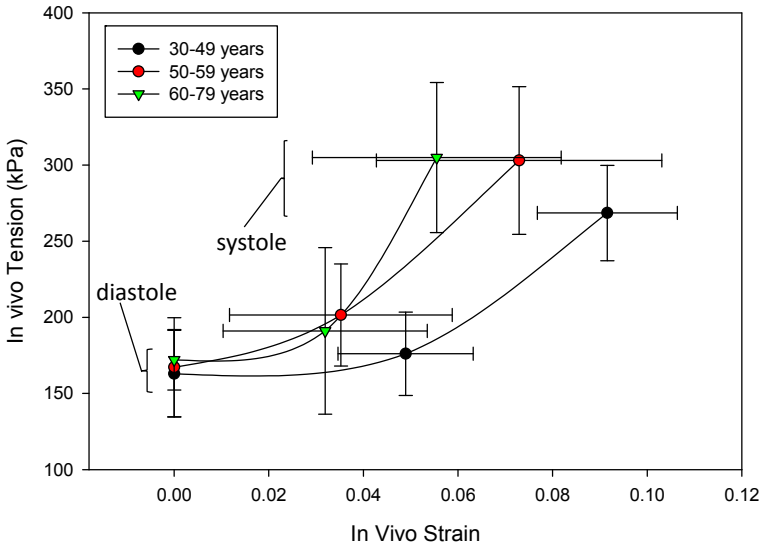

Figure 3.19 *In vivo* tension versus strain responses of the 3 age groups with lower points representing the diastolic condition, the upper points representing the systolic condition, and the middle points representing an intermediate phase, plotted as the mean value with bi-directional standard deviation bars.

The mean pressure-strain modulus was compared between patient age groups (Figure 3.20a). The mean pressure-strain modulus for the young patients was significantly less than that of both the middle-aged ($p=0.018$) and old patients ($p<0.001$). The mean pressure-strain modulus of the middle-aged patients group was also less than that of the old patients group, although not significantly ($p=0.276$). Figure 3.20b shows that the pressure-strain modulus was also found to be significantly lower among normotensive patients of all ages as compared to the hypertensive patients ($p=0.002$).

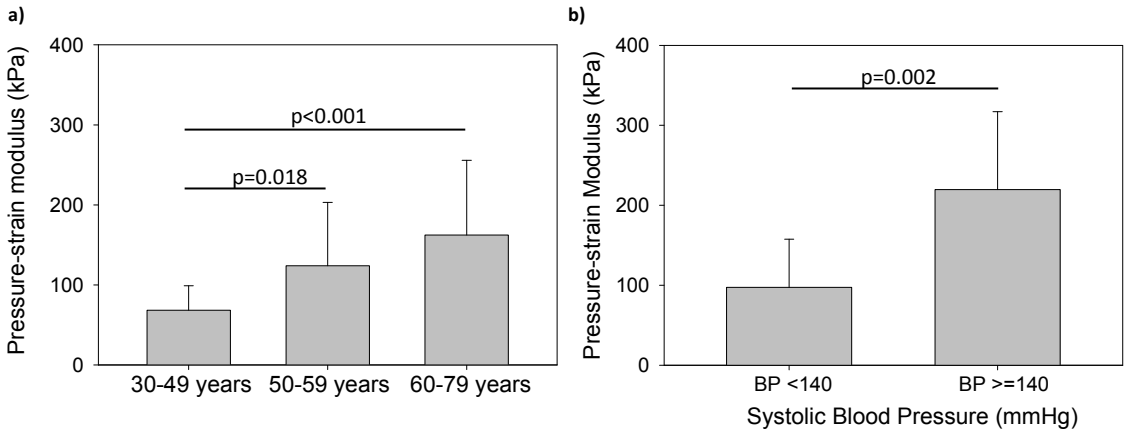

Figure 3.20 Comparison of the mean pressure-strain modulus value between (a) patients in each of the 3 age groups, and (b) normotensive and hypertensive patients, each plotted with standard deviation bars.

3.3.2 *In vitro* human AA tissue characteristics

3.3.2.1 Specimen characteristics

There were differences in the AA tissue specimens between the age groups. The 80-89 and 90-99 year old samples were all thinner than the four 50-59 year old samples. The mean thickness for the 50-59 year old samples was 2.39±0.24 mm, while the mean thicknesses for the 80-89 and 90-99 year old groups were 1.52±0.23 mm and 1.55±0.18 mm respectively. Also, many of the tissue samples for patients >80 years contained some degree of calcification as shown in Figure 3.21, whereas this was not the case for the younger (50-59 years) samples.

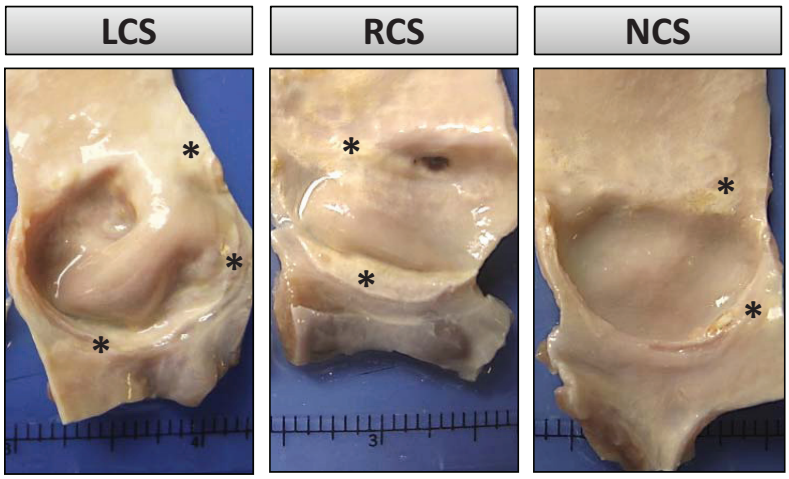

Figure 3.21 Representative images of the Left-Coronary Sinus (LCS), Right-Coronary Sinus (RCS) and Non-Coronary Sinus (NCS) of a human aortic root adopted from [33]. Asterisks indicate locations of calcium deposition in the lumen layer of the aortic wall. [1mm sub-division for all images]

3.3.2.2 Biaxial test responses

The equi-biaxial responses in the circumferential and longitudinal directions for each of the samples tested are shown in Figure 3.22. The responses for each group were very consistent. The tissue samples for the older groups (>80 years) were much stiffer than the younger (50-59 year old) samples. In the older samples, there was a very rapid transition from the lower toe region to the deeper stress-strain curve. Conversely, the younger tissues behaved nearly linearly with greater extensibility at low stresses. The most pronounced linear response was observed in the stress-strain behavior of 50-59 year old AA samples in the low stress range of < 40 kPa. The age-related stiffening is even more evident from comparing the mean equi-biaxial responses for each group shown in Figure 3.23.

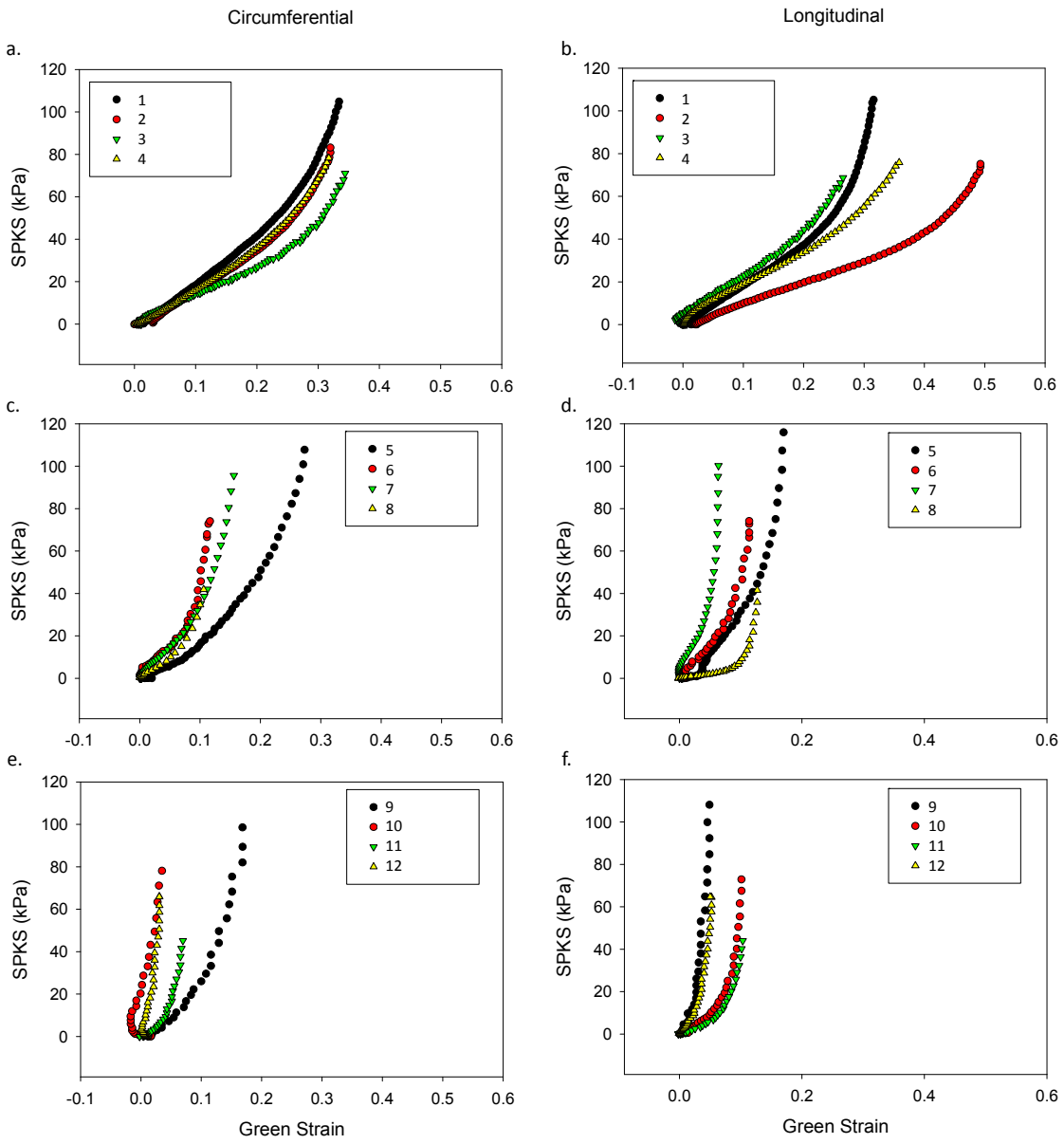

Figure 3.22 Human AA equi-biaxial response in the circumferential and longitudinal directions for age groups a) and b) 50-59 years, c) and d) 80-89 years, and e) and f) 90-99 years.

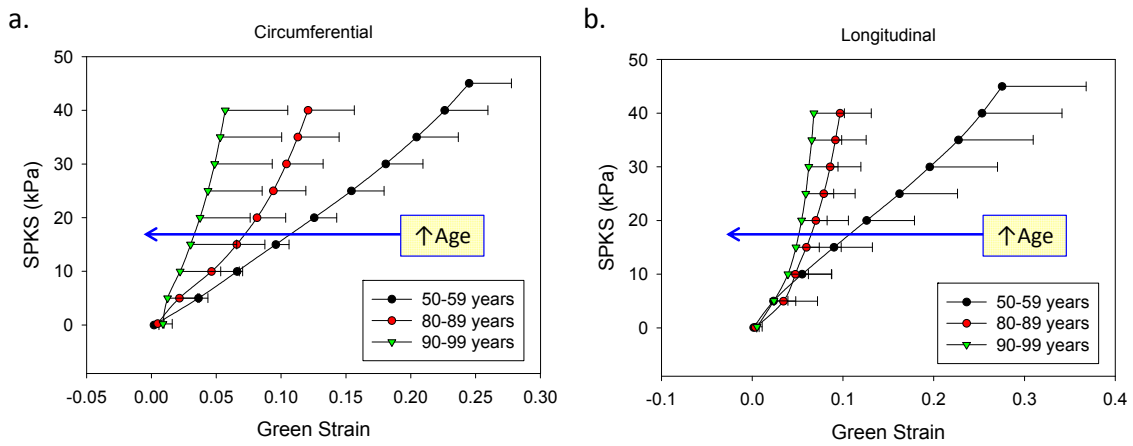

Figure 3.23 Mean human AA equi-biaxial responses for the 50-59 years, 80-89 years, and 90-99 years age groups in the a) circumferential and b) longitudinal directions plotted with standard error bars.

3.3.2.3 Histology

Histological analysis showed structural differences between the human and porcine tissues. Representative images (Figure 3.24) were taken of an 82-year old human AA specimen (ID #6) and a porcine AA specimen through the tissue thickness in the longitudinal direction at an objective magnification of 40X. VVG stain effectively rendered elastin fibers black, collagen fibers pink, and smooth muscle brown. The porcine tissues contain a higher proportion of elastin than the human tissues, which contain a higher proportion of collagen. The elastin fibers in the porcine tissues also appeared to be more undulated than the elastin fibers in the human samples which were thinner and straighter.

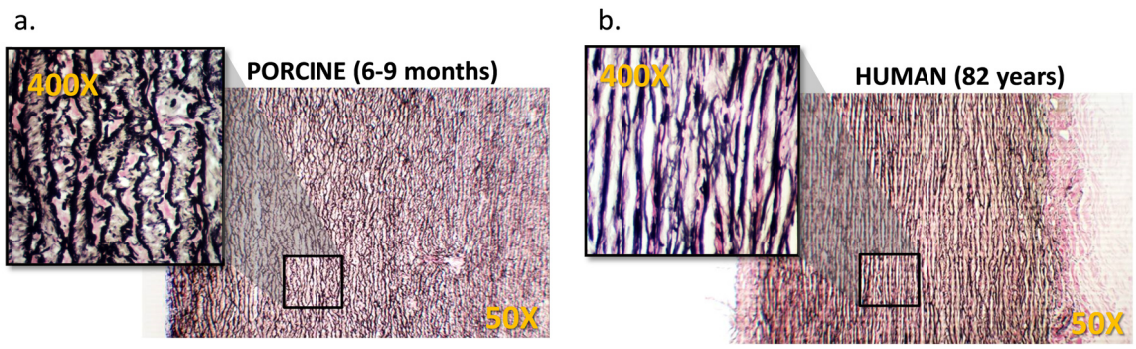

Figure 3.24 Representative AA tissue histological sections for a) 6-9 month old porcine model and b) 82 year old human stained with VVG stain. Collagen is rendered pink, elastin black, and smooth muscle brown. Note that the collagen and elastin fiber waviness in the porcine tissue is absent in the aged human sample.

3.3.3 Constitutive modeling of human AA aging

3.3.3.1 Material parameters of age-dependent AA response

The Fung model was able to capture the human AA biaxial responses to a high degree of accuracy. The Fung model parameters to fit the mean biaxial responses for each age group are given in Table 3-3. These parameters were used to generate the entire estimated human AA pressure versus diameter response for each age group. The resultant analytical human AA pressure versus diameter responses are shown in Figure 3.25 plotted with the corresponding *in vivo* measured pressure and diameter points for the 50-59 year age group, and the estimated *in vivo* pressure and diameter points for the 80-90 and 90-99 year age groups based on the linear regression models (Eqs. (3.24)-(3.27)). The estimated pressure versus diameter responses are consistent with the *in vivo* measurements.

Table 3-3 Fung model coefficients for human AA for different age groups

Age (yrs)	$c\ (kPa)$	A_1	A_2	A_3	A_4	A_5	A_6
50-59	37.94	3.76	3.29	0.10	1.10	0.15	0.26
80-89	6.42	32.50	38.93	0.10	22.61	1.32	0.56
90-99	1.57	212.64	170.75	5.20	95.23	0.21	-1.09

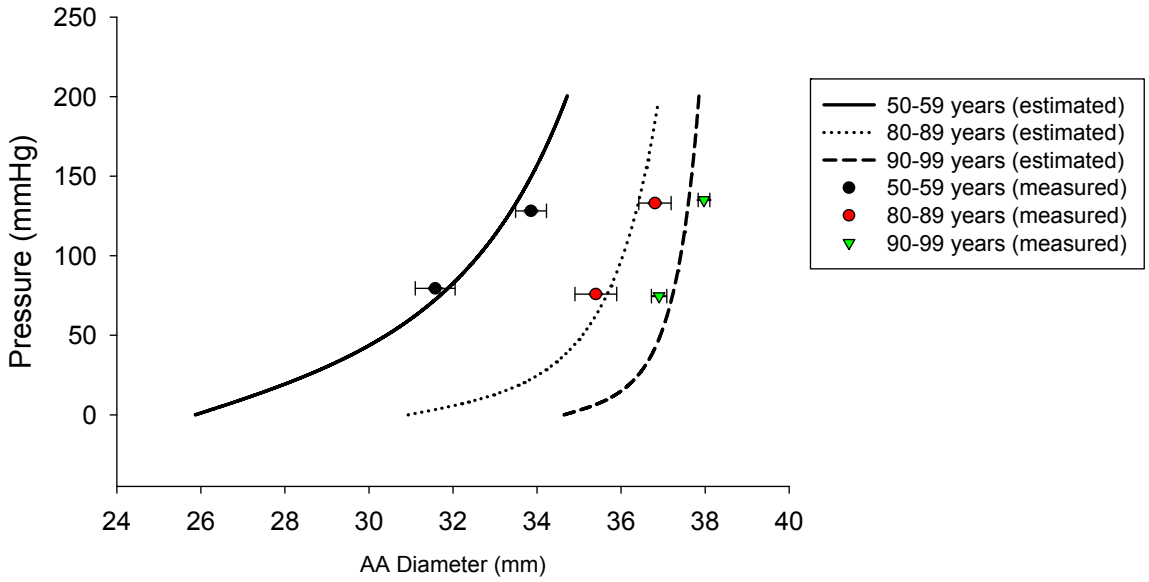

Figure 3.25 Estimated human AA pressure versus diameter response from the unpressurized state to the 200 mmHg pressurized state. The age-dependent *in vivo* diastolic and systolic diameters and pressures are also plotted as a reference.

3.3.3.2 Material parameters of AA aging response

The time-dependent inelastic constitutive framework of Chapter 2 was able to describe the aging phenomena of the human AA with the model parameters given in Table 3-4.

Table 3-4 Human AA aging model parameters.

Initial modified-Holzapfel model tissue material parameters							
$c_1\ (kPa)$	c_2	c_3	$\bar{I}_1^m$	$k_1\ (kPa)$	k_2	θ	D
18.55	1.0	7.0	3.8	0.1	1.5	0.0	5e-4
Inelastic model matrix material parameters							
$\psi_{min_m}\ (\frac{\sqrt{kN}}{m})$	$\psi_{max_m}\ (\frac{\sqrt{kN}}{m})$	n_{max_m}	α_m	β_m	D_{psmax_m}		
1.00	50.0	100.0	1.0	20.0	1.6		
Inelastic model fiber material parameters							
$\psi_{min_f}\ (\frac{\sqrt{kN}}{m})$	$\psi_{max_f}\ (\frac{\sqrt{kN}}{m})$	n_{max_f}	α_f	β_f	D_{psmax_f}		
0.50	50.0	100.0	1.0	10.0	0.8		

The single-element cyclic systolic loading simulation using the parameters in Table 3-4 demonstrated the altered geometry and mechanical properties of AA tissue in response to cyclic loading. As illustrated in Figure 3.26, the model stress-free geometry becomes significantly larger in the planar (circumferential and longitudinal) dimensions as a result of accumulating permanent sets. The FE predicted permanent sets at the 50, 80, and 90 year states are given in Table 3-5. The corresponding circumferential permanent sets estimated from analyzing the human AA *in vivo* and *in vitro* mechanical property data in section 3.2.4.2.1 are also given in Table 3-5. It can be seen that, at corresponding age points, the FE predicted and analytically estimated permanent set in the circumferential direction were in good agreement. The FE predicted permanent sets in the circumferential and longitudinal directions were the same at the 80 year state, but the permanent set in the longitudinal had become more significant by the 90 year state.

The change in the AA tissue properties is demonstrated by the altered stress-strain response. The FE predicted human AA equi-biaxial responses referenced to the current state (without permanent set) for the 50-59 year, 80-89 year, and 90-99 year states are

plotted against the corresponding experimental data as shown in Figure 3.27. The simulation results agree well with the experimental data for each age state.

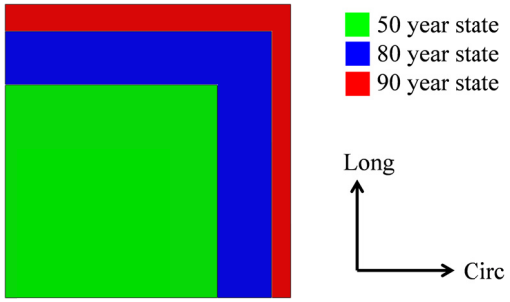

Figure 3.26 Overlay of the stress-free single-element FE model geometry at the 50 year, 80 year, and 90 year states, showing increased planar (circumferential and longitudinal) dimensions with age.

Table 3-5 Comparison of estimated human AA permanent set (PS) with aging with the FE predicted PS with aging in the circumferential (Circ) and longitudinal (Long) directions.

Patient Age (yrs)	Estimated Circ PS	FE Age (yrs)	FE Predicted Circ PS	FE Predicted Long PS
50-59	0.00	50	0.00	0.00
80-89	0.26	80	0.28	0.28
90-99	0.39	90	0.40	0.45

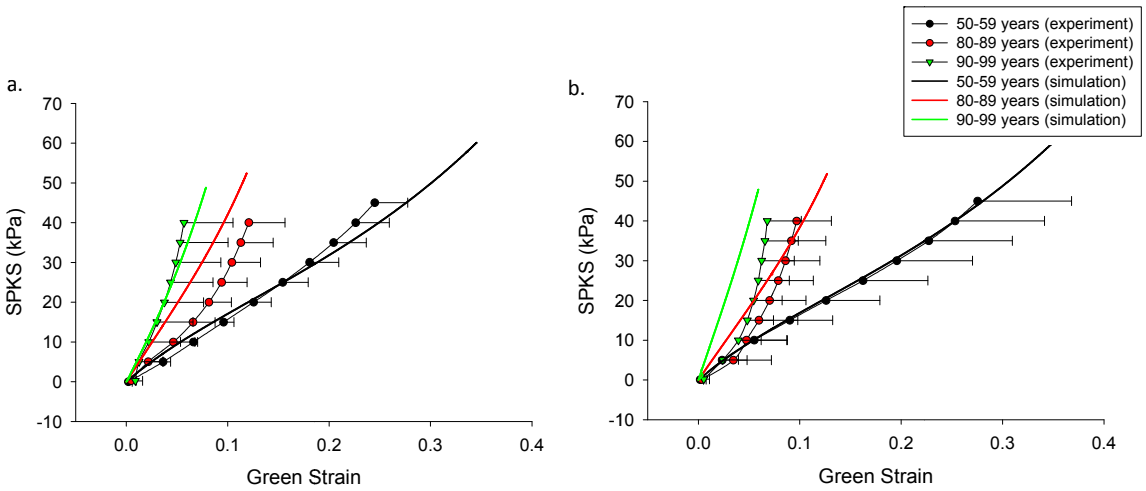

Figure 3.27 Comparison between the experimental and FE predicted human AA response with aging in the a) circumferential and b) longitudinal directions showing good agreement. Note all data is referenced to the current configuration.

3.3.4 Initial human AA inflation

Systolic AA inflation at the 50 year state was simulated in both patients to ensure that AA inflation using the initial AA aging model parameters and the stress-free vessel geometry resulted in realistic AA deformation. The FE deformed meshes at systole, were compared to the original meshes generated from the surface geometries segmented from the CT data. The inaccurate boundary conditions and loading conditions at the arch and descending aorta, resulted in discrepancies between the FE deformed geometry and the original CT systolic geometry surrounding these locations; however, the AA portion of the deformed FE mesh, the region of interest, matched the ground truth. Figure 3.28 shows the AA portion of the FE deformed geometry at systole for patient 1 overlaid with the initial CT surface geometry. The FE predicted systolic AA diameter for patient 1 was 34.4 mm compared to the ground truth diameter of 35.3 mm, giving a percent error of 2.61%. The FE predicted systolic AA diameter for patient 2 was 37.6 mm compared to the ground truth diameter of 39.1 mm, giving a percent error of 3.89%. Therefore, the FE simulations resulted in realistic AA deformation under uniform pressurization.

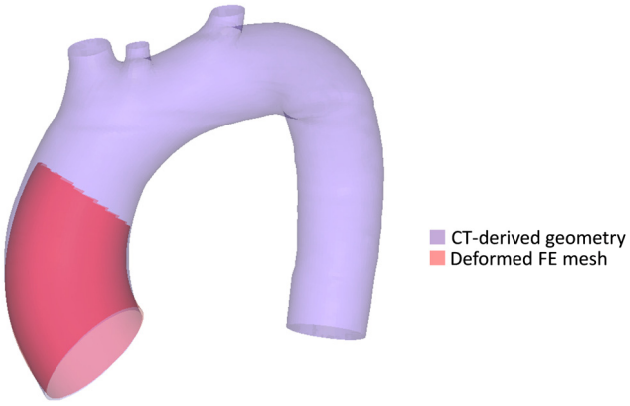

Figure 3.28 Overlay of the FE deformed AA geometry under systolic pressurization and the original systolic AA surface geometry segmented from the CT data showing good correspondence.

3.3.5 Effect of aging on the human AA structural properties

Aging was simulated in both AA models using the parameters in Table 3-4 by applying physiological pressurization cycles. The AA geometries changed over the course of the simulations due to the changing AA material properties and loading conditions. As a result, the AA became dilated, elongated and more curved with continued cycling. The AA geometries at the 50 year and 80 year states under diastolic tension are overlaid with each other in Figure 3.29, showing these changes. Note that the 80 year old AA diastolic geometries are significantly larger even though they are under slightly less pressure than the 50 year old geometries, because the diastolic pressure is inversely related to age (Eq. (3.24)).

Contour plots of the circumferential and axial AA permanent set are shown in Figure 3.30 for patient 1 and Figure 3.31 for patient 2. At each age state, the axial permanent set stretches were larger than the circumferential permanent set stretches. Patient 2 had larger permanent sets at each age compared to patient 1. In both patients, the peak axial permanent sets were located on the outer curvature of the vessel, particularly at the arch. The peak circumferential permanent set stretches were located at the proximal end of the AA towards the inner curvature, where the axial permanent set stretches were small.

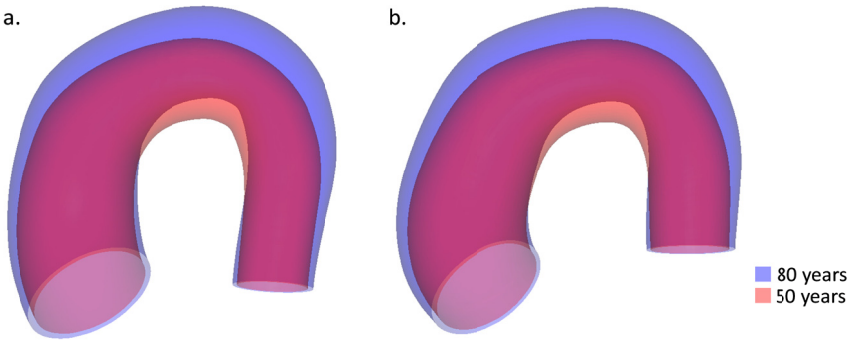

Figure 3.29 Overlay of the FE deformed AA geometry at end diastole at the 50 year (red) and 80 year (blue) states for a) patient 1 and b) patient 2, showing at the aorta has significantly dilated and elongated and the curvature has increased over the course of the simulation.

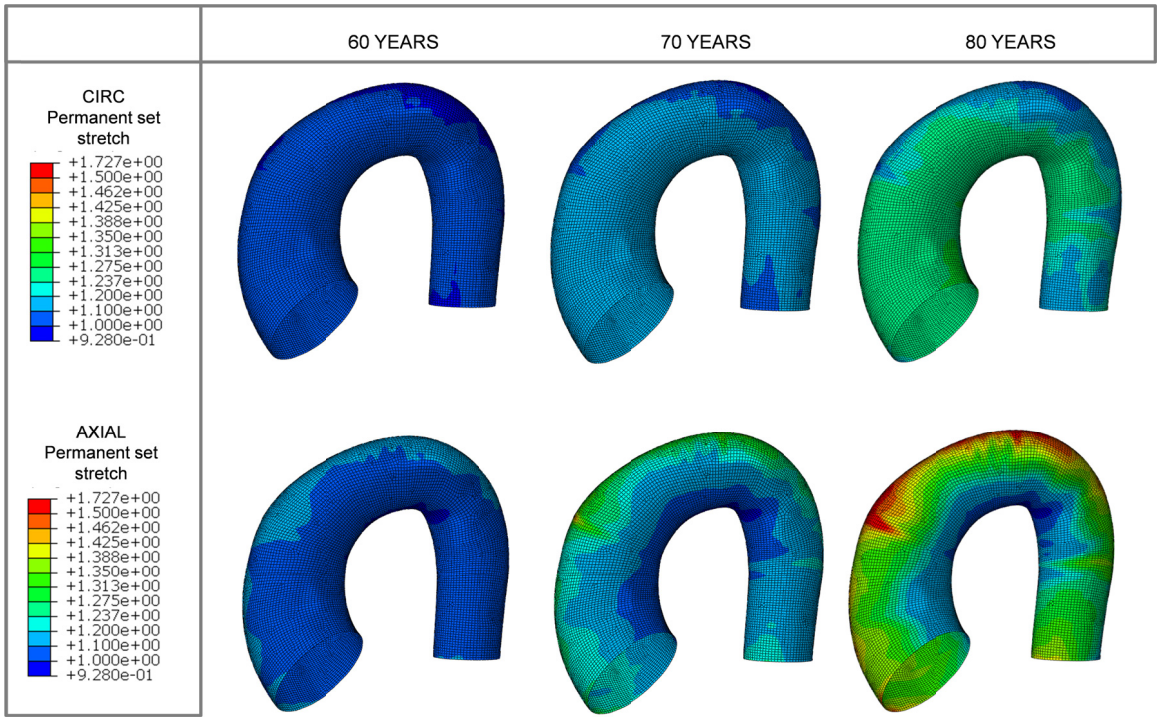

Figure 3.30 FE predicted aorta wall circumferential (CIRC) and axial permanent set distributions for patient 1 showing larger axial permanent sets at each age.

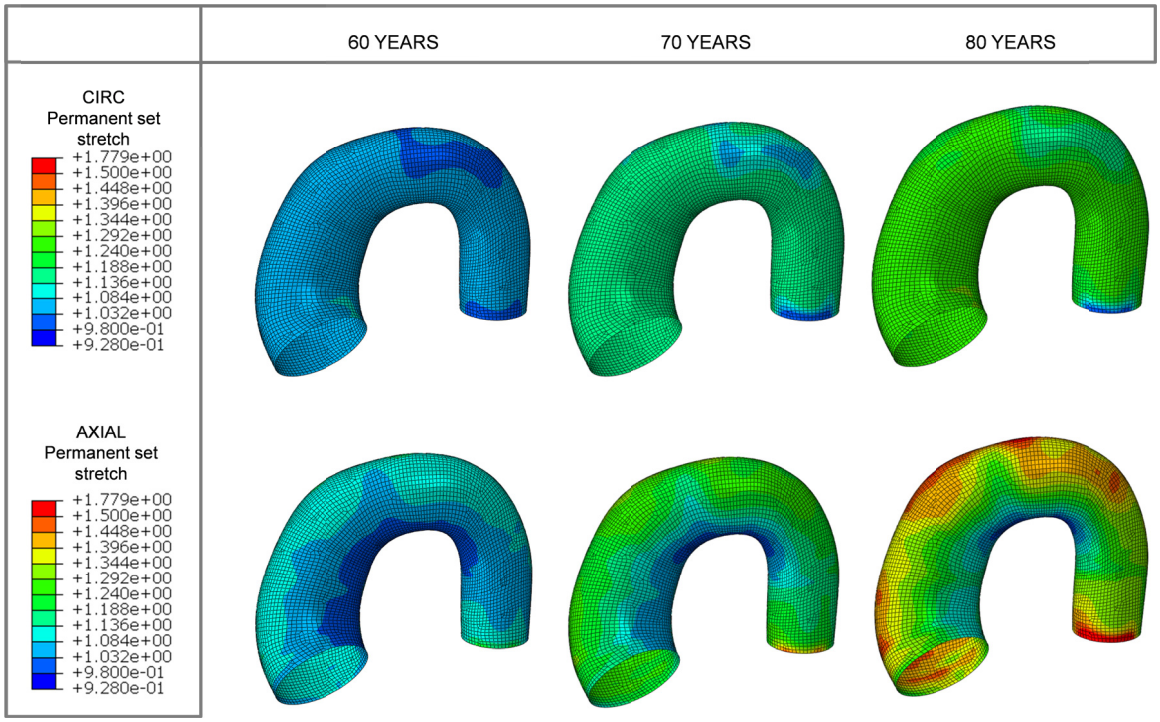

Figure 3.31 FE predicted aorta wall circumferential (CIRC) and axial permanent set distributions for patient 2.

3.3.5.1 Comparison with in vivo AA structural property data

The simulated AA structural property changes were compared to the age-dependent *in vivo* structural data. Overall, the FE predictions followed the same trends as the *in vivo* data. The diastolic and systolic diameters for both patients increased with age as shown in Figure 3.33. The diastolic diameter increased at a slightly faster rate than the systolic diameter: 0.112 mm/year and 0.115 mm/year versus 0.072 mm/year and 0.074 mm/year for patients 1 and 2 respectively, which is in agreement with the *in vivo* diastolic diameter and systolic diameter growth rates of 0.128 mm/year and 0.099 mm/year determined through linear regression (Eqs. (3.26) and (3.27)).

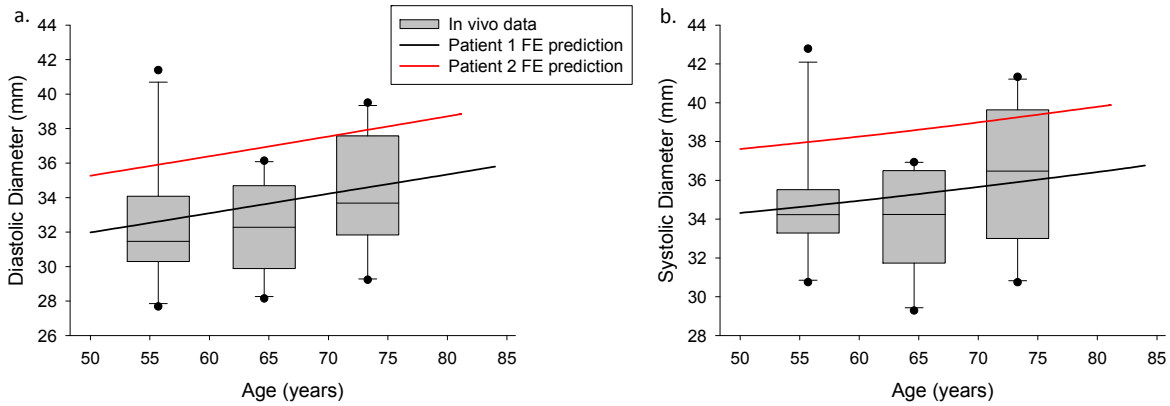

Figure 3.32 FE predicted and *in vivo* measured AA diameter at a) end diastole and b) peak systole for each age.

The simulated AA structural mechanics were also compared to the *in vivo* data. Again, the FE predictions followed the same trends as the *in vivo* data. The physiological circumferential strain decreased with age and the pressure-strain modulus increased with age in both patients as shown in Figure 3.33. The mean physiological circumferential strain determined from the *in vivo* analysis for 56±3 year olds, 65±3 year olds, and 73±2 year olds, was 0.072±0.03, 0.051±0.026, and 0.052±0.022 respectively. The FE predicted physiological strains at 56, 65, and 73 years for patient 1 were 0.063, 0.049, and 0.039, and for patient 2 were 0.057, 0.044, and 0.035 respectively (Figure 3.33a). The mean pressure-strain modulus determined in the *in vivo* analysis for 56±3 year olds, 65±3 year olds, and 73±2 year olds, was 124±80 kPa, 189±118 kPa, and 136±54 kPa respectively. The corresponding measurements predicted by FE for patient 1 were 110 kPa, 145 kPa, and 196 kPa, and for patient 2 were 121 kPa, 160 kPa, and 215 kPa respectively. Thus, good agreement between the *in vivo* and FE results was obtained for both the physiological circumferential strain and the pressure-strain modulus at each level.

The initial strain was lower in patient 2 but decreased at a similar rate as in patient 1, where the rate of change in the strain decreased slightly with aging (Figure 3.33a). The initial pressure-strain modulus was higher in patient 2 but increased at a similar rate as in patient 1 (Figure 3.33b). In both patients the rate of change in the pressure-strain modulus with age increased with aging.

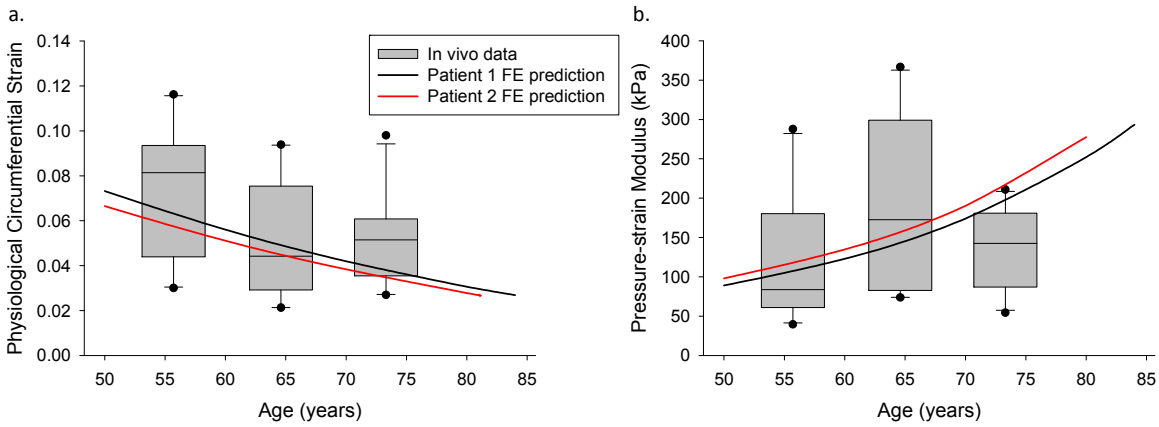

Figure 3.33 FE predicted and *in vivo* measured AA a) physiological circumferential strain and b) pressure-strain modulus.

The AA distensibility at each level was also calculated from the simulation results (Figure 3.34). Similar to the physiological circumferential strain, the distensibility decreased over aging in both patients, and the distensibility for patient 2 was lower than that of patient 1 at each time point. The rate of change in the distensibility versus age curve decreased with aging.

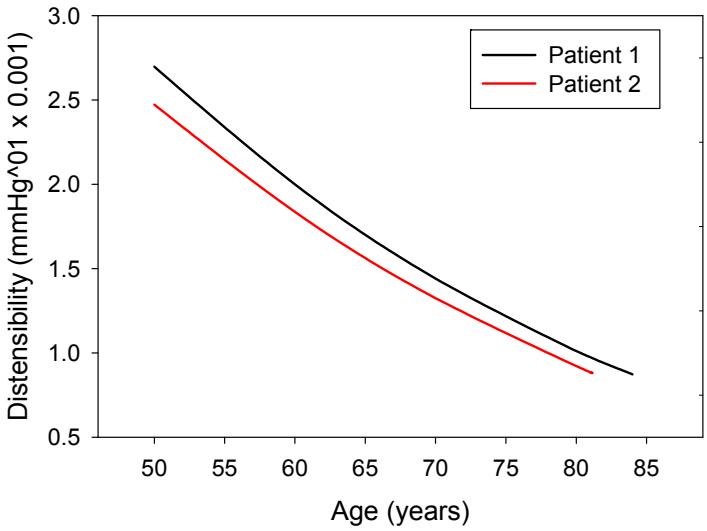

Figure 3.34 FE predicted ascending aorta distensibility from age 50 years to 80 years.

3.3.6 Effect of aging on the human AA wall stress

Contour plots of the aortic wall stress generated by FE for both patients were analyzed at each decade level (Figure 3.35). The aortic wall stress was largest at the proximal AA where the diameter was largest at each age level, and the magnitude of the stress increased with aging. The peak wall stress was located near the inner curvature at each age state, but over aging new stress concentrations developed, indicated by the arrows in Figure 3.35 at the 80 year age level.

The peak max Principal stress (**MPS**) was plotted versus age for both patients in Figure 3.36. Figure 3.36 shows that the peak AA wall stress increases significantly with age. From age 50 years to 80 years, the peak wall stress increased by 49% in patient 1 and 34% in patient 2. The MPS was initially lower in patient 1 but increased at an accelerated rate compared to that in patient 2.

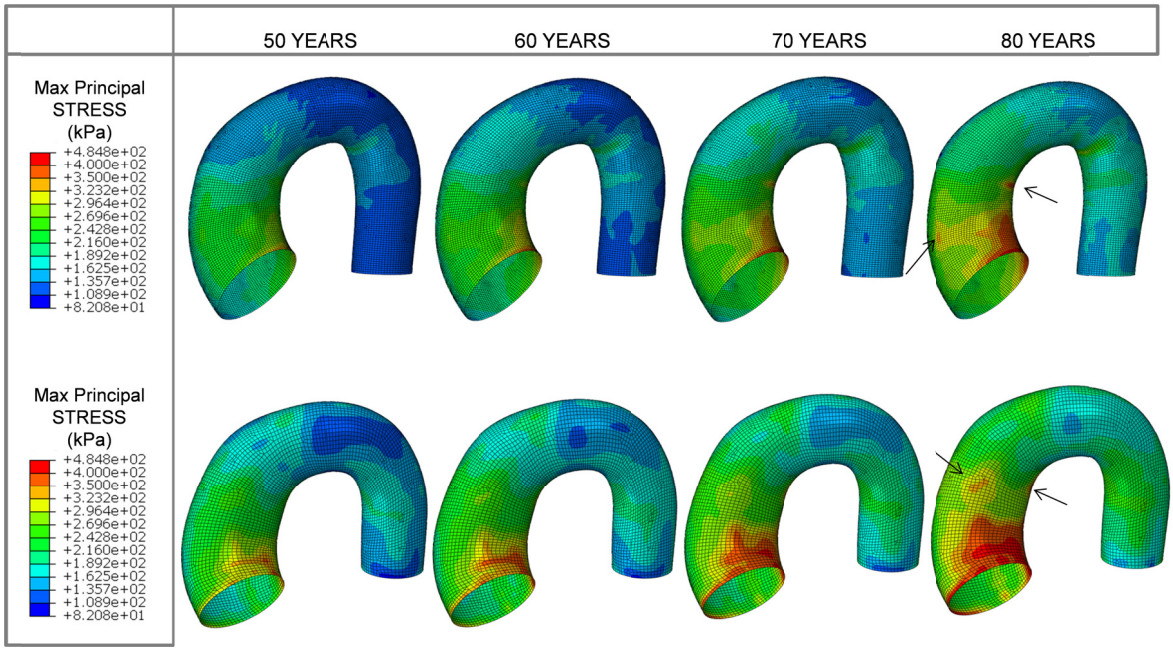

Figure 3.35 FE predicted aorta wall max principal stress distributions for patient 1 (top) and patient 2 (bottom) showing increased stress throughout the vessel from 50 years to 80 years, and the development of new stress concentrations indicated by the arrows at 80 years.

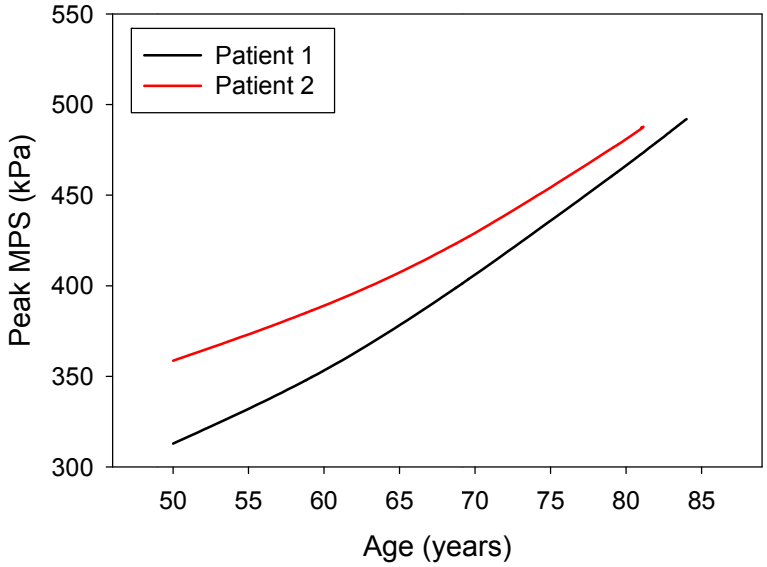

Figure 3.36 FE predicted ascending aorta peak max principal stress from age 50 years to 80 years.

3.4 Discussion

3.4.1 Age-related AA structural property changes

Overall, the age-dependent trends observed in this study for the AA are in line with findings from other studies on the *in vivo* mechanics of the abdominal [177, 187, 192, 224, 230-232] and descending aorta [177, 187, 230] as well as the aortic arch [177]. The aortic tissue stiffness was shown to increase with aging; however the degree of aortic stiffening may differ along the length of the aorta [177, 187, 230].

The mean AA diameter measurement for all of our patients (i.e., non-age -phase specific) was 33.0±3.3 mm, which is similar to the mean AA diameters measured by CT as reported in [175] (32.0±4.2 mm), [178] (~32 mm), [176] (32±3 mm), [173] (33.6±4.1 mm), [182] (32±4 mm), and [186] (33.5±3.6mm). In addition, the AA diameter in this study was positively correlated with the patient age, as reported by other studies [174-180, 182, 186]. According to the linear regression presented in Figure 3.17, the mean AA diameter dilates 0.12 cm per decade, whereas the corresponding value reported for male patients is 0.15 cm per decade in [176], and 0.1 cm per decade in [179].

The mean circumferential strain between diastole and systole for our young group (42.6±5.3 years) was 0.092± 0.03 and for our old group (68.9±5.2 years) was 0.056±0.03. Morrison *et al.* [178] reported a similar value of 0.103±0.038 for young patients (41 years), and a much smaller value of 0.026±0.012 for old patients (68 years). The difference between our results and those of Morrison *et al*. [178] may be due to their inclusion of both male and female patients (5 men and 2 women), and relatively small sample sizes (n=7 for both young and old groups). Although not quantified here, similar

age-related changes to the female AA mechanical properties are expected. Waddell *et al*. [203] suggest that age-related arterial stiffening in women is even more pronounced than in men. Young women tend to have lower, while older women have higher, arterial stiffness than age-matched men [203], which may explain the more extreme strain values measured in [178].

Overall, the AA mechanics seem to go through a transition period during a patient's fifties, when mechanical properties start to decline. There were no significant differences between the 30-39 year old and 40-49 year old groups; however, the AA diameter was larger, the circumferential strain was smaller, and the pressure-strain modulus was larger in the 50-59 year old patients than in patients under 50 years. By the age of 60 years, the AA properties had further declined. However, beyond 60 years the AA properties declined only slightly, with no significant differences between the 60-69 year old and 70-79 year old groups. Incidentally, 60 years is the approximate onset age for thoracic aortic aneurysm [233]. Given that reduced elasticity is also characteristic of the dilated aorta [234], the reduced compliance of the AA beyond age 60 years may predispose dilation.

As the aging aorta dilates and stiffens, the systolic pressure may increase and the diastolic pressure may decrease [235], which were both observed in this study (Figure 3.18b). We also observed that on average, patients with hypertension have an AA pressure-strain modulus which is over twice that of normotensive patients (Figure 3.20b). Ganten *et al.* [192] suggest that increased arterial stiffness may be both the cause and the effect of the concurrent increase in hypertension amongst aging patients. A recent study by Craiem *et al*. [189], shows that the mean AA diameter in age- and gender-matched

individuals is also higher in hypertensive patients compared to normotensive patients. Regardless of the cause, the increase in systolic blood pressure and dilation of the AA will increase the AA wall tension, which may render older patients more susceptible to aneurysm formation and dissection. O'Rourke *et al.*[236] also attributes arteriosclerotic changes in the microvasculature of the end organs (e.g., heart, kidneys, brain, etc.) to increased aortic stiffness.

3.4.2 Age-related AA tissue property changes

The results from the *in vitro* human AA characterization tests mirrored these trends. The equi-biaxial data (Figure 3.23) clearly showed AA stiffening with age in both the circumferential and longitudinal directions which is consistent with other reports in the literature [205, 211]. The most dramatic differences in the biaxial responses were between the 50-59 year and 80-89 year groups. This may be partly due to the large age difference between the groups; however, the results of the *in vivo* property study, as well as the biaxial data presented by Haskett et al. [205], suggest that beyond the age of 60 years, the tissue properties have already significantly declined.

In the AA, the collagen and elastin fibers are wavy in young patients, and it has been hypothesized that they become straightened out [209] and more aligned [205] over time contributing to higher stiffness. Increased tissue stiffness may be associated with detrimental microstructural changes such as elastin fragmentation [237], that may weaken the tissue. In Figure 3.24 it can be seen that in the aged (82 year old) human AA sample, the collagen and elastin fibers were nearly straight [154]. Because, the collagen and elastin fibers in the aged human AA were relatively straight, when loaded, more collagen fibers would be recruited to bear tension, attributing to higher stiffness, which explains

the age-related stiffening in the AA tissue (Figure 3.23). Collagen fiber un-crimping and elastin fiber fracture may also explain the concurrent positive correlations observed in the *in vivo* study between diameter and age, as well as pressure-strain modulus versus age. The slightly larger and more significant increase in diastolic diameter per year (0.13 mm, p=0.0014) compared to the systolic diameter (0.10 mm, p=0.0081) also suggests collagen fiber straightening and elastin fiber fracture, because these changes would be realized by significant dilation of the diastolic diameter with little change to the systolic diameter, due to the concurrent reduction in elasticity.

3.4.3 Constitutive modeling of human AA aging response

In this study, a modified strain energy function for the matrix components was proposed (Eq. (2.12)) in order to fit both the biaxial response and the AA structural response at the initial (50-59 year) state. Using the original matrix strain energy function (Eq. (2.11)), in order to fit the linear low-stress portion of the stress-strain response, parameter c_2 had to be very small, and then the AA dilation at physiological pressures predicted by FE were unrealistically large, because c_2 determines the high stress range stiffness. By adding an extensibility limiting parameter (I_{1_m}), both the linear portion of the low stress response ($I_1 < I_{1_m}$) and the rapid stiffening of the tissue response at $I_1 \geq I_{1_m}$ could be captured. The resultant initial AA material parameters were able to describe the equi-biaxial behavior of the 50-59 year old human AA, as well as the AA physiological structural response.

The AA aging model parameters determined in this study can capture the transition of the human AA equi-biaxial response from the 50-59 year old state to the 80-

89 year old and 90-99 year old states (Figure 3.27). To our knowledge, this is the first model that can capture the experimentally-derived tissue response at different age states. Additionally, the model can capture the estimated circumferential permanent set with age. Unfortunately, the AA permanent set in the longitudinal direction could not be determined from the *in vivo* data for comparison; however, the finding that the predicted permanent set was more significant in the longitudinal direction corresponds with the experimental observations that permanent sets are more significant perpendicular to the preferred fiber orientation in aortic tissues [144].

3.4.4 Computational modeling of human AA aging

3.4.4.1 Finite element modeling of the human AA

The predicted AA wall stresses at systole were consistent with thoracic aorta FE results in the literature. The peak vessel wall stress in both patients was located along the inner curvature of the proximal AA at the maximum diameter level, consistent with published FE results for the non-dilated [73] and dilated thoracic aorta [76, 118]. The peak wall stress value in both patients at the 80 year state was approximately 500 kPa, which is similar to what we found in our FE analysis of ascending aorta aneurysms under systolic pressure (486±140 kPa) [118]. The unique aspects of our models presented in this study are that the AA tissue properties were defined with a nonlinear, anisotropic material model based on biaxial testing data of healthy human AA, and the FE wall deformation and physiological diameter change was validated against CT data.

3.4.4.2 Comparison with in vivo human AA measurements

The FE simulations results were very consistent with the *in vivo* AA property data at corresponding age states. The FE predicted aging trends including: increased diameter, decreased physiological strain, and increased pressure-strain modulus, correspond to the *in vivo* data. The age-dependent systolic inflation FE simulation results were also consistent with other *in vivo* AA measurements in the literature. Koullias et al. [226] quantified the *in vivo* AA distensibility in 20 patients with a mean age of 64±2.61 years using epiaortic echocardiography. They found that the normal AA has a distensibility of 2.499±0.49 $mmHg^{-1}$ x 0.001 and a percentage diameter change of 6.745 over the cardiac cycle, which are consistent with the results calculated in this study, where patient 1 had a distensibility of 1.75 $mmHg^{-1}$ x 0.001 and a physiological circumferential strain of 0.0502, and patient 2 had a distensibility of 1.62 $mmHg^{-1}$ x 0.001 and a physiological circumferential strain of 0.0456 at age 64 years. The good agreement between the FE and *in vivo* results serve to validate that the AA aging constitutive model combined with the FE modeling techniques presented in this study can accurately describe AA structural property changes with aging.

3.4.4.3 Effects of aging on human AA mechanics

The FE AA aging simulations demonstrated that the age-related tissue stiffening, dilation and elongation, and systolic pressure amplification in the AA act to increase the vessel wall stress over time as expected. Interestingly, these effects were accelerated in patient 2 which had a larger initial diameter compared to patient 1, which is consistent with clinical observations that wall stress increases [226] and distensibility decreases as the aorta enlarges [226, 238]. By using an FE approach using patient-specific aortic

geometry models we eliminated the assumption of cylindrical geometry needed to calculate the vessel wall stress from *in vivo* measurements or theoretical models. Thus, changes in the wall stress distribution with aging could also be visualized for the first time (Figure 3.35).

3.4.5 Limitations

The aorta moves during the cardiac cycle, so it was difficult to measure the *in vivo* strain at the exact same location of the aorta in each phase. Others have adopted a local reference frame defined by anatomical markers to avoid this problem [178]; however, using 3D reconstruction of AA geometries and overlaying the geometries at different phases offers a good approximation of using the same measurement location, with little post-processing required. Furthermore, the 3D reconstruction method utilizes CT data with superior resolution to MRI, and allowed for AA circumference measurements, which eliminated the circular cross-section assumption for the strain calculations. Therefore, we assume the strain measurements presented here, accurately describe the *in vivo* AA behavior. The mechanical properties in the axial direction were not measured. Morrison *et al.* [178] measured the length of the aorta along the centerline path from the left coronary artery to the third intercostal artery to measure the axial mechanics, however the imaging data available in our study often did not include the aortic arch; thus, leaving no anatomical markers for consistent length measurements. Also because all of the patients studied in the *in vivo* analysis were referred for cardiac CT, some displayed cardiovascular risk factors such as hypertension and coronary artery disease. Therefore, this patient sample may have slightly more extreme AA tissue properties than the normal healthy age-matched patient population. However, because the clinical

characteristics are similar for each group, the gender-specific, age-based comparison is valid.

The AA luminal pressure at diastole and systole were not available in this study, and, were thus, assumed to be equivalent to the corresponding pressure measurements taken by sphygmomanometer at the brachial artery. It has been shown that peripheral blood pressure may overestimate the pressure-strain modulus and wall tension in young patients [236]. Furthermore, the AA pressure waveform for each patient was assumed to follow the same shape although increased tissue stiffness has been shown to amplify pressure spikes in the AA pressure waveform [239]. Therefore, for these reasons, the increase in pressure-strain modulus with aging is likely underestimated in this analysis. The use of simultaneous pressure recordings with gated CT images would have eliminated the need for this assumption.

The sample sizes for the *in vitro* mechanical tests were relatively small: a larger sample size would provide more conclusive results, and help with the constitutive modeling. Given that the 50-59 year old *in vivo* AA properties already exhibited deteriorated mechanics compared to patients below 50 years old, the initial parameters used in the AA aging constitutive model should be for patients younger than 50; however, because there is no such biaxial data available for younger patients, we used the 50-59 year old response as the initial property. Through this initial study, we have shown that the constitutive framework can capture age-related AA changes thus, upon the availability of younger human AA biaxial data, the model parameters could be retuned in the future. Quantifying the failure properties of human AA tissues at various ages is particularly important for refining the ψ_{max_m} and ψ_{max_f} parameters. More thorough

characterization of the tissue microstructure will also be important for assessing the relationships between collagen fiber un-crimping and the tissue level dilation. Possible regional property differences within the AA tissues studied were not considered in order to simplify the experimental procedure. It may be necessary to expand the model in the future to include growth and remodeling to describe tissue microstructural changes in response to mechanical and biological stimuli to study disease progression. Also, long-term clinical follow-up data, for example clinical CT images for a patient at different ages, are needed to validate the predictability of the model. At this point we can only claim that the model can interpolate the bulk age-related AA structural property changes between 50-59 years and 60-69 and 70-79 years given the known tissue property changes from 50-59 years to 80-89 and 90-99 years.

Several simplifications were also made in the FE models. There could be some error in the reconstructed AA models and presented diameter measurements due to the resolution of the images. Vessel residual stress was ignored in this analysis. Therefore, 2D shell elements were utilized to represent the neutral axis wall response. The AA tissue properties were assumed to be homogeneous throughout the FE models, because only the AA was tested; however, the aorta tissue properties may be region specific [205]. Vessel inflation was simulated by applying a uniform pressure to the luminal surface and hence fluid flow was ignored. The luminal pressure was assumed to be equivalent to the patient's cuff pressure.

3.5 Conclusions

In this study the age-dependent human AA structural and tissue properties were quantitatively assessed. The *in vivo* structural properties were measured from multi-

phase clinical CT image data, and the tissue properties were characterized through *in vitro* mechanical tests. The results of this study show that the AA mechanics deteriorate with aging, i.e. diameter increases, systolic expansion decreases, and pressure-strain modulus increases. These changes are likely due to the degradation of elastin and collagen fiber un-crimping. Nearly straightened collagen and elastin fibers were observed in the 80 year old AA histology.

These data were used in the development of a novel AA aging constitutive model based on the time-dependent inelastic framework of Chapter 2. The developed model was able to capture the evolution of the human AA equi-biaxial response at age 50-59 years, to 80-89 years, and 90-99 years. The constitutive model was then utilized in FE simulations of AA aging in 2 patient-specific aorta models to investigate how the AA mechanics evolve over time.

The FE results in terms of the diameter, systolic expansion, and pressure-strain modulus at corresponding age states were in good agreement with the *in vivo* data. Thus, the constitutive framework and FE modeling approaches developed in this study can be used to describe tissue- and organ-level property changes in the human AA due to natural aging. The simulation results also showed that the AA wall stress increases significantly with aging, likely predisposing to aneurysm and dissection.

The ultimate goal of this research is to develop a computational tool that can be used to evaluate a patient's risk of disease and rupture over time. Such a tool would be particularly beneficial for determining timely surgical intervention for patients with ascending aorta aneurysm. In order to do this, the AA aging model parameters must be

recalibrated for aneurysm tissues in a similar fashion. The human AA aging model in this study represents the baseline model which can capture the bulk changes in AA tissue properties and structural properties in response to natural aging.

4 MODELING OF BIOPROSTHETIC HEART VALVE FATIGUE DAMAGE

In the previous chapter, we used the theoretical and computational framework developed in Chapter 2 to model human ascending aorta aging. In this chapter we used the theoretical and computational framework to model the fatigue damage process of bioprosthetic heart valve (**BHV**) biomaterials following a similar overall approach.

Currently, the only clinically proven effective, long-term treatment for valvular heart disease is open-chest cardiac valve repair or replacement surgery. Typically the diseased native valve is replaced with either a mechanical or tissue-derived BHV. BHVs can better replicate normal valvular hemodynamics, but they have limited durability. An improved understanding of the BHV fatigue process could provide scientific rationale for improved device design. Thus, in this chapter we developed a constitutive model of the glutaraldehyde-treated bovine pericardium (**GLBP**) fatigue response utilizing uniaxial fatigue experimental data presented in the literature [105]. GLBP was chosen as a representative BHV leaflet material. This model was then used in conjunction with finite element (**FE**) simulations of cyclic BHV deformation to investigate the impacts of leaflet fatigue damage on the device durability. Leaflet fatigue was first simulated in a surgically implanted aortic valve (**SAV**). The simulation results were in good agreement with the known failure modes of SAVs [240-244], which served to validate the modeling approaches. These same approaches were then taken to predict the impacts of leaflet fatigue damage in transcatheter aortic valves (**TAV**) for which the durability and failure

modes are currently unknown. The results show that the durability of TAVs will be reduced compared to that of SAVs, particularly in non-optimal deployment configurations. Some of the results of this chapter are published in [131, 245].

4.1 Introduction

4.1.1 Heart valve structure and function

The heart has four cardiac valves, namely the aortic, mitral, tricuspid and pulmonic valves, which maintain unidirectional blood flow through the heart during the cardiac cycle. These four valves are primarily passive structures i.e., they open and close due to the differential blood pressure on each side of the valve leaflets. Diseases of the aortic and mitral valves, on the left side of the heart, are much more prevalent than those of the tricuspid and pulmonic valves on the right.

The aortic valve (**AV**) (Figure 4.1a), residing in the aortic root (Figure 4.1b), consists of three leaflets, namely the left-, right- and non-coronary leaflet. These three leaflets may differ in size and are not necessarily symmetrically aligned (120 degrees apart from each other) [246]. Microscopically, each leaflet is composed of three layers: the ventricularius, spongiosa, and fibrosa. Each layer contains a different amount of elastin, collagen, glyosaminoglycans and proteoglycans.

The mitral valve is a complex yet elegantly structured cardiac valve that consists of an annulus, two leaflets, approximately 25 chordae tendineae, two papillary muscles, and the underlying left ventricular myocardium (Figure 4.1c). The mitral annulus, similar to the aortic annulus, is subdivided into the lateral (anterior) portion, mainly composed of cardiac muscle, and the septal (posterior) portion of fibrous tissue. The anterior mitral

leaflet is connected via the aortic-mitral curtain to the AV, and the posterior mitral leaflet is hinged on the posterior mitral annulus (Figure 4.1d). Microscopically, the leaflets are composed of multiple layers - the atrialias, spongiosa, fibrosa and ventricularis.

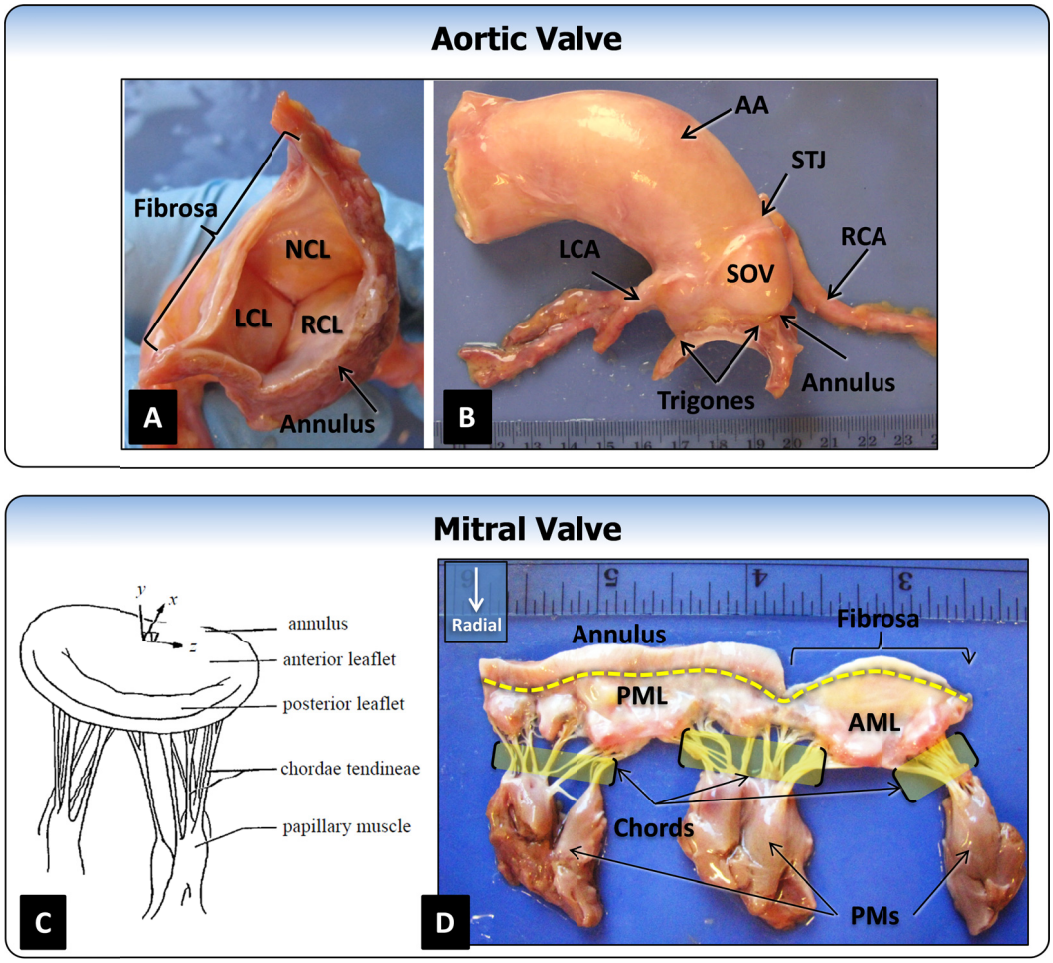

Figure 4.1 Photographs of the structure of a human excised aortic root showing (a) the entire circumference of the annulus comprised of fibrous and muscular regions and the coapting aortic leaflets, non-coronary (NCL), left-coronary (LCL) and right-coronary (RCL) leaflets; (b) the same aortic root with the ascending aorta (AA), right- (RCA) and left- (LCA) coronary arteries, non-coronary sinus of Valsalva (SOV), sinotubular junction (STJ) and trigone regions. (c) The illustration of the mitral valve anatomical structures and (d) the photograph of a human excised mitral valve showing the mitral annulus, anterior (AML) and posterior (PML) leaflets, fibrous region, chordae tendineae (chords) and papillary muscles (PMs).

4.1.2 Heart valve disease

Heart valve disease is a significant cause of morbidity and mortality. In the United States, heart valve disease is responsible for about 22,000 deaths per year. In the past two decades, major advances have been made in diagnostic methods in interventional cardiology as well as surgical procedures that enhance our understanding of the natural history of valvular heart disease, and thus, increase patient survival. However, valve procedures still have an overall in-hospital mortality rate of 4.22%, a figure that is much higher than that of other cardiac procedures [247].

The two most common presentations of valve disease are aortic stenosis (**AS**) and mitral valve regurgitation (**MR**). AS is the abnormal narrowing of the AV, which partially obstructs the outflow of blood from the left ventricle. MR is an abnormal leakage of blood from the left ventricle back into the left atrium during systole.

4.1.3 Clinical management of heart valve disease

Currently, the only clinically proven effective, long-term treatment for valvular heart disease is open-chest cardiac valve repair or replacement surgery. Typically with aortic valve disease, the native valve is replaced with either a mechanical or tissue-derived BHV. BHVs offer superior hemodynamics and eliminate the need for anticoagulants accompanying mechanical valve replacement. For these reasons, BHVs have been widely used to treat valvular disease for over forty years [248]. Now with the advent of minimally invasive implantation techniques, a new breed of BHVs amenable to transcatheter delivery, TAVs, have emerged [249, 250].

TAV intervention is now the standard-of-care treatment for inoperable patients and a viable alternative option for high-risk patients with symptomatic AS [251]. Since the first TAV procedure in 2002 [252], TAVs have been implanted in more than 150,000 patients worldwide [253]. Short and mid-term clinical results are promising: TAV intervention can significantly improve valve hemodynamics and patient quality of life with the added benefits of lower operative risk and shorter recovery time compared to SAV replacement [254, 255]. However, little is known about the long-term durability of these devices, owing in part to the relative immaturity of TAV intervention and the advanced age and illness of the patients selected for this treatment. To date, TAV intervention is still not considered for lower-risk patients: SAV replacement with either a mechanical or bioprosthetic valve remains the gold standard.

TAV implantation into an existing BHV, to treat stenosis or regurgitation in either a failed SAV or an ill positioned TAV, is also a growing trend for high-risk patients. There are currently 4 TAV devices used in these valve-in-valve (**ViV**) procedures: the Edwards SAPIEN/XT, the Medtronic CoreValve, the Medtronic Melody valve, and the St Jude Portico valve [255]. TAV implantation within a failed SAV has been shown to be feasible and safe with a reported procedural success rate of 93.1% in the largest reported TAV-in-SAV registry to date with 202 patients across 38 centers [256]. Considering this success rate with the morbidity and mortality associated with valve reoperation, ViV treatment for SAV failure will likely become an increasingly attractive option for both patients and clinicians [257], particularly with the recent shift towards the implantation of bioprosthetic SAVs versus mechanical heart valves [258].

4.1.4 Limited durability of bioprosthetic heart valves

Yet the main limitation of BHVs continues to be the long-term durability owing to calcification or fatigue-induced structural deterioration of the tissue leaflets [259]. Consequently, BHVs often need to be replaced within 10 years of implantation, and in as little as 5 years in younger patients [259]. It has been suggested that these failures are caused by localized leaflet damage at stressed regions, but the mechanisms of BHV leaflet fatigue and failure are incompletely understood.

It is, however, clear that BHV design features have an impact on the long-term durability. For instance, the Ionescu-Shiley (**IS**) SAV was taken off the market for its subpar durability of approximately 5 years [240, 260-264], due to design flaws shortly after its release. IS valve failures were often associated with leaflet tearing initiating at the commissures and propagating down the suture attachments as shown in Figure 4.2 from Lawford et al. [265]. For this reason, second generation pericardial SAVs, including the Carpentier-Edwards Perimount (**CEP**), incorporated a flexible stent to act as a cushion and reduce stresses acting on the leaflets [242]. The CEP valve has an *in vivo* durability of up to 20 years. After extensive study, the inferior durability of the IS valve compared to the CEP valve has been hypothesized to be the result of several factors: very little stent-tip deflection (due to the rigid stent), thin leaflets, and poor leaflet coaptation causing "pin-wheeling" of the leaflets [241]. In rare cases, early CEP valve structural failures have also been observed [244]. These failures are thought to be largely due to heterogeneity in the structure and properties of the glutaraldehyde-treated bovine pericardium (**GLBP**) leaflets, which leads to leaflet tearing and/or prolapse due to elongation of one or more of the leaflets [242-244].

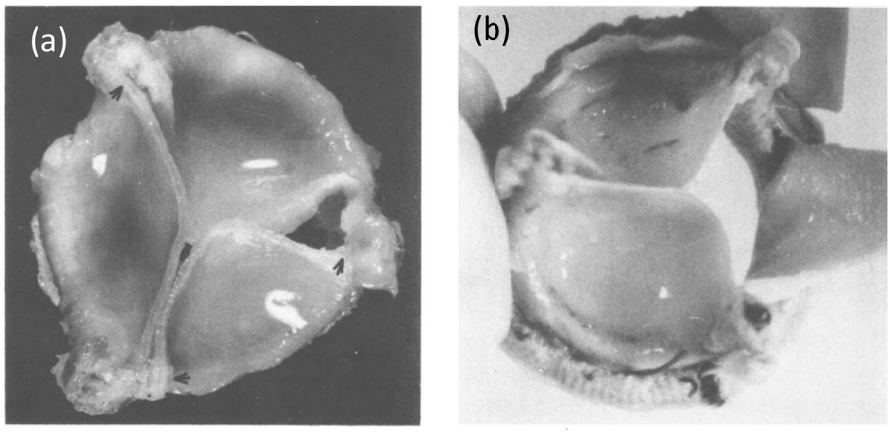

Figure 4.2 Explanted Ionescu-Shiley BHVs from Lawford (Lawford, Black et al. 1987) displaying (a) leaflet sagging and damage near the commissure and (b) leaflet tearing along the suture attachments.

Fatigue of TAV leaflets will become an increasingly critical and prevalent problem in the coming years. TAV durability has been widely recognized by the valve industry and clinicians [266, 267] as one of the critical issues limiting its use in low-risk patients, with longer life expectancies than the current high-risk TAV patients. Indeed, TAV structural failures as early as 3 years after implantation have been cited [268, 269]. Interestingly, 9 of the 10 TAV devices currently available are comprised of GLBP or porcine pericardium leaflets, similar to traditional SAVs in which leaflet durability is limited. Furthermore, because TAVs must be crimped into a small diameter catheter for delivery and deployment, they are subject to additional design constraints such as thinner leaflets and lack of valve stent-tip deflection, which may further impede long-term durability. To further complicate matters, because in TAV intervention the diseased native tissue is not removed and the device is not sutured into place like SAVs, the deployed device may not be fully or uniformly expanded, which could distort the configuration of the leaflets.

TAV underexpansion is particularly a problem with ViV procedures. In ViV procedures the newly implanted TAV is typically oversized (larger in diameter) with respect to the inner diameter of the previous prosthesis to prevent paravalular leak and valve migration [270, 271]. While oversizing has been shown to reduce the risk of moderate to severe paravalvular leak in patients [272-274], the degree of oversizing remains controversial. ViV implantation was recently approved for the CoreValve device in 2015, but typically ViV procedures are performed as an "off-label" usage of TAV devices. Consequently there are little guidelines in terms of proper TAV sizing and positioning for clinicians to go by. Excessive oversizing may preclude full expansion of the TAV due to the non-deformable stent of the previous prosthesis which restricts the TAV from fully expanding [252, 275, 276]. Valve underexpansion has been shown to distort the configuration of the leaflets [277, 278] and can affect transvalvular gradients and effective orifice areas [271, 279-285]. Thus, ViV is typically not recommended in SAVs smaller than 21 mm [255]. The ViV configuration is also believed to affect leaflet durability by two primary mechanisms: 1) overhanging of the leaflets over the stent during opening and 2) twisting and overhanging of the leaflets over each other during valve closure [257, 270, 271].

Furthermore, it has been shown that poor leaflet coaptation [132, 286] will reduce the durability of bioprosthetic SAVs; thus, it follows that the durability of TAVs that exhibit poor leaflet coaptation as seen under non-optimal deployment conditions (elliptical, underexpanded, non-uniformly expanded) [153], would be further reduced. Therefore, there is a critical need for more comprehensive studies on the long-term

durability of TAV devices in various configurations to assess deployment strategies and provide insight for improved design.

4.1.5 Valve durability analyses

Several groups have adopted whole valve device fatigue tests using accelerated wear testers (**AWT**), which can mimic *in vivo* hemodynamics, to gain a better understanding of BHV fatigue mechanisms. AWT testing is also used frequently in commercial settings. In fact, the International Standards Organization [48] and the Food and Drug Administration [287] recommend that new BHV designs be tested up to 200 million cycles using AWTs to evaluate the fatigue performance. The fatigue effects observed in BHV materials include: softening, strength reduction, and collagen alteration. Billiar and Sacks [288] found a significant reduction in the ultimate tensile strength and alteration of the planar biaxial mechanical properties of porcine BHV leaflets after 200 million of cycles of AWT tests. Hilbert et al. [289] used polarized light optics to characterize damage to the BHV collagen fiber architecture due to accelerated testing. For GLBP, they measured a 37% increase of collagen fiber crimp period after 360×10^6 cycles [289]. Similarly, Liao et al. [290] observed loss of collagen crimp and leaflet thinning in decellurized aortic valves. Smith et al. [291] observed increased curvature and collagen fiber distortion in the central belly region of porcine BHV leaflets to 500×10^6 AWT cycles [291]. Sacks and Smith [292] showed that this fiber damage can occur in localized regions, likely those subjected to high stresses, far before any gross structural changes become evident. Similarly, Purinya et al. [293] found a ~50% reduction in the strength of BHVs after only 48 months of *in vivo* implantation, indicating that fatigue damage can occur rapidly in the leaflet tissue. Wells et al. [49] observed

irreversible alteration of the glutaraldehyde crosslinks in porcine BHV leaflets after just $50x10^6$ cycles. Vyavahare et al. [259] and Raghavan et al. [294] also observed leaflet microstructural changes including damage to the type I collagen [259] and loss of GAG content [259, 294].

These studies have been particularly useful in identifying concentrated damage regions within the leaflets and flawed designs. However, although AWTs can imitate the *in vivo* hemodynamics, it remains difficult to isolate the specific effects of various BHV design parameters on the durability of the leaflets when using this technique. The *in vivo* mechanical environment is quite complex for heart valve applications. Different areas of the leaflets may experience drastically different loading conditions. Therefore, BHV durability assessment is largely based on the visual inspection of the leaflets following AWT cycling, and this method is both time-consuming and expensive.

4.1.6 Experimental characterization of heart valve biomaterial fatigue properties

Alternatively to whole valve tests, several groups have adopted isolated BHV material fatigue tests to characterize the effects of cyclic loading on the tissue properties in a more controlled way (precise application of displacement or loads). Early studies include those by Broom to characterize the effects of uniaxial fatigue in chemically fixed bovine and porcine mitral valve tissue [295, 296] as well as porcine aortic valve tissue [297]. Continued cycling induced a reduction in tissue compliance and collagen crimp [295-297]. Broom concluded that preserving the natural collagen fiber crimp in fixed valve tissues will improve the fatigue properties of the tissue [297], although this point is somewhat controversial [298]. Sun et al. [105] and Sellaro et al. [137] have since investigated the uniaxial tensile fatigue properties of GLBP. The results of [137]

demonstrated a strong dependency between the GLBP fatigue properties and the collagen fiber orientation with respect to the applied loading. In GLBP specimens cycled along the fiber direction, slight stiffening was observed in the fiber direction [105], with little change to the cross-fiber direction, inducing slightly increased mechanical anisotropy [105, 137]. These results can be explained physically by increased fiber alignment and un-crimping in the fiber direction [105, 137]. The specimens cycled in the cross-fiber direction again became stiffer along the loading direction, while the cross-loading direction or fiber direction became more compliant. This resulted in a complete reversal of the tissue mechanical anisotropy after fatigue, and can be explained by reorientation of the collagen fibers towards the direction of applied load [137]. Permanent set was observed in both groups presenting as elongation in the loading direction and contraction in the cross-loading direction [105, 137]. Collagen conformational changes were evident after only 20 million cycles of fatigue, which represents approximately 7 months *in vivo* [137]. García Páez et al. [299, 300] have adopted a more physiologically relevant cyclic pressurization experimental set up for characterizing the fatigue properties of gluraladehyde-treated pericardium. They argue that the tissue durability can be estimated from the energy consumed during the initial loading cycles. The limitation of these studies is that they represent low fatigue states (≤4500 cycles) and the fatigue induced property changes were not rigorously determined.

Tissue bending is also a primary loading modality in heart valve applications. The leaflet experiences curvatures of up to $0.6mm^{-1}$ during diastole [301]. Vesely et al. [302] examined the opening characteristics of porcine BHVs and found correlation between areas of high bending curvature and tearing in the leaflets. Furthermore, in the

uniaxial fatigue studies by Broom [295-297], the tissues were subjected to compressive flexure upon unloading and this flexure was thought to be the cause of collagen fiber disruption apart from un-crimping. Yet, there has been little work to characterize the fatigue effects of cyclic bending in heart valve tissues. Only Mirnajafi et al. [303] have adopted an isolated cyclic bending test for valve tissue. Cyclic flexural fatigue of glutaraldehyde-treated porcine aortic valve leaflets induced a marked loss of flexural rigidity in just 10 million cycles [303]. Their results suggest that the primary mechanism of early to mid-level fatigue damage of porcine BHVs may be delamination induced by cyclic flexure damage as shown in the histological slides in Figure 4.3 from Mirnajafi et al. [303]. This is in contrast to pericardial BHVs in which tissue damage is thought to be a result of high tensile stress [303]. The discrepancy in fatigue mechanisms may be a result of the structural differences between leaflet and pericardial tissues. The aortic valve leaflet has a distinct tri-layer structure with the spongiosa layer, largely comprised of non-collagenous glycosaminoglycans (GAGs) and proteoglycans (PGs), between the mainly fibrous fibrosa and ventricularis layers composed of collagen and elastin. GLBP has a much more homogenous structure. Raghavan et al. [294] have shown that glutaraldehyde only stabilizes the collagen component of the porcine BHV leaflets, and thus GAGs leach out under conditions of fatigue [259]. For this reason, the long-term fatigue response of glutaraldehyde-treated tissues is primarily based on the collagen fibers. This loss of GAGs may be responsible for the delamination of the ventricularis and fibrosa layers, the increased flexural rigidity of the leaflets, and has been suggested to be a pathway for leaflet calcification [259]. It has been suggested that chemical modifications such as the addition of neomycin to the typical glutaraldehyde tissue

treatment [294] could help stabilize GAGs in addition to collagen to help mitigate this mechanism of porcine BHV fatigue. The loss of elastin supporting the collagen framework may also expedite fatigue and un-crimping of the collagen fibers.

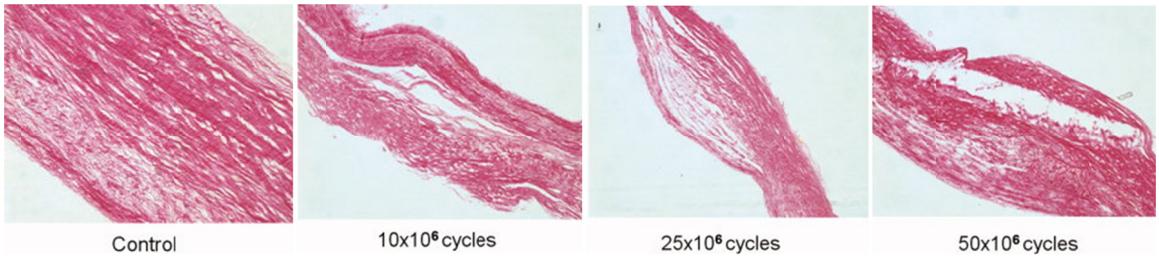

Figure 4.3 Histological sections of porcine BHV leaflet specimens showing progressive delamination with increasing levels of bending fatigue adapted from Mirnajafi et al. [303].

4.1.7 Computational studies on bioprosthetic heart valves

The limitation of the isolated material test approach is that tissue fatigue constitutive and computational models are still needed to bridge the tissue level fatigue damage to the device level fatigue damage. For a quantitative and efficient assessment of BHV performance, attention has turned towards computational analyses of BHV function [81, 304-306]. It is commonly accepted that BHV durability can be improved by reducing high stress concentrations in the leaflets.

Computational studies have shown that by changing BHV design, through varying manufacturing techniques [307], leaflets shapes [308], and frame mounting methods [245, 306, 307, 309], the stress distribution pattern acting on the leaflets could be altered. It has been shown through FE analysis that TAV leaflets experience higher stresses and strains [310] than traditional SAV leaflets, particularly in the presence of aortic calcification resulting in non-circular, asymmetric stent deployment [153, 311].

Several FE models [119, 120, 123] have been developed to analyze the biomechanics involved with TAV implantation in specific patients. Auricchio *et al.* [119] simulated both Edwards SAPIEN stent crimping and deployment through balloon inflation in a patient-specific aortic root model. From the simulation they were able to determine the effect of device positioning on the leaflet and aortic wall stresses. Wang *et al.* [123] developed a patient-specific FE model to quantify the biomechanical interaction between the TAV stent and the stenotic AV. This analysis included the modeling of the native aortic leaflets, ascending aorta and surrounding myocardium, which were defined by biaxial testing data of human aortic tissues [154, 312]. From the simulation results, Wang *et al.* [123] show that calcium deposits on the leaflets may inhibit stent expansion and ultimately result in paravalvular leak. A limitation of the biomechanics studies on TAV devices, they have been confined to the TAV function [153, 310, 311, 313, 314] and interaction with the surrounding tissue [79, 119-123] immediately following implantation. However, a peak stress analysis at a single snap shot in time may not be sufficient to predict BHV durability. Under cyclic loading, the leaflets will undergo stress-softening and permanent set, thus, both the tissue properties and leaflet geometry is changing over time, and both factors may change the stress distribution throughout the valve life cycle.

4.1.8 Motivation of this study

While it is well known that BHVs have limited durability, the fatigue damage process is still not well understood. Much of this insight comes from comparing clinical outcomes for various SAV designs, and although these studies were very useful to determine critical valve design issues, *in vivo* studies are not well controlled due to

patient variability and this retrospective approach is unsuitable for investigating new designs. This is an issue for TAV devices for which long-term *in vivo* data is currently unavailable: currently the durability and potential failure modes of TAV devices remain unknown. Before TAV intervention can be considered a potential alternative treatment for lower-risk patients with longer life expectancies, there is a pressing need for new strategies to evaluate and improve leaflet durability.

The experimental characterization of BHV tissue fatigue properties through AWT and isolated tissue fatigue tests have provided important insight on the fatigue damage mechanisms of the tissue under cyclic loading including: collagen conformational changes on the cellular level, collagen fiber un-crimping on the microstructural level, and permanent set and changes in compliance on the tissue level. However, it is difficult to quantify the effects of precise loading through AWT tests, and the isolated fatigue tests have been limited to uniaxial loading conditions, which cannot replicate the *in vivo* loading conditions of BHVs. Consequently, there is still a jump between understanding the BHV tissue material fatigue response and the BHV structural fatigue response.

Constitutive models describing the fatigue damage process of BHV biomaterials are needed to interpolate and extrapolate the isolated tissue fatigue experimental data to different cycle and loading states. Simulation-based fatigue analyses can then be used to translate tissue-level fatigue to BHV device-level fatigue. However, there is limited experimental data on the fatigue properties of BHV leaflet materials and even less on the modeling and simulation of fatigue in these tissues.

4.2 Methods

4.2.1 Overview of study design

Therefore, in this chapter, the inelastic time-dependent constitutive model described in Chapter 2 was used to model the fatigue behavior of GLBP, a representative BHV biomaterial, under uniaxial tension utilizing isolated GLBP fatigue experimental data presented in the literature [105]. The developed GLBP fatigue damage constitutive model was then implemented in computational simulations to analyze BHV fatigue under cyclic loading. The first set of computational simulations involved SAVs to investigate the effect of the leaflet and stent elastic properties as well as the leaflet thickness on the device durability. The simulation results were compared to the known failure modes of SAVs to validate the modeling approach. The validated modeling approaches were then applied to TAV devices to predict the durability of TAVs in normal and underexpanded configurations. The overall study design is illustrated in the flow chart of Figure 4.4.

This marks the first study where fatigue damage was simulated for BHV applications and the effect of BHV design parameters on the durability were quantitatively assessed. This computational approach to assess leaflet fatigue is advantageous in terms of efficiency (i.e. hours of simulation time versus the months it may take to fabricate and test valves via accelerated wear testers), and also because it enables well-controlled, side-by-side engineering design comparisons. For instance, the precise effects of various design features (leaflet shape, free edge height, leaflet thickness, etc.) on BHV leaflet durability can be quantitatively assessed and compared. Although, there is little data to rigorously determine the GLBP fatigue parameters [131] used in this study, the comparison between cases provides invaluable insight into the

specific effects of BHV design features on long-term BHV durability. This computational approach to studying BHV durability will hopefully benefit the valve community: allowing researchers to efficiently evaluate new BHV designs prior to AWT testing.

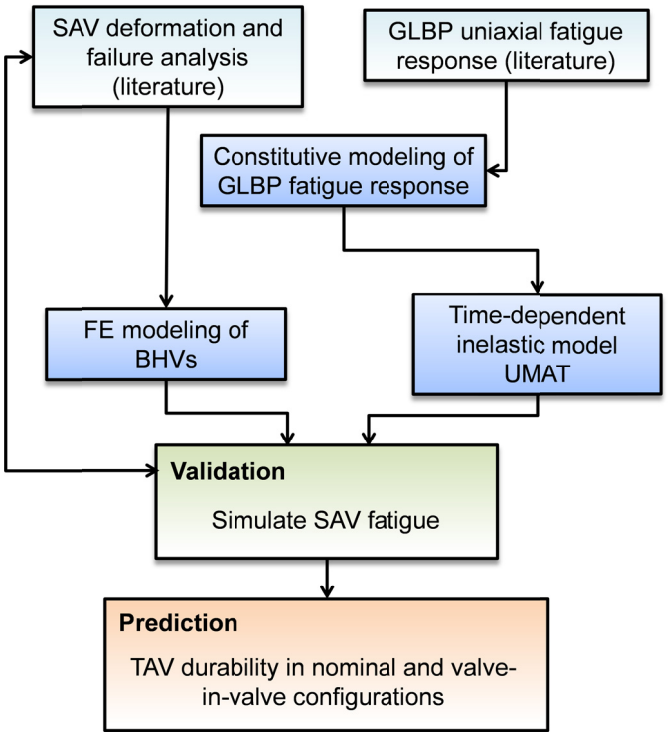

Figure 4.4 Overview of the computational fatigue analysis of bioprosthetic heart valves study design.

4.2.2 Constitutive modeling of GLBP tissues

4.2.2.1 Determination of un-fatigued GLBP tissue properties

The un-fatigued GLBP leaflet properties were derived from biaxial tests for each of the 3 dissected GLBP leaflets of a CEP valve presented by Sun [85] shown in Figure 4.5. The three leaflet properties are referred to as L1 (Figure 4.5a), L2 (Figure 4.5b), and L3 (Figure 4.5c). For the purpose of this study, GLBP was assumed to be an

incompressible ($\det \boldsymbol{F} = 1$), anisotropic, nonlinear, hyperelastic material [145] and the un-fatigued strain energy, W^0, was expressed by the generalized Fung-type strain energy function [32] (Eq. (1.20)) for the planar biaxial response of soft biological tissues. The Fung-model parameters presented in [85] to fit the L1, L2, and L3 responses are given Table 4-1.

Table 4-1 Fung model parameters for CEP valve leaflets adapted from Sun [85].

Specimen	$c\ (kPa)$	A_1	A_2	A_3	A_4	A_5	A_6
Leaflet 1 (L1)	14.42	70.37	61.27	5.11	14.20	2.01	3.10
Leaflet 2 (L2)	9.95	192.18	56.85	1.00	34.00	4.00	2.00
Leaflet 3 (L3)	25.32	274.77	21.82	15.66	50.41	41.86	2.00

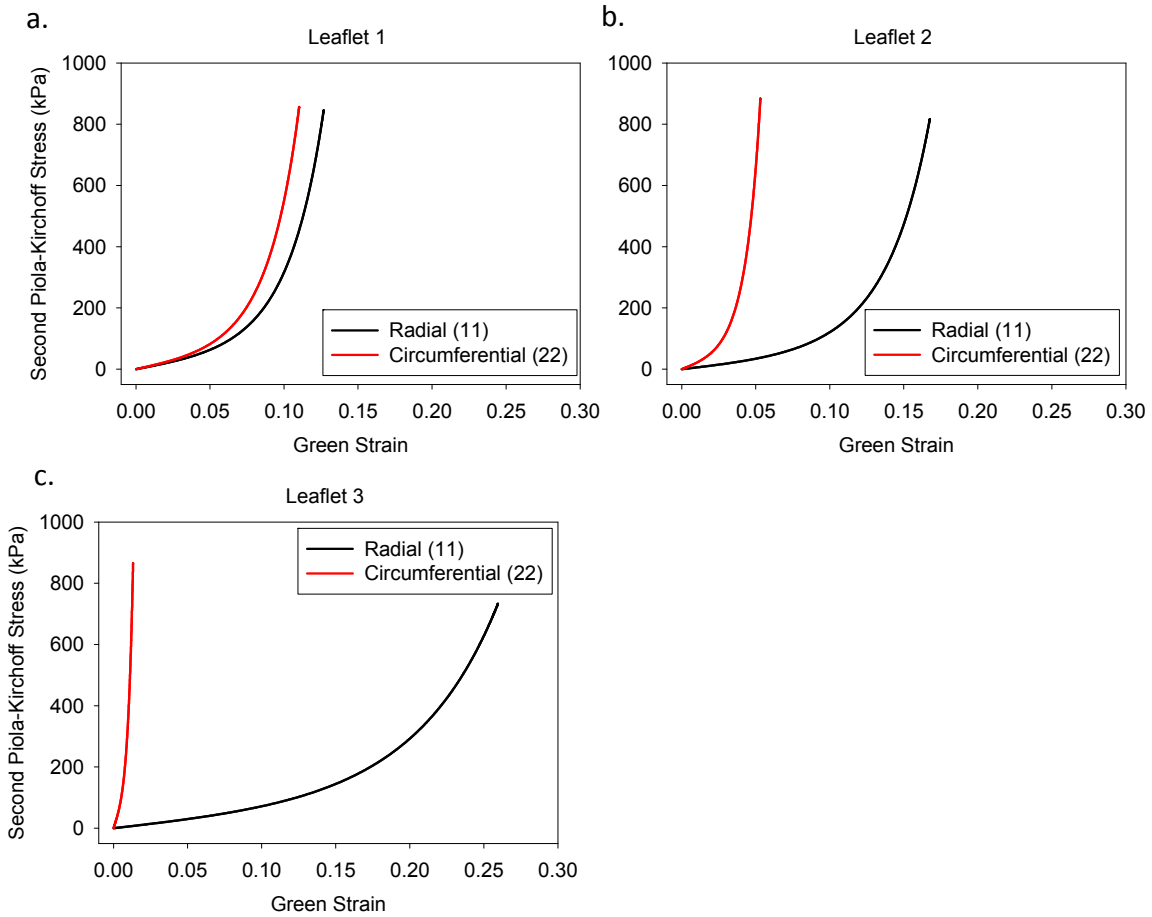

Figure 4.5 Equi-biaxial response for each leaflet property: a) L1, b) L2, and c) L3, in the radial and circumferential directions.

To investigate the fatigue effects to the matrix and fiber components of GLBP distinctly, the initial L2 property was also fit with the modified-Holzapfel structural-based strain energy function [87] (Eqs. (2.11) and (2.13)) using a Marquardt-Levenberg non-linear regression algorithm with Matlab software (Mathworks, Natick, MA).

4.2.2.2 Determination of fatigued state GLBP tissue properties

The evolution of GLBP stress-softening was defined by Eq. (2.24) and the evolution of permanent set was defined by Eq. (2.27). Accordingly, the time-dependent inelastic model was calibrated to the experimental fatigue data of GLBP subjected to cyclic uniaxial testing reported previously by Sun et al. [105]. In the experiment, it was shown that GLBP exhibited stiffening after fatigue loading (Figure 4.6a) with a mean permanent set of 7.1% in the loading direction (**LD**), with little change to the stiffness in the cross-loading direction (**XD**) but with a mean permanent set of -7.7% (Figure 4.6b). Therefore, the sample became longer along the loading axis and narrower along the cross-loading axis as expected. Figure 4.7a illustrates the apparent tissue stiffening along the LD due to cyclic fatigue loading when the permanent set is not included. However, when the permanent set is included, it can be seen that the tissue stiffness has indeed degraded as a result of fatigue loading (Figure 4.7b). This effect is likely due to the reorientation of collagen fibers and loss of collagen crimp [105, 137].

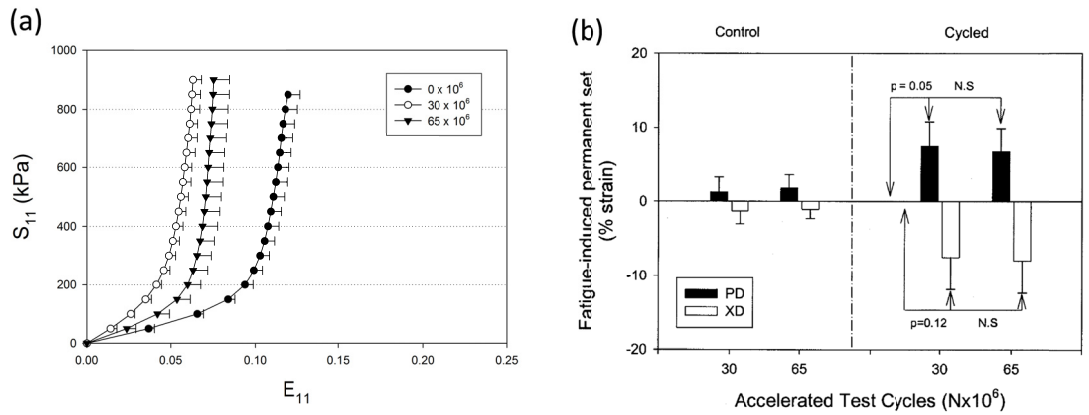

Figure 4.6 Fatigue induced (a) stiffening in the loading direction and (b) permanent set of GLBP specimens subjected to uniaxial stretch cycles adapted from Sun et al. [105].

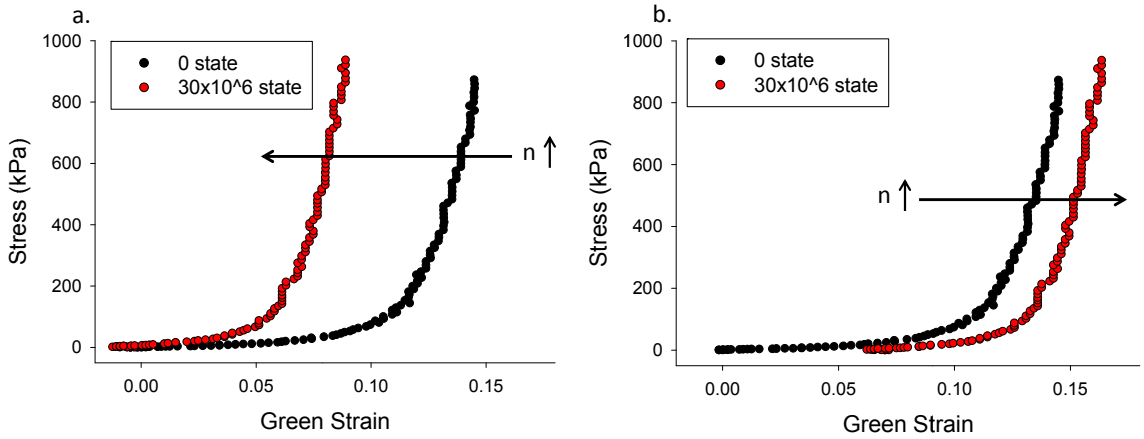

Figure 4.7 Fatigue-induced property changes in the loading direction referenced to the a) current, fatigued state, and b) initial, un-fatigued state for a representative sample adapted from Sun et al. (Sun, Sacks et al. 2004).

The un-fatigued GLBP specimen biaxial data [105] was fitted in the least-squares sense to determine the un-fatigued state Fung model parameters (Eq. (1.20)). The equi-biaxial testing data of a GLBP specimen is illustrated in Figure 4.8a.

4.2.2.2.1 Determination of GLBP equivalent strain limits

The value $\psi_{\min} = 4.67\frac{\sqrt{\mathrm{kN}}}{\mathrm{m}}$ was determined from a BHV simulation reported previously [81]. The value $4.67\frac{\sqrt{\mathrm{kN}}}{\mathrm{m}}$ is the maximum equivalent strain exhibited by the

leaflets during closure and under an imposed pressure of approximately 120 mmHg. Thus, our assumption is that under the peak equivalent strain of $4.67\frac{\sqrt{\text{kN}}}{\text{m}}$, this particular BHV will fail after 10 patient years. The equivalent strain limit $\psi_{\max}$ was determined through uniaxial failure tests (Figure 4.9) with $\psi_{\max} = 4.32\text{x}10^5\frac{\sqrt{\text{kN}}}{\text{m}}$ corresponding to a failure strain of approximately 0.45. The contour plot of equivalent strain with $\psi_{\min} = 4.67\frac{\sqrt{\text{kN}}}{\text{m}}$ and $\psi_{\max} = 4.32\text{x}10^5\frac{\sqrt{\text{kN}}}{\text{m}}$ marking the damage evolution region is illustrated in Figure 4.8b.

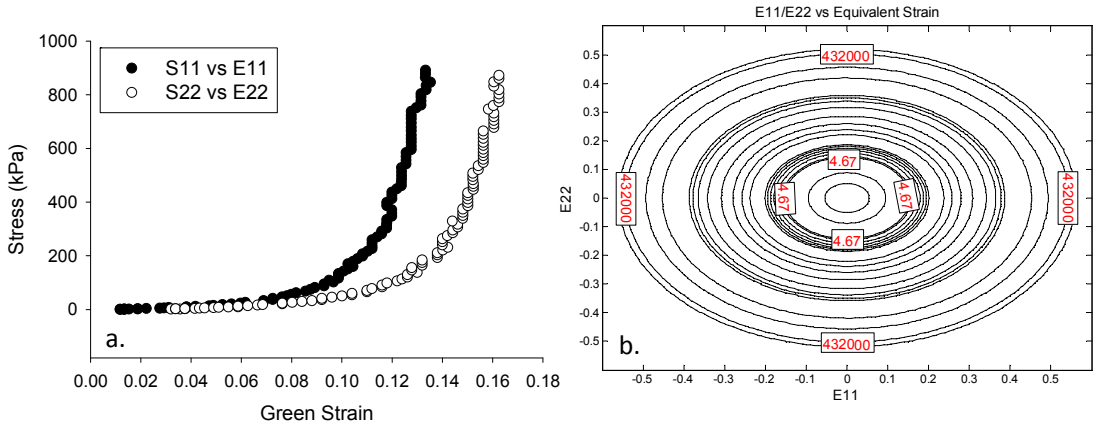

Figure 4.8 (a) Equi-biaxial response of GLBP specimen at the un-fatigued state [105]. (b) Contour plot of equivalent strain with $\psi_{\min} = 4.67\frac{\sqrt{\text{kN}}}{\text{m}}$ and $\psi_{\max} = 4.32\text{x}10^5\frac{\sqrt{\text{kN}}}{\text{m}}$ marking the damage evolution region.

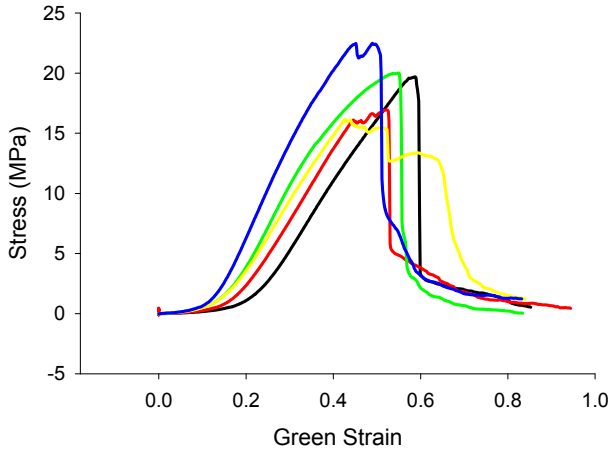

Figure 4.9 Uniaxial failure test data for 5 GLBP specimens with a mean failure strain of approximately 0.45 corresponding to $\psi_{max} = 4.32x10^5 \frac{\sqrt{kN}}{m}$.

4.2.2.2.2 Inverse finite element method to determine GLBP fatigue damage model parameters

The maximum number of cycles to failure, n_{max}, as well as the damage criterion, ψ_{min} and ψ_{max}, were assumed to be known constants. The maximum number of loading cycles, n_{max}, was set to 368 million cycles which corresponds to approximately 10 patient years assuming a heart rate of 70 bpm. However, to reduce computational cost, in the simulation, $n_{max,}$ was proportionally scaled from 368 million with the parameter $N = 1x10^6$, a scaling factor relating the number of simulated cycles, to the number of real-time cycles. Thus, 368 simulated cycles is equivalent to 368 million real-time cycles.

Due to a lack of experimental fatigue data under different loading conditions (i.e., Ξ_n^{peak} values), the true values for α and β of Eq. (2.21) for GLBP are unknown. For this study, because the parameter α predominately affects the damage evolution response at large (near failure) Ξ_n^{peak} values and has a minimal impact on the damage evolution at

low values Ξ_n^{peak}, as shown in Figure 2.4, it is assumed to not have a major impact on fatigue-related GLBP property changes which accumulate over years at relatively low (physiological) Ξ_n^{peak} values. Therefore, α was set to 1. The parameter β was determined through an inverse FE procedure to reflect the known degree of softening and permanent sets after $30x10^6$ cycles of uniaxial loading.

FE model setup

To determine β, a uniaxial fatigue simulation was developed to mimic the experimental protocol in [105]. The simulated test specimen was modified from the multi-element model used in the UMAT verification tests of section 2.3.5.1.2 so that the top and bottom 2 rows of elements act as the grips used to secure the tissue specimen in the experimental set-up. Therefore, damage was not considered in those elements. The test specimen model consisted of 400 plane stress elements to allow for a test specimen geometry of 25 mm x 25 mm x 0.4 mm. The simulation consisted of 3 steps: 1) un-fatigued state biaxial tension under load control imposed by evenly spaced nodal forces along both axes to apply a first Piola Kirchhoff stress ratio $P_{LD}:P_{XD}$ = 1:0.1 to the specimen, similar to the corresponding biaxial test protocol [105], 2) 30 cycles of uniaxial tension to a peak strain of 16% imposed by a uniform displacement applied to the top and bottom rows of elements, which corresponds to $30x10^6$ cycles in real time and 3) at the $30x10^6$ state, biaxial tension with identical loading as in step 1. Fatigue damage accumulation was only considered in step 2). The uniaxial tension tests in steps 1) and 3) were simply to facilitate comparison between the simulation results and the experimental fatigue data in [105]. The amount of damage per simulated cycle was scaled up to reflect

approximately $1x10^6$ cycles real-time. based on the fatigue model parameters by setting N to $1x10^6$. The β parameter was adjusted until the simulated fatigued-state biaxial response extracted from the step 3 simulation results matched the corresponding $30x10^6$ cycle state experimental data, and the predicted permanent set in LD matched that measured experimentally.

4.2.2.3 Description of distinct matrix and fiber fatigue damage

The evolution of GLBP stress-softening and permanent set were also defined by component through Eqs. (2.22)-(2.23) and Eq. (2.29) respectively. It can be seen from Figure 4.17 and Eqs. (2.11) and (2.13) that the stress-strain responses and the respective strain energy components (i.e., peak equivalent strain and damage) for the matrix and fiber constituents are drastically different. One would expect the threshold for the fibers to be higher than that for the matrix. Thus, under the same loading condition, the fiber reinforced direction may accumulate less fatigue damage than the cross-fiber direction. All of these factors warrant the development of a fatigue damage model to include distinct matrix and fiber descriptions.

However, since the GLBP fatigue experiment in [105] was only conducted along the preferred fiber direction, the distinct matrix and fiber fatigue parameters cannot be uniquely determined. For the purpose of this study, the matrix fatigue damage parameters were assumed to be identical to that of the bulk tissue determined in section 4.2.2.2. Therefore, the overall GLBP tissue failure is assumed to be due to the matrix components. Accordingly, the n_{max_f} was assumed to be higher than n_{max_m}, and was set to 500 million cycles. Alternatively, the minimum equivalent strain threshold to induce damage could be defined separately for each constituent. Clearly, there is a pressing need

to collect the relevant fatigue experiment data to calibrate and validate the GLBP fatigue model.

4.2.3 Computational modeling of bioprosthetic heart valve fatigue

4.2.3.1 SAV model generation

The SAV FE model was developed and validated previously by Sun *et al*. [81] (Figure 4.10). Briefly, the tri-leaflet SAV model consisted of GLBP tissue leaflets mounted onto a metal stent. The stent and sutures attaching the leaflets to the stent were constructed using beam elements. The stent was assigned a Young's modulus of 160.1 GPa and a Poisson ratio of 0.3, while the sutures were assigned a Young's modulus of 4.14 GPa and a Poisson ratio of 0.3. The leaflets were attached to the valve stent and modeled using quadrilateral large strain shell elements. The leaflets were prescribed a nominal thickness of 0.43 mm corresponding to the mean thickness of GLBP tissues used to fabricate CEP valves [85]. Each leaflet had its own local coordinate system for material property definitions (see Figure 4.11) that were fully defined by the constitutive law, Eq. (2.39) and the GLBP fatigue parameters determined in section 4.2.2.2. The contact between two leaflets was modeled using a master-slave contact pair (an option in ABAQUS). The leaflet that was stiffer in the radial direction was assigned the master surface while the other was specified as the slave surface.

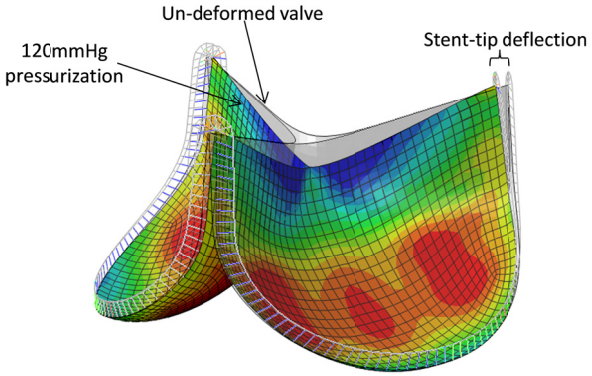

Figure 4.10 SAV finite element model constructed from shell elements in the pressurized state overlapped with the initial un-deformed geometry.

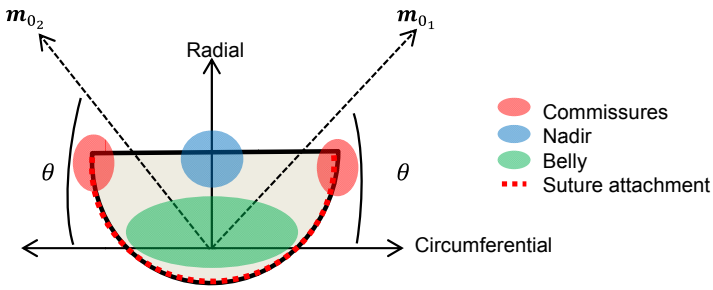

Figure 4.11 Diagram of the leaflet material orientations and the fiber orientations drawn on the 2D leaflet schematic.

An additional SAV FE model was developed using the exact same geometry, except 3D continuum brick elements (C3D8H) in ABAQUS were used to construct the leaflets to give a leaflet thickness of 0.4 mm to correspond to commercial CEP valves. The purpose of using brick elements rather than shell elements is because brick elements are more accurate for modeling bending. While tension is the primary loading condition on the leaflets during valve closure, bending is a significant loading condition during valve opening. Thus, by using brick elements, the effect of valve opening on the leaflet fatigue damage could be more accurately modeled. The SAV FE model in the fully open and fully closed configurations is shown in Figure 4.12. The SAV stent was allowed to

deform to accommodate approximately 5º of stent-tip deflection under the peak pressure load of 120 mmHg (Figure 4.12b). In this model, the stent and sutures, leaflet material orientations, and leaflet contact were modeled the same as previous. In this case, the initial leaflet material properties were defined based on the biaxial testing of the L2 tissue, which was modeled with the modified-Holzapfel model parameters given in Table 4-2. The leaflet fatigue properties were defined distinctly for the matrix and fiber components based on the GLBP tissue fatigue parameters determined in section 4.2.2.3.

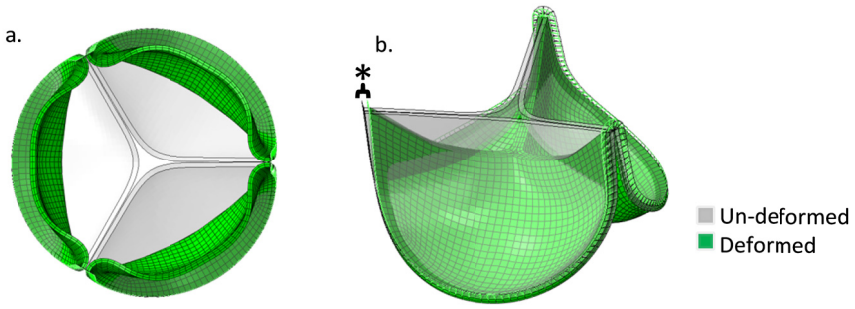

Figure 4.12 Overlay plots of the un-deformed and deformed SAV FE models using brick elements in the a) open position and b) closed position.

4.2.3.2 Finite element modeling of TAVs

The FE model of a generic 23 mm diameter TAV developed previously by Li and Sun [310] was also used for this study. The TAV leaflets were also modeled using large-strain brick (C3D8H) elements, and prescribed a thickness of 0.25 mm similar to commercial TAV devices. The TAV FE model in the fully open and fully closed configurations is shown in Figure 4.13. The TAV stent was not included in the simulations because the deformation of the stent is assumed to be minimal; thus, the stent-attachment nodes were fixed in space to mimic attachment to the non-deformable stent. The leaflet material orientations and contact was modeled identically to the SAV

models. The initial leaflet material properties were again defined based on the biaxial testing of the L2 tissue, which was modeled with the modified-Holzapfel model parameters given in Table 4-2, and the leaflet fatigue properties were defined by the GLBP tissue fatigue parameters determined in section 4.2.2.3.

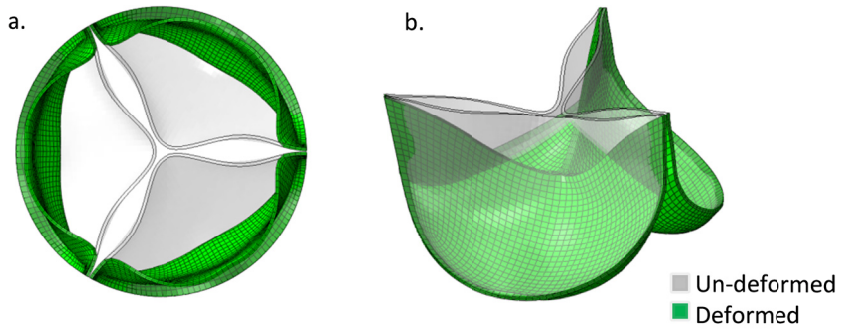

Figure 4.13 Overlay plots of the un-deformed and deformed TAV FE models in the nominal configuration in the a) open position and b) closed position.

4.2.3.3 FE simulation

A quasi-static approach was used to analyze the deformation of the valve models from a stress-free position to a fully loaded configuration with the effects of fatigue by applying cyclic pressurization to the leaflets. The amount of damage per simulated cycle was scaled up to reflect approximately $10x10^6$ cycles real-time based on the fatigue model parameters by setting N to $10x10^6$. The simulation results (stress, strain, damage, etc.) were extracted for each loading cycle. Values from the elements along the stent-attachments were ignored to avoid potentially inaccurate boundary effects. While the amount of damage at certain cycle states may not be accurate, due to limited experimental data, the variable, N, nominalizes the simulated cycle state. Although the precise timing of fatigue events cannot be predicted, through well-controlled side-by-side comparison, the effects of valve design on the leaflet durability can be assessed.

In a pilot study, systolic opening of the valves was simulated by applying a uniform pressure of 4 mmHg to the ventricular surface of the leaflets (Figure 4.12a and Figure 4.13a), and diastolic closure of the valves was simulated by applying a uniform pressure of 120 mmHg to the aortic side of the leaflets (Figure 4.12b and Figure 4.13b) We found that the peak leaflet stresses and strains were consistently lower in the fully open configuration compared to the fully closed configuration (Figure 4.14). Additionally, fatigue damage due to 1) cyclic opening and closing, and 2) just cyclic closing was simulated in the SAV model. In the cyclic opening and closing simulation, one cycle consisted of applying a sinusoidal pressure waveform to the ventricular side of the leaflets from a minimum of 0 mmHg to a peak of 4 mmHg, and then applying a sinusoidal pressure waveform to the aortic side of the leaflets from a minimum of 0 mmHg to a peak of 120 mmHg. In the cyclic closing only simulation, one cycle consisted only of applying the sinusoidal pressure waveform to the aortic side of the leaflets. Contour plots of the peak equivalent strain, as well as the matrix and fiber damages at the 9N fatigue state for each fatigue loading condition are shown in Figure 4.15. The peak equivalent strain was slightly underestimated at the commissures and the central portion of the free edge under the closing only fatigue condition compared to the opening and closing condition; however, the overall resultant damage patterns were nearly identical under both fatigue loading conditions. Given that opening did not significantly impact the SAV leaflet damage and required much more time to run, only cyclic closing was considered in the TAV fatigue simulations, and all comparisons between the SAV and TAV fatigue simulations in the proceeding sections are made between the cyclic closing fatigue simulations. The fatigue simulation results including

the leaflet stress, strain, equivalent strain, matrix and fiber damage factors were extracted at each fatigue cycle state for comparison. Values from two layers of boundary elements along the stent-attachments were ignored to avoid potentially inaccurate boundary effects.

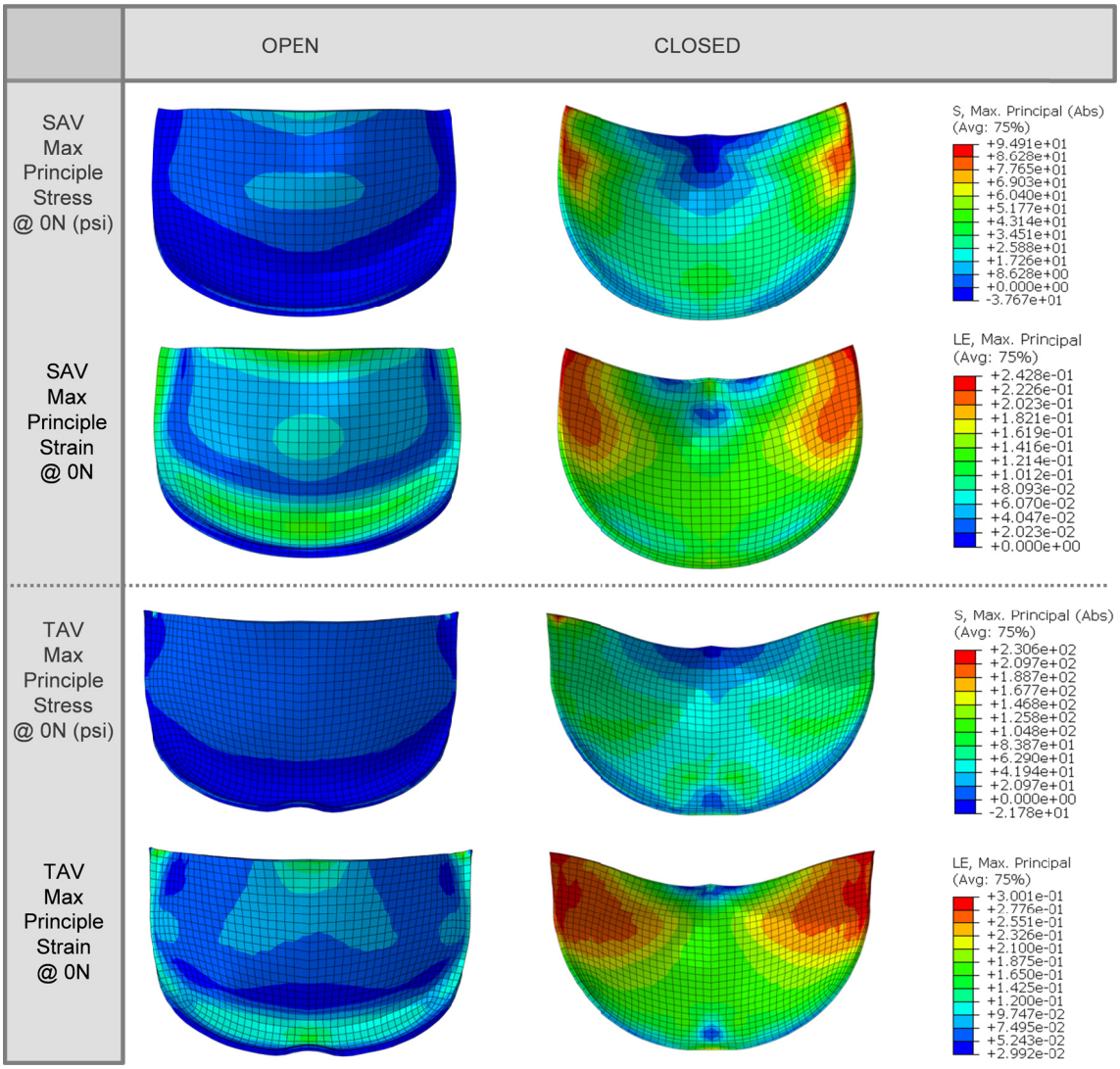

Figure 4.14 Contour plots of the max principal stress and max logarithmic strain for each valve in the open and closed configurations at the 0N state. In each valve the leaflet stresses and strains were higher in the closed position with peak values located at the commissures (red) and minimum values at the nadir (blue). All contour plots are shown on the aortic side of the leaflet deformed geometry at peak pressurization.

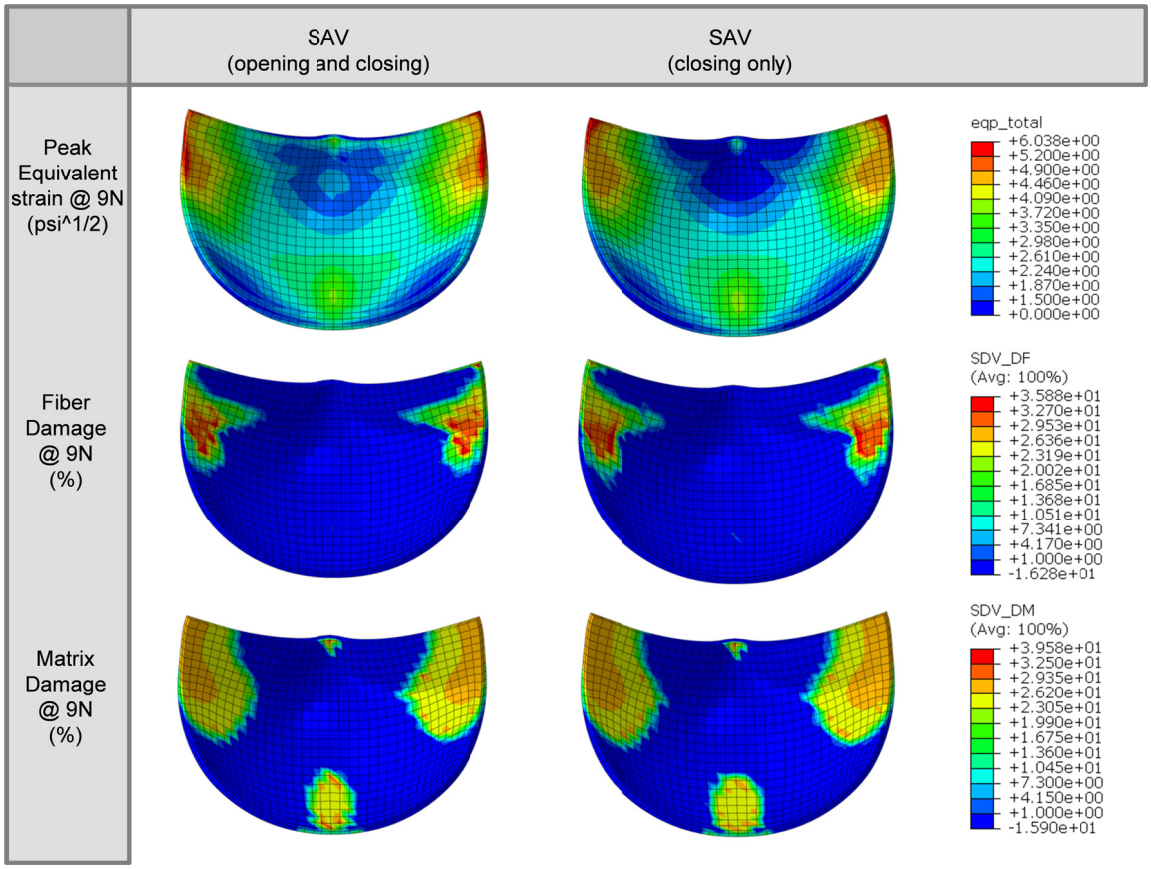

Figure 4.15 Contour plots of the peak equivalent strain, fiber and matrix damage in the SAV leaflets due to cyclic opening and closing and cyclic closing only at the 9N state, showing slightly higher peak equivalent strains due to cyclic opening and closing at the free edge, but nearly identical fiber and matrix damage patterns.

4.2.3.3.1 Parametric study of the effect of leaflet and stent properties on SAV durability

In an effort to investigate the effects of leaflet and stent material properties on the BHV durability, we conducted a parametric study. The effect of the un-fatigued leaflet properties was tested by comparing three nominal valve cases: **L1** – all three leaflets were assigned the L1 property (Figure 4.5a), **L2** – all leaflets were assigned the L2 property (Figure 4.5b), and **L3** – all leaflets were assigned the L3 property (Figure 4.5**c**). The effect of mismatched leaflets was tested by comparing 3 additional cases: **L1/L2/L3** – each leaflet was assigned a distinct un-fatigued property, **2 L1/ L2** – two leaflets were

assigned the L1 property while the other was assigned the L2 property, and **L1/ 2 L2** – two leaflets were assigned the L2 property while the other was assigned the L1 property.

The effect of the leaflet thickness was investigated by testing two additional cases with the L2 leaflet property: **L2-thin –** using a leaflet thickness of 0.35 mm, and **L2-thick –** using a leaflet thickness of 0.5 mm. The 0.35 mm and 0.5 mm thicknesses represent the typical range for GLBP tissues used to fabricate SAVs.

The effect of valve stent-tip deflection was investigated by altering the stent modulus by ±40%, referred to as the **1.4E** and **0.6E** cases respectively, in the L1 (L1 0.6E, L1 1.4E) and L2 (L2 0.6E, L2 1.4E) nominal valves. The **Rigid** case, where the stent modulus was unchanged, albeit all degrees of freedom of the stent were fixed in space to prevent any stent-tip deflection, was also studied. Each BHV model was subjected to up to 30N simulated cycles of fatigue.

4.2.3.3.2 Comparison study of SAV versus TAV durability

To estimate the durability of TAV devices, the durability of the SAV and TAV models under identical loading and with identical leaflet properties were quantified and compared. The SAV model with brick elements was used in the comparison.

4.2.3.3.3 Parametric study of the effect of underexpansion on TAV durability

Cyclic diastolic closure of TAVs was simulated in two steps. First, the aortic side of the leaflets were slightly pressurized to 10% of the peak pressure (~12 mmHg) and the nodes along the leaflet stent-attachment lines were radially displaced towards the center of the valve by 0 mm, 0.5 mm, 1 mm, and 1.5 mm to reduce the valve radius and achieve the nominal, and 1 mm, 2 mm, and 3 mm underexpanded (**UE**) cases (Figure 4.16a). In a

size 23 mm TAV with an internal diameter of 22 mm, these UE cases represent 4.5%, 9.1%, and 13.6% underexpansion respectively. Note that 10% to 15% underexpansion is generally considered acceptable in clinical practice [271]. Qualitatively, this approach resulted in realistic distortion of the leaflets (Figure 4.16b). The stent-attachment nodes were then fixed in space at this new location for the duration of the simulations to mimic attachment to a rigid stent. Then diastolic pressurization cycles from the minimum pressure of ~12 mmHg to a peak pressure of ~120 mmHg were applied to the aortic side of the leaflets to investigate the effects of repetitive loading.

The deformed valve geometries were imported into HyperMesh 12.0 (Altair HyperWorks, MI), for dimensional analysis. The leaflet coaptation area under the peak diastolic pressure of 120 mmHg was measured as the surface area of the contacting regions of adjacent leaflets. The degree of leaflet pin-wheeling upon valve closure was quantified in terms of the minimium bending radius (**MBR**) of the leaflet free edge per the methods proposed by Corden et al. [315]. The leaflet MBR was also measured along the radial mid-line, the line bisecting the leaflet in the radial direction. Briefly, the deformed coordinates of the nodes along the leaflet free edge and radial mid-line were exported and used to generate spline curves using Matlab (Mathworks, MA). The central difference method was used to calculate the approximate derivatives of the spline curves in order to calculate the line curvatures and bending radii for each case.

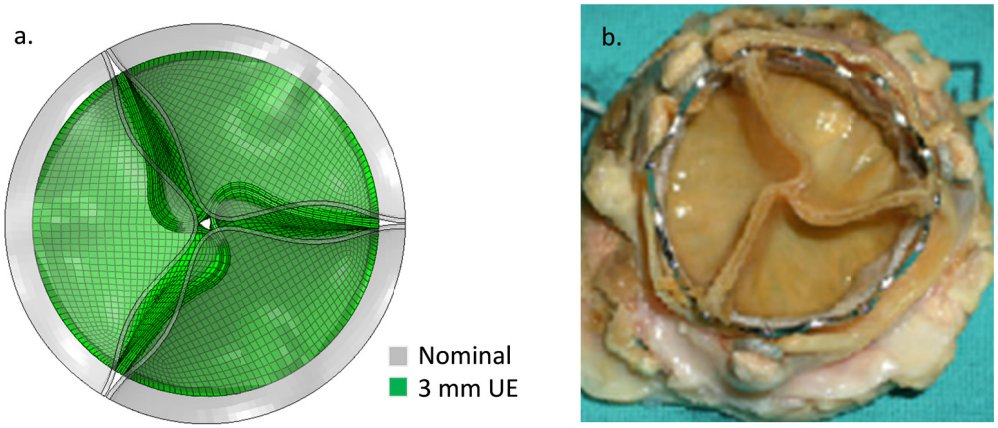

Figure 4.16 a) The 3 mm UE TAV FE model after inward radial displacement of the stent-attachment line overlaid with the nominal TAV model under minimum pressure. b) A failed explanted 26 mm Sapien XT TAV implanted in a 27 mm Carpentier-Edwards SAV (adapted from [268]).

4.3 Results

4.3.1 Constitutive modeling of GLBP uniaxial fatigue response

4.3.1.1 Material parameters of un-fatigued GLBP response

The modified-Holzapfel model parameters to fit the L2 property are given in Table 2-2. The constitutive model was able to capture the response well (Figure 4.17). The matrix contribution to the overall stress was kept small compared to the fiber contribution during the parameter fitting, because the fibers are estimated to be over 100X stiffer than the matrix materials [316].

Table 4-2 Modified-Holzapfel model parameters for CEP valve leaflets.

Specimen	$c_1\ (kPa)$	c_2	$k_1\ (kPa)$	k_2	θ (°)	$D\ (kPa^{-1})$
Leaflet 2 (L2)	30.03	3.47	74.50	63.19	43.11	1e-5

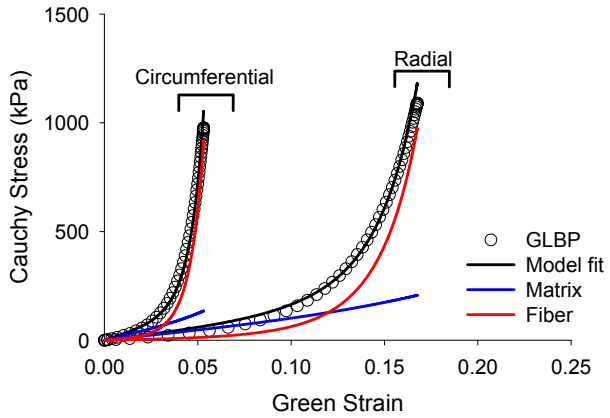

Figure 4.17 GLBP L2 equi-biaxial response from Sun [85] (open circles), with the modified-Holzapfel model fit (black lines), and the contributions from the matrix (blue lines) and fibers (red lines) to the overall response.

4.3.1.2 Material parameters of fatigued GLBP response

The fitted GLBP fatigue parameters for use with the Fung-type strain energy function are given in Table 4-3. The GLBP material parameters for use with the modified-Holzapfel strain energy function are given in Table 4-4. These parameters were able to capture the uniaxial fatigue response of GLBP as described in the proceeding sections.

Table 4-3 GLBP fatigue parameters for use with the Fung strain energy function.

Initial Fung model tissue material parameters						
C (kPa)	A_1	A_2	A_3	A_4	A_5	A_6
0.58	76.19	198.0	28.02	50.9	-9.67	0.17
Inelastic model material parameters						
$\psi_{min}\left(\frac{\sqrt{kN}}{m}\right)$	$\psi_{max}\left(\frac{\sqrt{kN}}{m}\right)$	$n_{max}\ (N^{-1})$	α	β	$D_{psmax_{11}}$	$D_{psmax_{22}}$	$D_{psmax_{12}}$
4.67	431,840.00	$368x10^6$	1.00	10.0	0.1	0.1	0.05

Table 4-4 GLBP fatigue parameters for use with the modified-Holzapfel strain energy function.

Initial modified-Holzapfel model tissue material parameters					
$c_1\ (kPa)$	c_2	$k_1\ (kPa)$	k_2	θ	D
30.03	3.47	74.50	63.19	43.11	1e-5
Inelastic model matrix material parameters					
$\psi_{min_m}\ (\frac{\sqrt{kN}}{m})$	$\psi_{max_m}\ (\frac{\sqrt{kN}}{m})$	$n_{max_m}(N^{-1})$	α_m	β_m	D_{psmax_m}
4.67	431,840	$368x10^6$	1.0	10.0	0.105
Inelastic model fiber material parameters					
$\psi_{min_f}\ (\frac{\sqrt{kN}}{m})$	$\psi_{max_f}\ (\frac{\sqrt{kN}}{m})$	$n_{max_f}(N^{-1})$	α_f	β_f	D_{psmax_f}
4.67	431,840	$500x10^6$	1.0	10.0	n/a

The uniaxial fatigue simulation using the parameters in Table 4-3 are demonstrated the altered geometry and mechanical properties of the tissue specimen in response to cyclic loading. As illustrated in Figure 4.18, the test specimen becomes clearly distorted throughout cyclic loading as a result of accumulating permanent sets. The specimen became elongated in the LD and narrowed along the XD, as observed experimentally. The specimen geometry change after $30x10^6$ fatigue cycles is evident in the stress-free state (Figure 4.18). The total permanent sets accumulated after $30x10^6$ simulated fatigue cycles presented as the average Green strains at the zero stress-state in the central 16 elements were -0.0105 in the XD, 0.0698 in the LD, and 0.001 in shear which agree well with the experimentally observed values [105]. Damage was highest near the sides of tissue at the grips as expected, with a maximum stress softening factor of 1.0 indicating tissue tearing at these locations. The stress softening factor throughout the center of the specimen was approximately 0.698.

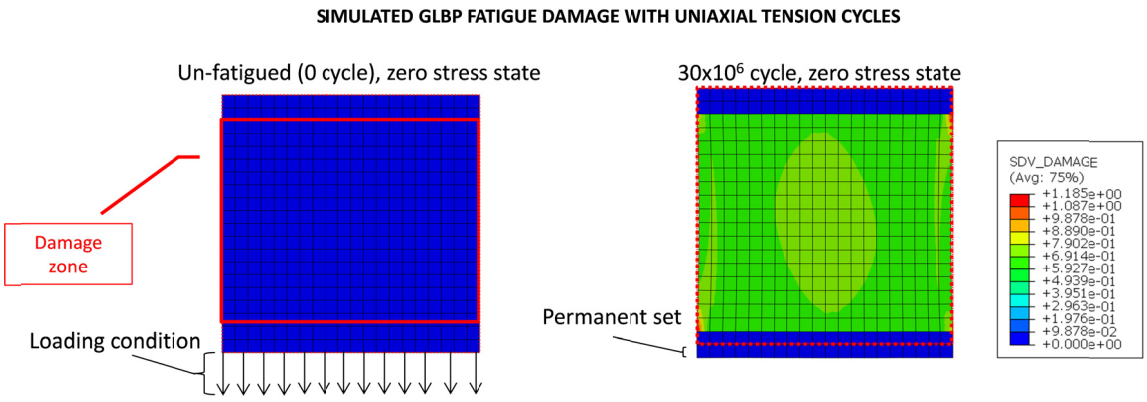

Figure 4.18 Schematic of the initial model geometry and loading conditions on the left and specimen at the stress-free state after simulated fatigue with a contour plot of the damage on the right. The red solid line represents the damage zone and the red dotted line represents the un-fatigued geometry.

The change in the specimen mechanical properties is demonstrated by the altered stress-strain response. The mean stress-strain responses were extracted from the central 16 elements of the model where the stress and strain were nearly uniform. In Figure 4.19 the stress-strain response was extracted from the same elements during steps 1 and 3 of the simulation and were plotted against the experimental fatigue data from [105]. The simulation results agree well with the experimental data for both the 0 cycle (un-fatigued) state and the $30x10^6$ cycle state. In Figure 4.19 a non-zero strain of approximately 0.0698 at zero stress is shown for the $30x10^6$ cycle state response.

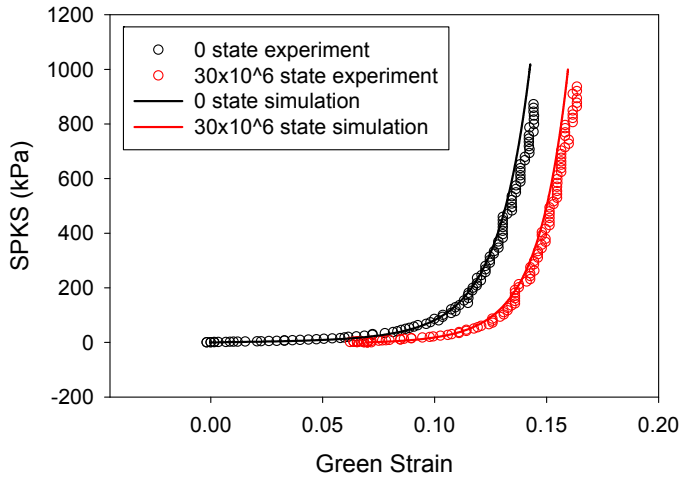

Figure 4.19 The uniaxial stress-strain response under load control of the simulated specimen compared to the actual specimen at the 0 state and the $30x10^6$ state.

4.3.2 Effect of cyclic loading on BHV function

Cyclic loading induced leaflet material property and geometry changes in each case. Some degree of fatigue damage was evident in each of the leaflets, with peak damages on the aortic side of the leaflets, for each of the BHVs studied. This damage caused the leaflets to "sag" in all cases. Figure 4.20a&b shows the overlaid leaflet geometry for the L1 valve at the 0N and 30N states under ~120mmHg pressure. The leaflet free edge was lowered but leaflet coaptation was maintained by leaflet sagging particularly in the belly region of the leaflet. Leaflet fatigue damage also induced changes in the leaflet stress distribution. Contour plots of the max principal stress in the L1 valve leaflet at the 0N (Figure 4.20c) and 30N (Figure 4.20d) states show that the leaflet peak stress is originally along the suture attachment line on the aortic side of the leaflet, but at the highly fatigued state, the leaflet peak stress is located at the commissure on the ventricular side of the leaflet.

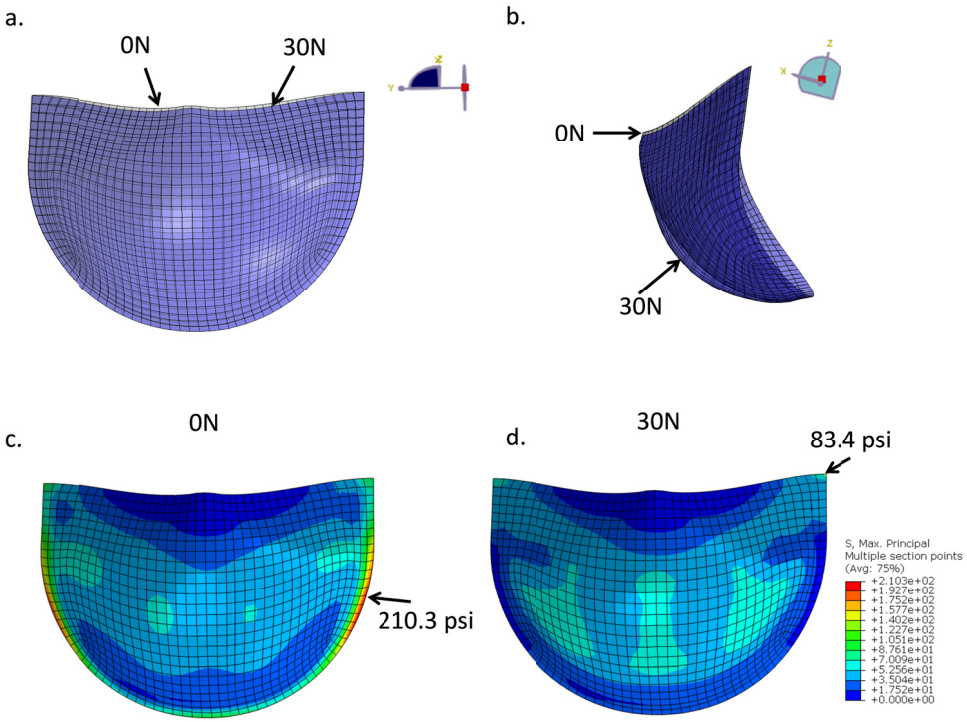

Figure 4.20 Overlaid L1 valve leaflet geometry in the fully pressurized state after 0N cycles of fatigue (gray) and 30N cycles of fatigue (blue). a) (Front view) sagging of the leaflet free edge at the 30N state and b) (side view) increased curvature in the leaflet at the 30N state which is particularly pronounced in the belly region. The L1 leaflet max principal stress distribution on the aortic side of the leaflet at the c) 0N and d) 30N states. The arrows indicate the peak stress location.

4.3.3 Leaflet property parametric study

In each simulation, the valve model was subjected to 20N cycles of pressurization. In 3 cases, the L3, L1/L2/L3 and 2 L1/L2 cases, the simulation diverged prior to the 20N cycle mark. The remaining 3 simulations completed successfully. The three nominal cases displayed very different initial leaflet stress distribution patterns (Figure 4.21a), which translated to very different fatigue damage patterns (Figure 4.21b). Both the L1 and L3 valves had high stress and concentrations and fatigue damage along the suture attachment lines below the commissures. The L2 valve leaflets had much lower peak stresses which were located at the sides of the belly region, in from the suture

attachments. The leaflet fatigue damage region was largest in the L1 valve. The damage was most significant along the suture attachments but also appeared along the belly and commissures. In the L2 valve, the fatigue damage was very minimal and in the region corresponding to the peak stresses, while in the L3 valve, in addition to the damage along the suture attachments, damage accumulated at the free edge due to twisting of the leaflets upon cyclic closure. The L1 and L2 nominal valves both displayed good leaflet coaptation and no fatigue damage at the leaflet free edge.

In the leaflet mismatch cases, the initial leaflet stresses, particularly along the commissures, increased in each leaflet (Figure 4.21a), which accelerated fatigue damage in these regions (Figure 4.21b). The L2 leaflet stress distribution in the mismatch cases was altered dramatically with much higher peak stresses which moved towards the suture attachment lines. Fatigue damage was greatly accelerated in the L2 leaflet in each of the mismatch cases. The stress distributions and damage patterns in the L1 and L3 leaflets in the mismatch cases were similar to the respective nominal cases. However, a small amount of damage along the L1 leaflet free edge was induced in the mismatch cases due to the compromised leaflet coaptation in these cases, where one or two leaflets would "lean" over the others.

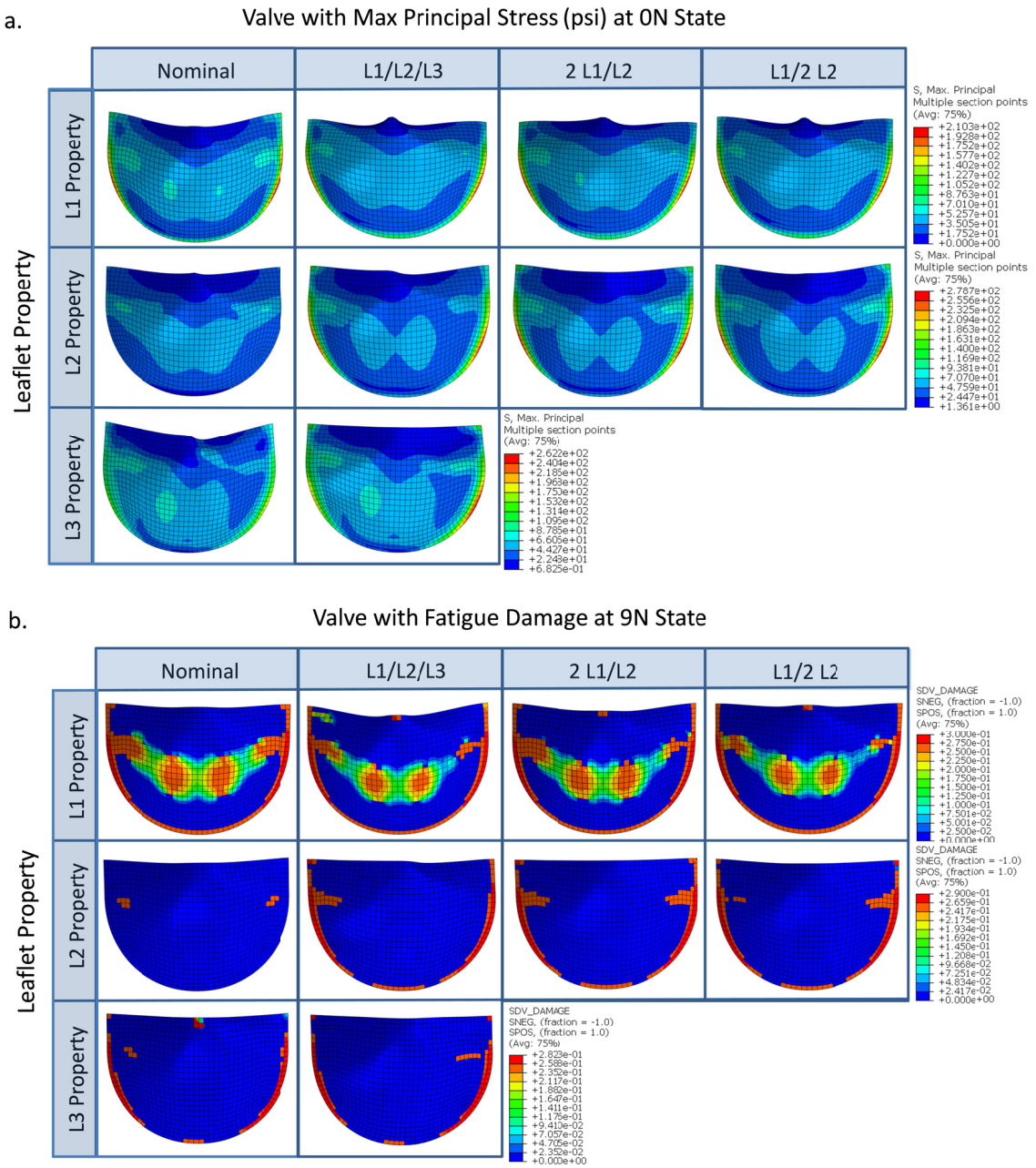

Figure 4.21 Contour plots of the a) max principal stress at the un-fatigued and fully loaded state and b) the 9N state fatigue damage on the aortic side of the leaflet for each valve of the leaflet property parametric study.

The leaflet peak stress, equivalent strain and damage factor (D_s), were extracted at each cycle for each case (Figure 4.22a-c). The L2 valve displayed the lowest peak leaflet stresses, equivalent strains, and damage throughout cycling. Interestingly, of the nominal

cases, the L3 valve had the highest initial peak stress, which was ~25% higher than that of the L1 valve; however, the L1 valve had much higher peak equivalent strains throughout cycling, and consequently, greater leaflet damage. The leaflet property mismatch cases all displayed higher peak leaflet stresses than the nominal cases; however, they displayed similar peak equivalent strains to the L1 valve throughout cycling. The damage factor in the L1/L2/L3 was accelerated compared to all other cases. Damage in the 2 L1/L2 and L1/2 L2 valves accumulated at a similar rate to the L1 valve. The peak damage factor vs. cycle curve in each case was extrapolated to complete leaflet failure ($D_s = 1$) to estimate the fatigue life of each valve. Figure 4.22d shows the normalized fatigue life of each valve, to the L2 nominal valve. According to this analysis, the fatigue lives of the L1, L1/L2/L3, 2 L1/L2, and L1/2 L2 valves were reduced by over 15% compared to the L2 valve.

The leaflet thickness had a significant impact on both the L2 valve leaflet peak stress at the un-fatigued state and the accumulated fatigue damage at the 20N fatigued state (Figure 4.23). The overall stress distribution of the L2 valve was not affected by changing the thickness. However, it did affect the magnitude of the stress, as expected. This resulted in a much larger damage region in the L2-thin valve and a smaller damage region in the L2-thick valve at the 20N state.

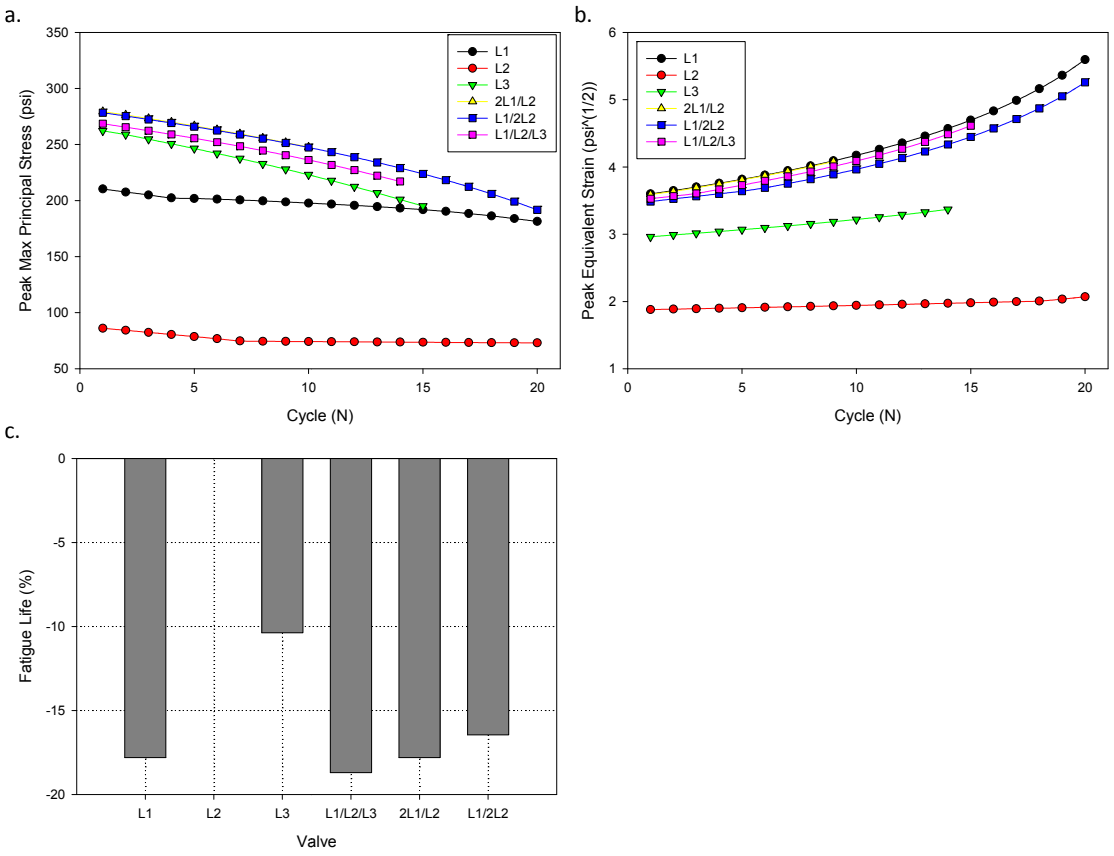

Figure 4.22 The effect of leaflet material properties on the peak leaflet a) maximum principal stress and b) equivalent strain. c) The normalized fatigue life of each valve compared to the L2 valve.

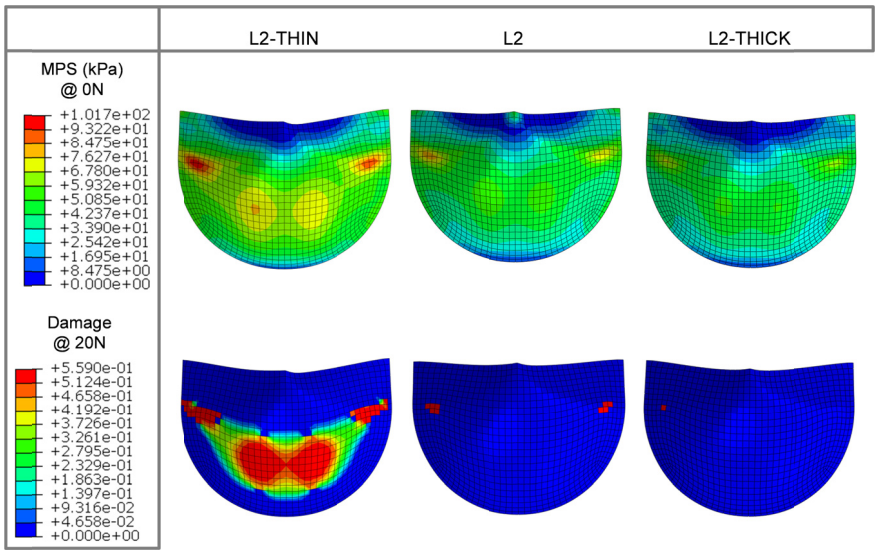

Figure 4.23 Contour plots of the a) max principal stress at the un-fatigued (0N) and fully loaded state and b) the 20N state fatigue damage on the aortic side of the leaflet for each valve of the leaflet thickness parametric study.

The leaflet peak stress was increased throughout cycling in the L2-thin valve and decreased in the L2-thick valve compared to the L2 nominal as shown in Figure 4.24a. The peak equivalent strain was also higher and increased much more rapidly over cycling in the L2-thin valve than the L2 nominal and L2 thick valves (Figure 4.24b). These effects reduced the fatigue life of the L2-thin valve compared to the L2 and L2-thick valves (Figure 4.24c). The fatigue life of the L2-thick valve was slightly improved compared to the L2 valve.

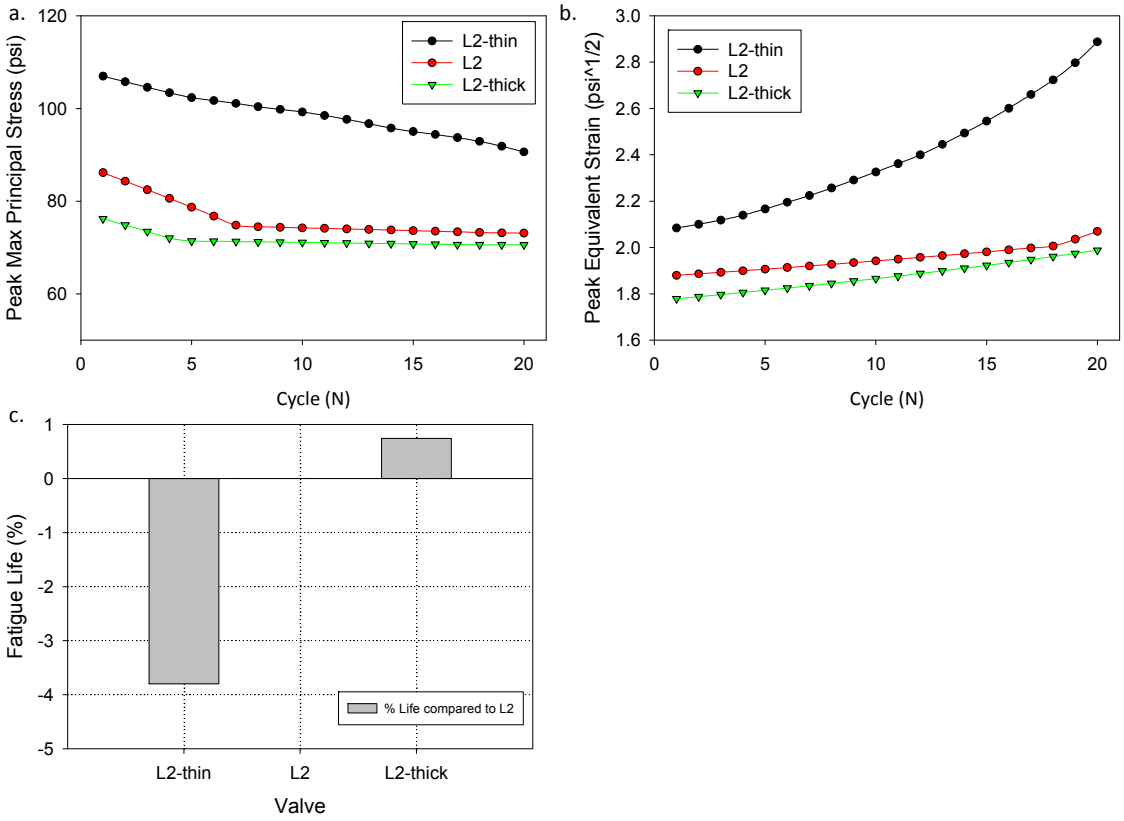

Figure 4.24 The effect of the leaflet thickness on the peak L2 leaflet a) maximum principal stress and b) equivalent strain observed during valve closure at each cycle. The normalized fatigue life of each of the valves with altered leaflet thickness compared to the nominal L2 valve.

4.3.4 Stent property parametric study

In each simulation the valve model was subjected to 20N cycles of pressurization. All eight altered stent simulations completed successfully. Changing the stent modulus altered the amount of stent-tip deflection in the L1 and L2 valves to similar degrees. The L1 and L2 nominal valves had stent-tip deflections of 5.3° and 5.9° respectively. Decreasing the stent modulus by 40% (0.6E) increased the L1 and L2 stent-tip deflections to 8.0° and 8.8°. Increasing the stent modulus by 40% (1.4E) decreased the deflection in the L1 and L2 valves to 4.0° and 4.5° respectively (see Figure 4.25), while the "Rigid" formation prevented any stent deflection. Altering the stent modulus had a negligible effect on the L1 leaflet coaptation: in each case there was a small gap between the leaflets upon closure. However, the stent modulus affected the leaflet coaptation of the L2 valve. The nominal L2 valve had perfect leaflet coaptation, and decreasing the modulus caused slight leaflet pin-wheeling in the L2 0.6E case. Increasing the L2 stent modulus caused a small gap upon valve closure in the L2 1.4E case and a more significant gap in the L2 Rigid case.

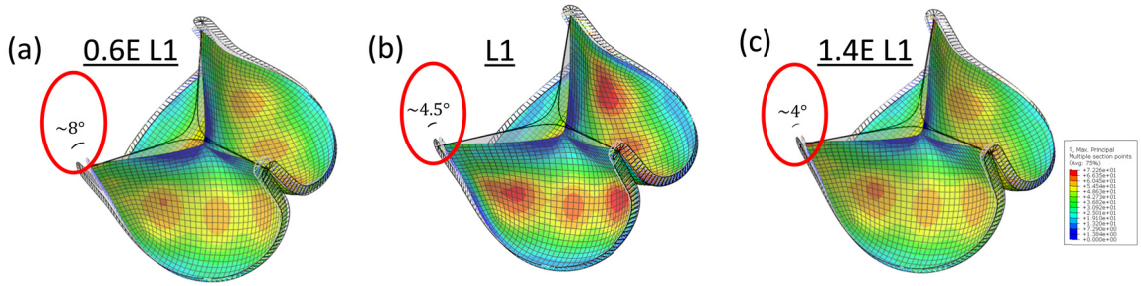

Figure 4.25 The effect of the stent elastic modulus on the degree of stent-tip deflection for the L1 valve.

In both the L1 and L2 nominal valves, decreasing the degree of stent-tip deflection increased leaflet stresses particularly in the belly and commissure regions

(Figure 4.26a), which induced greater fatigue damage in these regions (Figure 4.26b). For each of the L1 cases, the peak leaflet stresses were located along the leaflet suture attachments. The L2 nominal, L2 0.6E and L2 1.4E valves all had leaflet peak stresses on the sides of the leaflet belly region, while the L2 Rigid valve had peak stresses at the commissures.

The L1 leaflet peak stresses (Figure 4.27a) and equivalent strains (Figure 4.27c) throughout cycling were only minimally affected by the altered stent property, where increasing stent-tip deflection decreased leaflet stresses and equivalent strains. The trends were less consistent for the L2 valve, because the peak stresses and equivalent strains did not correspond to the same region of the leaflet in each case. All of the altered stent-tip deflection L2 cases resulted in higher initial peak leaflet stresses and equivalent strains than the nominal L2 (Figure 4.27b&d). Similar, to the leaflet property parametric study, the peak damage factor vs. cycle curves for each valve in the stent property parametric study were extrapolated to estimate the valve fatigue life. The stent property had a minimal effect on the L1 valve fatigue life (Figure 4.27e) of less than 1%. For the L2 valve, the altered stent-tip deflection had a greater impact on the valve life (Figure 4.27f), where the rigid stent reduced valve durability by ~2.5%, although this is still not very significant.

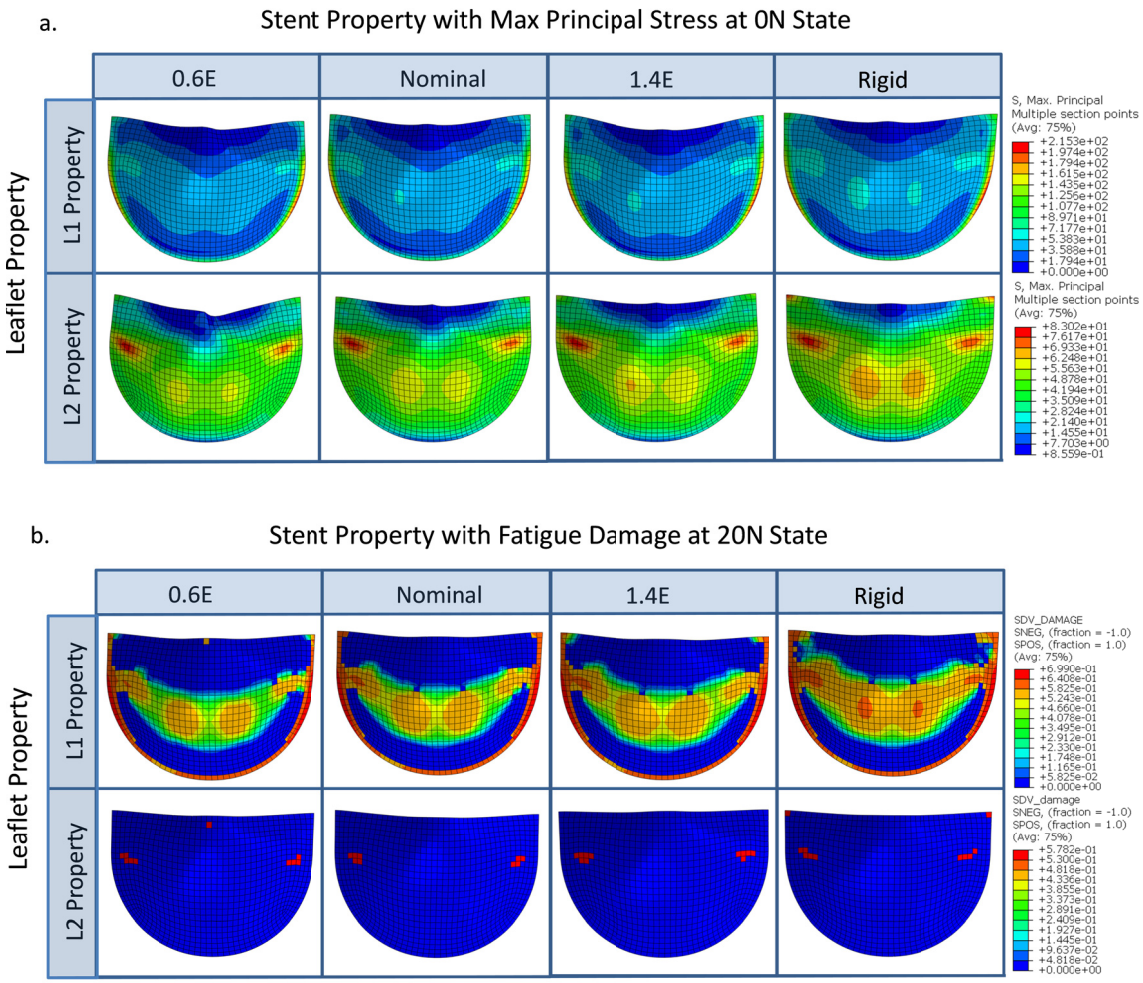

Figure 4.26 Contour plots of the a) max principal stress at the un-fatigued and fully loaded state and b) the 20N state fatigue damage on the aortic side of the leaflet for each valve of the stent property parametric study.

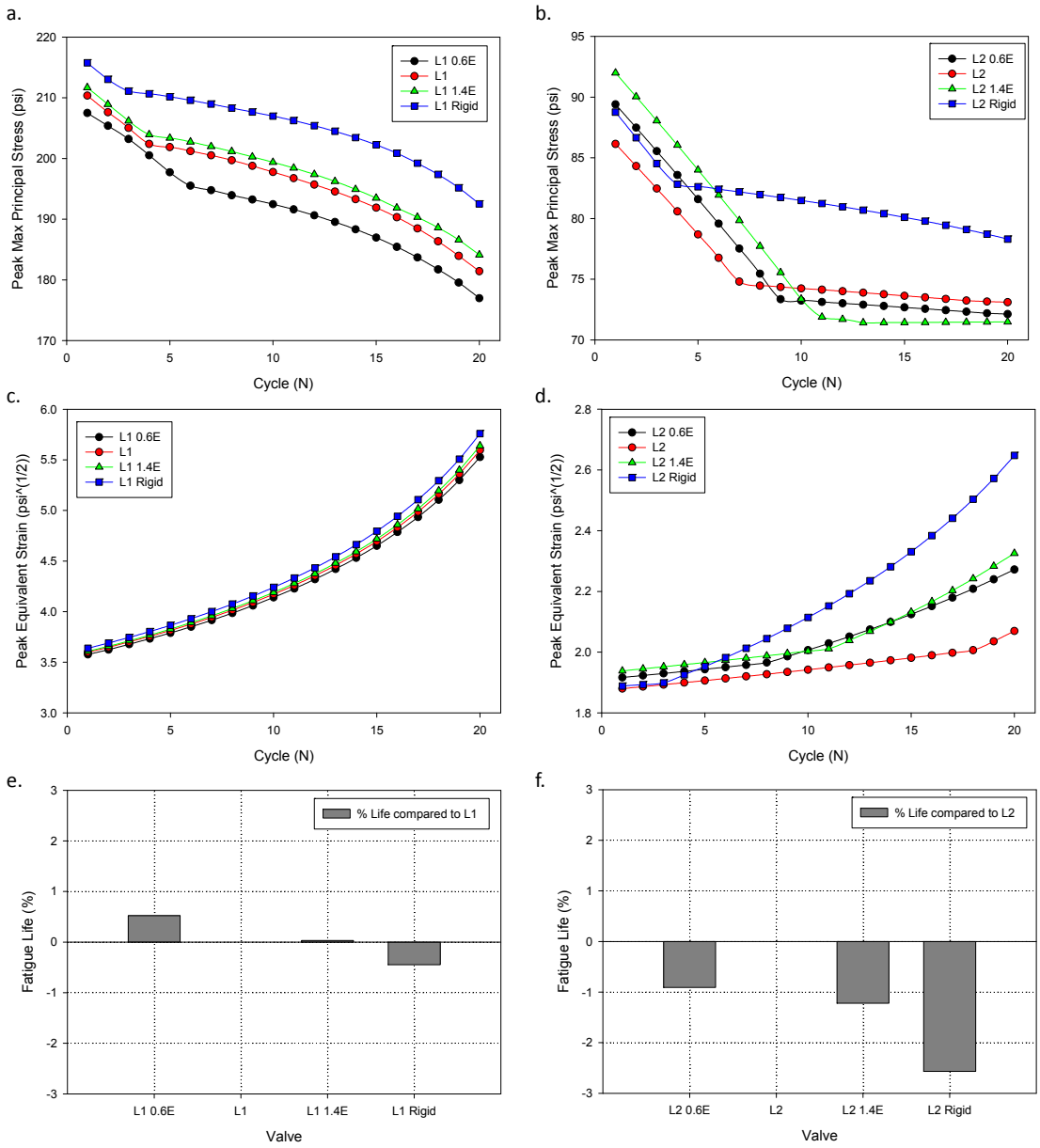

Figure 4.27 The effect of the stent elastic modulus on the peak L1 leaflet a) maximum principal stress and c) equivalent strain observed during valve closure at each cycle. The effect of the stent elastic modulus on the peak L2 leaflet b) maximum principal stress and e) equivalent strain observed during valve closure at each cycle. The normalized fatigue life of each of the e) L1 and f) L2 leaflet property valves with altered stent properties compared to the corresponding nominal valves.

4.3.5 Comparison study of SAV and TAV leaflet fatigue

The SAV fatigue simulation ran until complete local failure of the matrix ($D_{s_m} = 1$) at the 28N fatigue state, which caused a numerical singularity and solution

divergence. The TAV fatigue simulation only ran until the 9N fatigue state due to numerical instability. The peak leaflet strain and equivalent strain were compared between the two valves for each cycle (Figure 4.28). In each case, the peak values were higher in the TAV compared to the SAV at corresponding cycle states. The initial (0N state) peak strain and equivalent strain values in the TAV leaflets were 26% and 51% higher than the respective SAV leaflet values. The TAV peak strain and equivalent strain values at the 9N fatigued state corresponded to the values observed in the SAV leaflets at the 23N state (Figure 4.28). Therefore, the leaflet peak equivalent strain, max principal stress, and max principal strain contours in the fully closed valve configuration were compared between the TAV at the 9N state and the SAV at the 23N state (Figure 4.29a). While the peak values were similar, the respective contour plots show that a larger area of the TAV leaflet was subjected to high strains compared to the SAV leaflet, and the TAV leaflet had higher stress throughout. In each case, the peak equivalent strains, stresses, and strains were located near the commissures and along the stent-attachments, which contributed to the most significant damages in these regions of the leaflets.

The peak equivalent strain, max principal strain and stress contours are also shown for the SAV at the 28N state representing the failure state in Figure 4.29b. The leaflet failure points correspond to the peak equivalent strain and max principal strain concentrations near the commissures. The SAV leaflet stress contour plot at the 28N state shows that the stress distribution homogenized from the 0N state (Figure 4.14).

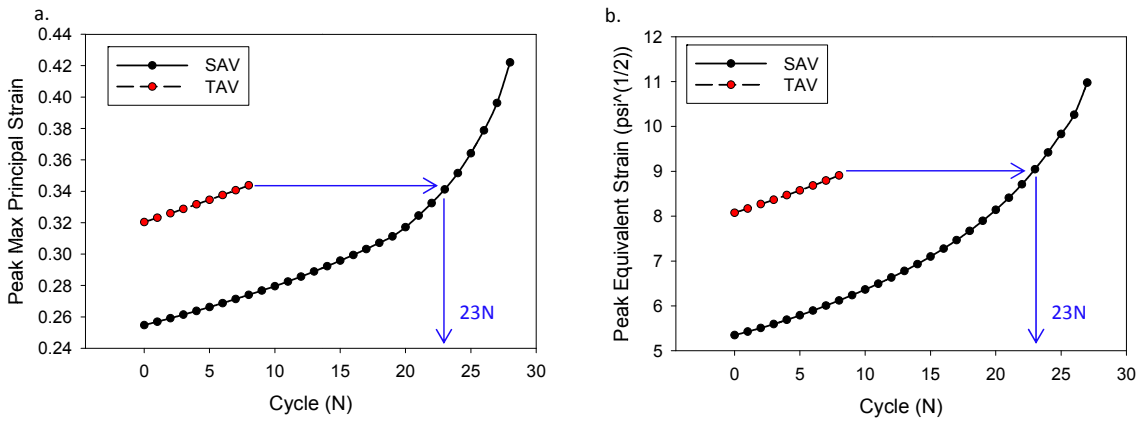

Figure 4.28 The peak a) max principal strain and b) equivalent strain observed in the leaflets for each case and cycle.

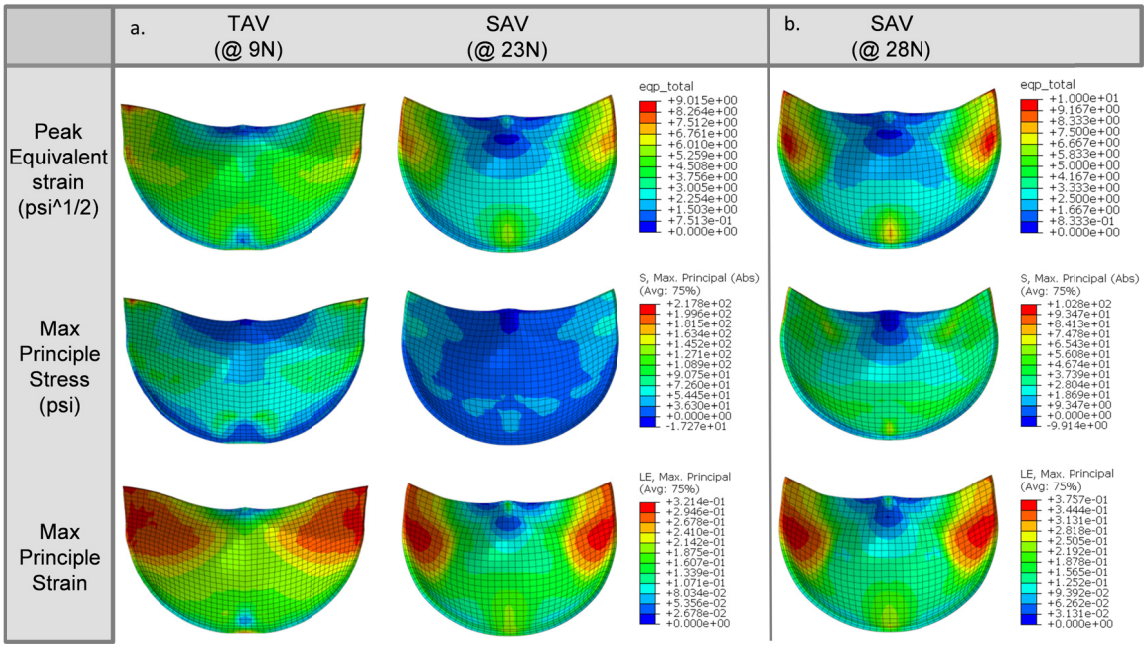

Figure 4.29 a) Contour plots of the peak equivalent strain, max principal stress, and max principal strain of the TAV at the 9N state and the SAV at the 23N showing similar patterns and peak values. b) Contour plots of the peak equivalent strain, max principal stress, and max principal strain of the SAV at failure (28N state).

4.3.6 Parametric study of TAV underexpansion

In each UE case, the leaflets exhibited leaflet redundancy and pin-wheeling upon valve closure (Figure 4.30b-d). The reduced valve area caused a nearly linear increase in the leaflet coaptation area with the degree of UE (Figure 4.31a). At the unfatigued state

the coaptation increased from 21.9% of the leaflet area in the nominal case to 33.1% of the leaflet area in the 3 mm UE case. The coaptation areas also increased slightly over fatigue cycling. The pin-wheeling effect also tended to increase the leaflet curvature at the free edge as shown by the decreased MBR at the free edge in the 2 mm and 3 mm UE cases (Figure 4.31b). The MBR was actually slightly higher at the free edge in the 1 mm UE case than the nominal, because the pin-wheeling effect was very minor. The MBR at the free edge tended to decrease slightly with continued cycling. The MBR along the radial mid-line also decreased with the degree of underexpansion because the leaflet redundancy caused the belly region to sag (Figure 4.31b). This effect worsened with fatigue as permanent set accumulated and the leaflets became larger.

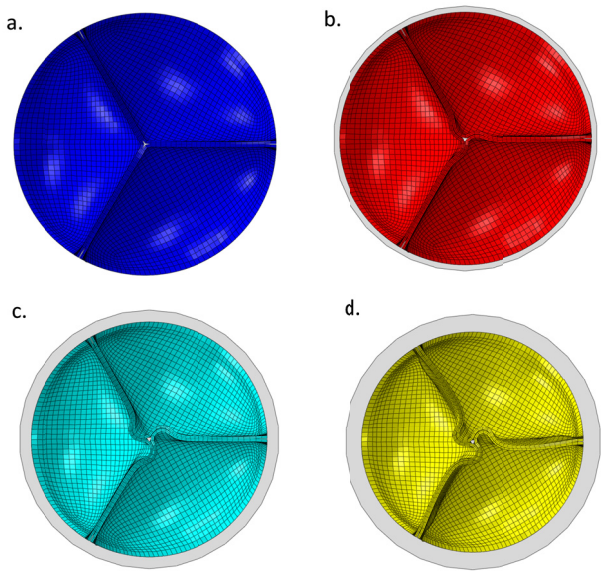

Figure 4.30 Leaflet coaptation upon full closure in the a) nominal, and b) 1 mm, c) 2 mm, and d) 3 mm stent diameter reduction cases overlaid with a circle of the original stent diameter (gray).

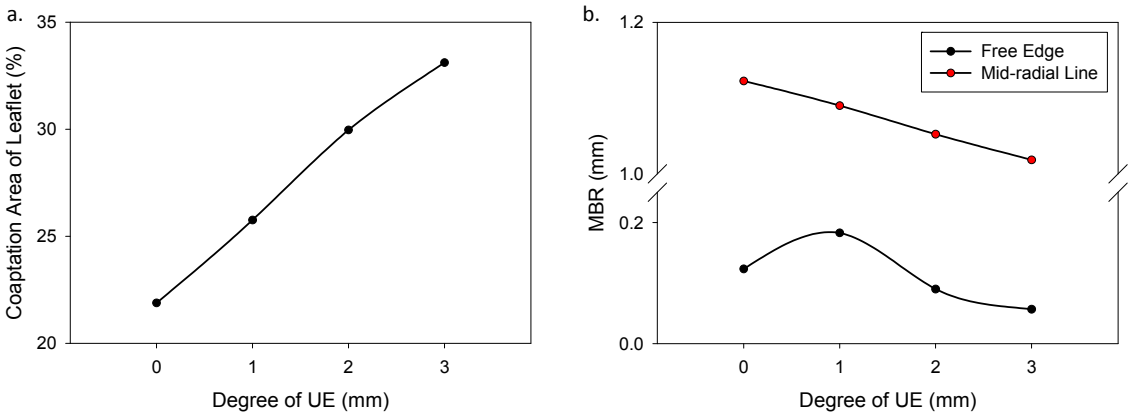

Figure 4.31 a) The percent area of leaflet coaptation, b) the MBR of the leaflet free edge and radial mid-line versus the degree of underexpansion at the 0N state.

The peak leaflet stress during closure along the commissures, belly, and nadir were compared for each case. The normalized peak stresses compared to the nominal case at the 0N state are shown in Figure 4.32. The underexpanded configuration resulted in increased tensile stresses at the commissures and decreased tensile stresses in the belly region (Figure 4.32a). The peak tensile stress was also increased in the 2 mm and 3 mm UE cases at the nadir compared to the nominal valve. The peak compressive stresses consistently increased in all regions of the leaflets with increasing degree of underexpansion (Figure 4.32b). In the nominal and 1 mm UE cases the peak tensile stress was located at the commissures and the peak compressive stress was at the nadir due to coaptation. In the 2 mm and 3 mm UE cases the peak tensile and compressive stresses were both located near the commissures along the suture attachments due to significant leaflet bending in these regions.

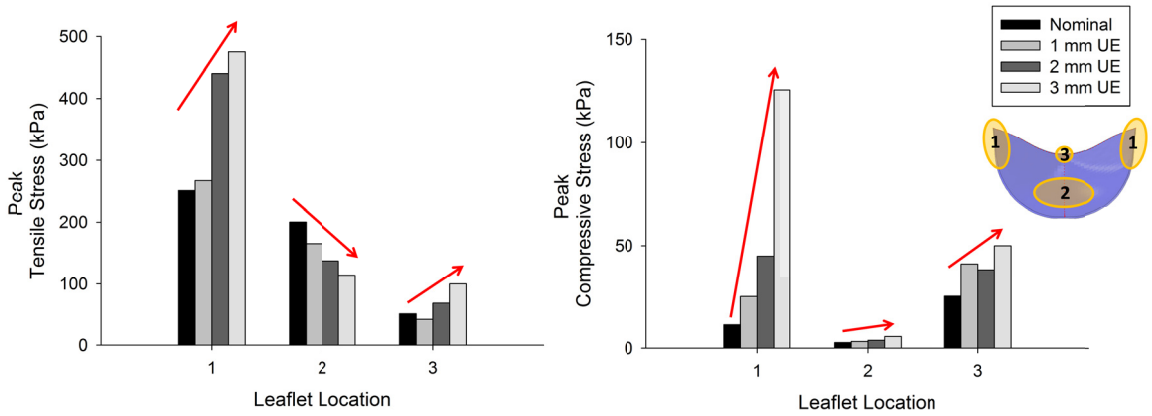

Figure 4.32 Peak a) tensile and b) compressive stress for each valve at the 0N state in different regions of the leaflet: 1) along commissures, 2) belly, and 3) nadir.

The nominal TAV had the most uniform peak equivalent strain distribution in the leaflets, which translated to the most uniform damage patterns for both the matrix and fiber components (Figure 4.33). In the UE cases, the overall damage area was reduced, but damage was accelerated at the free edge and suture attachments corresponding to the elevated stresses and equivalent strains in these regions. The damage became more concentrated with increasing degree of underexpansion, as the maximum peak equivalent strain values tended to increase (Figure 4.34). The overall peak equivalent strain was initially lowest in the 1 mm UE; however, surpassed that of the nominal valve at the 4N state (Figure 4.34b). The maximum peak equivalent strain was initially located at the commissures in the nominal case, but shifted slightly downwards along the suture attachments at the 8N state. The maximum peak equivalent strains were located at this region along the suture attachments throughout each of the UE simulations. The maximum peak equivalent strain increased slightly more rapidly in each of the UE cases compared to the nominal fully expanded case with continued cycling.

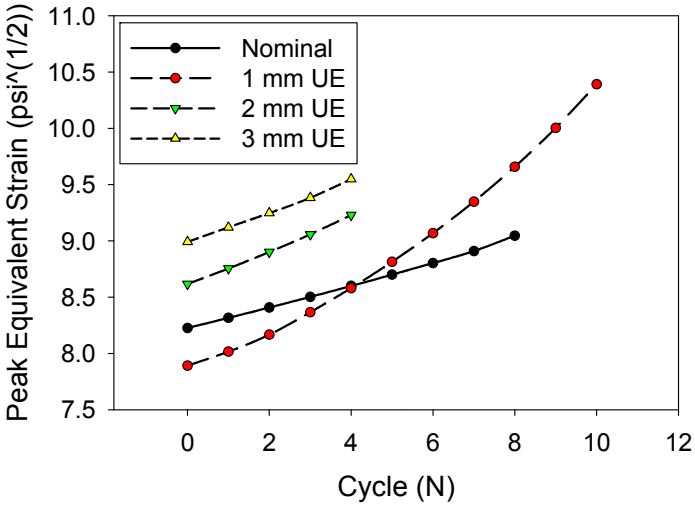

Figure 4.33 The peak equivalent strain observed in the leaflets for each case and cycle.

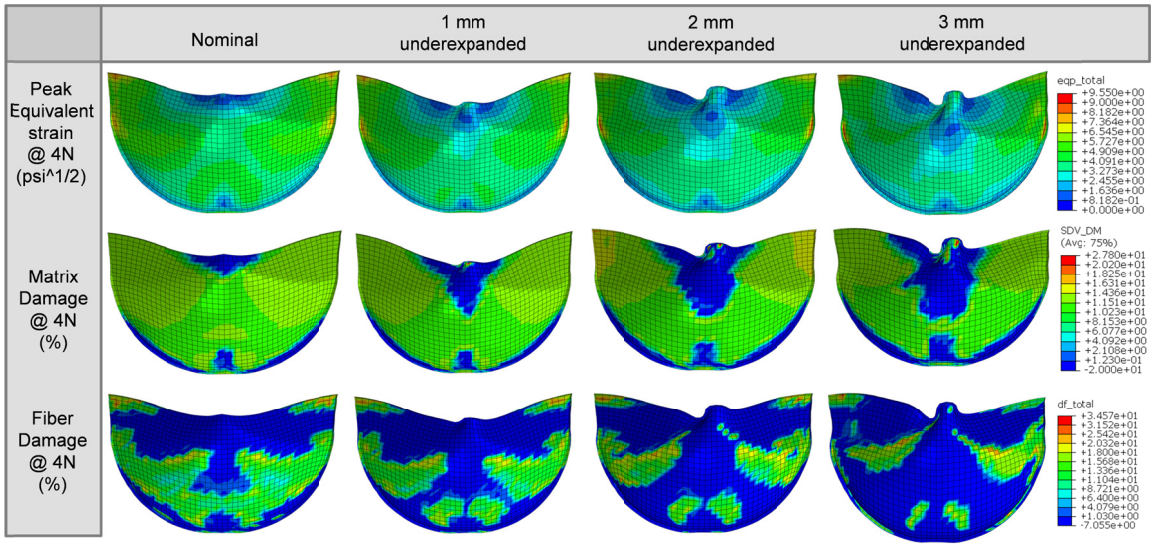

Figure 4.34 Contour plots of the peak equivalent strain and the matrix and fiber damage at the 4N cycle fatigued state for each case.

4.4 Discussion

4.4.1 Constitutive modeling of GLBP fatigue response

The theoretical and computational framework of Chapter 2 was able to quantitatively describe the changing mechanical and structural properties of GLBP tissue strips subjected to uniaxial tension cycles. While the experimental data available is

limited, the results of this study show that the modeling approach is suitable for modeling the GLBP fatigue response. The developed constitutive model can thus be used in conjunction with FE analysis to investigate the impacts of BHV design features on the durability of the GLBP leaflets, as in this chapter, and could also be used to investigate the durability of GLBP patches for various applications.

4.4.2 Effect of cyclic loading on SAV function

The added effects of fatigue-induced stress softening and permanent set caused changes in the leaflet stress distributions and often the region of peak stress in the leaflet. Therefore, the region of peak stress in the un-fatigued leaflet may not necessarily correspond to the ultimate failure region. Fatigue also caused the leaflets in each case to sag, particularly in the central belly region of the leaflet (Figure 4.20). This phenomena was also observed in porcine BHVs subjected to 500×10^6 cycles of accelerated wear testing [291], where the leaflets exhibited increased curvature particularly in the central belly region. The areas of increased curvature were correlated to areas with collagen fiber distortion [291] or damage, which agrees well with the simulated results. Leaflet sagging may increase the coaptation area throughout cycling and accelerate damage at the free edge of the leaflets.

4.4.3 Effect of leaflet properties on SAV durability

The results of this study suggest that SAV durability is highly dependent on the leaflet properties. Unsurprisingly, the best leaflet properties, L2 and L3, were highly anisotropic with higher stiffness in the circumferential direction, similar to the native valve property [312]. The worst the leaflet property, L1, was nearly isotropic, which translated to fatigue damage over a much larger area of the leaflets compared to the L2

and L3 valves. The fact that the initial leaflet peak stresses in the L1 valve were lower compared to those of the L3 valve, demonstrates that an initial peak leaflet stress analysis may not be appropriate for assessing valve durability. The initial peak leaflet equivalent strain may be a superior metric for assessing valve fatigue, because this value accounts for the total leaflet deformation.

The three leaflet property mismatch cases were associated with higher leaflet stresses and fatigue damage along the leaflet commissures and suture attachments compared to the nominal valves. This helps explain why mechanical failures of SAVs are often associated with leaflet tears in the vicinity of the commissures and/or suture attachments, regardless of the specific design [242, 317-319]. The L1/L2/L3 valve had the shortest fatigue life of all the valves studied. Fatigue damage was also accelerated in the 2 L1/L2 and L1/2 L2 valves compared with the L2 nominal valve: the damage in these valves was similar to that in the L1 nominal valve. Thus, the valve durability is only as good as the worst leaflet. However, the 2 L1/L2 and L1/2 L2 valves were slightly more durable than the L1/L2/L3 valve, which suggests that leaflet property homogeneity also plays a role in the valve durability and supports leaflet heterogeneity as a failure mode of pericardial SAVs [242-244]. Of course in reality, it may be challenging to build BHVs with identical leaflet material properties; however, careful selection of the tissue used for fabrication may significantly improve the durability of BHVs. Indeed, leaflet sorting based on mechanical properties has been adopted by the heart valve industry for the BHV manufacturing process.

The leaflet fatigue damage increased with a decrease in leaflet thickness as expected. This result is intuitive because as the leaflet thickness is reduced, the stress is

increased, and corresponds to the clinical observation that thinner leaflets are associated with reduced durability [241]. Surprisingly, the leaflet material properties still had a more significant impact on the valve durability than the leaflet thickness. The results of this parametric study have implications for TAVs which require thinner leaflets. Interestingly, although the L2-thin valve had accumulated damage over a larger area of the leaflet at the 20N state compared to the L2-Rigid valve, the peak damage was similar in both valves. This suggests that the lack of stent-tip-deflection and thin leaflets have a similar detrimental impact on the valve durability; although, the leaflet thickness would likely have a more significant impact on the durability when reduced below 0.35 mm. Thus, some mechanism to provide stent-tip deflection in TAVs may be important.

4.4.4 Effect of stent properties on SAV durability

As expected, reduction of the stent-tip deflection resulted in higher peak leaflet stresses and fatigue damage in the commissure regions. Mechanical failures of the IS valve were associated with tears in the leaflets along the free edges near the top of the struts [240, 320-322], which agrees with this result (Figure 4.26b). Reduction of the stent-modulus redistributed the peak stresses and fatigue damage away from the commissures, towards the leaflet free edge, yet, did not always translate to better durability. At some minimum threshold stent-tip deflection value, leaflet fatigue damage will exceed that of the nominal stent.

In the L1 stent property parametric study, although increasing the degree of stent-tip deflection consistently resulted in lower leaflet stresses, equivalent strains and fatigue damage particularly in the commissure regions, some degree of fatigue damage was accrued in the commissure regions in each case. This result is supported by the clinical

finding that commissural tears continue to be a mechanism of BHV failure, even in designs with flexible stents [323].

In the L2 stent property parametric study, all of the altered stent cases resulted in higher leaflet stresses, equivalent strains and fatigue damage than the nominal case. The incorporation of stent-tip deflection eliminated leaflet fatigue damage in the regions of the commissures completely, yet increased damage at the free edges. The leaflet peak stresses and equivalent strains over cycling followed a similar pattern for the L2, L2 0.6E, and L2 1.4E cases, likely because the peak values in each case corresponded to the same region of the leaflet, towards the sides of the belly region. The peak stresses and equivalent strains for the L2 Rigid leaflets followed a different pattern, but these peak values corresponded to different regions of the leaflets: the commissures. Leaflet fatigue damage seems to propagate differently in different regions. It is clear that the complexity of the BHV design can cause confounding effects on the durability. Overall, the degree of stent-tip deflection had a lesser impact on leaflet durability than the leaflet material properties, and affected valves with different leaflet material properties differently.

4.4.5 Effect of leaflet coaptation on SAV durability

For clinical or experimental cases, where the full leaflet stress and equivalent strain distributions are unknown, the leaflet coaptation upon closure may also be a useful qualitative indicator of BHV durability. The L2 valve had essentially perfect leaflet coaptation and the least amount of fatigue damage in the leaflets. In the leaflet property mismatch cases, one or two of the leaflets would lean over the others due to the differences in stiffness of the contacting materials. The greater the disparity between the leaflets, the more appreciable the leaflet leaning upon closure became. The leaning was

most significant in the L1/L2/L3 valve which had the greatest amount of fatigue damage. The leaning is also likely responsible for the high stress concentrations at the suture attachment lines in the L1/L2/L3, L1/2 L2, and 2 L1/L2 valves. Leaflet leaning may initiate a positive feedback mechanism for leaflet tearing. For instance, if a leaflet leans more to one side than the other, higher stress will be applied to the opposing side of the leaflet along the suture attachment, and as that area becomes damaged, the leaflet leaning will become more pronounced.

Pin-wheeling of the leaflets may also compromise leaflet durability. In the L3 and reduced stent modulus cases, leaflet pin-wheeling upon closure induced fatigue damage at the leaflet free edge. Interestingly, the leaflet max principal stress is often low at the free edge despite high equivalent strains and damage in this region with leaflet pin-wheeling. This is because the leaflets undergo significant compressive strains in this region and the principal stress is actually at a minimum, which further supports the use of the equivalent strain in place of the max principal stress for assessing valve durability.

4.4.6 Effect of including distinct matrix and fiber descriptions

Overall, including distinct matrix and fiber descriptions in the SAV model did not significantly impact the SAV fatigue simulation results. The peak equivalent strain contours for both SAV models showed peak values near the commissures and along the suture attachments, and in both cases SAV failure was predicted at the 28N cycle state due to tissue failure at these regions. However, by including separate mechanisms for distinct matrix and fiber damages in this study, matrix damage was revealed in regions of low stress, albeit large strains such as the lower belly region of the SAV leaflet (Figure

4.15). This effect is due to the marked anisotropy of the tissue which allows the leaflets to achieve large strains in the radial direction under low stress. By comparing the contour plots of the max principal stress and strain in the SAV leaflets shown in Figure 4.14 with the matrix and fiber damage contour plots in Figure 4.15, it appears that matrix damage corresponded to regions of high strain, while damage to the fibers corresponded to regions of high stress. Damage at the nadirs (Figure 4.15) due to significant compressive stresses (Figure 4.14) was also predicted unlike in our previous study. The leaflet may be particularly susceptible to fatigue damage under compressive loading, because fibers are typically assumed to only bear load under tension, thus, the weaker matrix components must support all compressive stresses. In these regions where only the matrix is damaged, the fibers may become debonded from the surrounding matrix causing delamination. Thus, while the inclusion of distinct matrix and fiber damage descriptions did not change the predicted failure location for this case, in cases where the leaflets may be undergoing larger bending deformations or compressive stresses, it could have a significant impact on the conclusions of the study.

4.4.7 Computational fatigue analysis of surgical bioprosthetic valves

Overall the results of the SAV fatigue simulations were very robust and corresponded to the known failure mechanisms of SAVs very well. The following factors were associated with accelerated fatigue of the GLBP leaflets: heterogeneity of leaflet elastic properties, thin leaflets, poor leaflet coaptation, and little stent-tip deflection. Each of these factors has long since been known to accelerate fatigue of SAVs [240-244]. Furthermore, regardless of the leaflet and stent properties, the simulated leaflet fatigue damage was highest along the commissures and suture

attachments, which correspond with the known failure locations of SAVs [240, 320-323]. Therefore, the SAV fatigue damage modeling approach presented can be used to predict realistic BHV fatigue patterns, and thus was used to investigate TAV fatigue mechanisms.

4.4.8 Comparison of SAV and TAV leaflet fatigue damage

Similar to the recently published FE results comparing SAV and TAV leaflet mechanics at the un-fatigued state [310], the leaflet stresses and strains were significantly higher in the TAV compared to the SAV. The TAV leaflet peak equivalent strains remained significantly higher than the SAV leaflet values at corresponding cycle states throughout fatigue life. This translated to elevated peak damage values and larger damage areas in the TAV leaflets at any given cycle state. In both valves, these peak leaflet damages were predicted near the commissures and along the stent-attachments, which corresponds with the known failure regions of SAV leaflets [242, 317-319]. Unfortunately, TAV leaflet fatigue until complete failure could not be simulated. However, considering that the peak strain and equivalent strain values of the TAV leaflets at the 9N state corresponded to the respective peak values of the SAV leaflets at the 23N state (Figure 4.29), and it is known that SAVs have a durability of approximately 20 years, we can estimate the durability of TAVs. If we scale the SAV failure point, 28N, to be equivalent with 20 years, 23N represents about 16 years and 82% of the fatigue life. Assuming proportional fatigue damage in the TAV, the 9N state represents 82% of the fatigue life; thus, the expected durability of TAVs is about 7.8 years. This result has important clinical implications: the limited durability of TAVs compared to SAVs must be taken into consideration when evaluating whether lower-risk AS patients

should receive TAV replacement versus SAV replacement. TAV durability will likely be further reduced in the setting of non-optimal deployments where the stent is under-expanded or elliptical in shape [324], which may disturb normal coaptation and increase leaflet curvatures [324], as well as stresses and strains [153]. TAV leaflet fatigue analysis under various deployment configurations is necessary in order to develop design and deployment strategies for optimizing TAV durability.

4.4.9 Effect of TAV underexpansion on durability

There have been few quantitative studies on the effects of non-optimal deployment configurations on TAV mechanics. Sun et al. [153] used FE analysis to investigate the effect of elliptical stent deployment on TAV leaflet stresses and strains, which they found to be significantly increased compared to those in the nominal cylindrical stent. Smuts et al. [278] have also used FE to study the effects of leaflet design, mismatched leaflet properties, stent under and overexpansion, as well as asymmetric expansion, on the deformation of the leaflets under hypotensive (50 mmHg) pressurization. They showed that the leaflets will fold over each other in the 1 mm UE case, similar to our result. This is the first study to our knowledge which investigated TAV leaflet mechanics in the setting of stent underexpansion with the added effects of GLBP tissue fatigue.

The UE cases all exhibited leaflet redundancy, pin-wheeling, and sagging in the belly region upon closure, which lead to increasingly heterogeneous leaflet stress and peak equivalent strain distributions (Figure 4.32 and Figure 4.34). From the substantial compressive stresses (Figure 4.32b) and leaflet curvatures in the UE valves (Figure 4.31b), it is clear that tissue bending becomes a more significant loading condition during

TAV closure in the UE configuration. The combination of increased coaptation and considerable leaflet pin-wheeling of the significantly underexpanded valves (≥ 2 mm), increased the leaflet free edge curvature (Figure 4.31b), and resulted in stress concentrations and accelerated tissue fatigue damage at the nadirs (Figure 4.34). The exaggerated leaflet sagging (Figure 4.31b) and twisting in these cases also dramatically increased the peak leaflet stresses and equivalent strains at the suture attachments compared to the nominal case (Figure 4.32 and Figure 4.34). This finding was in agreement with the results of our previous fatigue simulation study of SAVs, where valves that exhibited poor leaflet coaptation had accelerated damage along the suture attachments [245], and the clinical finding that poor coaptation is a predictor of poor durability in SAVs [286].

Although failure could not be simulated, the leaflet maximum peak equivalent strains in the 2 mm and 3 mm UE valves were significantly higher than those in the 1 mm UE and nominal cases at corresponding cycle states (Figure 4.33). Although the peak equivalent strain was initially lower in the 1mm UE case than in the nominal case, it increased more rapidly with cycling and quickly surpassed that of the nominal case at the 4N state (Figure 4.33). These results indicate that TAV underexpansion will compromise the durability of the leaflets, and that leaflet tissue fatigue damage accumulates faster with increasing degrees of underexpansion. In each of the UE cases, the maximum peak equivalent strain values were along the suture attachments just below the commissures (Figure 4.34), thus, the expected mode of leaflet fatigue failure for TAVs in the ViV configuration is along the suture attachments. The maximum peak equivalent strain values in the nominal TAV leaflets were located at the commissures until the 8N fatigue

state when the maximum value moved slightly further down suture attachment line. Therefore, TAVs in the fully expanded configuration are also expected to fail just below the commissures along the suture attachments, the known failure region of SAV leaflets [242, 317-319].

Clinically a range of 10% to 15% underexpansion is generally considered acceptable [271]. All of the cases presented here fall within or below this range, with 3 mm of underexpansion representing only 13.6% underexpansion. The simulation results indicate that up to 5% underexpansion may be acceptable (1 mm underexpansion case), but beyond this level, leaflet tensile and compressive stresses increase dramatically, which will compromise durability. It is important to note that the degree of acceptable underexpansion is also likely dependent on the valve design. The leaflet curvature and coaptation areas at closure may be useful non-design specific indicators of the leaflet durability.

Regardless, the results of this study suggest that the true inner diameter of a previous prosthesis is of critical importance in selecting an appropriately sized TAV. Knowing the labelled size of the SAV may not be enough: the mechanism of failure may also be of importance. Regurgitant valves with torn leaflets may have relatively larger inner diameters, while calcified or thrombosed valves may have smaller or asymmetric inner diameters [271]. Conservative oversizing may also be justified in standard TAV procedures cases where the native aortic valve leaflets are heavily calcified and non-deformable. New TAV devices that are intentionally designed to be deployed within a smaller prosthesis with a larger central gap between the leaflets at the undeformed

configuration may reduce the likelihood of paravalvular leak without negatively impacting the leaflet durability.

4.4.10 Limitations of this study

In this study, the GLBP fatigue damage model parameters were fit to experimental data at one set peak equivalent strain [131]. The dependence of the peak equivalent strain on the fatigue-induced softening and permanent set is unknown. A more comprehensive data set is necessary to determine the true unique fatigue model parameters to capture the fatigued response of GLBP. However, although the amount of fatigue damage in each case presented here is dependent on the fatigue model parameters chosen which were not rigorously determined through experiments, this approach is valid for studying the effects of BHV design parameters on durability through well-controlled, side by side comparison. It is also important to note that the optimal BHV leaflet and stent properties presented here are likely valve design dependent.

Structural valve degeneration due to calcification was not considered in this study. Calcification tends to occur in the areas of high stress during function [320], thus, the fatigue damage areas for each case presented here may also represent areas most susceptible to calcification. It has been suggested that calcific and non-calcific damage may be synergistic, where collagen disruption could expose new calcium nucleation sites or mechanical damage may occur due to stress concentrations created by local calcium deposits [318, 325]. Therefore, the leaflet damage regions presented here may represent locations most likely to calcify. It may also be necessary to include non-affine deformation modes of the tissue constituents, i.e. fiber slippage or breakage, to determine the mechanisms of BHV leaflet fatigue damage.

The combined effect of tissue softening and permanent set over cycling created numerical instabilities in the simulations, particularly in the TAV simulations, where damage was accumulating at an accelerated rate, and was highly concentrated. At these damage concentration zones, adjacent elements may have very different D_s and D_{ps} values which creates discontinuities in the material properties and affects numerical convergence. For this reason, TAV fatigue could only be simulated up to the 9N state, whereas in the SAV case, the incremental damage per cycle was low and more homogeneous, and more advanced fatigued states could be simulated (up to 28N). An explicit solver could potentially improve numerical convergence; however, at this time, an implicit code is needed to accurately simulate the tissue fatigue response.

4.5 Conclusions

In this study, GLBP fatigue was modeled with the time-dependent inelastic constitutive law derived in Chapter 2. A GLBP uniaxial fatigue FE simulation replicating the experimental protocol of Sun et al. [105], demonstrated that the FE modeling approach presented in this chapter can quantitatively capture the material fatigue response of GLBP including the stress softening and permanent set phenomena.

The GLBP fatigue damage model was then implemented in BHV FE simulations to assess GLBP leaflet fatigue damage in BHV applications. The effects of the SAV leaflet and stent elastic properties on the durability of the leaflets were investigated in a parametric study. The following factors were associated with accelerated fatigue of the GLBP leaflets: heterogeneity of leaflet elastic properties, thin leaflets, poor leaflet coaptation, and little stent-tip deflection. Each of these factors has long since been known to accelerate fatigue of BHVs [240-244], but this is the first study to show that

this is analytically the case. Thus, the modeling framework presented here can predict realistic BHV structural level damage.

Once it was verified that the modeling approaches developed in this chapter could replicate BHV fatigue mechanisms both on the material (GLBP) and structural levels, the same approaches were taken to predict TAV durability under normal and underexpanded configurations. The results of this study suggest that even when properly deployed, the durability of TAV devices will be significantly reduced compared to SAVs to about 7.8 years. The simulation results show that TAV underexpansion by $\geq$ 2mm results in significantly higher tensile and compressive leaflet stresses which will ultimately limit the durability of the leaflets, while slight underexpansion (1 mm) has a minimal effect on the leaflet durability. However, the degree of acceptable underexpansion will likely depend on the particular valve design. The results of this study warrant further investigation of ViV mechanics.

TAV and ViV interventions are expected to grow in the coming years: TAV intervention can significantly improve valve hemodynamics and patient quality of life for inoperable and high-risk AS patients with the added benefits of lower operative risk and shorter recovery time compared to SAV replacement. However, one of the determining factors limiting the use of TAV devices in younger and healthier patients with longer life expectancies is the unknown durability. Furthermore, TAVs do not always fully expand clinically when deployed within either a heavily calcified native aortic valve or a non-compliant failed prosthesis in ViV procedures.

The computational approach for studying fatigue of BHV leaflets developed in this study may be an invaluable tool for evaluating the durability of new BHV designs, including the next generations of TAVs which also often utilize chemically-treated pericardium leaflets. This approach can provide a fully quantitative analysis of specific design factors on the BHV durability to facilitate durable design, and could serve as a prerequisite to AWT testing to dramatically speed up the design cycle time.

5 CONCLUSIONS

In this chapter, we will summarize the main findings of the previous chapters. Then we will discuss the clinical impacts and future directions related to this thesis.

5.1 Summary

In Chapter 1, we summarized the current state-of-the-art methods for characterizing and modeling the mechanical properties of soft collagenous tissues. We discuss the limitations of existing models for describing fatigue and aging effects in soft tissue, as well as the motivation and aims of this work.

In Chapter 2, we presented a theoretical and computational framework to describe the time-dependent dissipative property changes of soft tissues due to fatigue and aging including the accumulation of stress-softening and permanent set. By perturbing the model parameters, we demonstrated that the model can describe a wide range of time-dependent, inelastic effects, making the framework suitable for many applications. A uniaxial tissue fatigue simulation was presented to show that the computational framework predicts realistic anisotropic changes in tissue properties in response to cyclic loading. In the following two chapters, Chapter 3 and Chapter 4, the theoretical and computational framework was applied to model age-dependent ascending aorta (**AA**) tissue property changes in natural human aging, and cycle-dependent tissue property changes in bioprosthetic heart valve (**BHV**) devices fabricated with glutaraldehyde-treated bovine pericardium (**GLBP**) leaflets.

In Chapter 3, we characterized the age-related structural and mechanical property changes of the human AA through *in vivo* and *in vitro* measurements. We utilized this data in conjunction with the theoretical and computational framework of Chapter 2, in the development of a constitutive model of human AA aging. The human AA aging constitutive model was then implemented in patient-specific AA FE models, and the effects of aging were simulated. The FE predicted AA structural property changes were validated against *in vivo* measurements. The simulation results showed that the AA wall stresses increase over time, and this increase becomes significant after many years.

In Chapter 4, we utilized GLBP uniaxial fatigue data presented in the literature, to develop a constitutive model of the GLBP fatigue response using the theoretical and computational framework of Chapter 2. The GLBP fatigue damage model was implemented in parametric FE simulations of BHV deformation to investigate the impacts of BHV design factors on durability. We found that the following factors were associated with accelerated fatigue of the GLBP leaflets in surgically implanted BHVs (**SAV**): heterogeneity of leaflet elastic properties, thin leaflets, poor leaflet coaptation, and little stent-tip deflection, which correspond to the known failure modes [240-244]. Thus, we used this same approach to predict effects of GLBP fatigue damage in transcatheter implanted valves (**TAV**) for which the durability and failure modes are currently unknown.

The major contributions of this thesis are:

i) Theoretical framework for modeling time-dependent irreversible soft tissue property changes

ii) Computational framework for simulating time-dependent irreversible soft tissue property changes in FE models

iii) Constitutive model to describe age-related human AA tissue property changes

iv) Computational methodology for simulating age-related human AA structural property changes

v) Constitutive model to describe fatigue-induced property changes in GLBP, a representative BHV biomaterial

vi) Computational framework for simulating leaflet fatigue damage in BHVs

5.2 Clinical relevance

The theoretical and computational framework for modeling soft collagenous tissue fatigue and aging effects developed in Chapter 2 of this thesis may facilitate durable tissue-derived device design, and improve understanding of the impacts of aging on soft tissue properties and organ function. The benefits of a computational platform are that it could be used for general applications, i.e. tissue types, anatomies, loading conditions and it permits quantitative and efficient analyses.

The phenomenological baseline human AA aging model developed in Chapter 3 of this thesis can capture the general changes in AA tissue properties and structural properties in response to natural aging. While the model may be refined and more rigorously validated upon the availability of additional *in vivo* and *in vitro* experimental data in future studies, we demonstrated the feasibility of using the developed modeling approaches to assess how the AA mechanics, i.e. stiffening, wall stress, systolic expansion, in a patient-specific model will evolve over time. This is important because

impacts of age-related AA stiffening include: increased systolic pressure, which causes cardiac hypertrophy and increased ventricular oxygen consumption, and increased risk for the development of cardiovascular disease. A computational model to noninvasively predict the AA functional changes over time in a particular patient would thus be a powerful clinical diagnostic tool for identifying patients at risk and timing potential interventions.

The BHV fatigue damage model developed in Chapter 4 of this thesis can capture the failure modes that have been empirically observed over decades of BHV implantation, and effects of various design factors on the durability of BHVs. Again, more experimental fatigue data for GLBP is needed to refine the model; however, we demonstrated that a computational approach could be used to assess BHV durability. Currently, durability is one of the primary limiting factors preventing the use of BHVs across all patient populations. Ultimately the techniques established in this thesis could facilitate the design of more durable valves and lead to improved long-term patient outcomes.

5.3 Future directions

5.3.1 Refinement of the time-dependent inelastic theoretical framework

There are several limitations of the theoretical framework presented in Chapter 2, which should be addressed in future studies. Due to limited experimental data on soft tissue aging and fatigue damage effects, a linear progression of the stress softening and permanent set parameters at a given equivalent strain over cycling was assumed. Both of these values may evolve faster during the initial cycles, thus, Eqs. (2.24)-(2.26) and

(2.27)-(2.34) may be modified in the future to accommodate non-linearity, provided that experimental data to describe such nonlinear behavior become available. Furthermore, to give the model more flexibility, the functional form of the permanent set should be independent of the loading condition. As presented, the permanent sets in each direction under any applied loads are assumed to be proportional to the D_{psmax} measured under the uniaxial loading condition. Again, more experimental data is necessary to determine an appropriate functional form for the permanent set. Through the soft tissue uniaxial fatigue experiment described in section 2.2.11, tissue specimens would be subjected to displacement-controlled loading cycles to a given peak strain, and the tissue stress-strain response and dimensions would be measured throughout fatigue life to yield the necessary stress-softening vs. peak equivalent strain vs. cycle, and permanent set vs. peak equivalent strain vs. cycle relationships to refine the model.

The theoretical and computational framework developed in Chapter 2 is phenomenological. Thus, it cannot describe microstructural changes in the tissue due to fatigue and natural aging, only changes in the bulk tissue-level mechanical response and geometry. The focus of this study is to model the degradation of tissue mechanical function, rather than modeling soft tissue microstructural-level changes in response to biological and mechanical stimuli. The benefit of a phenomenological model is that it can be more easily implemented in FE where the effects of fatigue and aging can be simulated in realistic anatomical geometries under physiological loading. In order to gain mechanistic insight into the progression of soft tissue aging and fatigue damage, first, further efforts to experimentally characterize the multi-scale tissue aging and fatigue effects are necessary, in order to determine how microstructural changes manifest in the

overall tissue-level mechanical properties. For instance, the elastin and collagen architecture of a tissue sample at various fatigue states could be assessed through non-destructive multi-photon imaging, in order to determine the relationships between elastin fragmentation and collagen fiber un-crimping with changes in the tissue-level mechanical response and geometry. These data could be incorporated in structural-based constitutive models with distinct descriptions of matrix and fiber damages which would provide more insight into the mechanisms governing fatigue- and age-related soft tissue property changes.

The theoretical and computational framework developed in Chapter 2 is also based on continuum theory. It may be necessary to include non-affine deformation modes of the tissue constituents, i.e. fiber slippage or breakage, to further investigate the mechanisms of soft tissue aging and fatigue damage effects. A non-affine approach may also be necessary for modeling the delamination process between tissue layers: where the progressive fracture of fibers binding adjacent layers will initiate delamination. Delamination is not a significant failure mode of pericardial heart valves [303], because the tissue structure is relatively homogeneous through the thickness. However, delamination is a critical tissue failure mode for the AA, which has a tri-layer structure with the intima, media, and adventitia layers, each with distinct material properties. Therefore, future work should include experimental peel tests of aorta tissues to determine the binding strength between the individual layers, and the appropriate way of modeling such failure modes.

Further work should also include expanding the model to include growth and remodeling to describe tissue microstructural changes in response to mechanical and

biological stimuli to study disease progression. Tissue remodeling plays an important role in the durability of living tissues and tissue engineering constructs, while enzymatic degradation and calcification will limit the durability of tissue-derived implants and decellurized scaffolds. However, while there is strong evidence that mechanical factors induce cellular changes in tissues little has been done to mathematically model these effects. Because the computational approach of Chapter 2 is based on the FE method, tissue structure and property changes are realized in the model through the evolving material parameters (D_s and $\boldsymbol{D_{ps}}$), loading conditions, and/or boundary conditions, first we need to precisely quantitative the impacts of biological events on one or more of these factors. Therefore, incorporating biological factors in the modeling framework would require some fundamental experimental work using animal models or *in vitro* bioreactors to study the relationships between mechanical stimuli and changes in tissue-level mechanical properties.

5.3.2 Advances in the computational modeling of soft tissue aging and fatigue effects

There are also several limitations of the computational modeling methods that should be addressed in future work. For the AA (Chapter 3) and BHV (Chapter 4) computational models, tissues were treated as homogeneous materials both in-plane and through the tissue thickness. However, the aorta [205] and GLBP [326] tissue properties may be region specific. It would be relatively straightforward to model continuum damage to a multi-layer material using the framework developed in Chapter 2. In order to do this, the specific time-dependent inelastic material model parameters must be determined for each layer of the tissue, i.e. intima, media, and adventitia for the AA. In the computational model, each layer of the tissue would then be modeled with a distinct

set of elements which would be described by the time-dependent material parameters for the corresponding tissue layer. Layer-specific tissue properties will be essential for modeling the delamination process, although this may also require refinement of the theoretical model as discussed in section 5.3.1. The same approach can be used for modeling in-plane regional property differences. As long as the time-dependent inelastic material model parameters can be determined for the different regions, the parameters can be applied to the corresponding regions in the computational model. One of the challenges with determining the heterogeneous, regional tissue properties lies with the experimental methods. Typically soft tissue properties are determined through planar biaxial mechanical tests, for which homogeneity is assumed to calculate the material stress-strain response. Therefore, to determine the layer-specific tissue properties, the layers must be dissected from each other and tested individually. The dissection process can be time-consuming and challenging, and may result in damage of the layers. To assess regional property differences, many tissues samples, i.e. around the vessel circumference and along the length, must be tested. However, the minimum biaxial test specimen size is ~ 10 mm x ~10 mm, therefore, the spatial resolution of the regional material properties that can be measured in this way, is relatively poor. Another approach which we plan to take in the future is to use imaging techniques such as multi-photon microscopy to quantify the spatially varying fiber architecture throughout a tissue sample. Then these experimentally-derived statistical fiber distributions could be incorporated into the computational models to more accurately represent the tissue heterogeneity.

Although the presence of residual stress in arteries is well known [32], residual stress was ignored in the AA FE models of Chapter 3. In a residually stressed artery, the inner wall is initially under compression, while the outer wall is under tension. Somewhere through the wall thickness the residual stress is zero, this location is referred to as the "neutral axis". The experimental and simulation results presented in Chapter 3, thus, represent the vessel neutral axis response. Exclusion of the residual stress could have a significant impact on the transmural wall stresses, but is not thought to affect the neutral axis response. This is why 2D shell elements, representing neutral axis responses, rather than 3D brick elements were used to construct the FE models. It has been proposed that the residual stress develops due to differential growth rates of the individual tissue layers [93]. Thus, in the future, we may use a growth and remodeling framework to incorporate residual stress [327] in our computational models by prescribing differential growth rates to the individual tissues layers.

Furthermore, fluid flow was not considered in either the AA (Chapter 3) or BHV (Chapter 4) computational models. The loading acting on the AA wall and BHV leaflets was simplified and prescribed as a uniform quasi-static pressure; thus, a purely structural approach was taken. Fluid flow induced shear stresses are thought to play an important role in the development of aortic aneurysm and dissection. For the purpose of optimizing BHV design, including the fluid flow may not be necessary, because different valve designs can be assessed in a side-by-side manner under the same loading condition so the optimal design can be determined; however, experimental AWT methods would still be necessary to evaluate the effect of dynamic loading on the computationally-optimized design. In the future, the theoretical and theoretical framework of Chapter 2 could be

used in fluid-structure interaction simulations to investigate the effects of more physiologically relevant loading conditions on aging and fatigue damage of soft tissues.

Finally, the combined effect of tissue softening and permanent set over cycling created numerical instabilities in the simulations, particularly in simulations, where damage was accumulating at an accelerated rate, and was highly concentrated. At these damage concentration zones, adjacent elements may have very different D_s and $\boldsymbol{D_{ps}}$ values which creates discontinuities in the material properties and affects numerical convergence. For this reason, it is often difficult to simulate tissue aging and fatigue damage to the point of failure. Currently, this can only be achieved when the incremental damage per cycle is low and the damage pattern is relatively homogeneous. In the future, the model could be implemented in an explicit solver to potentially improve numerical convergence; however, at this time, an implicit code is needed to accurately simulate the tissue fatigue response.

5.3.3 Evaluation of ascending aorta aneurysm rupture risk over time

The AA aging model presented in Chapter 3 is mainly limited by the available experimental data. The sample sizes for the *in vitro* mechanical tests were relatively small: a larger sample size would provide more conclusive results, and help with the constitutive modeling. Given that the 50-59 year old *in vivo* AA properties already exhibited deteriorated mechanics compared to patients below 50 years old, the initial parameters used in the AA aging constitutive model should be for patients younger than 50; however, because there is no such biaxial data available for younger patients, we used the 50-59 year old response as the initial property. Quantifying the failure properties of human AA tissues at various ages is particularly important for refining the ψ_{max_m} and

ψ_{max_f} parameters. Nevertheless, ultimately our motivation for developing a time-dependent AA modeling framework is to develop a computational tool to predict ascending aorta aneurysm (**AsAA**) rupture risk over time. Through this initial study, we have shown that the constitutive framework can capture age-related AA changes thus, upon the availability of AsAA tissue property data at various states of disease progression, the model parameters could be retuned in the future.

Aortic aneurysms present significant clinical risk as 50% of untreated aortic aneurysms will rupture within 1 year [194]. AsAA rupture is a catastrophic event with an estimated mortality rate of up to 90% [328]. AsAA rupture is preventable by elective surgical repair which is typically recommended for patients with an AsAA dilated to 55 mm or greater [201, 226]. However, the overall AsAA diameter may not accurately reflect a patient's risk [201, 329, 330]: small aneurysms (< 45 mm) have been known to rupture [201]. Ultimately, AsAA rupture is a mechanical event occurring when the vessel wall stress exceeds the strength of the tissue. For this reason, attention has turned towards biomechanical analyses to better understand the underlying mechanisms governing AsAA pathogenesis [71-77, 331].

In an additional study from our group [332] (see Appendix A), the tissue elastic and failure strength properties were characterized for AsAA tissues resected from patients undergoing elective AsAA repair. Patients with concomitant bicuspid aortic valve (**BAV**) and bovine aortic arch (**BAA**) were studied specifically to gain a better understanding of why these patients may be more susceptible to AsAA and dissection [333-335]. BAV and BAA are common congenital malformations of the aortic anatomy. In BAV, the aortic valve is formed with only two leaflets rather than the typical three,

and in BAA the innominate and left carotid arteries originate from a common stem off the aortic arch rather than distinct branches as in most patients. The mechanical testing data was used to analytically predict the AsAA wall stresses and rupture criteria [331], i.e. AsAA diameter and blood pressure to induce rupture, for each patient in a follow-up study (see Appendix B). Through this analysis, decreased AsAA tissue compliance in addition to increased wall tension was identified as a potential marker for rupture risk. A limitation of the analytical method [331] was that an idealized cylindrical AsAA geometry was assumed and thus the effect of the patient's specific AsAA geometry on the vessel wall stress was not taken into account. This analysis also did not account for the time-dependent material property changes of AsAAs. Therefore, the timing of adverse events could not be predicted.

Therefore, we hope to adapt the phenomenological human AA aging model developed in Chapter 3 of this thesis to describe the progression of AsAA in the future. We recently developed a method to simulate AsAA rupture using FE in order to estimate the blood pressure needed to rupture the vessel. Representative simulation results are shown in Figure 5.1. The ultimate goal of this research is to develop a computational tool that can be used to evaluate a patient's risk of rupture over time. Currently, we can only assess a patients risk at the time of evaluation. Thus, the time-dependent inelastic AsAA tissue properties must be integrated into these computational models. Such a computational tool would facilitate timely surgical intervention and improve AsAA patient outcomes. In order to do this, the AA aging model parameters must be recalibrated for AsAA tissues. This will require additional *in vitro* mechanical testing of AsAA samples following the methods in Appendix A for tissues at different stages of

disease. It will also require long-term follow-up clinical image data for AsAA patients in order to measure the changes in the *in vivo* structural properties over time per the methods in section 3.2.2. This data would then be used in part to calibrate the time-dependent inelastic model parameters and in part to validate the simulation predictions.

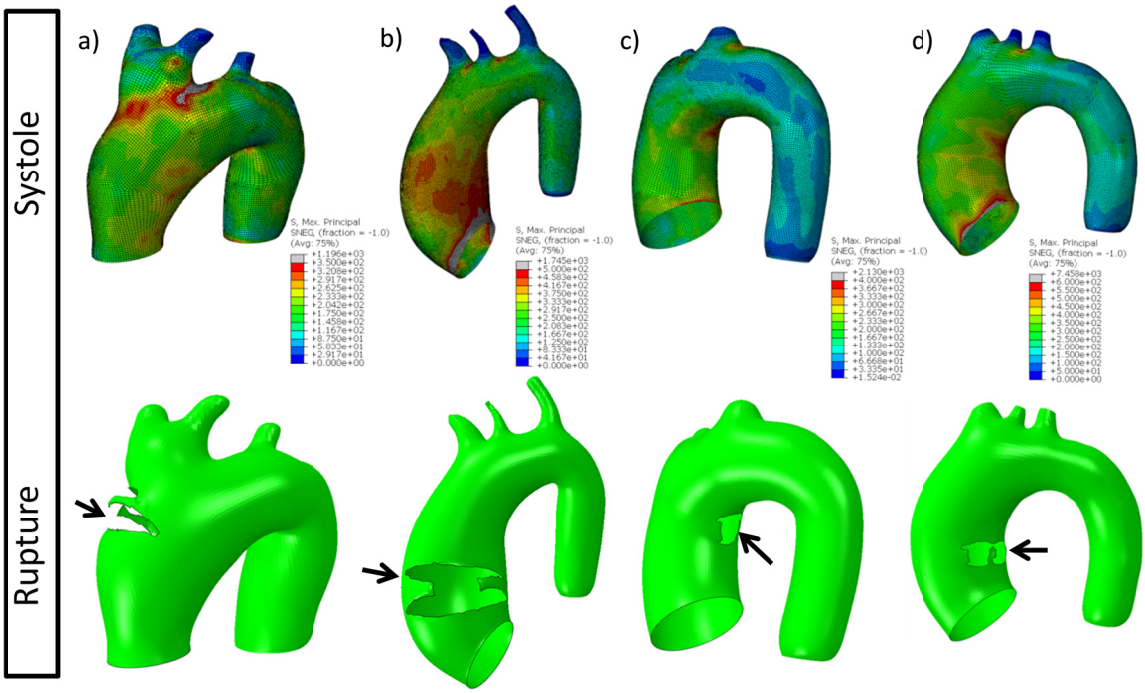

Figure 5.1 Representative patient-specific AsAA FE results. a) Patient 1 results, representing essentially no risk, showing rupture on the outer curvature at a pressure of $14xP_{sys}$. b) Patient 2 results, representing low risk, showing rupture on the anterior side at a pressure of $6xP_{sys}$. c) Patient 3 results, representing moderate risk, showing rupture on the outer curvature at a pressure of $3xP_{sys}$. d) Patient 4 results, representing high risk, showing rupture on the inner curvature at a pressure of $1xP_{sys}$. The black arrows indicate the rupture location.

5.3.4 Experimental characterization of bioprosthetic heart valve tissue fatigue response

At this time, there is not sufficient experimental data to properly calibrate the GLBP fatigue damage model developed in Chapter 4. The GLBP fatigue damage model parameters presented in this thesis were fit to experimental data at one set peak equivalent strain [131]. The dependence of the peak equivalent strain on the fatigue-

induced softening and permanent set is unknown. A more comprehensive data set is necessary to determine the true unique fatigue model parameters to capture the fatigued response of GLBP. Through parametric studies we investigated the relative durability of BHVs comprised with GLBP leaflets in Chapter 4 [132, 133], but the timing of fatigue events is unknown. Proper calibration of the models requires extensive mechanical and structural analysis of GLBP tissues at various fatigue states. GLBP tissues must be fatigued under various loading magnitudes for various numbers of cycles in order to generate the needed data, as described in section 2.2.11. Thus, significant future effort will be dedicated to collecting and modeling experimental GLBP fatigue test data.

5.3.5 Computational based design optimization of bioprosthetic heart valves

Once the GLBP fatigue damage model has been properly calibrated, we hope to use it to perform computational BHV fatigue analyses, which can be provide a fully quantitative analysis of specific design factors on the BHV durability to facilitate durable design. First, the computational models developed in Chapter 4 should be validated through comparison with experimental data. This would require testing real valve prototypes using AWT and measuring the leaflet strain under static pressurization per Sun et al. [81] at various fatigue states for comparison with the computational results. Once validated, this computational approach for valve durability analysis could serve as a prerequisite to AWT testing to dramatically speed up the design cycle time.

One significant upcoming application will be the design of durable next generation transcatheter heart valves. Our simulation results indicate that TAV durability can be expected to be reduced compared to SAVs even in the nominal circular deployment configuration, and worse still in the under-expanded configuration (Chapter

4). With the growing interest in ViV procedures and transcatheter mitral replacement, optimizing transcatheter heart valve durability will be an important area of future research. An additional advantage of a computational durability method is that it allows for patient-specific analyses. For instance, the BHV fatigue model developed in this study could potentially be coupled with patient-specific TAVR deployment computational simulations [79, 123] to assess TAV durability in a particular patient, which could be compromised due to the patient's unique aortic characteristics, or in the case of ViV - their existing BHV device design.

5.4 Conclusions

The mechanical properties of soft tissues are not stagnant. They evolve over time, due to repetitive loading, the aging process, and disease progression. Over the course of a life cycle, these changes manifest to reduce the functional capacity of native tissues and the durability of non-viable tissue-derived devices. The numerical methods developed in this thesis aim to model and predict tissue material property changes over time, and how these changes impact overall tissue or tissue-derived device function. It is hoped that such tools could be used to determine patients at risk, and plan timely interventions to avoid catastrophic tissue rupture or device failure. This thesis work represents the first step in developing such tools.

APPENDIX A – BIOMECHANICAL CHARACTERIZATION OF ASCENDING AORTIC ANEURYSM WITH CONCOMITANT BICUSPID AORTIC VALVE AND BOVINE AORTIC ARCH

A.1 INTRODUCTION

Thoracic aorta aneurysms represent the 18th most common cause of death in adults [201]. Approximately 6-9% of people age 65 and older in the Western world have an aortic aneurysm [194]. There are a number of conditions that have been linked to aortic dilation including Marfan syndrome, Loeys-Dietz syndrome, Ehlers-Danlos syndrome type IV, arterial tortuosity syndrome, autosomal dominant polycystic kidney disease, and autosomal recessive cutis laxa type 1 [328]. In addition to these disorders there appears to be a strong genetic link associated with aortic aneurysms, as up to 20% of patients referred for thoracic aortic aneurysm or dissection have family members with the same condition [201].

The development of ascending aortic aneurysms (**AsAA**) may also be linked to anatomical anomalies. It is well known that patients with a bicuspid aortic valve (**BAV**, a condition in which two of the three aortic leaflets fuse together) are more likely to develop AsAA than patients with a normal, tricuspid aortic valve. In the United States, approximately four million people harbor a BAV, making BAV the most common congenital malformation [335]. Approximately 50% of BAV patients will develop an AsAA and 5% will experience aortic dissection in their lifetime [336]. There is some debate on whether the high prevalence of ascending aortic aneurysms in BAV patients is

due to abnormal aortic hemodynamic stresses or intrinsic material property differences rendering the aortic wall weaker than in normal patients [337-339] .

More recently, a link between bovine aortic arch anatomy and thoracic aortic aneurysms has also been suggested [334]. In the majority of patients (74%), there are three great vessels branching from the aortic arch: the innominate artery, the left carotid artery, and the left subclavian artery [340]. However, there are many other possible anatomic configurations of the aortic arch – the most common being the "bovine aortic arch" (**BAA**) configuration, in which the innominate and the left carotid arteries originate from a common stem off the aortic arch [340]. Although, BAA is generally thought to be a benign anatomical difference, recent research shows the incidence of BAA dissection is significantly higher among patients with an AsAA than among the general population [334]. Again, it is unclear why BAA patients may be more susceptible to AsAA formation. This may be due to altered hemodynamics or possible innate aortic tissue property differences in these patients.

Rupture of the aortic wall is generally accepted as mechanical failure of the vessel due to a combination of excessive hemodynamic forces [218, 237, 328, 341] and degeneration of the medial wall [337, 339, 342-345]. The microstructural components, mainly elastin, collagen fibers and smooth muscle cells (SMCs) play an important role in maintaining proper structure and function of the aortic wall. Damage to the elastic fibers and aortic dilation might cause increased wall stiffness and stress. Eventually, acute aortic dissection and rupture can occur in response to certain dramatic events such as a spike in blood pressure during intense physical or emotional exertion [201]. Therefore, an

understanding of the elastic properties and the microstructure of the vessel wall is important in predicting the risk of wall rupture.

The goal of this study was to characterize the mechanical and failure properties of non-dissecting AsAA patients without a BAV or a BAA and compare with those patients co-harboring a BAV or a BAA. Histological analysis of the wall microstructure of the three tissue groups was also performed. A thorough quantification of the AsAA tissue properties for these three patient groups may offer insight into the underlying mechanisms of AsAA development in these patients.

A.2 MATERIALS AND METHODS

A.2.1 Clinical data and aortic specimens

Aortic specimens were obtained from a total of 55 patients who underwent elective ascending aortic aneurysm surgery at Yale-New Haven Hospital between December 2008 and September 2010. Patients who experienced aortic dissection prior to surgery were excluded from the study. Upon perioperative harvest, the specimens were fresh frozen and stored in a -80°C freezer, see Figure A.1. Once the tissue specimens were transported to the lab, they were cryopreserved [346] at -80°C prior to mechanical testing. The use of human tissues in this study was approved by the Research Compliance Office of the University of Connecticut. The patients were divided into three groups: AsAA - patients without BAV or BAA (n = 20), BAV – patients with BAV but without BAA (n = 20), and BAA – patients without BAV but with BAA (n = 15).

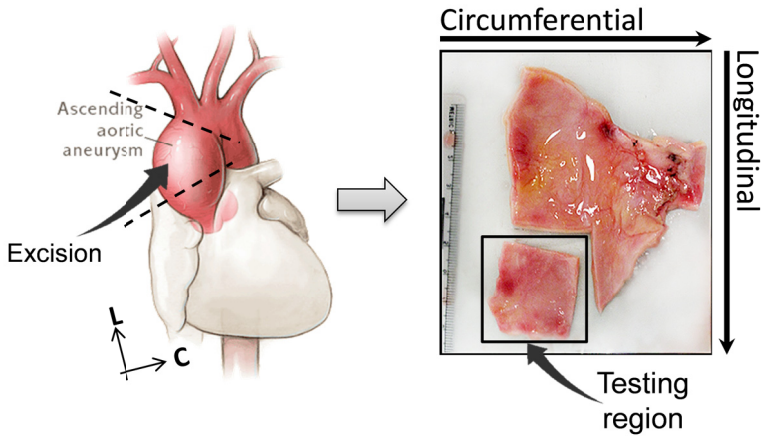

Figure A.1 Illustration of a representative testing sample and its orientation with respect to the excising region of the ascending aortic aneurysm. C – circumferential, L – longitudinal.

A.2.2 Mechanical Tests

A.2.2.1 Planar biaxial mechanical test

Frozen samples were submerged in a 37˚C water bath until totally defrosted, following the two-stage slow thawing method to remove the cryopreserving agent [346]. The tissue thickness was measured at six regions with a thickness gauge (Mitutoyo, Model 7301) and the average value was recorded. Each specimen was then biaxially tested according to the methods previously presented [347]. Briefly, all specimens were trimmed into square specimens with a side length of ~20 - 25 mm and mounted in a trampoline fashion, with the specimen circumferential (**CIRC**) and longitudinal (**LONG**) directions aligned with the primary axes of the biaxial test fixture. All specimens were tested in a Ca^{2+}-free and glucose-free Tyrode solution (mM: NaCl 136.9, KCl 2.7, $MgCl_2$ 1.05, $NaHCO_3$ 11.9, $NaHPO_4$ 0.47, EGTA 2.0, and 0.1M papaverine) at 37°C. A tension-controlled test protocol was utilized [82] and converted to the first Piola Kirchhoff stress, P, wherein the ratio of CIRC (11) to LONG (22) that is P_{11} : P_{22} was kept constant with

the shear terms $P_{12} = P_{21} = 0$. All specimens were stretched to a maximum membrane stress value of 120 kPa (or ~300g), which is the approximate tension in a thin cylindrical tube 2 cm in diameter and 2 mm in thickness at 120 mmHg [348]. Preconditioning was performed to minimize tissue hysteresis. Each tissue specimen was preconditioned for at least 40 continuous cycles with $P_{11} : P_{22} = 1 : 1$. Seven successive protocols were performed using ratios $P_{11} : P_{22} = 1 : 0.3$, 1 : 0.5, 1 : 0.75, 1 : 1, 0.75 : 1, 0.5 : 1, and 0.3 : 1. This range was chosen for extensive coverage of the in-plane stress state [82]. The in-plane Green strain tensor **E** was calculated from the deformation gradient, **F**, using $\mathbf{E} = \frac{1}{2}(\mathbf{F}^T\mathbf{F} - 1)$. The tensor **P** was calculated using $\mathbf{P} = \mathbf{f}/(T\mathbf{L})$ where **f** are the current measured loads in each direction, T is the initial thickness of the specimen, and **L** are the unloaded reference specimen dimensions in the CIRC and LONG directions. The second Piola-Kirchhoff stress tensor **S** was obtained using $\mathbf{S} = \mathbf{F}^{-1}\mathbf{P}$.

The tissue stiffness was quantified by means of the secant modulus at both the low (60 kPa) and high membrane stress (120 kPa) regions under the equibiaxial loading protocol ($P_{11} : P_{22} = 1 : 1$). The 60 and 120 kPa stress values correspond to the approximate hoop stresses, calculated from Laplace's law, for the dilated aorta with a diameter of 5 cm and wall thickness of 2 mm under 40 and 80 mmHg pressure respectively. Due to the limitation of the biaxial test set-up, i.e. using hooks to apply loads, the tissues could not be loaded to the stress level corresponding to a systolic pressure of 120 mmHg without damaging the specimens. The extensibility of the samples was calculated via the areal strain equation, $e = \lambda_{11,max}\,\lambda_{22,max} - 1$, where $\lambda_{11,max}$ and $\lambda_{22,max}$ are the circumferential and longitudinal peak stretch values from the equi-biaxial protocol, respectively. The degree of anisotropy (DA) was analyzed using the

ratio of peak Green strains DA = $E_{11,max}/E_{22,max}$. A DA value of 1 indicates an isotropic tissue response, whereas other values represent various degrees of anisotropy.

A.2.2.2 Uniaxial failure test

Following the biaxial test, each specimen was cut into strips about 15 mm x 5 mm in both the circumferential and longitudinal directions. In some cases only one uniaxial specimen was prepared in either the circumferential or the longitudinal direction due to limited tissue size. The specimens were tested with a Tinius Olsen uniaxial machine (Horsham, PA). The force and deformation in terms of stretch were measured continuously as the specimen was loaded to failure. The ultimate tensile strain ($\mathbf{UT_E}$) and strength ($\mathbf{UT_S}$) were determined from the maximum tension which correlated to the complete rupture of the specimen.

A.2.2.3 Histological analysis

A total of 10 samples in each group were selected for qualitative histological analysis of the medial degenerative characteristics of aortic aneurysm. The central region of each specimen was cut out and fixed in 10% formalin for 24 hours prior to histological processing. After a series of dehydration steps by varying alcohol concentrations, samples were embedded in paraffin, sectioned at 5 μm in thickness and then mounted on microscope slides. After deparaffinization, slides were stained with Verhoeff Van-Gieson (**VVG**) and Movat pentachrome stains. The VVG stain distinguishes elastic fibers as black, collagen fibers as red, and muscle fibers as a duller red or light brown color, and Movat stain is for visualization of blue mucoid material. The hematoxyline and eosin (**H&E**) stain was also used to visualize the nuclei of SMCs. Qualitative analysis of degenerative features of the aneurysmal tissues was performed through images obtained

from an Olympus U-TVO.5xC digital camera coupled to an Olympus BX40 light microscope.

The tissue microstructure was quantitatively assessed from a histological section from the central testing region. The thickness measurements of each layer and the area fractions of elastin and collagen fibers were measured from the 2D images of histological slides using ImageJ software (Bethesda, MD). The intima, media and adventitial layer thicknesses were measured at 5 locations along the specimen length and the average values were obtained. The percent thickness of each layer was calculated relative to the overall wall thickness. The elastin, collagen and SMC/matrix components of the media layer were quantified using the color segmentation method by splitting the color channels and thresholds. The three fields of view (**FOV**) with equivalent area across the media thickness were selected (per 2D image). The area fractions of each component were then obtained by averaging the relative content measured from the three selected FOVs.

A.2.2.4 *Statistical analyses*

All measurements are presented as a mean ± standard deviation. The analysis of variance (**ANOVA**) test followed by the Holm-Sidak test and the Dunn's Method test were used to compare between groups. The Student's t-test was used to determine significant differences between the mean values for two variables. For comparison between circumferential and longitudinal responses, the paired Student's t-test was employed. Non-parametric tests, including the Wilcoxon signed-rank test and Mann-Whitney rank sum test, were utilized for non-normally distributed sample groups. Outliers were identified and removed when necessary for comparison across groups. Correlation was determined using the Pearson's correlation coefficient (r) and the non-

parametric Spearman Rank Order. A probability, p-value, less than 0.05 was considered to indicate a statistically significant difference between the groups, with a $p < 0.001$ indicating high statistical significance. Statistical analyses were performed using SigmaPlot (V11.0, Systat Software Inc., San Jose, CA).

A.3 RESULTS

A.3.1.1 Sample characteristics

Table A-1 summarizes the clinical patient data. There were no significant differences in age ($p = 0.417$), diameter ($p = 0.877$) or Aortic Size Index (ASI) [201] ($p = 0.402$) between the three patient groups. On average, the diameters were below 5.5 mm, and the ASI values were below the moderate risk level for all groups (see [201] for the ASI risk level classification). The percentages of hypertensive patients (systolic pressure higher than 140 mmHg) for AsAA patients was 20% (n = 4), 25% (n = 5) for BAV patients and 13% (n = 2) for BAA patients. The mean thickness of the BAV samples (1.88 ± 0.20 mm) was significantly lower than that of the AsAA samples (2.09 ± 0.35 mm, $p = 0.021$), but there was no difference with respect to the BAA samples (2.18 ± 0.55 mm, $p = 0.072$). The mean thickness of the ASAA and BAA samples were not significantly different, $p = 0.566$. Significant positive correlation between thickness and diameter was observed in the BAV group, $r = 0.52$, $p = 0.023$ (Figure A.2a). No strong correlation was found in the AsAA and BAA patient groups. From Figure A.2b, it appears that thickness and ASI increase with age, however, the correlation coefficients were not significant.

Table A-1 Summary of patients' information.

	ASAA	BAV	BAA	p-value
All age (n)	59.45 ± 7.86 (20)	55 ± 9.65 (20)	58.07 ± 14.70 (15)	0.417
M:F	3:1	3:1	11:4	-
Diameter (mm)	4.94 ± 0.48	5.01 ± 0.50	4.93 ± 0.53	0.877
ASI	2.51 ± 0.58	2.54 ± 0.35	2.39 ± 0.37	0.402
Hypertension (n,%)	4 (20%)	5 (25%)	2 (13%)	-

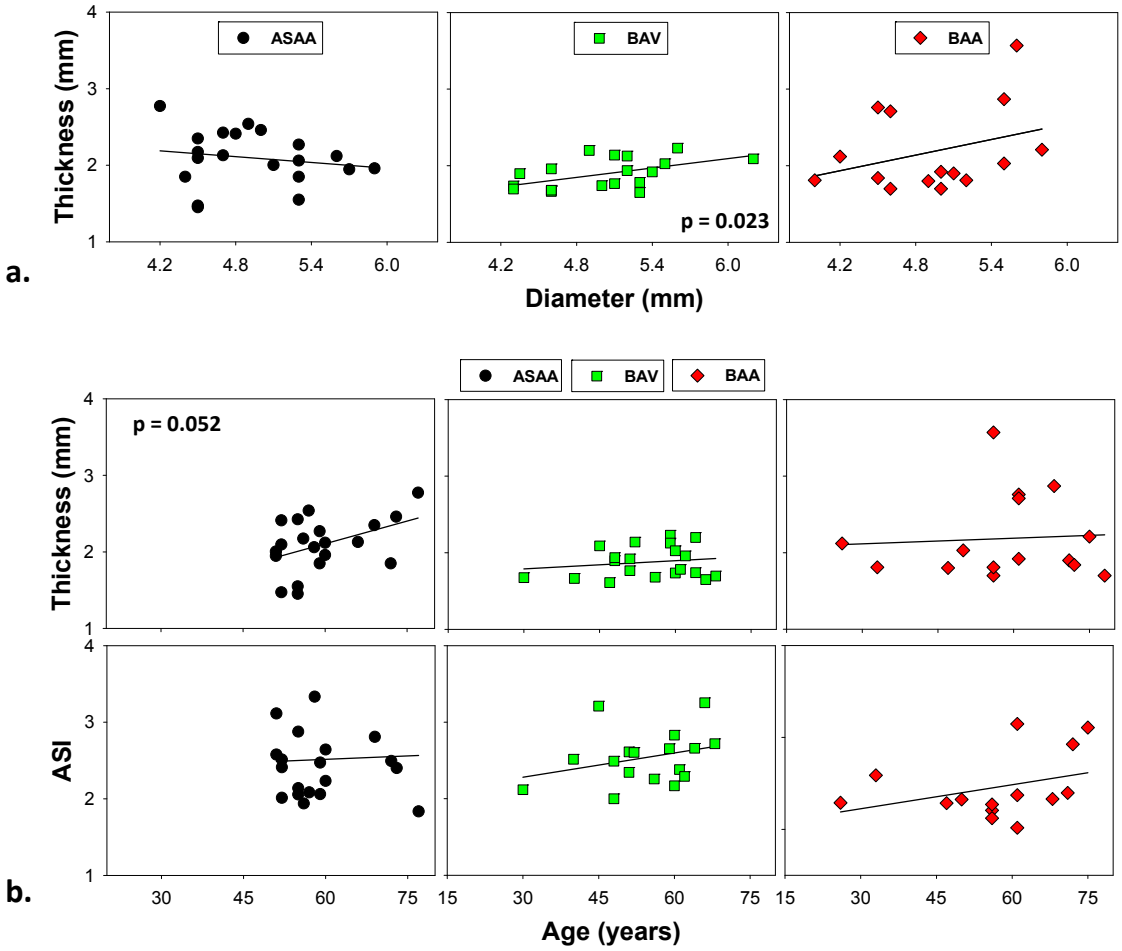

Figure A.2 (a) Diameter and thickness relationship of ASAA, BAV and BAA patient groups, the BAV group showed a strong correlation (p = 0.02); (b) a consistent trend of increasing thickness and ASI with increasing age in all groups, the ASAA group showed a near significant correlation between thickness and age (p = 0.052).

A.3.1.2 Biaxial stress-strain responses

The mean equibiaxial stress-strain curves in the CIRC and LONG directions for the three patient groups are shown in Figure A.3. The mean AsAA and BAA curves

exhibited a somewhat nonlinear characteristic upon a peak stress of 120 kPa, with the CIRC direction being stiffer than the LONG direction, while the BAV response was more isotropic and linear. Both directional responses of the BAV group were stiffer than those of the AsAA and BAA groups. The LONG directional responses of AsAA and BAA groups were similar.

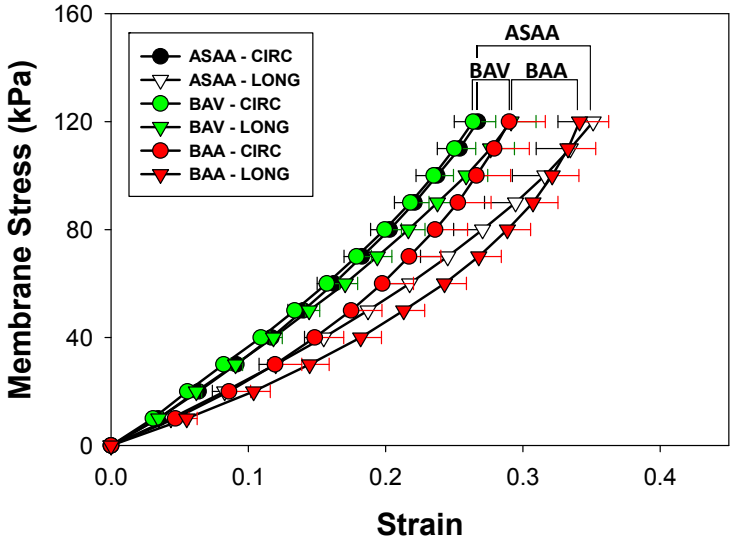

Figure A.3 Mean and standard error equibiaxial stress-strain responses of ASAA, BAV and BAA patient groups in the circumferential (CIRC) and longitudinal (LONG) directions.

A significant difference in tissue stiffness was observed in the LONG direction at 60 kPa membrane stress where the BAV group was significantly stiffer than the AsAA group ($p = 0.024$) and the BAA group ($p < 0.001$), see Figure A.4. A similar trend was observed at 120 kPa between the BAV and AsAA groups ($p = 0.072$) and between the BAV and BAA groups ($p = 0.072$). For the CIRC tissue stiffness, the BAV group showed the highest stiffness compared to the AsAA ($p = 0.473$) and BAA ($p = 0.152$) groups at 60 kPa, but the stiffness values at 120 kPa were similar among all the groups ($p = 0.890$, one-way ANOVA). The CIRC direction was stiffer than the LONG direction for the

AsAA ($p = 0.012$ at 60 kPa, $p = 0.068$ at 120 kPa) and BAA ($p = 0.004$ at 60 kPa, $p = 0.025$ at 120 kPa) samples, but not for the BAV samples ($p = 0.407$ at 60 kPa, $p = 0.744$ at 120 kPa).

The mean areal strain of the BAV samples was significantly less than the AsAA ($p = 0.041$) and BAA ($p = 0.004$) tissues at a low membrane tension, see Figure A.4**c**. The mean DA values of AsAA, BAV, and BAA samples indicated that the BAV specimens were more isotropic than the AsAA and BAA tissue samples, see Figure A.4d.

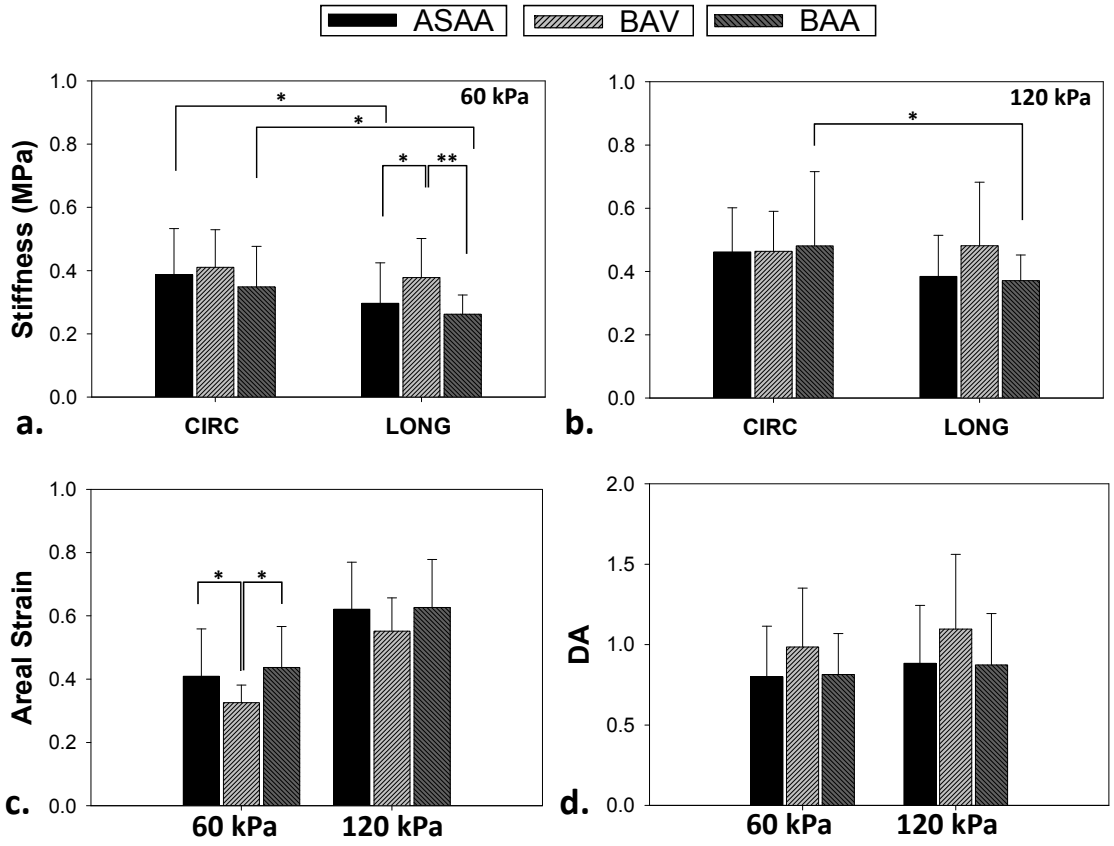

Figure A.4 **(**a) The relationship between age and areal strain at 60 and 120 kPa for AsAA, BAV and BAA patient groups, and (b) a significant negative correlation between ultimate tensile strain and age was observed in the circumferential (CIRC) direction of BAV samples and longitudinal (LONG) direction of BAA samples.

A.3.1.3 Uniaxial mechanical responses

No significant difference in the mean UT_E was found between the CIRC and LONG directions or across the groups (Figure A.5a). The mean CIRC UT_S values were larger than the mean LONG UT_S in all sample groups, but the difference was significant only in the AsAA group ($p = 0.016$). The mean LONG UT_S of the BAV group was significantly higher than the AsAA group ($p = 0.006$) (Figure A.5b).

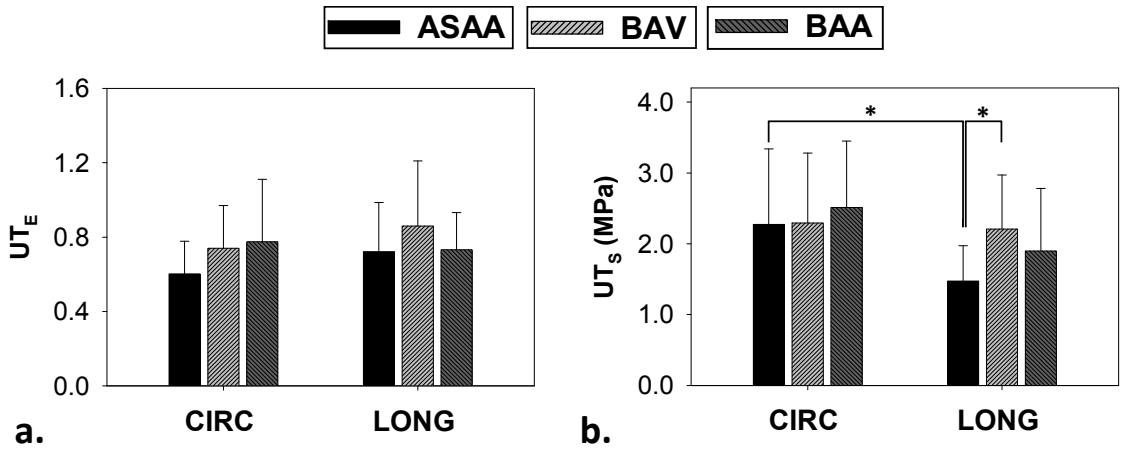

Figure A.5 Comparison of the mean circumferential (CIRC) and longitudinal (LONG) stiffnesses at (a) low (60 kPa) and (b) high (120 kPa) membrane tensions between ASAA, BAV and BAA patient groups; (c) mean extensibility and (d) mean degree of anisotropy (DA) of ASAA, BAV and BAA tissue samples at low and high membrane tensions. (*) indicates a statistical significance with $p < 0.05$, (**) indicates a highly statistical significance with $p < 0.001$. Data presented as mean and standard deviation.

A.3.1.4 Age and mechanical data correlation

No significant correlation was found between age and biaxial mechanical data in all three groups; however, a trend was observed in all groups where the areal strain decreased with age (Figure A.6a). There was no strong correlation between age and uniaxial data for the AsAA group. However, for the BAV group, the ultimate CIRC UT_E significantly decreased with age, $r = -0.630$, $p = 0.003$ (Figure A.6b). For the BAA group,

the UT_E decreased significantly with age in the LONG direction (r = -0.622, p = 0.048) but not in the CIRC direction (p = 0.060).

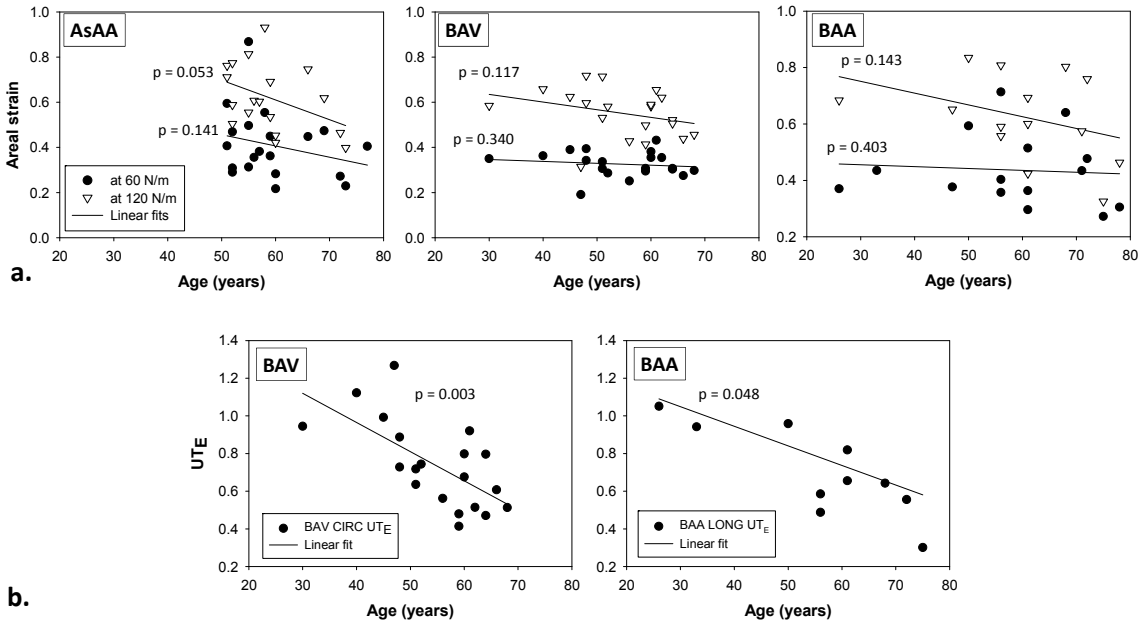

Figure A.6 (a) The relationship between age and areal strain at 60 and 120 kPa for AsAA, BAV and BAA patient groups, and (b) a significant negative correlation between ultimate tensile strain and age was observed in the circumferential (CIRC) direction of BAV samples and longitudinal (LONG) direction of BAA samples.

A.3.1.5 Hypertension

The LONG stiffness of the AsAA hypertensive group was significantly higher than that of the normotensive, with p = 0.017 at 60 kPa (see Table A-2). Similarly, a significant difference between hypertensive and normotensive BAA groups was only observed in the LONG stiffness at 60 kPa (p = 0.049). Although statistical significance was not achieved, in general, the mean directional stiffness of hypertensive groups was greater than the normotensive groups (see Table A-2) for both the AsAA and BAA groups. Although BAV samples did have on average the highest stiffness at both low and high membrane tensions, there was no significant difference between hypertensive and

normotensive properties. This could be due to the highly variable data and small sample sizes. Comparison between the hypertensive and normotensive failure properties were not conducted due to small sample sizes.

Table A-2 Comparison of stiffness at 60 kPa tension between hypertensive and normotensive patients among AsAA, BAV and BAA patient groups.

		Stiffness at 60 kPa				
		n	HTN	*n*	NTN	*p*
ASAA	*Circ*	3	453.45 ± 193.78	17	269.54 ± 96.30	0.427
	Long	3	467.65 ± 275.42	17	369.89 ± 89.00	0.017*
BAV	*Circ*	5	375.88 ± 117.39	15	422.16 ± 121.27	0.466
	Long	5	316.96 ± 294.62	15	345.62 ± 305.16	0.513
BAA	*Circ*	2	379.42 ± 55.56	13	344.48 ± 136.12	0.732
	Long	2	339.94 ± 43.60	13	250.15 ± 55.19	0.049*

CIRC – Circumferential, LONG – Longitudinal, HTN – Hypertensive, NTN – Normotensive. (*) indicates a statistical significance.

A.3.1.6 Histology

The microstructure of the aneurysmal aortic tissues from 10 samples in each group was qualitatively analyzed from the two-dimensional images. Histologic changes including cystic medial necrosis (**CMN**) or medial degeneration often occur in the AsAA medial wall. Within the degenerated region, disruption and disorganization of the elastic lamella resulting in collapsed lamella and elastic fiber fragmentation, focal loss of smooth muscle cell (**SMC**) and accumulation of mucoid material and/or the presence of cysts within basophilic substances are typically found [349-352].

Figure A.7a shows the circumferential cross section of the aortic wall from a 58-year-old patient with AsAA only. This sample exhibited the histopathologic features of tissue degeneration. According to the grading system by de Sa *et al.* [353], the sample

had a grade 2 or a moderate degree of SMC loss, resulting in several collapsed elastic lamella Figure A.7a, as arrows). Loss of SMCs, indicated by the absence of the cell nuclei (see Figure A.7b), were noted in all samples analyzed. A representative BAV sample from a 56-year-old patient is shown in Figure A.7**c**, where Movat pentachrome stain revealed mucoid accumulation (grade 1 according to [353] or mild) between the elastic lamella (yellow arrows) and smooth muscle cell reorientation (double-head arrow). The most severe (or grade 3 [353]) samples for each group were displayed in Figure A.8. These samples exhibited extensive medial damages including fragmentation and focal loss of elastin fibers and SMCs, increase of ground substances or mucoid materials. Intimal and adventitial thickening of the aorta wall due to fibrosis characterized by an increase in collagen, were also observed. In summary, 20% of both AsAA and BAA samples exhibited severe degeneration, while the remaining samples displayed mild to moderate degeneration. Only one BAV sample (see Figure A.8) displayed signs of severe damage while the majority of samples had only mild to moderate damage. None of the hypertensive AsAA and BAA aortas had any severe medial wall damage, while the severely damaged BAV sample was from a hypertensive patient. No conclusion could be drawn for the hypertension effect since only a small number of hypertensive patients were histologically analyzed.

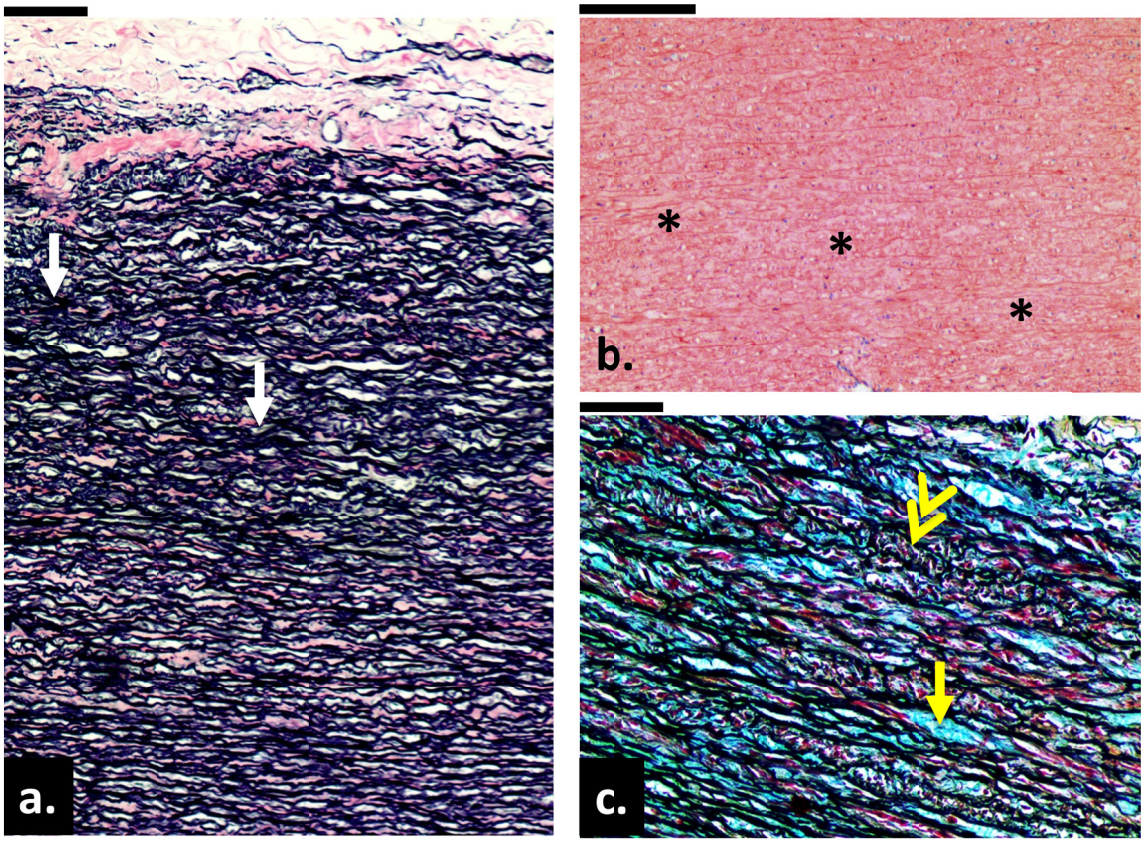

Figure A.7 (a) A circumferential cross section of the aortic wall from a 58-year-old patient with AsAA only. Note the changes in the elastic lamella including collapsed lamella (yellow arrows) and fragmentation of elastic fibers (white arrow). Image was stained with Verhoeff Van-Gieson stain. (b) Evidence of focal loss of SMC cells through loss of cell nuclei (asterisks) in the media layer from an 80-year-old AsAA only patient. (c) A cross section of the aortic wall from a 56-year-old patient with BAV and aortic stenosis. There are evidences of mucoid accumulation in between the elastic lamella (yellow arrow) throughout the media layer and the disorientation of the smooth muscle cells (double-head arrow). Image was stained with Movat pentachrome. (Bar = 200μm)

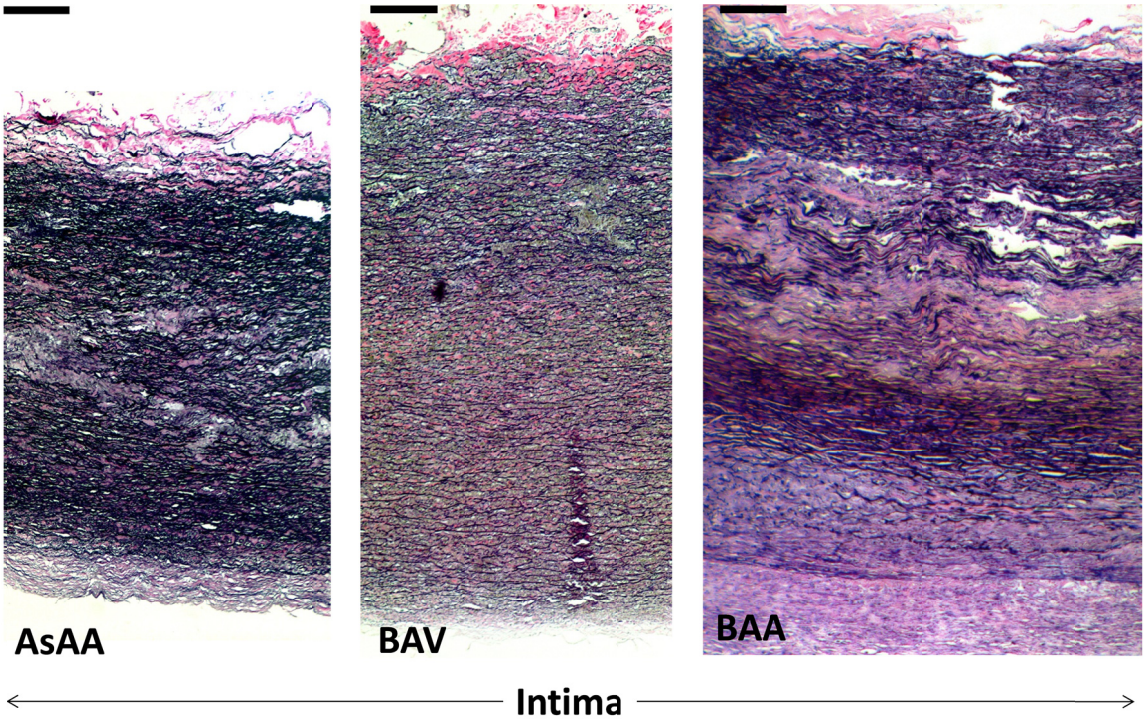

Figure A.8 A circumferential cross section through the thickness of aortic walls from (a) a 52-year-old AsAA patient (b) a 61-year-old BAV patient and (c) a 75-year-old BAA patient. Severe damages of the elastic lamella and intima thickening due to fibrosis were observed in these images. Image was stained with Verhoeff Van-Gieson stain. (Bar = 200μm).

Figure A.9a displays the percentiles of each layer thickness for AsAA, BAV and BAA groups. The BAV specimens displayed a larger media thickness than AsAA and BAA ($p = 0.024$) samples. Conversely, the intima thickness of BAV specimens was significantly thinner than that of the AsAA specimens ($p = 0.045$). Strong correlations between the dilated diameter and BAA media thickness ($r = -0.736$, $p = 0.02$) and BAA intima thickness ($r = 0.728$, $p = 0.02$) were found. The adventitial thickness was similar in all sample groups. Differences between the elastin, collagen and SMC and matrix contents between sample groups were not significant. However, a higher area density of elastin was found in BAA samples compared to AsAA and BAV samples. Less SMC and matrix contents were found in BAA samples.

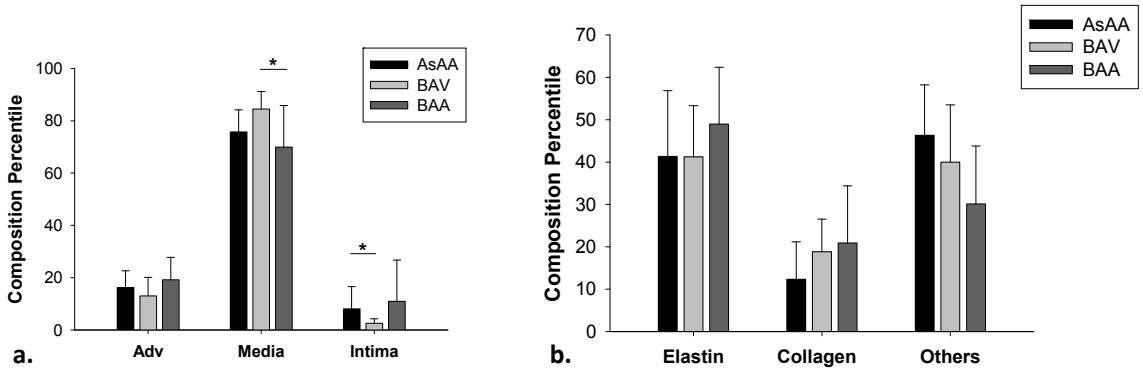

Figure A.9 (a) The percentiles of intima, media and adventitial layers in the AsAA (n = 10), BAV (n = 10) and BAA (n = 9) patient groups, (b) the percentiles of elastin, collagen and SMCs and ground substances in the media layer of each patient group.

A.4 DISCUSSION

In this study, we investigated the mechanical and microstructural properties of aortic tissues from patients harboring ascending aortic aneurysm (AsAA) with and without concomitant bicuspid aortic valve (BAV) or bovine aortic arch (BAA) for comparison across patient groups.

A.4.1 Tissue properties of AsAA

There is limited data on the mechanical properties of the dilated ascending aorta subjected to planar biaxial testing. Choudhury *et al.* [354] performed biaxial mechanical tested in five AsAA samples but only in the circumferential direction. Their mean strain modulus at high stress of about 0.45 MPa was similar to our circumferential AsAA stiffness. Another study was done by Okamoto *et al.* [216] who showed biaxial stress-strain responses for one of their 65 year old AsAA patients from which the moduli were approximately 0.5 MPa in both directions.

The tensile strengths for AsAA samples obtained from uniaxial tensile test were previously reported in the literature. Vorp *et al*. [218] reported the mean tensile strength

of their AsAA samples in the CIRC and LONG directions as 1.18 ± 0.12 and 1.21 ± 0.09 MPa, respectively. Garcia-Herrera *et al.* [219] found the tensile strengths of their AsAA samples to be 1.19 ± 0.13 MPa circumferentially and 0.88 ± 0.12 MPa longitudinally. The mean failure stresses of AsAA specimens found by Iliopoulos *et al.* [237] were about 1.70 and 1.00 MPa in the CIRC and LONG directions, respectively. The mean tensile strengths of our AsAA samples (2.27 and 1.47 MPa, respectively) demonstrated that the tissues were stronger in the CIRC direction but similar in the LONG direction compared to other studies.

A.4.2 Bicuspid aortic valve effect

Overall, our study indicates that aneurysmal BAV tissues were different in both mechanical and structural properties compared to the AsAA and BAA groups. BAV samples were stiffer than the AsAA and BAA samples in both directions. Similarly, Choudhury *et al.* [354] reported in their study that BAV tissues were significantly stiffer than AsAA tissues at low strain, and Duprey *et al.* [227] also found significantly higher stiffness in the CIRC BAV response compared to their AsAA group.

BAV samples were also found to be isotropic than AsAA and BAA samples with a mean degree of anisotropy approaching 1 (0.99 ± 0.37 and 1.10 ± 0.47, $p = 0.756$, at low and high membrane stresses, respectively). Our findings are in agreement with Choudhury *et al.* and Okamoto *et al.* [216] who report no significant anisotropy in BAV samples. However, Duprey *et al.* [227] found anisotropy in the uniaxial responses of BAV tissues with the CIRC being stiffer than the LONG direction, and Garcia-Herrera *et al.* [219] reported a statistically significant difference in the directional responses in their BAV samples. Both Duprey *et al.* and Garcia-Herrera *et al.* determined BAV tissue

anisotropy from uniaxial tensile tests rather than bixaxial tests which might explain their opposing findings.

The altered mechanical properties of the BAV tissues may also be explained in part by differences in the underlying microstructure. The overall thickness of the BAV samples was found to be smallest compared to other groups, which could possibly contribute to its relatively high stiffness. However, the BAV media was thicker than that of AsAA and BAA samples. We found positive correlation between diameter and thickness in BAV tissues, which may indicate tissue remodeling to reduce the wall stress. Despite having the highest medial thickness among the sample groups, the BAV samples had the lowest elastin content, which correlates well with other reports of less elastin in the BAV aortic wall compared to that associated with normal tricuspid valves [350, 354]. The lower elastin content along with the evidence of elastin fragmentation in the BAV samples may be the result of an underlying pathology in BAV aortas and may explain the loss of extensibility at low load.

Interestingly, the tensile failure properties of BAV samples were similar to those of the AsAA and BAA groups despite the differences in mechanical properties and tissue structure. Although, patients with BAV are more likely to experience aortic dissection and rupture during their lifetimes [355], our tensile failure test results suggest that the strength of AsAA tissue is comparable in patients with and without BAV. This is in line with the conclusion of Tadros *et al.* [350] that BAV-associated ascending aortic aneurysms dissect and rupture at a size comparable to that of aneurysms due to other etiologies. Hence, higher risk of dissection and rupture in BAV patients may be due to the higher prevalence and earlier onset age of aortic dilation in these patients [350].

A.4.2.1 Bovine aortic arch effect

The epidemiological linkage between aneurysm and BAA was investigated by Malone et al [356] who found a statistically strong association between BAA and AsAA in patients over 70 years old and concluded that BAA should be considered a potential risk factor for thoracic aortic aneurysm. To our knowledge, this is the first study aimed to characterize the mechanical properties of aneurysmal aortic tissues in BAA patients. The BAA tissues were anisotropic with the CIRC direction being significantly stiffer than the LONG direction. We found similar mechanical and failure properties between the AsAA and BAA samples. These results suggest that ascending aortic aneurysm may occur in both patient groups as a result of the same underlying pathology. However, the underlying trigger for ascending aortic dilation in BAA patients remains unknown.

The quantitative histological analyses showed no significant differences in medial thickness and fiber composition between BAA and AsAA tissues; however, the BAA samples had the highest elastin and collagen contents. The BAA samples also had the highest intimal and adventitial thicknesses. The medial layer, in contrast, was smallest among the groups. Moreover, there was a strong negative correlation between the medial thickness and the overall diameter, and a strong positive correlation between the intimal thickness and diameter. It may be necessary to test and compare the non-aneurysmal ascending aorta tissues in BAA and healthy patients to determine whether BAA tissues are innately different than normal.

A.4.2.2 Aging effect

Aging arteries progressively stiffen and dilate [160]. As expected, we found a consistent trend of decreasing areal strain with increasing patient age across the groups.

The ultimate tensile strength of BAV and BAA tissues were also found to decrease with age. Note that the comparatively narrow age range of the AsAA patient group may have prevented us from determining an age-related decline in strength.

A.4.2.3 Hypertension effect

Prolonged hypertension generally provokes medial degeneration [357, 358] and worsen mechanical properties of the vessel wall [359, 360]. We did not see a distinct difference in the medial wall of hypertensive patients in any group. However, there was a significant increase in tissue stiffness in the longitudinal direction in hypertensive AsAA and BAA patients compared to normotensive AsAA and BAA patients. There was no difference in stiffness between the hypertensive and normotensive BAV patients. Currently there is some debate on the relationship between increased aortic stiffness and blood pressure: it may be a positive feedback relationship. It is suggested that the stiffening and dilation of the aorta act to increase systolic and decrease diastolic blood pressure; however, the initial cause of tissue stiffening may be increased systolic pressure [235]. There seems to be a linkage between severity of aortic stenosis and hypertension [361] but it cannot be determined in this study because only a small number of patients in each group acquired aortic stenosis ($n < 3$). There was no difference in stiffness between the hypertensive and normotensive BAV patients. Again, larger sample sizes are needed to achieve a desired level of statistical power for detecting any pathological effect on the aortic mechanical properties.

A.4.2.4 Limitation and future study

The comparison between aneurysmal tissues would be more accurate if the tissue was tested fresh, however, fresh human aneurysmal tissue is difficult to obtain. In this

study, we utilized the cryopreservation technique for tissue storage which has been shown to minimize damage to the elastic components of blood vessels [346]. Our results were comparable to the results reported in the literature for tissue mechanics and strength as mentioned earlier. A dog-bone shaped sample is recommended for minimizing and homogenizing stress at the middle section. However, due to limited sample size, we were not able to cut the samples into a dog-bone shape, which might slightly affect our calculation. Other limitations of this study include the small sample sizes. Degenerative changes in the aortic wall involve complex and variable processes, and thus a larger sample size is required to determine the mechanisms of disease and its correlation with various clinical entities. A larger sample size and an extended age range could possibly demonstrate some age related differences between the groups. Other methods have been implemented for studying aneurysmal aorta tissues [362-364] where an initial tear was created in the intima layer and either force or pressure was applied to study the dissection propagation as hemodynamic forces increased. However, we did not focus on the initial tear or the dissection parameter in this study; instead we compared the tissue ultimate tensile strength between the three groups. Additionally, the quantitative analyses of specific layer thickness did not account for shrinkage after histological processing. The fiber contents were approximated based on the 2-D cross section areas at the central testing regions, thus did not represent the volume content.

We did see subtle differences in the structural layers and fiber composition between groups. Future work may include mechanical tests of each layer of the aortic wall which could possibly reveal some differences between the patient groups. Moreover, the linkages between the extracellular matrix proteins, wall remodeling and tissue

mechanics in these samples require a parallel comprehensive bio-molecular study, which may help to provide a better understanding of the underlying pathologies responsible for weakening the aortic wall.

A.5 CONCLUSION

In this study, we investigated the biomechanical properties of ascending aorta aneurysmal tissues with and without bicuspid valve and bovine aortic arch conditions. We found that the BAV tissues were stiffer than both AsAA and BAA tissues, and the BAA tissues were similar to the AsAA tissues. Tissue anisotropy was found in AsAA and BAA tissues but not BAV tissues. Our histological analyses showed local aortic wall abnormalities characterized by elastin fragmentation, cystic medial necrosis, loss of smooth muscle cells and accumulation of mucoid ground substances within the medial layer. The BAV samples were thinnest with less elastin than AsAA and BAA samples, which may have attributed to the altered mechanical properties of these tissues, i.e. loss of extensibility at low load. Despite these differences, there was no apparent difference in the tissue strength found between the groups, which suggest that each of the patient groups may have a similar risk of rupture. The present findings might help to better understand the underlying mechanisms of dilation in BAV and BAA patients and aid in developing numerical and computational models for improved assessment and prediction of thoracic aortic aneurysmal rupture potential.

APPENDIX B – PREDICTIVE BIOMECHANICAL ANALYSIS OF ASCENDING AORTIC ANEURYSM RUPTURE POTENTIAL

B.1 Introduction

Aortic aneurysm is a leading cause of death of adults [365], often claiming lives without any premonitory signs or symptoms. Adverse clinical outcomes of aortic aneurysm are preventable by elective surgical repair; however, identifying at-risk individuals is difficult [366]. Currently the decision to repair an ascending aortic aneurysm (**AsAA**) lies predominantly on the aneurysm diameter: namely, patients with an AsAA dilated to 5.5 cm or greater are recommended for surgery [201, 226]. However, the reliability of the diameter criterion to predict aneurysm rupture and dissection has been largely debated in the literature [201, 329, 330]. Ruptured AsAAs at diameters less than 4.5 cm have been documented [201].

Recent studies have shown that the peak vessel wall stress in abdominal aortic aneurysms may be a more reliable rupture criterion than the overall diameter, as the peak wall stress for ruptured aneurysms is about 60% higher than for non-ruptured [196, 197]. In a study by Koullias et al. [226] the ascending aortic wall stress was estimated *in vivo*. They found that the aneurismal wall stress in a hypertensive patient with an AsAA 6 cm in diameter may exceed the strength of the tissue [226]. However, this conclusion may not be sufficient to assess rupture risk on a patient-specific level, because the AsAA tissue elastic properties and failure strength are different for each individual. The aortic tissue strength may be compromised by underlying microstructural changes brought on

by aging [216, 217], disease progression [218], or other factors [219, 220]. Therefore, the patient-specific tissue strength and the aortic wall stress are both critical for assessing AsAA rupture potential.

In this study, we performed a biomechanical analysis of the passive AsAA tissue elastic properties and failure strength. A total of 50 AsAA patients were studied among 3 sub-groups: AsAA – patients without a bicuspid aortic valve (**BAV**) or bovine aortic arch (**BAA**) (n=20), ASAA-BAV – patients with a BAV (n=17), and ASAA-BAA – patients with BAA and without a BAV (n=13). We developed a novel analytical method to characterize the experimental data and predict the *in vivo* failure criteria (aneurysm diameter and blood pressure) on a patient specific level. We focus on AsAA patients with concomitant BAV and BAA in this study, because BAV has long since been known as a risk factor of AsAA and dissection [335], and a recent study by the Yale Aortic Institute [334] suggests a link between BAA and dissection. The failure criteria for each patient group were compared to determine whether the presence of BAV or BAA elevates rupture risk in patients with AsAA.

The details of the experimental methods, data and results are presented in part 1 [332] of this study, while the focus of this paper (part 2) is the analytical methods and results to predict AsAA rupture risk in different patient groups.

B.2 METHODS

B.2.1 Patient Selection

AsAA tissue specimens were collected perioperative from 50 patients undergoing elective AsAA repair at Yale – New Haven hospital between December 2008

and September 2010 and stored fresh at -80°C. Once the fresh frozen specimens were transported to our lab, the samples were cryopreserved [346] and stored at -80°C until they could be tested (refer to Fig.1 in [332]). The use of human tissues in this study was approved by the Research Compliance Office of the University of Connecticut. The 50 AsAA patients studied were divided among 3 sub-groups: AsAA – patients without a BAV or BAA (n=20), AsAA-BAV – patients with a BAV (n=17), and AsAA-BAA – patients with BAA and without a BAV (n=13). The mean patient age was 58.2 ± 11.6 years and the ratio of male to female patients was 38:12. The following clinical data were provided for each patient: the systolic/diastolic blood pressure, age, gender, height, weight, aneurysm diameter, and presence of a BAV or a BAA. The AsAA diameter provided by the Yale Aortic Institute for each patient was assumed to correspond to the systolic condition, because the clinical practice is to record the largest diameter observed. The patient characteristics are summarized in Table B-1.

Table B-1 Summary of patients' characteristics.

Patient Group	Age	Gender (M:F)	Pdias (mmHg)	Psys (mmHg)	Dsys (cm)	Height (in)	Weight (lbs)
AsAA	64.1±8.33	15:5	76.4±8.97	133.6±16.9	4.92±0.44	69.3±4.52	203.0±41.5
BAV	53.9±9.66	13:4	73.4±10.9	124.6±18.7	5.02±0.49	67.7±3.33	186.3±38.3
BAA	55.0±14.8	3:10	73.2±11.2	131.8±15.8	4.91±0.54	65.1±15.8	194.3±33.2
p-value	**0.012**	-	0.583	0.273	0.765	0.180	0.393

B.2.2 Biomechanical Testing

B.2.2.1 Planar biaxial mechanical test

The tissue specimens were defrosted via the published method [346] and inspected for the presence of calcification and evidence of prior dissection before undergoing mechanical testing. The biaxial tests were performed [332] according to the

methods of Sacks and Sun [82]. Briefly, specimens were submerged in a bath of Ca^{2+}-free and glucose-free Tyrode solution (mM: NaCl 136.9, KCl 2.7, $MgCl_2$ 1.05, $NaHCO_3$ 11.9, $NaHPO_4$ 0.47, EGTA 2.0, and 0.1M papaverine) at 37°C for the duration of each test, which consisted of preconditioning for at least 40 continuous cycles followed by tension-controlled loading protocols at the following first Piola Kirchhoff tension, $\boldsymbol{\tau}$, ratios: τ_{11}: τ_{22} = 0.75:1, 0.5:1, 0.3:1, 0.1:1, 1:1, 1:0.75, 1:0.5, 1:0.3, and 1:0.1 (see Figure B.1**a**). An illustrative set of biaxial data is given in Figure B.1**b-c** for one specimen. For a more complete description of the biaxial mechanical testing, please refer to part I of this study [332].

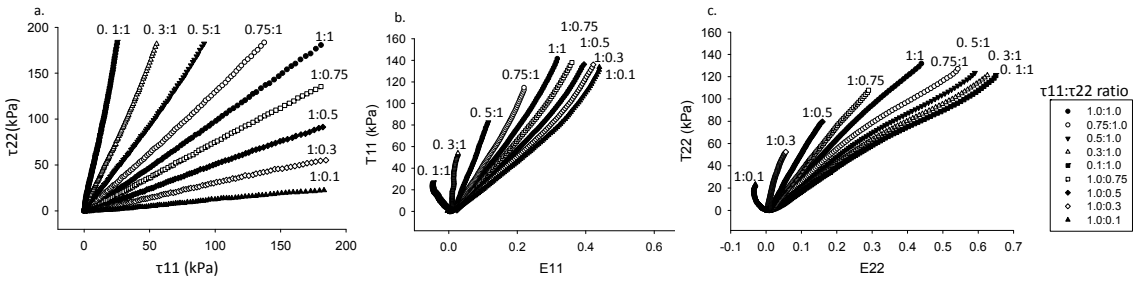

Figure B.1 (a) τ_{11} vs. τ_{22} plot, (b) τ_{11} vs. E11 plot, and (c) τ_{22} vs. E22 plot with all biaxial test protocols.

B.2.2.2 Uniaxial tensile failure test

The uniaxial failure properties of the tissue specimens were also quantified in part 1 of this study [332]. Briefly, thin strips of tissue approximately 15 mm x 5 mm in size were cut along both the circumferential and longitudinal directions of the biaxial test specimens. Each strip of tissue was loaded to failure with a Tinius Olsen uniaxial test device (Horsham, PA). From the uniaxial test data, the yield (**YT**) and ultimate tension (**UT**) were determined for each specimen in each anatomical direction. The **YT** represents the points in the tension-strain curves where the slope decreases marking the

elastic limits of the tissue, while the **UT** represents the highest tension values in each direction. Representative failure test data is presented for one AsAA patient in Figure B.2. Further details on the uniaxial tensile failure test can be found in [332].

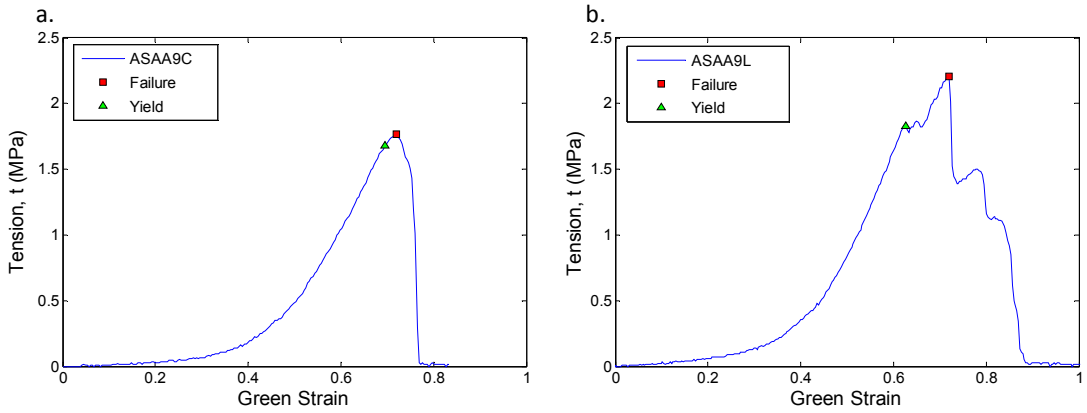

Figure B.2 Uniaxial failure test in the (a) circumferential and (b) longitudinal directions for a selected patient with blue and red asterisks corresponding to the yield and ultimate Cauchy tension values respectively.

B.2.3 Predictive Modeling

B.2.3.1 Constitutive modeling of biaxial testing data

The AsAA tissue specimens were assumed to be anisotropic, incompressible, nonlinear hyperelastic materials. Therefore, the second Piola Kirchhoff stress ($\boldsymbol{S}$) can be expressed as

$$\boldsymbol{S} = \frac{\partial W}{\partial \boldsymbol{E}}, \tag{B.1}$$

where $\boldsymbol{E}$ represents the Green-Lagrangian strain tensor and W is a strain energy function. The experimental data was fitted with the generalized Fung-type strain energy function [32] for the planar biaxial responses of soft biological tissues given by the following equations:

$$W = \frac{c}{2}(e^{Q} - 1), \tag{B.2}$$

$$Q = A_1E_{11}^2 + A_2E_{22}^2 + 2A_3E_{11}E_{22} + A_4E_{12}^2 + 2A_5E_{11}E_{12} + 2A_6E_{22}E_{12}\,, \tag{B.3}$$

where c and A_{1-6} are the material constants. The Cauchy stress tensor, $\boldsymbol{\sigma}$, can then be calculated by

$$\boldsymbol{\sigma} = \boldsymbol{J^{-1}FSF^{T}}, \tag{B.4}$$

where $\boldsymbol{F}$ is the deformation gradient and J is the determinant of $\boldsymbol{F}$. The tension tensor in the spatial description, $\boldsymbol{t}$, can be obtained by

$$\boldsymbol{t} = h\boldsymbol{\sigma}, \tag{B.5}$$

where h is the deformed tissue thickness.

To fit and extrapolate the 1:0.5 protocol biaxial testing data to higher loads, $\boldsymbol{F}$ was incremented, and $\boldsymbol{t}$ was determined for each increment through Eqs. (B.1)-(B.5).

B.2.3.2 Extrapolation of the biaxial testing protocol

Several assumptions were made in order to calculate the aortic wall tension. The AsAA tissue was assumed to be of a closed-end, thin-walled cylinder as in previous studies [219, 226-228]. The assumed cylindrical shape may be valid for aneurysms of the ascending aorta proximal to the ligamentum arteriosum, because unlike descending and abdominal aortic aneurysms, these are typically diffuse and relatively homogenous, with no significant intraluminal thrombus [201]. According to the Laplace law, the ratio of the circumferential to longitudinal Cauchy stress in the aortic wall is 1:0.5. Thus, we utilized the 1:0.5 τ_{11}: τ_{22} protocol of the biaxial testing data assuming that this protocol most closely approximates the *in vivo* condition, and extrapolated the tissue response to a level at which tensile failure could occur. Throughout the derivation, the subscript "*11*" refers

to the circumferential direction, while the subscript "*22*" refers to the longitudinal direction of the tissue specimen.

In order to extrapolate the biaxial data, the deformation gradient, $\boldsymbol{F}$, must be incremented in each direction, and the increments of F_{11} and F_{22} are not arbitrary, rather they are dependent on the material properties and the loading conditions. To extrapolate the raw biaxial test data, given that the τ_{11}: τ_{22} ratio is kept at 1:0.5, E_{12}=E_{21}=0, and F_{11} is incremented, we have

$$0.5\tau_{11} = \tau_{22}\,. \tag{B.6}$$

Using Eqs. (B.1)-(B.3) and (B.6), and $\boldsymbol{E} = \frac{1}{2}(\boldsymbol{F}^T\boldsymbol{F} - \boldsymbol{I})$, we get

$$\begin{aligned}\frac{1}{2}(A_1F_{11}^3 - A_1F_{11} + A_3F_{11}F_{22}^2 - A_3F_{11}) \\ = A_2F_{22}^3 - A_2F_{22} + A_3F_{22}F_{11}^2 - A_3F_{22}\,,\end{aligned} \tag{B.7}$$

and by reorganizing Eq. (B.7), we have

$$\begin{aligned}A_3F_{22}^3 + \left(-\frac{1}{2}A_3F_{11}\right)F_{22}^2 + (-A_2 + A_3F_{11}^2 - A_3)F_{22} \\ + \frac{1}{2}[-A_1F_{11}^3 + (A_1 + A_3)F_{11}] = 0.\end{aligned} \tag{B.8}$$

Therefore, F_{22} can be solved in terms of F_{11} and the Fung model coefficients by solving for the roots of the cubic function in Eq.(B.8). Equation (B.8) was solved numerically using the built-in "fzero" function in Matlab (Natick, MA), and the resulting, real-number, F_{22} value for each F_{11} increment was used in subsequent calculations. Now, assuming tissue incompressibility, i.e. $\lambda_{11}\lambda_{22}\lambda_{33} = 1$, $\boldsymbol{t}$ along each principal axis

was then determined from Eq. (B.9) for each $\boldsymbol{F}$ increment where $\boldsymbol{T}$ is the tension in the material description analogous to $\boldsymbol{S}$.

$$\boldsymbol{t} = \frac{h}{H} J^{-1} \boldsymbol{F}\boldsymbol{T}\boldsymbol{F}^T = \lambda_{33} \boldsymbol{F}\boldsymbol{T}\boldsymbol{F}^T . \tag{B.9}$$

B.2.3.3 *Calculation of the unloaded (0 mmHg) aneurysm diameter, D_0*

The resected AsAA tissue specimens were not in intact tubular form; therefore, the unloaded diameter was unknown and had to be calculated. The circumferential Cauchy wall tension, $t_{11_{sys}}$, at the patient's systolic blood pressure, p_{sys}, was calculated by the Laplace equation,

$$t_{11_{sys}} = p_{sys} \frac{D_{sys}}{2}, \tag{B.10}$$

where D_{sys} is the diameter of the aneurysmal vessel at p_{sys}, as measured preoperatively through image analysis. From the extrapolated biaxial data, the circumferential strain, $E_{11_{sys}}$, corresponding to $t_{11_{sys}}$, was determined (see Figure B.3a). From $E_{11_{sys}}$, the aneurysm stretch in the circumferential direction, $\lambda_{11_{sys}}$, at p_{sys} can be determined as,

$$\lambda_{11_{sys}} = \sqrt{2E_{11_{sys}} + 1.} \tag{B.11}$$

Since the D_{sys} at p_{sys} is known from the provided patient data, the aneurysm diameter at the unloaded (0 mmHg) state can then be determined as,

$$D_0 = \frac{D_{sys}}{\lambda_{11_{sys}}}. \tag{B.12}$$

B.2.3.4 *Calculation of the specimen yield and failure criteria*

Once D_0 is known, it is possible to generate the entire pressure vs. diameter curve. The diameter, *D*, at each strain increment is calculated by Eq. (B.13), and is used to calculate the pressure, *P*, at each strain increment by Eq. (B.14).

$$D = \lambda_{11} D_0 \tag{B.13}$$

$$P = \frac{2t_{11}}{D} \tag{B.14}$$

Aneurysm tissue yielding is assumed to occur when either the yield tension, determined by uniaxial failure tests, in the circumferential direction, YT_c, or the longitudinal direction, YT_l , are exceeded. The ultimate tension in each direction, UT_c and UT_l , are assumed to indicate rupture. From the extrapolated biaxial data, the circumferential and longitudinal strains leading to tissue yielding (E_{11^y}, E_{22^y}) and failure (E_{11^f}, E_{22^f}) were determined to satisfy the following relations: $\boldsymbol{t}(E_{11^y}, E_{22^y}) = \boldsymbol{YT}$ and $\boldsymbol{t}(E_{11^f}, E_{22^f}) = \boldsymbol{UT}$, respectively (see Figure B.3b). The circumferential stretches associated with yield and failure were obtained by replacing $E_{11_{sys}}$ in Eq. (B.11) with the yield and failure strains respectively, given explicitly as

$$\lambda_{11^{fc}} = \sqrt{2E_{11^{fc}} + 1}, \qquad \lambda_{11^{fl}} = \sqrt{2E_{11^{fl}} + 1}. \tag{B.15}$$

The failure diameter and pressure associated with these stretches were then obtained through Eqs. (B.16)-(B.18).

$$D_{fc} = \lambda_{11^{fc}} D_0, \qquad D_{fl} = \lambda_{11^{fl}} D_0 \tag{B.16}$$

$$P_{fc} = \frac{2UT_c}{D_{fc}} \tag{B.17}$$

$$P_{fl} = \frac{4UT_l}{D_{fl}} \tag{B.18}$$

The lower of the two yield pressure values (circumferential and longitudinal) was considered to be the yield pressure and the lower rupture pressure value was considered to be the rupture pressure. The corresponding aneurysm diameters were considered the yield and rupture diameter respectively.

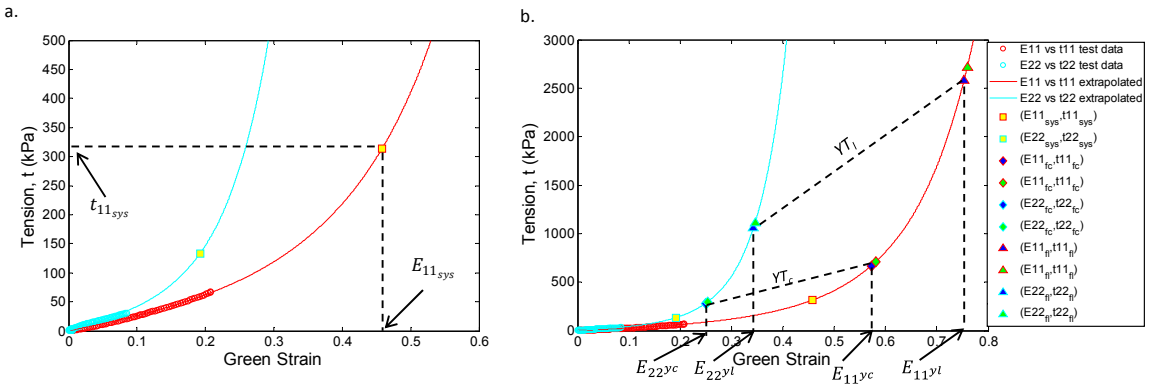

Figure B.3 (a) Extrapolated biaxial test data with raw test data represented by open circles and the biaxial test data generated by the extrapolation method represented by the lines. The circumferential strain, $E_{11_{sys}}$, at the systolic blood pressure is determined from the extrapolated biaxial data. (b) Extrapolated data with dotted lines to indicate the yield criteria (blue markers) and rupture criteria (green markers). Only the yield strains are indicated on the figure for clarity. In this case, the sample yields in the circumferential direction.

B.2.4 Data and Statistical Analysis

Risk of AsAA tissue yielding and rupture was assessed as the "diameter risk", defined as the ratio of the aneurysm diameter at systole to the predicted aneurysm yield (D_{sys}/D_y) and failure diameter (D_{sys}/D_f), as well as the "pressure risk", defined as the ratio of the systolic blood pressure to the predicted yield (P_{sys}/P_y) and failure pressure

(P_{sys}/P_f). Note that a value of 1 indicates imminent yielding and rupture; therefore, as these ratios approach unity, a patient's risk increases. The aortic size index (**ASI)** [233] was calculated for each patient as the aortic diameter normalized to the patient body surface area. The ASI has been shown to be a significant indicator of thoracic aortic aneurysm rupture potential [233]. The pressure-strain modulus, PS_{mod}, [223-225] was also calculated as a measure of the physiological aortic compliance given by

$$PS_{mod} = \frac{D_{dias}(P_{sys} - P_{dias})}{D_{sys} - D_{dias}}, \tag{B.19}$$

where the subscript "dias" refers to the diastolic condition.

The Spearman rank non-parametric test was used to determine correlation between the following patient characteristics and the predicted yielding and rupture risk: systolic/diastolic blood pressure, age, gender, ASI, PS_{mod}, presence of calcification, presence of a BAV, presence of a BAA, and systolic wall tension. For the binary parameter categories, patients received a value of 1 for the presence of calcification, BAV, BAA, or male gender and a 0 for an absence of these characteristics. The Mann-Whitney rank sum test was used to compare the means between two groups. A p-value $\leq$ 0.05 was assumed to signify a statistically significant difference between the means. Predicted values are presented as a mean ± standard deviation.

B.3 RESULTS

B.3.1 Predictive analysis

The Fung-type model of Eqn. 2 was able to capture the biaxial mechanical testing data for 50 patients with a high degree of accuracy. The mean $\tau_{11}: \tau_{22} = 1: 0.5$ biaxial

test responses for each patient group were fit with the Fung-type model of Eqn. 2: the convex and conditioned set of coefficients per Sun and Sacks [145] for each group are given in Table B-2. Note that the shear stresses and strains were included in the biaxial testing dataset for Fung-model fitting, which is why parameters $A_4 - A_6$ are non-zero values; however, neglecting the shear terms for biaxial test data extrapolation in the principal directions had a negligible effect on the model fit of the 1:0.5 protocol responses. The pressure-diameter response for each patient was then extracted, and the mean curve for each patient group is shown in Figure B.4 with standard error bars. The aneurysm yielding and rupture criteria were also determined for each patient. Briefly, AsAA, AsAA-BAV, and AsAA-BAA patients were predicted to experience rupture at an aneurysm diameter of 5.52 ± 0.8 cm, 5.7 ± 0.6 cm, and 5.4 ± 0.6 cm, with 552.9 ± 234.0 mmHg, 557.3 ± 201.0 mmHg, and 649.1 ± 201.6 mmHg of pressure respectively. There were no statistical differences between the mean predicted yielding and rupture criteria among the three patient groups (Figure B.5). The complete table of results can be found in Table B-3.

Table B-2 Fung coefficients for the mean 1:0.5 biaxial test response for the three patient groups.

Patient Group	C	A_1	A_2	A_3	A_4	A_5	A_6	R^2
AsAA	16.207	18.814	39.89	-17.73	11.67	0.1	0.15	0.997
BAV	42.725	2.802	2.000	0.993	11.110	-0.885	2.108	0.995
BAA	20.512	10.321	28.870	-10.520	38.586	-9.492	13.220	0.991

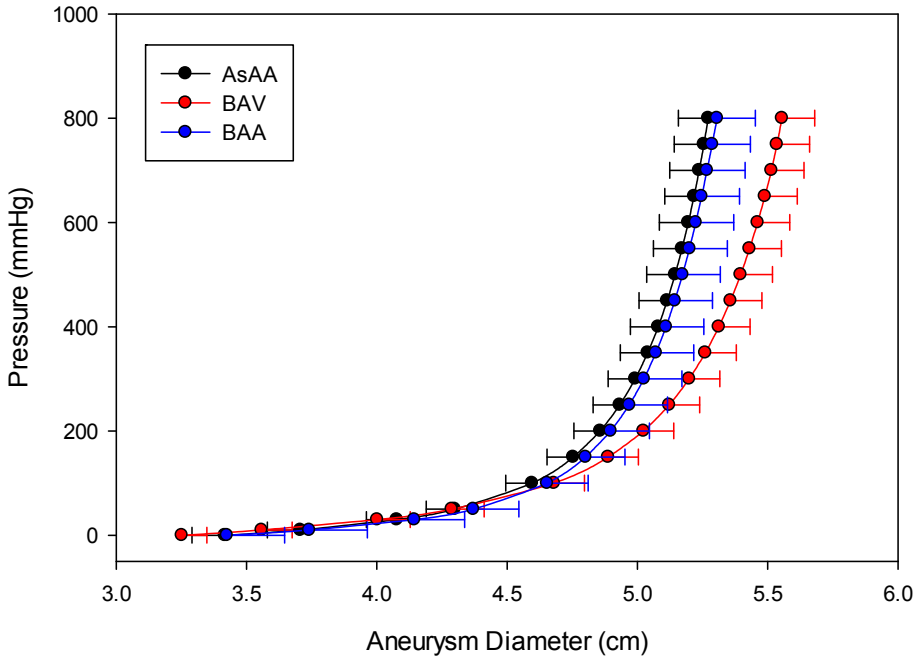

Figure B.4 The average aneurysm pressure versus diameter response response for each patient group shown with standard error bars (for clarity).

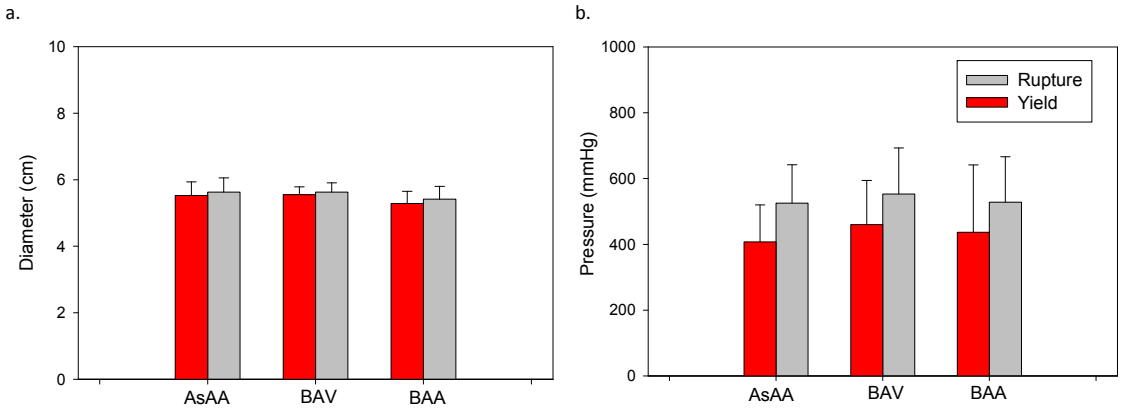

Figure B.5 The mean predicted (a) diameter and (b) blood pressure at yield (red) and rupture (gray).

Table B-3 Yield and rupture criteria defined for 50 patients.

Sample	D_{sys} (cm)	P_{sys} (mmHg)	PS_{mod} (kPa)	D_y (cm)	D_f (cm)	P_y (mmHg)	P_f (mmHg)	D_{sys} /D_y	D_{sys} /D_f	P_{sys}/ P_y	P_{sys}/ P_f
AsAA1	4.7	130	181.61	4.75	5.11	150.96	465.60	0.99	0.92	0.86	0.28
AsAA2	4.7	136	98.80	5.90	5.92	973.69	1016.60	0.80	0.79	0.14	0.13
AsAA3	4.8	101	87.42	5.69	5.92	484.41	814.88	0.84	0.81	0.21	0.12
AsAA4	4.2	112	136.79	4.44	4.46	225.01	238.49	0.95	0.94	0.50	0.47
AsAA5	5.4	149	1193.10	5.49	5.50	883.00	1030.50	0.98	0.98	0.17	0.14
AsAA6	4.9	150	594.61	4.86	4.90	109.16	153.57	1.01	1.00	1.37	0.98
AsAA8	4.9	119	74.14	7.49	7.71	412.08	443.01	0.65	0.64	0.29	0.27
AsAA9	4.7	131	123.83	5.23	5.25	481.55	503.70	0.90	0.90	0.27	0.26
AsAA10	5.2	147	644.46	5.35	5.36	627.33	650.51	0.97	0.97	0.23	0.23
AsAA11	5.0	178	152.04	5.43	5.59	377.50	530.46	0.92	0.89	0.47	0.34
AsAA12	5.3	115	127.45	5.86	5.99	399.24	566.39	0.90	0.89	0.29	0.20
AsAA13	4.6	138	423.99	4.75	4.75	373.78	393.44	0.97	0.97	0.37	0.35
AsAA14	4.4	128	190.70	4.60	4.73	245.43	438.30	0.96	0.93	0.52	0.29
AsAA15	5.9	128	171.02	6.53	6.60	601.95	752.09	0.90	0.89	0.21	0.17
AsAA16	5.6	143	116.20	5.96	6.20	255.10	382.75	0.94	0.90	0.56	0.37
AsAA17	5.3	119	169.37	5.76	5.79	500.95	545.94	0.92	0.92	0.24	0.22
AsAA22	5.3	131	154.95	5.97	6.00	720.90	792.40	0.89	0.88	0.18	0.17
AsAA23	4.5	150	257.29	4.67	4.69	322.96	363.36	0.96	0.96	0.46	0.41
AsAA24	4.5	133	164.89	4.95	5.02	471.36	608.53	0.91	0.90	0.28	0.22
AsAA25	4.5	134	122.15	4.91	4.93	347.57	367.26	0.92	0.91	0.39	0.36
AsAA Average	4.92	133.60	259.24	5.43	5.52	448.20	552.89	0.91	0.90	0.40	0.30
AsAA STDEV	0.44	16.91	271.20	0.75	0.78	226.25	234.01	0.08	0.08	0.29	0.19
BAV1	4.6	141	177.28	4.99	5.02	434.70	484.50	0.92	0.92	0.32	0.29
BAV2	5.6	120	220.46	5.97	6.00	385.06	420.40	0.94	0.93	0.31	0.29
BAV3	6.2	144	172.55	6.78	6.84	516.53	601.85	0.91	0.91	0.28	0.24
BAV6	4.35	119	119.90	4.81	4.89	408.90	545.40	0.91	0.89	0.29	0.22
BAV8	4.3	138	86.49	5.19	5.11	931.89	986.40	0.83	0.84	0.15	0.14
BAV9	5.2	105	160.79	5.72	5.84	522.65	829.23	0.91	0.89	0.20	0.13
BAV10	5.1	140	118.66	5.91	5.95	685.40	767.90	0.86	0.86	0.20	0.18
BAV11	5.0	133	145.97	5.54	5.56	478.14	498.81	0.90	0.90	0.28	0.27
BAV12	5.4	106	78.27	6.33	6.46	375.33	463.36	0.85	0.84	0.28	0.23
BAV13	5.3	140	168.39	5.63	5.66	330.51	360.77	0.94	0.94	0.42	0.39
BAV14	4.6	114	59.41	6.08	6.52	411.48	788.38	0.76	0.71	0.28	0.14
BAV15	4.6	141	152.51	4.97	5.04	404.64	504.03	0.92	0.91	0.35	0.28
BAV16	5.2	131	103.31	5.97	6.16	450.10	686.50	0.87	0.84	0.29	0.19
BAV17	4.9	104	105.62	5.39	5.53	254.88	347.25	0.91	0.89	0.41	0.30
BAV18	4.6	75	84.23	5.12	5.14	279.10	292.50	0.90	0.90	0.27	0.26
BAV19	5.3	134	152.54	5.89	5.92	558.34	616.50	0.90	0.89	0.24	0.22
BAV20	5.1	133	119.72	5.35	5.52	203.17	280.70	0.95	0.92	0.65	0.47
BAV Average	5.02	124.59	130.95	5.63	5.72	448.87	557.32	0.89	0.88	0.31	0.25
BAV STDEV	0.49	18.74	42.72	0.53	0.57	170.95	201.03	0.05	0.05	0.11	0.09
BAA1	4.5	127	86.67	5.34	5.42	674.40	801.63	0.84	0.83	0.19	0.16
BAA3	4.2	153	149.43	4.64	4.73	428.36	666.01	0.91	0.89	0.36	0.23
BAA4	5.8	138	571.38	5.99	6.01	802.90	859.98	0.97	0.97	0.17	0.16
BAA5	5.0	128	133.94	5.78	5.73	556.48	726.00	0.87	0.87	0.23	0.18
BAA7	5.2	139	170.19	5.29	5.47	168.42	263.45	0.98	0.95	0.83	0.53
BAA8	5.0	115	124.19	5.21	5.70	175.79	366.55	0.96	0.88	0.65	0.31
BAA9	4.5	105	93.57	5.30	5.25	562.53	655.94	0.85	0.86	0.19	0.16
BAA10	4.7	136	333.84	4.90	4.93	433.40	499.70	0.96	0.95	0.31	0.27
BAA11	4.7	164	360.49	4.85	4.99	359.80	797.50	0.97	0.94	0.46	0.21
BAA14	4.0	136	118.54	4.21	4.47	234.26	531.50	0.95	0.89	0.58	0.26
BAA16	5.2	133	575.02	5.37	5.41	628.45	1003.80	0.97	0.96	0.21	0.13
BAA19	5.5	123	242.39	5.77	5.87	376.54	648.25	0.95	0.94	0.33	0.19
BAA20	5.5	116	115.11	6.14	6.44	308.67	617.77	0.90	0.85	0.38	0.19
BAA Average	4.91	131.77	236.52	5.29	5.42	439.23	649.08	0.93	0.91	0.38	0.23
BAA STDEV	0.53	15.75	172.79	0.55	0.55	196.74	201.56	0.05	0.05	0.20	0.10

B.3.2 Statistical Analysis

The Spearman rank order correlation test was used to determine correlation between the predicted patient tissue yielding and rupture risk with the clinically measured characteristics. Several statistically significant trends were observed (Table B-4). An elevated yield diameter risk (D_{sys}/D_y) was significantly associated with increases in the systolic blood pressure (hypertension), age, PS_{mod}, and systolic wall tension, while an elevated rupture diameter risk (D_{sys}/D_f) was also significantly associated with these characteristics, and additionally with increasing ASI. This indicates that an increase in blood pressure, age, PS_{mod}, systolic wall tension, or ASI may decrease the elastic capacity of AsAA tissue, i.e. $D_{sys}/D_f \rightarrow 1$. The PS_{mod} was the most significant predictor of both the D_{sys}/D_y and D_{sys}/D_f with p-values of 2.0E-7 (Figure B.6a).

There were no observed correlations at the 5% significance level between the pressure risk factors (P_{sys}/P_y and P_{sys}/P_f) and the clinically measured parameters. Due to the strong correlation between the diameter risk and the PS_{mod}, the pressure risk factors were compared between the patients with high tissue compliance (PS_{mod} <100kPa) to those with low tissue compliance (PS_{mod} ≥100kPa) (Figure B.6b). Note that a PS_{mod} value of 100kPa represents a normal ascending aorta value for male patients between the ages of 30 and 79 years [155]. Patients with high compliance (PS_{mod} <100kPa) had a mean P_{sys}/P_y of 0.22 ± 0.06, which was significantly lower (p = 0.0027) than those with low compliance (PS_{mod} ≥100kPa) which had a mean P_{sys}/P_y of 0.39 ± 0.23. The rupture pressure risk, P_{sys}/P_f, was also lower among the PS_{mod} < 100kPa patients with a mean of 0.18 ± 0.06, than the PS_{mod} ≥ 100kPa patients with a mean of 0.28 ± 0.15, with a p-value of 0.0057.

Table B-4 Correlation between yield/rupture risk and patient clinical characteristics

Characteristic	P_{sys}	P_{dias}	D_{sys}	D_{dias}	Age	Gender	ASI	PS_{mod}	Cal	BAV	BAA	t_{sys}
D_{sys}/D_y ρ	0.460	0.220	0.092	0.227	0.300	-0.188	0.243	0.806	0.116	-0.203	0.033	0.469
p-value	0.001	0.125	0.522	0.113	0.034	0.190	0.116	2.00E-7	0.445	0.156	0.818	0.001
D_{sys}/D_f ρ	0.493	0.161	0.119	0.254	0.353	-0.276	0.305	0.861	0.086	-0.203	0.033	0.469
p-value	3.10E-4	0.262	0.407	0.075	0.012	0.053	0.047	2.00E-7	0.574	0.156	0.818	0.001
P_{sys}/P_y ρ	0.193	0.255	-0.176	-0.154	0.088	0.033	-0.016	0.152	0.075	-0.098	0.049	0.035
p-value	0.178	0.074	0.221	0.284	0.543	0.822	0.920	0.290	0.621	0.497	0.735	0.810
P_{sys}/P_f ρ	0.272	0.268	-0.154	-0.129	0.231	-0.101	-0.016	0.188	0.0958	0.0161	-0.197	0.100
p-value	0.056	0.060	0.284	0.369	0.106	0.485	0.920	0.189	0.530	0.911	0.168	0.487

ρ =correlation coefficient, 'Cal'=calcification, and bold-face type indicates p-value<0.05

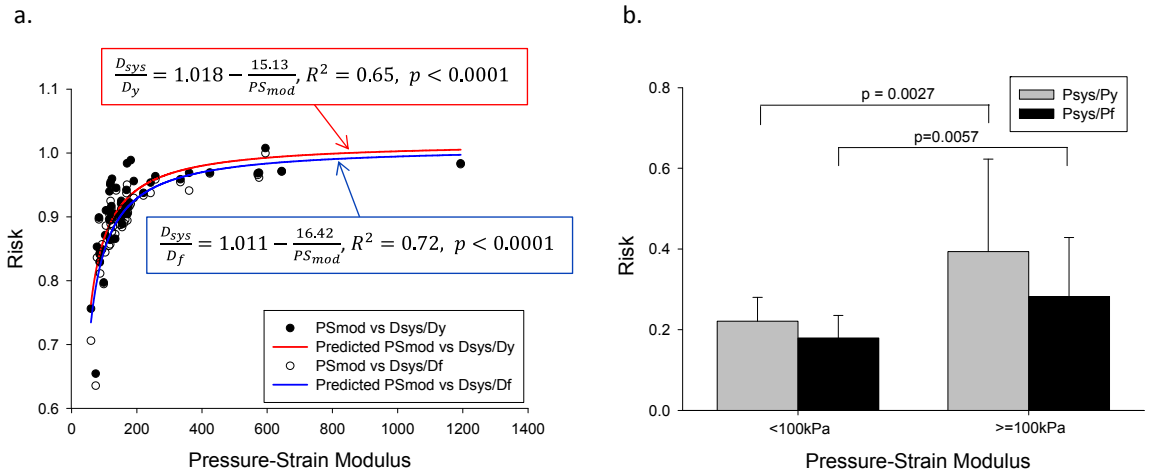

Figure B.6 (a) Yield risk quantified as D_{sys}/D_y and rupture risk as D_{sys}/D_f vs. the pressure-strain modulus, shows strong correlation. (b) Yield risk as P_{sys}/ P_y (gray) and rupture risk as P_{sys}/ P_f (black) for patients with a pressure-strain modulus less than 100kPa compared to those with a pressure-strain modulus greater than or equal to 100kPa.

B.4 DISCUSSION

B.4.1 Rupture characteristics of AsAA

The mean aneurysm diameter at yield was determined to be 5.4 ± 0.8 cm for AsAA patients, and 5.3 ± 0.6 cm for AsAA-BAA patients, which agree well with the clinically observed value of 5.31 cm at dissection [201]. The mean yield diameter predicted for AsAA-BAV patients (5.6 ± 0.5 cm) represents a slightly higher value than for AsAA and AsAA-BAA patients, yet slightly lower than the mean diameter of 6.0 ± 1.5 cm at dissection reported by Svensson et al. [367] in their study of 40 BAV patients.

However, that value may be somewhat overestimated due to rapid aortic expansion once dissection is initiated [367]. The mean predicted aneurysm diameter at rupture was 5.5 ± 0.8 cm for AsAA patients, 5.7 ± 0.6 cm for AsAA-BAV patients, and 5.4 ± 0.6 cm for AsAA-BAA patients, which are consistent with the clinical finding that a patient's risk of AsAA rupture greatly increases when the aneurysm has reached 6 cm in diameter [201], and reinforce the conclusion that such aneurysms should be electively repaired by 5.5 cm [201].

The predicted yield and rupture pressures for most of the patients are much higher than the physiological pressure range. The mean predicted yield/rupture pressure was 448.2 ± 226.3 mmHg / 552.9 ± 234.0 mmHg for AsAA patients, 448.9 ±171.0 mmHg / 557.3 ± 201.0 mmHg for AsAA-BAV patients, and 439.2 ± 196.7 mmHg / 649.1 ± 201.6 mmHg for AsAA-BAA patients, respectively. However, these values are reasonable considering it is estimated that an intravascular pressure of approximately 2500 mmHg is required to rupture the healthy human aorta [368, 369]. Although clinically blood pressures are not seen above 300 mmHg, extreme blood pressures can be observed in emotionally or physically stressful situations. In fact, dissections commonly occur during the winter months and in the early morning hours when blood pressures are known to be highest [201]. In a retrospective study of patients treated for acute aortic dissection at Yale University, 66% of patients recalled severe emotional stress or physical exertion at the time of their dissection [370]. For example, in a follow-up study the authors [371] reported 31 cases of aortic dissection of young men with no evidence of aortic aneurysm during weightlifting, where blood pressures exceeding 300mmHg have been observed [370, 371]. It is also important to note that the predicted AsAA rupture pressures

presented here are the pressure needed to rupture the tissue with its current material properties (i.e., at the time of elective surgery). As disease progresses the strength of the tissue may decline, and with it, the pressure to induce rupture.

For one patient, patient #AsAA6, the predicted yield pressure risk (P_{sys}/P_y) was 1.37 and rupture pressure risk (P_{sys}/P_f) was 0.98 (see Table B-3). Thus, according to our predictions, this patient should have experienced yielding already and possibly rupture at even slightly elevated blood pressures, yet none of the patients included in the study were known to have dissected/ruptured at the time of surgery. Examination of the resected AsAA6 ascending aortic aneurysm specimen at the tissue and microstructure levels revealed advanced aortic disease compared to the other samples (see Figure B.7a-c). There was evident disruption between the medial and adventitial layers of the wall, which indicates the onset of dissection (Figure B.7a). On the micro scale, the three layers of the aortic wall were severely damaged with evidence of intimal thickening, disruption and disorganization of the elastin network, and loss of smooth muscle cells with an accumulation of extracellular matrix ground substance and collagen in the media (Figure B.7c) [335, 353]. Therefore, although this patient was not diagnosed with dissection, it appears that tissue specimen tested was severely degenerated, which may explain our overly high predicted risk factor.

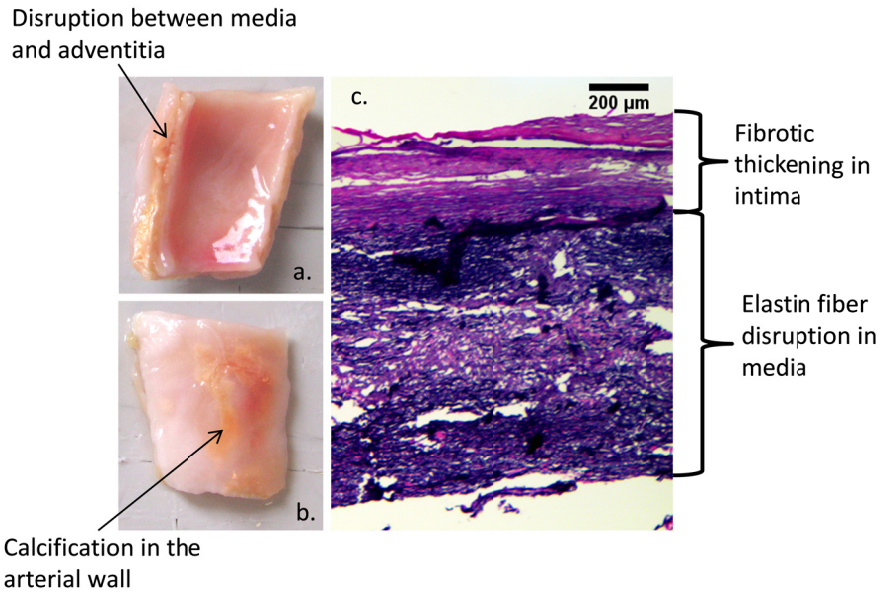

Figure B.7 (a) AsAA6 biaxial test specimen with the (b) intimal surface and (c) adventitial surface on top, and representative histological slice through the aortic wall with Verhoeff-VanGieson stain rendering elastin purple-black and collagen pink-purple.

B.4.2 Bicuspid aortic valve effect

Although there were no significant differences in the predicted failure characteristics among the patient groups, the predicted yield and rupture diameters for AsAA-BAV patients were slightly larger than for the AsAA and AsAA-BAA patients. These results suggest that AsAAs dissect at smaller diameters in patients without BAV, which is in agreement with the International Registry of Acute Aortic Dissections report that the proportion of dissections occurring at smaller sizes (<5.5 cm) was actually higher among patients without BAV or Marfan syndrome [350, 372].

AsAA-BAV patients also had slightly lower mean P_{sys}/P_y and P_{sys}/P_f ratios than AsAA patients. Again, these differences were not significant. The clinical finding that BAV patients are more likely to experience rupture and dissection than patients with a tricuspid aortic valve [350], may be explained by the higher prevalence rate and younger

onset age of aortic dilation in BAV patients [350, 373-376]. However, the difference between patient groups may also be explained in part by the younger age of AsAA-BAV patients (53.9±9.7 years) compared to the AsAA patients (64.1±8.3 years) analyzed in this study. It is well documented that the mechanical properties of the human aorta undergo significant changes with age, including dramatic stiffening beyond the age of 60 years [204, 205]; therefore, the differences in age between the AsAA and AsAA-BAV patients groups in this study may explain the higher predicted pressures for adverse events in the AsAA-BAV patient group.

B.4.3 Bovine aortic arch effect

The mean pressure versus diameter curves for both AsAA-BAA and AsAA patients were nearly identical (see Figure B.4). The predicted failure characteristics for AsAA-BAA patients were also similar to those for the AsAA patients. AsAA-BAA patients had a slightly lower mean predicted rupture risk than AsAA patients, but were also younger on average (55.0±14.8 years) than the AsAA patients. From this analysis, the presence of BAA does not appear to affect a patient's risk of ascending aortic rupture. A more thorough study comparing ascending aorta tissue properties in BAA and non-BAA patients with and without AsAA may be necessary for determining any association between BAA and AsAA.

B.4.4 Clinical indications of rupture potential

No correlation was determined between the aneurysm size and any of the yield and rupture risk ratios; yet, this is what is currently used clinically. Our results suggest that patients with stiff aortic aneurysm tissue are at higher risk for dissection and rupture, than those with more compliant tissue; therefore, the PS_{mod} may be a more appropriate

metric for the clinical *in vivo* and non-invasive evaluation of AsAA rupture risk. The patient risk quantified as the diameter risk (D_{sys}/D_y and D_{sys}/D_f) and pressure risk (P_{sys}/P_y and P_{sys}/P_f) increases dramatically when the PS_{mod} exceeds 100kPa. The mean P_{sys}/P_y and P_{sys}/P_f ratios for patients with low tissue compliance ($PS_{mod} \geq$ 100kPa) were 1.8 and 1.6 times larger than the corresponding ratios for patients with high tissue compliance ($PS_{mod} <$ 100kPa).

The statistical analysis also implicated elevated blood pressure, in addition to increased pressure-strain modulus, as a risk factor for AsAA rupture. Hypertension has long been known to be a risk factor for cardiovascular disease, and aortic stiffness has more recently been implicated as an indicator of aortic disease [160, 226]. These findings are in tune with what we know about vessel mechanics. Blood vessels will burst when the stress acting on the wall exceeds the strength of the wall. For an AsAA, the blood pressure induces stress on the vessel wall, while the pressure-strain modulus depends on the wall tissue properties, geometry, and loading conditions.

B.4.5 Limitations

This prediction approach is limited in part by the experimental data which was collected at a relatively low load range, thus, requiring the extrapolation technique to predict the high-load response. We assume that the analytical model can predict the tissue response up until the rupture point. Ideally, we could collect the experimental data to higher loads. It is possible that freezing the tissue specimens before testing may have affected the tissue mechanical properties. This analysis also did not account for the time-dependent material property changes of AsAAs. Therefore, the timing of adverse events cannot be predicted. Moreover, the tensile strength of the aorta under *in vivo* conditions

was assumed to be equivalent to the uniaxial tensile strength in each principal direction, while a Von-Mises type yield criterion may allow for a more accurate estimate of the tissue limits independent of the loading condition.

The AsAAs were assumed to be thin-walled tubes with a circular cross-section in this study. The tissue property around the circumference of the resected aneurysm was assumed to be homogeneous; however, some studies [227, 228, 234, 237, 354] suggest that the properties of the ascending aorta differ between the anterior and posterior regions. Although, a study by Azadani et al. [377] show that the properties of healthy human ascending aorta do not differ significantly around the aorta.

Because the *in vivo* tissue thickness was unknown, the vessel wall tension rather than the stress was used. We also did not include the vessel residual stress for this reason. By neglecting the *in vivo* wall thickness in the stress analyses we may be overestimating the true stress state of the vessel. The layer-specific material properties of the aortic wall were also not considered. Sokolis et al. [378] report differences in the uniaxial stress-strain and failure responses for the three layers of the AsAA wall. In the future it may be necessary to test the biaxial mechanical properties of each layer of the aortic wall and model the entire wall as a tri-layer composite, to enhance the accuracy of our risk assessment method.

B.5 Conclusions

In this study, the rupture potential of AsAAs was assessed in 50 patients, including patients with concomitant BAV and BAA. The aneurysmal tissue was resected from these patients prior to dissection or rupture, and through this biomechanical

analysis, we predicted the "future" yield and rupture criteria for each patient. Our main findings are as follows:

- No association could be made between the aneurysm diameter and rupture potential.
- Aortic tissue stiffening and hypertension may increase a patient's risk of rupture.
- BAV and BAA patients with AsAAs may have a similar risk of rupture as patients without either of these conditions.

The close symmetry between our results and those observed clinically supports the potential use of the analytical techniques developed in this study for future pre-operative evaluation of AsAA. Our results indicate that the pressure-strain modulus may be a more reliable indicator of rupture potential than the previously used maximum aneurysm diameter criteria, and can also be easily obtained clinically, making it an attractive rupture potential metric.

REFERENCES

1. Freed, A.D. and T.C. Doehring, *Elastic Model for Crimped Collagen Fibrils.* Journal of Biomechanical Engineering, 2005. **127**(4): p. 587-593.

2. Liao, J., *Mechanical and Structural Properties of Mitral Valve Chordae Tendineae*. 2003, Cleveland State University: Cleveland, Ohio.

3. Redaelli, A., et al., *Possible role of decorin glycosaminoglycans in fibril to fibril force transfer in relative mature tendons—a computational study from molecular to microstructural level.* Journal of Biomechanics, 2003. **36**(10): p. 1555-1569.

4. Raspanti, M., et al., *Direct Visualization of Collagen-Bound Proteoglycans by Tapping-Mode Atomic Force Microscopy.* Journal of Structural Biology, 1997. **119**(2): p. 118-122.

5. Eyre, D.R., et al., *Covalent Cross-linking of the NC1 Domain of Collagen Type IX to Collagen Type II in Cartilage.* Journal of Biological Chemistry, 2004. **279**(4): p. 2568-2574.

6. Natali, A.N., et al., *Characterization of soft tissue mechanics with aging.* IEEE Engineering in Medicine and Biology Magazine, 2008. **27**(4): p. 15-22.

7. Bailey, A.J., R.G. Paul, and L. Knott, *Mechanisms of maturation and ageing of collagen.* Mechanisms of Ageing and Development, 1998. **106**(1–2): p. 1-56.

8. da Silva Nina, V.J., *Surgical Repair of Stenotic Pulmonary Arteries in Tetralogy of Falllot, Cardiac Surgery - A Commitment to Science, Technology and Creativity*, M. Maluf and P.R.B. Evora, Editors. 2014.

9. Backer, C.L., *General Thoracic Surgery, 6th Edition*. Vol. Volume I - The Lung, Pleura, Diaphragm, and Chest Wall. 2005: Lippincott Williams & Wilkins.

10. Medtronic. *Freestyle Tissue Valve*. 22 Sep 2010; Available from: http://www.medtronic.com/patients/heart-valve-disease/about-surgery/our-heart-valve-products/freestyle-tissue-valve/.

11. Billiar, K.L. and M.S. Sacks, *Biaxial Mechanical Properties of the Natural and Glutaraldehyde Treated Aortic Valve Cusp---Part I: Experimental Results.* Journal of Biomechanical Engineering, 2000. **122**(1): p. 23-30.

12. Teoh, S.H., *Fatigue of biomaterials: a review.* International Journal of Fatigue, 2000. **22**(10): p. 825-837.

13. Peña, E., et al., *A constitutive formulation of vascular tissue mechanics including viscoelasticity and softening behaviour.* Journal of Biomechanics, 2010. **43**(5): p. 984-989.

14. Ehret, A.E. and M. Itskov, *Modeling of anisotropic softening phenomena: Application to soft biological tissues.* International Journal of Plasticity, 2009. **25**(5): p. 901-919.

15. Franceschini, G., et al., *Brain tissue deforms similarly to filled elastomers and follows consolidation theory.* Journal of the Mechanics and Physics of Solids, 2006. **54**: p. 2592-2620.

16. Peña, E., *Prediction of the softening and damage effects with permanent set in fibrous biological materials.* Journal of the Mechanics and Physics of Solids, 2011. **59**(9): p. 1808-1822.

17. Maher, E., et al., *Inelasticity of Human Carotid Atherosclerotic Plaque.* Annals of Biomedical Engineering, 2011. **39**(9): p. 2445-2455.

18. O'Rourke, M.F. and J. Hashimoto, *Mechanical Factors in Arterial Aging: A Clinical Perspective.* Journal of the American College of Cardiology, 2007. **50**(1): p. 1-13.

19. Millthorpe, B.K., *Xenografts for tendon and ligament repair.* Biomaterials, 1994. **15**(10): p. 745-752.

20. van Steensel, C.J., et al., *Failure of anterior cruciate-ligament reconstruction using tendon xenograft.* The Journal of Bone & Joint Surgery, 1987. **69**(6): p. 860-864.

21. Dahlstedt, L.J., P. Netz, and N. Dalen, *Poor results of bovine xenograft for knee cruciate ligament repair.* Acta Orthop Scan, 1989. **60**(1): p. 3-7.

22. Mays, P.K., et al., *Age-related changes in collagen synthesis and degradation in rat tissues. Importance of degradation of newly synthesized collagen in regulating collagen production.* Biochemical Journal, 1991. **276**(Pt 2): p. 307-313.

23. Narici, M.V., C. Maganaris, and N. Reeves, *Myotendinous alterations and effects of resistive loading in old age.* Scandinavian Journal of Medicine & Science in Sports, 2005. **15**(6): p. 392-401.

24. Zarkovic, K., et al., *Elastin aging and lipid oxidation products in human aorta.* Redox Biology, 2015. **4**(0): p. 109-117.

25. Hayflick, L., *How and why we age.* Experimental Gerontology, 1998. **33**(7–8): p. 639-653.

26. Pruchno, R.A., et al., *Successful Aging: Early Influences and Contemporary Characteristics.* The Gerontologist, 2010. **50**(6): p. 821-833.

27. Flatt, T., *A New Definition of Aging?* Frontiers in Genetics, 2012. **3**: p. 148.

28. Kovacic, J.C., et al., *Cellular Senescence, Vascular Disease, and Aging: Part 2 of a 2-Part Review: Clinical Vascular Disease in the Elderly.* Circulation, 2011. **123**(17): p. 1900-1910.

29. Yusuf, S., et al., *Effect of potentially modifiable risk factors associated with myocardial infarction in 52 countries (the INTERHEART study): case-control study.* The Lancet, 2004. **364**(9438): p. 937-952.

30. Dantas, A.P., F. Jiménez-Altayó, and E. Vila, *Vascular Aging: Facts and Factors.* Frontiers in Physiology, 2012. **3**: p. 325.

31. Sacks, M.S., *Biaxial mechanical evaluation of planar biological materials.* Journal of Elasticity, 2000. **61**: p. 199-246.

32. Fung, Y.C., *Biomechanics: Mechanical Properties of Living Tissues*. 2nd ed. 1993, New York: Springer Verlag. 568.

33. Li, K., et al., *Quantification of structural compliance of aged human and porcine aortic root tissues.* Journal of Biomedical Materials Research Part A, 2014. **102**(7): p. 2365-2374.

34. Osborne, W.A., *The elasticity of rubber balloons and hollow viscera.* Proc. R. Soc. Lond. Ser. B, 1909. **81**(551): p. 485-499.

35. Martin , C. and W. Sun, *Fatigue Damage of Collagenous Tissues: Experiment, Modeling and Simulation Studies.* 2015. **25**(1-2): p. 55-73.

36. Schechtman, H. and D.L. Bader, *Fatigue damage of human tendons.* Journal of Biomechanics, 2002. **35**(3): p. 347-353.

37. Wang, X.T., R.F. Ker, and R.M. Alexander, *Fatigue rupture of wallaby tail tendons.* Journal of Experimental Biology, 1995. **198**(3): p. 847-52.

38. Provenzano, P.P., et al., *Subfailure damage in ligament: a structural and cellular evaluation.* Journal of Applied Physiology, 2002. **92**(1): p. 362-371.

39. Ker, R.F., X.T. Wang, and A.V. Pike, *Fatigue quality of mammalian tendons.* Journal of Experimental Biology, 2000. **203**(8): p. 1317-1327.

40. Fung, D.T., et al., *Subrupture tendon fatigue damage.* Journal of Orthopaedic Research, 2009. **27**(2): p. 264-273.

41. Zec, M.L., et al., *Characterization of the fatigue behavior of the medial collateral ligament utilizing traditional and novel mechanical variables for the assessment of damage accumulation.* Journal of Biomechanical Engineering, 2010. **132**(1).

42. Schwab, T.D., et al., *Continuum damage mechanics (CDM) modelling demonstrates that ligament fatigue damage accumulates by different mechanisms than creep damage.* Journal of Biomechanics, 2007. **40**(14): p. 3279-3284.

43. Shepherd, J.H. and H.R.C. Screen, *Fatigue loading of tendon.* International Journal of Experimental Pathology, 2013. **94**(4): p. 260-270.

44. Banes, A.J., et al., *Mechanical load stimulates expression of novel genesin vivoandin vitroin avian flexor tendon cells.* Osteoarthritis and Cartilage, 1999. **7**(1): p. 141-153.

45. Devkota, A.C., et al., *Distributing a fixed amount of cyclic loading to tendon explants over longer periods induces greater cellular and mechanical responses.* Journal of Orthopaedic Research, 2007. **25**(8): p. 1078-1086.

46. Lavagnino, M., et al., *Effect of amplitude and frequency of cyclic tensile strain on the inhibition of MMP-1 mRNA expression in tendon cells: an in vitro study.* Connect Tissue Res, 2003. **44**(3-4): p. 181-7.

47. Flick, J., et al., *Cyclic loading alters biomechanical properties and secretion of PGE2 and NO from tendon explants.* Clinical Biomechanics, 2006. **21**(1): p. 99-106.

48. Scott, A., et al., *High strain mechanical loading rapidly induces tendon apoptosis: an ex vivo rat tibialis anterior model.* Br J Sports Med, 2005. **39**(5): p. e25.

49. Wells, S.M., T. Sellaro, and M.S. Sacks, *Cyclic loading response of bioprosthetic heart valves: effects of fixation stress state on the collagen fiber architecture.* Biomaterials, 2005. **26**(15): p. 2611-9.

50. Thornton, G.M. and S.J. Bailey, *Healing ligaments have shorter lifetime and greater strain rate during fatigue than creep at functional stresses.* Journal of Biomechanical Engineering, 2013. **135**(9).

51. Thornton, G.M. and S.J. Bailey, *Repetitive loading damages healing ligaments more than sustained loading demonstrated by reduction in modulus and residual strength.* Journal of Biomechanics, 2012. **45**(15): p. 2589-2594.

52. Soslowsky, L.J., et al., *Neer Award 1999. Overuse activity injures the supraspinatus tendon in an animal model: a histologic and biomechanical study.* J Shoulder Elbow Surg, 2000. **9**(2): p. 79-84.

53. Scott, A., et al., *Tenocyte responses to mechanical loading in vivo: A role for local insulin-like growth factor 1 signaling in early tendinosis in rats.* Arthritis & Rheumatism, 2007. **56**(3): p. 871-881.

54. Millar, N.L., et al., *Cytokines and apoptosis in supraspinatus tendinopathy.* J Bone Joint Surg Br, 2009. **91**(3): p. 417-24.

55. Huang, T.-F., S. Perry, and L. Soslowsky, *The Effect of Overuse Activity on Achilles Tendon in an Animal Model: A Biomechanical Study.* Annals of Biomedical Engineering, 2004. **32**(3): p. 336-341.

56. Glazebrook, M.A., et al., *Histological analysis of achilles tendons in an overuse rat model.* Journal of Orthopaedic Research, 2008. **26**(6): p. 840-846.

57. Fung, D.T., et al., *Early response to tendon fatigue damage accumulation in a novel in vivo model.* Journal of Biomechanics, 2010. **43**(2): p. 274-279.

58. Andarawis-Puri, N. and E.L. Flatow, *Tendon fatigue in response to mechanical loading.* J Musculoskelet Neuronal Interact, 2011. **11**(2): p. 106-14.

59. Andarawis-Puri, N., et al., *The relationships between cyclic fatigue loading, changes in initial mechanical properties, and the in vivo temporal mechanical response of the rat patellar tendon.* Journal of Biomechanics, 2012. **45**(1): p. 59-65.

60. Sun, H.B., et al., *Coordinate regulation of IL-1beta and MMP-13 in rat tendons following subrupture fatigue damage.* Clin Orthop Relat Res, 2008. **466**(7): p. 1555-61.

61. Sereysky, J.B., et al., *Structural and mechanical effects of in vivo fatigue damage induction on murine tendon.* Journal of Orthopaedic Research, 2012. **30**(6): p. 965-972.

62. Andersson, G., et al., *Tenocyte hypercellularity and vascular proliferation in a rabbit model of tendinopathy: contralateral effects suggest the involvement of central neuronal mechanisms.* Br J Sports Med, 2011. **45**(5): p. 399-406.

63. Asundi, K., K. King, and D. Rempel, *Evaluation of gene expression through qRT-PCR in cyclically loaded tendons: an in vivo model.* European Journal of Applied Physiology, 2008. **102**(3): p. 265-270.

64. Nakama, L.H., et al., *Evidence of tendon microtears due to cyclical loading in an in vivo tendinopathy model.* Journal of Orthopaedic Research, 2005. **23**(5): p. 1199-1205.

65. Cataloglu, A., R.E. Clark, and P.L. Gould, *Stress analysis of aortic valve leaflets with smoothed geometrical data.* Journal of Biomechanics, 1977. **10**: p. 153-158.

66. Kunzelman, K.S., et al., *Finite element analysis of the mitral valve.* The Journal of heart valve disease, 1993. **2**(3): p. 326-340.

67. Pouch, A.M., et al., *Semi-automated mitral valve morphometry and computational stress analysis using 3D ultrasound.* J Biomech, 2012. **45**(5): p. 903-7.

68. Stevanella, M., et al., *Mitral leaflet modeling: Importance of in vivo shape and material properties.* J Biomech, 2011. **44**(12): p. 2229-35.

69. Votta, E., et al., *The Geoform Disease-Specific Annuloplasty System: A Finite Element Study.* Annals of Thoracic Surgery, 2007. **84**(1): p. 92-101.

70. Krishnamurthy, G., et al., *Material properties of the ovine mitral valve anterior leaflet in vivo from inverse finite element analysis.* American Journal of Physiology - Heart and Circulatory Physiology, 2008. **295**(3): p. H1141-H1149.

71. Celi, S. and S. Berti, *Three-dimensional sensitivity assessment of thoracic aortic aneurysm wall stress: a probabilistic finite-element study.* European Journal of Cardio-Thoracic Surgery, 2014. **45**(3): p. 467-475.

72. Beller, C.J., et al., *Role of Aortic Root Motion in the Pathogenesis of Aortic Dissection.* Circulation, 2004. **109**(6): p. 763-769.

73. Nathan, D.P., et al., *Pathogenesis of Acute Aortic Dissection: A Finite Element Stress Analysis.* The Annals of Thoracic Surgery, 2011. **91**(2): p. 458-463.

74. Thubrikar, M., P. Agali, and F. Robicsek, *Wall stress as a possible mechanism for the development of transverse intimal tears in aortic dissections.* J Med Eng Technol, 1999. **23**(4): p. 127-34.

75. Suito, H., et al., *FSI analysis of the blood flow and geometrical characteristics in the thoracic aorta.* Computational Mechanics, 2014. **54**(4): p. 1035-1045.

76. Nathan, D.P., et al., *Increased Ascending Aortic Wall Stress in Patients With Bicuspid Aortic Valves.* The Annals of Thoracic Surgery, 2011. **92**(4): p. 1384-1389.

77. Pasta, S., et al., *Difference in hemodynamic and wall stress of ascending thoracic aortic aneurysms with bicuspid and tricuspid aortic valve.* Journal of Biomechanics, 2013. **46**(10): p. 1729-1738.

78. Shergold, O.A., N.A. Fleck, and D. Radford, *The uniaxial stress versus strain response of pig skin and silicone rubber at low and high strain rates.* International Journal of Impact Engineering, 2006. **32**(9): p. 1384-1402.

79. Wang, Q., et al., *Simulations of transcatheter aortic valve implantation: implications for aortic root rupture.* Biomech Model Mechanobiol, 2015. **14**(1): p. 29-38.

80. Humphery, J.D., *Cardiovascular Solid Mechanics*. 2002: Springer Verlag.

81. Sun, W., A. Abad, and M.S. Sacks, *Simulated bioprosthetic heart valve deformation under quasi-static loading.* J Biomech Eng, 2005. **127**(6): p. 905-14.

82. Sacks, M.S. and W. Sun, *Multiaxial Mechanical Behavior of Biological Materials.* Annu Rev Biomed Eng, 2003.

83. Labrosse, M.R., K. Lobo, and C.J. Beller, *Structural analysis of the natural aortic valve in dynamics: From unpressurized to physiologically loaded.* Journal of Biomechanics, 2010. **43**(10): p. 1916-1922.

84. Labrosse, M.R., et al., *Modeling leaflet correction techniques in aortic valve repair: A finite element study.* Journal of Biomechanics, 2011. **44**(12): p. 2292-2298.

85. Sun, W., *Biomechanical simulations of heart valve biomaterials*, in *Department of Bioengineering*. 2003, University of Pittsburgh: Pittsburgh. p. 240.

86. Weiss, J.A., B.N. Maker, and S. Govindjee, *Finite element implementation of incompressible, transversely isotropic hyperelasticity.* Computer Methods in Applied Mechanics and Engineering, 1996. **135**(1-2): p. 107-128.

87. Holzapfel, G.A., T.C. Gasser , and R.W. Ogden, *A new constitutive framework for arterial wall mechanics and a comparative study of material models.* J. Elasticity, 2000. **61**: p. 1–48.

88. Prot, V., et al., *On modelling and analysis of healthy and pathological human mitral valves: two case studies.* Journal of the mechanical behavior of biomedical materials, 2010. **3**: p. 167-177.

89. Stevanella, M., et al., *Mitral Valve Patient-Specific Finite Element Modeling from Cardiac MRI: Application to an Annuloplasty Procedure.* Cardiovascular Engineering and Technology, 2011. **2**(2): p. 66-76.

90. May-Newman, K. and F.C. Yin, *A constitutive law for mitral valve tissue.* J Biomech Eng, 1998. **120**(1): p. 38-47.

91. Conti, C.A., et al., *Dynamic finite element analysis of the aortic root from MRI-derived parameters.* Med Eng Phys, 2010. **32**(2): p. 212-21.

92. Auricchio, F., et al., *Simulation of transcatheter aortic valve implantation: a patient-specific finite element approach.* Computer Methods in Biomechanics and Biomedical Engineering, 2013.

93. Humphrey, J.D., *Cardiovascular solid mechanics: cells, tissues, and organs*. 2002, Springer-Verlag New York, Inc.

94. Gasser, T.C. and G.A. Holzapfel, *A rate-independent elastoplastic constitutive model for biological fiber-reinforced composites at finite strains: continuum basis, algorithmic formulation and finite element implementation.* Computational Mechanics, 2002. **29**(4-5): p. 340-360.

95. Holzapfel, G.A. and T.C. Gasser, *A viscoelastic model for fiber-reinforced composites at finite strains: Continuum basis, computational aspects and applications.* Computer Methods in Applied Mechanics and Engineering, 2001. **190**(34): p. 4379-4403.

96. Anssari-Benam, A., D.L. Bader, and H.R.C. Screen, *A combined experimental and modelling approach to aortic valve viscoelasticity in tensile deformation.* Journal of Materials Science: Materials in Medicine, 2011. **22**(2): p. 253-262.

97. Palacio-Torralba, J., et al., *Quantitative diagnostics of soft tissue through viscoelastic characterization using time-based instrumented palpation.* Journal of the Mechanical Behavior of Biomedical Materials, 2015. **41**: p. 149-160.

98. Simo, J.C., *On a fully three-dimensional finite-strain viscoelastic damage model: Formulation and computational aspects.* Computer Methods in Applied Mechanics and Engineering, 1987. **60**(2): p. 153-173.

99. Calvo, B., et al., *An uncoupled directional damage model for fibred biological soft tissues. Formulation and computational aspects.* International Journal for Numerical Methods in Engineering, 2007. **69**(10): p. 2036-2057.

100. Rodríguez, J.F., et al., *A stochastic-structurally based three dimensional finite-strain damage model for fibrous soft tissue.* Journal of the Mechanics and Physics of Solids, 2006. **54**(4): p. 864-886.

101. Li, D. and A.M. Robertson, *A Structural Multi-Mechanism Damage Model for Cerebral Arterial Tissue.* Journal of Biomechanical Engineering, 2009. **131**(10): p. 101013-8.

102. Pena, E., *Prediction of the softening and damage effects with permanent set in fibrous biological materials.* Journal of the Mechanics and Physics of Solids, 2011. **59**(9): p. 1808-1822.

103. Alastrué, V., et al., *Structural damage models for fibrous biological soft tissues.* International Journal of Solids and Structures, 2007. **44**(18-19): p. 5894-5911.

104. Balzani, D., S. Brinkhues, and G.A. Holzapfel, *Constitutive framework for the modeling of damage in collagenous soft tissues with application to arterial walls.* Computer Methods in Applied Mechanics and Engineering, 2012. **213–216**: p. 139-151.

105. Sun, W., et al., *Response of heterograft heart valve biomaterials to moderate cyclic loading.* Journal of Biomedical Materials Research Part A, 2004. **69A**(4): p. 658-669.

106. Miehe, C., *Discontinuous and continuous damage evolution in Ogden-type large-strain elastic materials.* European Journal of Mechanics. A, Solids, 1995. **14**(5): p. 697-720.

107. Humphrey, J.D. and K.R. Rajagopal, *A constrained mixture model for growth and remodeling of soft tissues.* Mathematical Models and Methods in Applied Sciences, 2002. **12**(03): p. 407-430.

108. Ateshian, G., et al., *Computational modeling of chemical reactions and interstitial growth and remodeling involving charged solutes and solid-bound molecules.* Biomechanics and Modeling in Mechanobiology, 2014. **13**(5): p. 1105-1120.

109. Lanir, Y., *Mechanistic micro-structural theory of soft tissues growth and remodeling: tissues with unidirectional fibers.* Biomechanics and Modeling in Mechanobiology, 2014: p. 1-22.

110. Gleason Jr, R.L. and J.D. Humphrey, *A 2D constrained mixture model for arterial adaptations to large changes in flow, pressure and axial stretch.* Mathematical Medicine and Biology, 2005. **22**(4): p. 347-369.

111. Baek, S., K.R. Rajagopal, and J.D. Humphrey, *A theoretical model of enlarging intracranial fusiform aneurysms.* Journal of Biomechanical Engineering, 2006. **128**(1): p. 142-149.

112. Eriksson, T., M. Kroon, and G.A. Holzapfel, *Influence of Medial Collagen Organization and Axial In Situ Stretch on Saccular Cerebral Aneurysm Growth.* Journal of Biomechanical Engineering, 2009. **131**(10): p. 101010-101010.

113. Watton, P.N. and N.A. Hill, *Evolving mechanical properties of a model of abdominal aortic aneurysm.* Biomechanics and Modeling in Mechanobiology, 2009. **8**(1): p. 25-42.

114. Watton, P.N., et al., *Modelling evolution and the evolving mechanical environment of saccular cerebral aneurysms.* Biomechanics and Modeling in Mechanobiology, 2011. **10**(1): p. 109-132.

115. Valentín, A., J.D. Humphrey, and G.A. Holzapfel, *A multi-layered computational model of coupled elastin degradation, vasoactive dysfunction, and collagenous stiffening in aortic aging.* Annals of Biomedical Engineering, 2011. **39**(7): p. 2027-2045.

116. Gould, P.L., et al., *Stress analysis of the human aortic valve.* Computers and Structures, 1973. **3**: p. 377.

117. Cataloglu, A., P.L. Gould, and R.E. Clark, *Validation of a simplified mathematical model for the stress analysis of human aortic heart valves.* Journal of Biomechanics, 1975. **8**(5): p. 347-348.

118. Martin, C., W. Sun, and J. Elefteriades, *Patient-specific finite element analysis of ascending aorta aneurysms*. 2015.

119. Auricchio, F., et al., *Simulation of transcatheter aortic valve implantation: a patient-specific finite element approach.* Comput Methods Biomech Biomed Engin, 2014. **17**(12): p. 1347-57.

120. Capelli, C., et al., *Patient-specific simulations of transcatheter aortic valve stent implantation.* Med Biol Eng Comput, 2012. **50**(2): p. 183-92.

121. Dwyer, H.A., et al., *Migration forces of transcatheter aortic valves in patients with noncalcific aortic insufficiency.* J Thorac Cardiovasc Surg, 2009. **138**(5): p. 1227-33.

122. Morganti, S., et al., *Simulation of transcatheter aortic valve implantation through patient-specific finite element analysis: two clinical cases.* J Biomech, 2014. **47**(11): p. 2547-55.

123. Wang, Q., E. Sirois, and W. Sun, *Patient-specific modeling of biomechanical interaction in transcatheter aortic valve deployment.* J Biomech, 2012. **45**(11): p. 1965-71.

124. Maher, E., et al., *An anisotropic inelastic constitutive model to describe stress softening and permanent deformation in arterial tissue.* Journal of the Mechanical Behavior of Biomedical Materials, 2012. **12**(0): p. 9-19.

125. Balzani, D., J. Schröder, and D. Gross, *Simulation of discontinuous damage incorporating residual stresses in circumferentially overstretched atherosclerotic arteries.* Acta Biomaterialia, 2006. **2**(6): p. 609-618.

126. Peña, E., et al., *On finite-strain damage of viscoelastic-fibred materials. Application to soft biological tissues.* International Journal for Numerical Methods in Engineering, 2008. **74**(7): p. 1198-1218.

127. Woo, S.L., et al., *Injury and repair of ligaments and tendons.* Annu Rev Biomed Eng, 2000. **2**: p. 83-118.

128. Christian Gasser, T., *An irreversible constitutive model for fibrous soft biological tissue: A 3-D microfiber approach with demonstrative application to abdominal aortic aneurysms.* Acta Biomaterialia, 2011. **7**(6): p. 2457-2466.

129. Humphrey, J.D. and G.A. Holzapfel, *Mechanics, mechanobiology, and modeling of human abdominal aorta and aneurysms.* Journal of Biomechanics, 2012. **45**(5): p. 805-814.

130. Eriksson, T.S.E., et al., *Modelling volumetric growth in a thick walled fibre reinforced artery.* Journal of the Mechanics and Physics of Solids, 2014. **73**: p. 134-150.

131. Martin, C. and W. Sun, *Modeling of long-term fatigue damage of soft tissue with stress-softening and permanent set effects.* Biomechanics and Modeling in Mechanobiology, 2012: p. DOI 10.1007/s10237-012-0431-6.

132. Martin, C. and W. Sun, *Simulation of long-term fatigue damage in bioprosthetic heart valves: effects of leaflet and stent elastic properties.* Biomechanics and Modeling in Mechanobiology, 2013: p. 1-12.

133. Martin, C. and W. Sun. *Modeling of fibrous soft tissue fatigue damage using a fiber-reinforced model*. in *Computer Methods in Biomechanics and Biomedical Engineering*. 2013. Salt Lake City, Utah, USA.

134. Buckley, M.R., et al., *Validation of an empirical damage model for aging and in vivo injury of the murine patellar tendon.* Journal of Biomechanical Engineering, 2013. **135**(4).

135. Arnoux, P.J., et al., *A Visco-hyperelastic Model With Damage for the Knee Ligaments Under Dynamic Constraints.* Computer Methods in Biomechanics and Biomedical Engineering, 2002. **5**(2): p. 167 - 174.

136. Hokanson, J. and S. Yazdani, *A constitutive model of the artery with damage.* Mechanics Research Communications, 1997. **24**(2): p. 151-159.

137. Sellaro, T.L., et al., *Effects of collagen fiber orientation on the response of biologically derived soft tissue biomaterials to cyclic loading.* Journal of Biomedical Materials Research Part A, 2007. **80A**(1): p. 194-205.

138. Wulandana, R. and A.M. Robertson, *An inelastic multi-mechanism constitutive equation for cerebral arterial tissue.* Biomechanics and Modeling in Mechanobiology, 2005. **4**(4): p. 235-248.

139. Peña, E.a. and M. Doblaré, *An anisotropic pseudo-elastic approach for modelling Mullins effect in fibrous biological materials.* Mechanics Research Communications, 2009. **36**(7): p. 784-790.

140. Natali, A.N., et al., *Anisotropic elasto-damage constitutive model for the biomechanical analysis of tendons.* Medical Engineering & Physics, 2005. **27**(3): p. 209-214.

141. Natali, A.N., et al., *A Transversally Isotropic Elasto-damage Constitutive Model for the Periodontal Ligament.* Computer Methods in Biomechanics and Biomedical Engineering, 2003. **6**(5-6): p. 329-336.

142. Dorfmann, A. and R.W. Ogden, *A constitutive model for the Mullins effect with permanent set in particle-reinforced rubber.* International Journal of Solids and Structures, 2004. **41**(7): p. 1855-1878.

143. Tanaka, E. and H. Yamada, *An inelastic constitutive model of blood vessels.* Acta Mechanica, 1990. **82**(1-2): p. 21-30.

144. Maher, E., et al., *Site specific inelasticity of arterial tissue.* Journal of Biomechanics, 2012. **45**(8): p. 1393-1399.

145. Sun, W. and M.S. Sacks, *Finite element implementation of a generalized Fung-elastic constitutive model for planar soft tissues.* Biomechanics and Modeling in Mechanobiology, 2005. **4**(2-3): p. 190-199.

146. Holzapfel, G.A., *Nonlinear solid mechanics*. 2000: John Wiley & Sons, Ltd.

147. Lubarda, V.A., *Constitutive analysis of large elasto-plastic deformation based on the multiplicative decomposition of deformation gradient.* International Journal of Solids and Structures, 1991. **27**(7): p. 885-895.

148. Sun, W., E.L. Chaikof, and M.E. Levenston, *Numerical approximation of tangent moduli for finite element implementations of nonlinear hyperelastic material models.* Journal of biomechanical engineering, 2008. **130**(6): p. 061003.

149. Fung, Y.C. and P. Tong, *Classical and computational solid mechanics. Advanced series in engineering science*. 2001: World Scientific Publishing.

150. Hildebrand, F.B., *Advanced Calculus for Applications*. 2ND 76 ed. 1976: Prentice Hall, Inc.

151. Sun, W., M.S. Sacks, and M.J. Scott, *Effects of boundary conditions on the estimation of the planar biaxial mechanical properties of soft tissues.* Journal of Biomechanical Engineering, 2005. **127**(4): p. 709-715.

152. Zhang, X.F., F. Andrieux, and D.Z. Sun, *Pseudo-elastic description of polymeric foams at finite deformation with stress softening and residual strain effects.* Materials & Design, 2011. **32**(2): p. 877-884.

153. Sun, W., K. Li, and E. Sirois, *Simulated elliptical bioprosthetic valve deformation: Implications for asymmetric transcatheter valve deployment.* Journal of Biomechanics, 2010. **43**(16): p. 3085-3090.

154. Martin, C., T. Pham, and W. Sun, *Significant differences in the material properties between aged human and porcine aortic tissues.* Eur J Cardiothorac Surg, 2011. **40**(1): p. 28-34.

155. Martin, C., et al., *Age-Dependent Ascending Aorta Mechanics Assessed Through Multiphase CT.* Annals of Biomedical Engineering, 2013. **41**(12): p. 2565-2574.

156. Tsamis, A., J.T. Krawiec, and D.A. Vorp, *Elastin and collagen fibre microstructure of the human aorta in ageing and disease: a review.* Journal of the Royal Society Interface, 2013. **10**(83): p. 20121004.

157. Bank, A.J., et al., *Contribution of Collagen, Elastin, and Smooth Muscle to In Vivo Human Brachial Artery Wall Stress and Elastic Modulus.* Circulation, 1996. **94**(12): p. 3263-3270.

158. Westerhof, N., N. Stergiopulos, and M. Noble, *Snapshots of hemodynamics: an aid for clinical research and graduate education.* 2005, New York, NY: Springer Science + Business Media, Inc.

159. Halloran, B.G., et al., *Localization of Aortic Disease Is Associated with Intrinsic Differences in Aortic Structure.* Journal of Surgical Research, 1995. **59**(1): p. 17-22.

160. O'Rourke, M., *Arterial stiffness, systolic blood pressure, and logical treatment of arterial hypertension.* Hypertension, 1990. **15**(4): p. 339-47.

161. Tsamis, A., A. Rachev, and N. Stergiopulos, *A constituent-based model of age-related changes in conduit arteries*. Vol. 301. 2011. H1286-H1301.

162. Sans, M. and A. Moragas, *Mathematical morphologic analysis of the aortic medial structure. Biomechanical implications.* Anal Quant Cytol Histol., 1993. **15**(2): p. 93-100.

163. Avolio, A., D. Jones, and M. Tafazzoli-Shadpour, *Quantification of Alterations in Structure and Function of Elastin in the Arterial Media.* Hypertension, 1998. **32**(1): p. 170-175.

164. Tsamis, A., N. Stergiopulos, and A. Rachev, *A Structure-Based Model of Arterial Remodeling in Response to Sustained Hypertension.* Journal of Biomechanical Engineering, 2009. **131**(10): p. 101004-101004.

165. Zulliger, M.A., et al., *A strain energy function for arteries accounting for wall composition and structure.* Journal of Biomechanics, 2004. **37**(7): p. 989-1000.

166. Hariton, I., et al., *Stress-driven collagen fiber remodeling in arterial walls.* Biomechanics and Modeling in Mechanobiology, 2007. **6**(3): p. 163-175.

167. Tsamis, A. and N. Stergiopulos, *Arterial remodeling in response to hypertension using a constituent-based model*. Vol. 293. 2007. H3130-H3139.

168. Alford, P., J. Humphrey, and L. Taber, *Growth and remodeling in a thick-walled artery model: effects of spatial variations in wall constituents.* Biomechanics and Modeling in Mechanobiology, 2008. **7**(4): p. 245-262.

169. Gleason, R.L. and J.D. Humphrey, *A 2D constrained mixture model for arterial adaptations to large changes in flow, pressure and axial stretch.* Mathematical Medicine and Biology, 2005. **22**(4): p. 347-369.

170. Hu, J.J., et al., *Biomechanics of the Porcine Basilar Artery in Hypertension.* Annals of Biomedical Engineering, 2007. **35**(1): p. 19-29.

171. Hu, J.-J., et al., *Time Courses of Growth and Remodeling of Porcine Aortic Media During Hypertension: A Quantitative Immunohistochemical Examination.* Journal of Histochemistry and Cytochemistry, 2008. **56**(4): p. 359-370.

172. Rachev, A. and R. Gleason, Jr., *Theoretical study on the effects of pressure-induced remodeling on geometry and mechanical non-homogeneity of conduit arteries.* Biomechanics and Modeling in Mechanobiology, 2011. **10**(1): p. 79-93.

173. Mao, S.S., et al., *Normal Thoracic Aorta Diameter on Cardiac Computed Tomography in Healthy Asymptomatic Adults: Impact of Age and Gender.* Academic Radiology, 2008. **15**(7): p. 827-834.

174. Garcier, J.M., et al., *Normal diameter of the thoracic aorta in adults: a magnetic resonance imaging study.* Surgical and Radiologic Anatomy, 2003. **25**(3): p. 322-329.

175. Hager, A., et al., *Diameters of the thoracic aorta throughout life as measured with helical computed tomography.* The Journal of Thoracic and Cardiovascular Surgery, 2002. **123**(6): p. 1060-1066.

176. Craiem, D., et al., *Aging Impact on Thoracic Aorta 3D Morphometry in Intermediate-Risk Subjects: Looking Beyond Coronary Arteries with Non-Contrast Cardiac CT.* Annals of Biomedical Engineering, 2011. **40**(5): p. 1028-1038.

177. Hickson, S.S., et al., *The Relationship of Age With Regional Aortic Stiffness and Diameter.* JACC: Cardiovascular Imaging, 2010. **3**(12): p. 1247-1255.

178. Morrison, T.M., et al., *Circumferential and longitudinal cyclic strain of the human thoracic aorta: Age-related changes.* Journal of Vascular Surgery, 2009. **49**(4): p. 1029-1036.

179. Aronberg, D.J., et al., *Normal thoracic aortic diameters by computed tomography.* Journal of computer assisted tomography, 1984. **8**(2): p. 247-250.

180. Rose, J.L., et al., *Influence of age and sex on aortic distensibility assessed by MRI in healthy subjects.* Magnetic Resonance Imaging, 2010. **28**(2): p. 255-263.

181. Nelson, A.J., et al., *Cardiovascular magnetic resonance-derived aortic distensibility: Validation and observed regional differences in the elderly.* Journal of Hypertension, 2009. **27**(3): p. 535-542.

182. Biaggi, P., et al., *Gender, Age, and Body Surface Area are the Major Determinants of Ascending Aorta Dimensions in Subjects With Apparently Normal Echocardiograms.* Journal of the American Society of Echocardiography, 2009. **22**(6): p. 720-725.

183. Redheuil, A., et al., *Reduced ascending aortic strain and distensibility: Earliest manifestations of vascular aging in humans.* Hypertension, 2010. **55**(2): p. 319-326.

184. Wedding, K.L., et al., *Measurement of vessel wall strain using cine phase contrast MRI.* Journal of Magnetic Resonance Imaging, 2002. **15**(4): p. 418-428.

185. Sugawara, J., et al., *Age-Associated Elongation of the Ascending Aorta in Adults.* JACC: Cardiovascular Imaging, 2008. **1**(6): p. 739-748.

186. Wolak, A., et al., *Aortic Size Assessment by Noncontrast Cardiac Computed Tomography: Normal Limits by Age, Gender, and Body Surface Area.* JACC: Cardiovascular Imaging, 2008. **1**(2): p. 200-209.

187. Taviani, V., et al., *Age-related changes of regional pulse wave velocity in the descending aorta using Fourier velocity encoded M-mode.* Magnetic Resonance in Medicine, 2010. **65**(1): p. 261-268.

188. Mirea, O., et al., *Effects of aging and body size on proximal and ascending aorta and aortic arch: Inner edge-to-inner edge reference values in a large adult population by two-dimensional transthoracic echocardiography.* Journal of the American Society of Echocardiography, 2013. **26**(4): p. 419-427.

189. Craiem, D., et al., *Three-dimensional evaluation of thoracic aorta enlargement and unfolding in hypertensive men using non-contrast computed tomography.* Journal of Human Hypertension, 2013.

190. Chue, C.D., et al., *Effects of age and chronic kidney disease on regional aortic distensibility: A cardiovascular magnetic resonance study.* International Journal of Cardiology, 2013.

191. Siegel, E., et al., *Aortic distensibility and its relationship to coronary and thoracic atherosclerosis plaque and morphology by MDCT: Insights from the ROMICAT Trial.* International Journal of Cardiology, 2013.

192. Ganten, M., et al., *Age related changes of human aortic distensibility: evaluation with ECG-gated CT.* European Radiology, 2007. **17**(3): p. 701-708.

193. Metafratzi, Z., et al., *The clinical significance of aortic compliance and its assessment with magnetic resonance imaging.* J Cardiovasc Magn Reson, 2002. **4**(4): p. 481-91.

194. Humphrey, J.D. and C.A. Taylor, *Intracranial and abdominal aortic aneurysms: similarities, differences, and need for a new class of computational models.* Annu Rev Biomed Eng, 2008. **10**: p. 221-46.

195. Wong, D.L., et al., *Regional aortic distensibility and its relationship with age and aortic stenosis: a computed tomography study.* The International Journal of Cardiovascular Imaging, 2015. **31**(5): p. 1053-1062.

196. Venkatasubramaniam, A.K., et al., *A Comparative Study of Aortic Wall Stress Using Finite Element Analysis for Ruptured and Non-ruptured Abdominal Aortic Aneurysms.* European Journal of Vascular and Endovascular Surgery, 2004. **28**(2): p. 168-176.

197. Fillinger, M.F., et al., *Prediction of rupture risk in abdominal aortic aneurysm during observation: Wall stress versus diameter.* Journal of Vascular Surgery, 2003. **37**(4): p. 724-732.

198. Li, Z.-Y., et al., *Association Between Aneurysm Shoulder Stress and Abdominal Aortic Aneurysm Expansion / Clinical Perspective.* Circulation, 2010. **122**(18): p. 1815-1822.

199. Laurent, S., et al., *Expert consensus document on arterial stiffness: methodological issues and clinical applications*. Vol. 27. 2006. 2588-2605.

200. Roman, M.J., et al., *Two-dimensional echocardiographic aortic root dimensions in normal children and adults.* The American Journal of Cardiology, 1989. **64**(8): p. 507-512.

201. Elefteriades, J.A. and E.A. Farkas, *Thoracic Aortic Aneurysm: Clinically Pertinent Controversies and Uncertainties.* J Am Coll Cardiol, 2010. **55**(9): p. 841-857.

202. Wilson, K.A., et al., *Ultrasonic measurement of abdominal aortic aneurysm wall compliance: A reproducibility study.* Journal of Vascular Surgery, 2000. **31**(3): p. 507-513.

203. Waddell, T.K., et al., *Women exhibit a greater age-related increase in proximal aortic stiffness than men.* Journal of Hypertension, 2001. **19**(12): p. 2205-2212.

204. Geest, J.P.V., M.S. Sacks, and D.A. Vorp, *Age Dependency of the Biaxial Biomechanical Behavior of Human Abdominal Aorta.* Journal of Biomechanical Engineering, 2004. **126**(6): p. 815.

205. Haskett, D., et al., *Microstructural and biomechanical alterations of the human aorta as a function of age and location.* Biomechanics and Modeling in Mechanobiology, 2010. **9**(6): p. 725-736.

206. Iliopoulos, D.C., et al., *Biomechanical properties and histological structure of sinus of Valsalva aneurysms in relation to age and region.* J Biomech, 2013. **46**(5): p. 931-40.

207. Labrosse, M.R., et al., *Mechanical characterization of human aortas from pressurization testing and a paradigm shift for circumferential residual stress.* Journal of the Mechanical Behavior of Biomedical Materials, 2013. **17**(0): p. 44-55.

208. Li, W.C., et al., *Biomechanical properties of ascending aorta and pulmonary trunk in pigs and humans.* Xenotransplantation, 2008. **15**(6): p. 384-9.

209. Wuyts, F.L., et al., *Elastic properties of human aortas in relation to age and atherosclerosis: A structural model.* Physics in Medicine and Biology, 1995. **40**(10): p. 1577-1597.

210. Groenink, M., et al., *The influence of aging and aortic stiffness on permanent dilation and breaking stress of the thoracic descending aorta*. Vol. 43. 1999. 471-480.

211. Azadani, A.N., et al., *Comparison of Mechanical Properties of Human Ascending Aorta and Aortic Sinuses.* The Annals of Thoracic Surgery, 2012. **93**(1): p. 87-94.

212. Spronck, B., et al., *A constitutive modeling interpretation of the relationship among carotid artery stiffness, blood pressure, and age in hypertensive subjects*. Vol. 308. 2015. H568-H582.

213. Horný, L., M. Netušil, and M. Daniel, *Limiting extensibility constitutive model with distributed fibre orientations and ageing of abdominal aorta.* Journal of the Mechanical Behavior of Biomedical Materials, 2014. **38**: p. 39-51.

214. Cheng, J.K., et al., *A fiber-based constitutive model predicts changes in amount and organization of matrix proteins with development and disease in the mouse aorta.* Biomechanics and Modeling in Mechanobiology, 2013. **12**(3): p. 497-510.

215. Zulliger, M.A., A. Rachev, and N. Stergiopulos, *A constitutive formulation of arterial mechanics including vascular smooth muscle tone*. Vol. 287. 2004. H1335-H1343.

216. Okamoto, R.J., et al., *Mechanical properties of dilated human ascending aorta.* Annals of Biomedical Engineering, 2002. **30**(5): p. 624-635.

217. Guinea, G.V., et al., *Factors influencing the mechanical behaviour of healthy human descending thoracic aorta.* Physiological Measurement, 2010. **31**(12): p. 1553-1565.

218. Vorp, D.A., et al., *Effect of aneurysm on the tensile strength and biomechanical behavior of the ascending thoracic aorta.* Annals of Thoracic Surgery, 2003. **75**(4): p. 1210-1214.

219. García-Herrera, C.M., et al., *Mechanical behaviour and rupture of normal and pathological human ascending aortic wall.* Medical and Biological Engineering and Computing, 2012: p. 1-8.

220. Sokolis, D.P., K.M. Lampropoulos, and D.C. Iliopoulos. *Gender variations in the mechanical properties of ascending aortic aneurysms*. in *Proceedings of the 7th IASTED International Conference on Biomedical Engineering, BioMED 2010*. 2010.

221. Wang, Q., et al., *Dimensional Analysis of Aortic Root Geometry During Diastole Using 3D Models Reconstructed from Clinical 64-Slice Computed Tomography Images.* Cardiovascular Engineering and Technology, 2011. **2**(4): p. 324-333.

222. Klocke, R., et al., *Arterial stiffness and central blood pressure, as determined by pulse wave analysis, in rheumatoid arthritis.* Annals of the Rheumatic Diseases, 2003. **62**(5): p. 414-418.

223. Hunter, K.S., et al., *In vivo measurement of proximal pulmonary artery elastic modulus in the neonatal calf model of pulmonary hypertension: development and ex vivo validation.* Journal of Applied Physiology, 2010. **108**(4): p. 968-975.

224. Lanne, T., et al., *Diameter and compliance in the male human abdominal aorta: Influence of age and aortic aneurysm.* European Journal of Vascular Surgery, 1992. **6**(2): p. 178-184.

225. Peterson, L.H., R.E. Jensen, and J. Parnell, *Mechanical Properties of Arteries in Vivo.* Circulation Research, 1960. **8**(3): p. 622-639.

226. Koullias, G., et al., *Mechanical deterioration underlies malignant behavior of aneurysmal human ascending aorta.* The Journal of Thoracic and Cardiovascular Surgery, 2005. **130**(3): p. 677.e1-677.e9.

227. Duprey, A., et al., *In Vitro Characterisation of Physiological and Maximum Elastic Modulus of Ascending Thoracic Aortic Aneurysms Using Uniaxial Tensile Testing.* European Journal of Vascular and Endovascular Surgery, 2010. **39**(6): p. 700-707.

228. Khanafer, K., et al., *Determination of the elastic modulus of ascending thoracic aortic aneurysm at different ranges of pressure using uniaxial tensile testing.* The Journal of Thoracic and Cardiovascular Surgery, 2011. **142**(3): p. 682-686.

229. Langerak, S.E., et al., *Impact of current cryopreservation procedures on mechanical and functional properties of human aortic homografts.* Transplant International, 2001. **14**(4): p. 248-255.

230. Gillessen, T., et al., *Age-related changes in the elastic properties of the aortic tree in normotensive patients: Investigation by intravascular ultrasound.* Eur J Med Res, 1995. **1**(3): p. 144-8.

231. Ãstrand, H., et al., *In vivo estimation of the contribution of elastin and collagen to the mechanical properties in the human abdominal aorta: Effect of age and sex.* Journal of Applied Physiology, 2011. **110**(1): p. 176-187.

232. Ahlgren, A.R., et al., *Stiffness and diameter of the common carotid artery and abdominal aorta in women.* Ultrasound in Medicine and Biology, 1997. **23**(7): p. 983-988.

233. Davies, R.R., et al., *Novel Measurement of Relative Aortic Size Predicts Rupture of Thoracic Aortic Aneurysms.* Ann Thorac Surg, 2006. **81**(1): p. 169-177.

234. Sokolis, D.P., et al., *Biomechanical response of ascending thoracic aortic aneurysms: association with structural remodelling.* Computer Methods in Biomechanics and Biomedical Engineering, 2012. **15**(3): p. 231-248.

235. Karamanoglu, M., et al., *An analysis of the relationship between central aortic and peripheral upper limb pressure waves in man.* European Heart Journal, 1993. **14**(2): p. 160-167.

236. O'Rourke, M.F., M.E. Safar, and V. Dzau, *The Cardiovascular Continuum extended: Aging effects on the aorta and microvasculature.* Vascular Medicine, 2010. **15**(6): p. 461-468.

237. Iliopoulos, D.C., et al., *Ascending thoracic aortic aneurysms are associated with compositional remodeling and vessel stiffening but not weakening in age-matched subjects.* The Journal of thoracic and cardiovascular surgery, 2009. **137**(1): p. 101-109.

238. Lee, J.J., et al., *Role of Computational Modeling in Thoracic Aortic Pathology: A Review.* Journal of Cardiac Surgery, 2014. **29**(5): p. 653-662.

239. O'Rourke, M.F., *Arterial aging: pathophysiological principles.* Vascular Medicine, 2007. **12**(4): p. 329-341.

240. Brais, M.P., et al., *Ionescu-Shiley Pericardial Xenografts: Follow-up of Up to 6 Years.* Ann Thorac Surg, 1985. **39**(2): p. 105-111.

241. Vesely, I. *Features of a long-lived tissue valve*. 2008-2011 [cited 2013 April 16]; Available from: http://www.valvexchange.com/patients/index.html.

242. Singhal, P., A. Luk, and J. Butany, *Bioprosthetic Heart Valves: Impact of Implantation on Biomaterials.* ISRN Biomaterials, 2013: p. 14.

243. Trowbridge, E.A., et al., *Pericardial heterografts. Toward quality control of the mechanical properties of the glutaraldehyde-fixed leaflets.* J Thorac Cardiovasc Surg., 1986. **92**(1): p. 21-8.

244. Fleisher, A.G., R.J. Lafaro, and R.A. Moggio, *Immediate structural valve deterioration of 27-mm Carpentier-Edwards aortic pericardial bioprosthesis.* The Annals of Thoracic Surgery, 2004. **77**(4): p. 1443-1445.

245. Martin, C. and W. Sun, *Simulation of long-term fatigue damage in bioprosthetic heart valves: effects of leaflet and stent elastic properties.* Biomech Model Mechanobiol, 2014. **13**(4): p. 759-70.

246. Thubrikar, M., *The Aortic Valve*. 1990, Boca Raton: CRC. 221.

247. AHA, *American Heart Association: Heart Disease and Stroke Statistics—2010 Update*. 2010.

248. Brewer, R., et al., *An in vivo study of the dimensional changes of the aortic valve leaflets during the cardiac cycle.* Journal of Thoracic and Cardiovascular Surgery, 1977. **74**: p. 645-650.

249. Munt, B. and J. Webb, *Percutaneous valve repair and replacement techniques.* Heart., 2006. **92**(10): p. 1369-72. Epub 2005 Dec 9.

250. Webb, J., et al., *Percutaneous transarterial aortic valve replacement in selected high-risk patients with aortic stenosis.* Circulation, 2007. **7**(116): p. 755-763.

251. Haussig, S., G. Schuler, and A. Linke, *Worldwide TAVI registries: what have we learned?* Clinical Research in Cardiology, 2014.

252. Cribier, A., et al., *Percutaneous transcatheter implantation of an aortic valve prosthesis for calcific aortic stenosis: first human case description.* Circulation., 2002. **106**(24): p. 3006-8.

253. Zhao, Z.G., et al., *Transcatheter aortic valve implantation in bicuspid anatomy.* Nature Reviews Cardiology, 2014.

254. Kodali, S.K., et al., *Two-Year Outcomes after Transcatheter or Surgical Aortic-Valve Replacement.* New England Journal of Medicine, 2012. **366**(18): p. 1686-1695.

255. Milburn, K., V. Bapat, and M. Thomas, *Valve-in-valve implantations: is this the new standard for degenerated bioprostheses? Review of the literature.* Clinical Research in Cardiology, 2014: p. 1-13.

256. Lange, R. and N. Piazza, *Transcatheter aortic valve-in-surgical aortic valve implantation: current status and future perspectives.* European Journal of Cardio-Thoracic Surgery, 2013. **44**(3): p. 403-406.

257. Webb, J.G. and D. Dvir, *Transcatheter Aortic Valve Replacement for Bioprosthetic Aortic Valve Failure: The Valve-in-Valve Procedure.* Circulation, 2013. **127**(25): p. 2542-2550.

258. Dvir, D., J. Webb, and S. Bleiziffer, *Transcatheter aortic valve implantation in failed bioprosthetic surgical valves.* JAMA, 2014. **312**(2): p. 162-170.

259. Vyavahare, N., et al., *Mechanisms of bioprosthetic heart valve failure: Fatigue causes collagen denaturation and glycosaminoglycan loss.* Journal of Biomedical Materials Research, 1999. **46**: p. 44-50.

260. Gabbay, S., et al., *Long-term follow-up of the Ionescu-Shiley mitral pericardial xenograft.* J Thorac Cardiovasc Surg., 1984. **88**(5 Pt 1): p. 758-63.

261. Nistal, F., et al., *Comparative study of primary tissue valve failure between Ionescu-Shiley pericardial and Hancock porcine valves in the aortic position.* Am J Cardiol, 1986. **57**(1): p. 161-4.

262. Cooley, D.A., et al., *Ionescu-Shiley bovine pericardial bioprostheses: clinical results in 2,701 patients* in *Biologic and bioprosthetic valves*, E. Bodnar and M. Yacoub, Editors. 1986, Yorke Medical Books: New York. p. 177.

263. Reul Jr, G.J., et al., *Valve failure with the Ionescu-Shiley bovine pericardial bioprosthesis: Analysis of 2680 patients.* Journal of Vascular Surgery, 1985. **2**(1): p. 192-204.

264. Nistal, F., E. Artinano, and I. Gallo, *Primary Tissue Valve Degeneration in Glutaraldehyde-Preserved Porcine Bioprostheses: Hancock I Versus Carpentier-Edwards at 4- to 7-Years' Follow-up.* Ann Thorac Surg, 1986. **42**(5): p. 568-572.

265. Lawford, P.V., et al., *The in Vivo Durability of Bioprosthetic Heart Valves-Modes of Failure Observed in Explanted Valves.* Engineering in Medicine, 1987. **16**(2): p. 95-103.

266. Genereux, P., et al., *Transcatheter aortic valve implantation: 10-year anniversary part II: clinical implications.* Eur Heart J, 2012. **33**(19): p. 2399-402.

267. Rodes-Cabau, J., et al., *Long-term outcomes after transcatheter aortic valve implantation: insights on prognostic factors and valve durability from the Canadian multicenter experience.* J Am Coll Cardiol, 2012. **60**(19): p. 1864-75.

268. Bruschi, G., et al., *Failed valve-in-valve transcatheter mitral valve implantation.* European Journal of Cardio-thoracic Surgery, 2014. **45**(4): p. e127-e127.

269. Kiefer, P., et al., *Reoperative Transapical Aortic Valve Implantation for Early Structural Valve Deterioration of a SAPIEN XT valve.* The Annals of Thoracic Surgery, 2013. **95**(6): p. 2169-2170.

270. Chevalier, F., J. Leipsic, and P. Généreux, *Valve-in-valve implantation with a 23-mm balloon-expandable transcatheter heart valve for the treatment of a 19-mm*

stentless bioprosthesis severe aortic regurgitation using a strategy of "extreme" underfilling. Catheterization and Cardiovascular Interventions, 2014.

271. Gurvitch, R., et al., *Transcatheter Valve-in-Valve Implantation for Failed Surgical Bioprosthetic Valves.* Journal of the American College of Cardiology, 2011. **58**(21): p. 2196-2209.

272. Willson, A.B., et al., *Three-dimensional aortic annular assessment by multidetector computed tomography predicts moderate or severe paravalvular regurgitation after transcatheter aortic valve replacement: a multicenter retrospective analysis.* Journal of the American College of Cardiology, 2012. **59**(13s1).

273. Faerber, G., et al., *Valve-in-valve transcatheter aortic valve implantation: the new playground for prothesis-patient mismatch.* J Interv Cardiol, 2014. **Mar 10**(doi: 10.1111/joic.12108).

274. Leon, M.B., et al., *Transcatheter Aortic-Valve Implantation for Aortic Stenosis in Patients Who Cannot Undergo Surgery.* New England Journal of Medicine, 2010. **363**(17): p. 1597-1607.

275. Schultz, C.J., et al., *Geometry and Degree of Apposition of the CoreValve ReValving System With Multislice Computed Tomography After Implantation in Patients With Aortic Stenosis.* Journal of the American College of Cardiology, 2009. **54**(10): p. 911-918.

276. Willson, A.B., et al., *Structural Integrity of Balloon-Expandable Stents After Transcatheter Aortic Valve Replacement: Assessment by Multidetector Computed Tomography.* JACC: Cardiovascular Interventions, 2012. **5**(5): p. 525-532.

277. Zegdi, R., et al., *Is It Reasonable to Treat All Calcified Stenotic Aortic Valves With a Valved Stent?: Results From a Human Anatomic Study in Adults.* Journal of the American College of Cardiology, 2008. **51**(5): p. 579-584.

278. Smuts, A.N., et al., *Application of finite element analysis to the design of tissue leaflets for a percutaneous aortic valve.* Journal of the Mechanical Behavior of Biomedical Materials, 2011. **4**(1): p. 85-98.

279. Webb, J.G., et al., *Transcatheter Valve-in-Valve Implantation for Failed Bioprosthetic Heart Valves.* Circulation, 2010. **121**(16): p. 1848-1857.

280. Leber, A.W., et al., *Aortic valve calcium score as a predictor for outcome after TAVI using the CoreValve revalving system.* International Journal of Cardiology, 2013. **166**(3): p. 652-657.

281. John, D., et al., *Correlation of Device Landing Zone Calcification and Acute Procedural Success in Patients Undergoing Transcatheter Aortic Valve Implantations With the Self-Expanding CoreValve Prosthesis.* JACC: Cardiovascular Interventions, 2010. **3**(2): p. 233-243.

282. Muñoz-García, A.J., et al., *Mechanisms, treatment and course of paravalvular aortic regurgitation after percutaneous implantation of the CoreValve aortic prosthesis.* International Journal of Cardiology, 2011. **149**(3): p. 389-392.

283. Koos, R., et al., *Association of aortic valve calcification severity with the degree of aortic regurgitation after transcatheter aortic valve implantation.* International Journal of Cardiology, 2011. **150**(2): p. 142-145.

284. Klotz, S., *Failed Valve-In-Valve Transcatheter Aortic Valve Implantation.* JACC: Cardiovascular Interventions, 2012. **5**(5): p. 591-592.

285. Azadani, A.N. and E.E. Tseng, *Transcatheter Heart Valves for Failing Bioprostheses: State-of-the-Art Review of Valve-in-Valve Implantation.* Circulation: Cardiovascular Interventions, 2011. **4**(6): p. 621-628.

286. Vesely, I., *The Influence of Design on Bioprosthetic Valve Durability.* 2001. **11**(3&4): p. 13.

287. *Draft guidance for industry and FDA staff. Heart valves-investigational device exemption (ide) and premarket approval (pma) applications, submitted for comment, January 2010*. 2010.

288. Billiar, K.L. and M.S. Sacks, *Long-term mechanical fatigue response of porcine bioprosthetic heart valves.* American Society of Mechanical Engineers, Bioengineering Division (Publication) BED, 1998. **39**: p. 343-344.

289. Hilbert, S.L., V.J. Ferrans, and W.M. Swanson, *Optical methods for the nondestructive evaluation of collagen morphology in bioprosthetic heart valves.* J Biomed Mater Res, 1986. **20**(9): p. 1411-21.

290. Liao, J., et al., *The Intrinsic Fatigue Mechanism of the Porcine Aortic Valve Extracellular Matrix.* Cardiovascular Engineering and Technology, 2012. **3**(1): p. 62-72.

291. Smith, D.B., et al., *Fatigue-induced changes in bioprosthetic heart valve three-dimensional geometry and the relation to tissue damage.* The Journal of heart valve disease, 1999. **8**(1): p. 25-33.

292. Sacks, M.S. and D.B. Smith, *Effects of accelerated testing on porcine bioprosthetic heart valve fiber architecture.* Biomaterials, 1998. **19**(11–12): p. 1027-1036.

293. Purinya, B., et al., *Biomechanical and structural properties of the explanted bioprosthetic valve leaflets.* J Biomech, 1994. **27**(1): p. 1-11.

294. Raghavan, D., B.C. Starcher, and N.R. Vyavahare, *Neomycin binding preserves extracellular matrix in bioprosthetic heart valves during in vitro cyclic fatigue and storage.* Acta Biomater, 2009. **5**(4): p. 983-92.

295. Broom, N.D., *The stress/strain and fatigue behaviour of glutaraldehyde preserved heart-valve tissue.* Journal of Biomechanics, 1977. **10**(11–12): p. 707-724.

296. Broom, N.D., *Fatigue-induced damage in glutaraldehyde-preserved heart valve tissue.* J Thorac Cardiovasc Surg, 1978. **76**(2): p. 202-11.

297. Broom, N.D., *An 'in vitro' study of mechanical fatigue in glutaraldehyde-treated porcine aortic valve tissue.* Biomaterials, 1980. **1**(1): p. 3-8.

298. Wells, S.M. and M.S. Sacks, *Effects of fixation pressure on the biaxial mechanical behavior of porcine bioprosthetic heart valves with long-term cyclic loading.* Biomaterials, 2002. **23**(11): p. 2389-2399.

299. Garcia Paez, J.M., et al., *Energy consumption as a predictor test of the durability of a biological tissue employed in cardiac bioprosthesis.* J Biomed Mater Res A, 2009. **89**(2): p. 336-44.

300. Paez, J.M., et al., *Durability of a cardiac valve leaflet made of calf pericardium: fatigue and energy consumption.* J Biomed Mater Res A, 2006. **77**(4): p. 839-49.

301. Swanson, W.M. and R.E. Clark, *Aortic Valve Leaflet Motion during Systole: Numerical-Graphical Determination.* Circulation Research, 1973. **32**(1): p. 42-48.

302. Vesely, I., D. Boughner, and T. Song, *Tissue Buckling as a Mechanism of Bioprosthetic Valve Failure.* The Annals of Thoracic Surgery, 1988. **46**(3): p. 302-308.

303. Mirnajafi, A., Z. Brett, and S.S. Michael, *Effects of cyclic flexural fatigue on porcine bioprosthetic heart valve heterograft biomaterials.* Journal of Biomedical Materials Research Part A, 2010. **94A**(1): p. 205-213.

304. Kim, H., et al., *Dynamic Simulation of Bioprosthetic Heart Valves Using a Stress Resultant Shell Model.* Annals of Biomedical Engineering, 2008. **36**(2): p. 262-275.

305. Christie, G.W., *Computer modelling of bioprosthetic heart valves.* Eur J Cardiothorac Surg, 1992. **6**(Suppl 1): p. S95-100.

306. Krucinski, S., et al., *Numerical simulation of leaflet flexure in bioprosthetic valves mounted on rigid and expansile stents.* Journal of Biomechanics, 1993. **26**(8): p. 929-943.

307. Leat, M.E. and J. Fisher, *The influence of manufacturing methods on the function and performance of a synthetic leaflet heart valve.* Proc Inst Mech Eng [H], 1995. **209**(1): p. 65-9.

308. Leat, M.E. and J. Fisher, *A synthetic leaflet heart valve with improved opening characteristics.* Med Eng Phys, 1994. **16**(6): p. 470-6.

309. Cacciola, G., G.W. Peters, and F.P. Baaijens, *A synthetic fiber-reinforced stentless heart valve.* J Biomech, 2000. **33**(6): p. 653-8.

310. Li, K. and W. Sun, *Simulated Thin Pericardial Bioprosthetic Valve Leaflet Deformation Under Static Pressure-Only Loading Conditions: Implications for Percutaneous Valves.* Annals of Biomedical Engineering, 2010. **38**(8): p. 2690-2701.

311. Gunning, P., T. Vaughan, and L. McNamara, *Simulation of Self Expanding Transcatheter Aortic Valve in a Realistic Aortic Root: Implications of Deployment Geometry on Leaflet Deformation.* Annals of Biomedical Engineering, 2014. **42**(9): p. 1989-2001.

312. Martin, C. and W. Sun, *Biomechanical characterization of aortic valve tissue in humans and common animal models.* Journal of Biomedical Materials Research: Part A, 2012. **100A**(6): p. 1591-1599.

313. Dwyer, H.A., et al., *Computational fluid dynamics simulation of transcatheter aortic valve degeneration.* Interact Cardiovasc Thorac Surg, 2009. **9**(2): p. 301-8.

314. Kuetting, M., et al., *In vitro assessment of the influence of aortic annulus ovality on the hydrodynamic performance of self-expanding transcatheter heart valve prostheses.* J Biomech, 2014. **47**(5): p. 957-65.

315. Corden, J., T. David, and J. Fisher, *Determination of the Curvatures and Bending Strains in Open Trileaflet Heart Valves.* Proceedings of the Institution of Mechanical Engineers, Part H: Journal of Engineering in Medicine, 1995. **209**(2): p. 121-128.

316. Wagenseil, J.E. and R.P. Mecham, *Elastin in large atery stiffness and hypertension.* J Cardiovasc Transl Res, 2013. **5**(3): p. 264-273.

317. Trowbridge, E.A. and C.E. Crofts, *Pericardial heterograft valves: an assessment of leaflet stresses and their implications for heart valve design.* J Biomech Eng, 1987. **9**(4): p. 345-55.

318. Schoen, F.J. and R.J. Levy, *Tissue heart valves: Current challenges and future research perspectives.* Journal of Biomedical Materials Research, 1999. **47**(4): p. 439-465.

319. Butany, J., et al., *Carpentier-Edwards Perimount Valves—Morphological Findings in Surgical Explants.* Journal of Cardiac Surgery, 2007. **22**(1): p. 7-12.

320. Schoen, F.J., et al., *Causes of failure and pathologic findings in surgically removed Ionescu-Shiley standard bovine pericardial heart valve bioprostheses: emphasis on progressive structural deterioration.* Circulation, 1987. **76**(3): p. 618-27.

321. Machida, H., et al., *A morphologic study of Carpentier-Edwards pericardial xenografts in the mitral position exhibiting primary tissue failure in adults in comparison with Ionescu-Shiley pericardial xenografts.* The Journal of Thoracic and Cardiovascular Surgery, 2001. **122**(4): p. 649-655.

322. Walley, V.M., et al., *Ionescu-Shiley valve failure II: Experience with 25 low-profile expiants.* Ann Thorac Surg, 1992. **54**(1): p. 117-122.

323. Vesely, I., *The evolution of bioprosthetic heart valve design and its impact on durability.* Cardiovascular Pathology, 2003. **12**(5): p. 277-286.

324. Stearns, G., et al., *Transcatheter aortic valve implantation can potentially impact short-term and long-term functionality: An in vitro study.* International Journal of Cardiology, 2014. **172**(3): p. e421-e422.

325. Schoen, F.J., *Pathology of bioprostheses and other tissue heart valve replacements*, in *Cardiovascular pathology, 2nd ed.*, M.D. Silver, Editor. 1991, Churchill Livingstone: New York. p. 1547-1605.

326. Sacks, M.S., C.J. Chuong, and R. More, *Collagen fiber architecture of bovine pericardium.* Asaio j, 1994. **40**(3): p. M632-7.

327. Olsson, T. and A. Klarbring, *Residual stresses in soft tissue as a consequence of growth and remodeling: application to an arterial geometry.* European Journal of Mechanics - A/Solids, 2008. **27**(6): p. 959-974.

328. Vorp, D.A., *Biomechanics of abdominal aortic aneurysm.* Journal of Biomechanics, 2007. **40**(9): p. 1887-1902.

329. Bonow, R., et al., *ACC/AHA Guidelines for the Management of Patients with Valvular Heart Disease. Executive Summary. A report of the American College of Cardiology/American Heart Association Task Force on Practice Guidelines (Committee on Management of Patients With Valvular Heart Disease).* J Heart Valve Dis., 1998. **7**(6): p. 672-707.

330. Fillinger, M.F., et al., *Anatomic characteristics of ruptured abdominal aortic aneurysm on conventional CT scans: implications for rupture risk.* Journal of Vascular Surgery, 2004. **39**(6): p. 1243-1252.

331. Martin, C., et al., *Predictive biomechanical analysis of ascending aortic aneurysm rupture potential.* Acta Biomaterialia, 2013. **9**(12): p. 9392-9400.

332. Pham, T.M., et al., *Biomechanical characterization of ascending aortic aneurysm with concomittant bicuspid aortic valve and bovine aortic arch.* Acta Biomaterialia, 2013. **9**(8): p. 7927-7936.

333. Wanamaker, K.M., et al., *Incidence of Aortic Arch Anomalies in Patients with Thoracic Aortic Dissections.* Journal of Cardiac Surgery, 2013. **28**(2): p. 151-154.

334. Hornick, M., et al., *Bovine Arch - A Marker for Thoracic Aortic Aneurysm*, in *15th World Congress on Heart Disease*. 2010: Vancouver, B.C., Canada.

335. Fedak, P.W.M., et al., *Clinical and pathophysiological implications of a bicuspid aortic valve.* Circulation, 2002. **106**(8): p. 900-904.

336. Yap, C.H., et al., *Dynamic deformation characteristics of porcine aortic valve leaflet under normal and hypertensive conditions.* American Journal of Physiology - Heart and Circulatory Physiology, 2010. **298**(2): p. H395-H405.

337. Jackson, V., et al., *Matrix metalloproteinase 14 and 19 expression is associated with thoracic aortic aneurysms.* Journal of Thoracic and Cardiovascular Surgery, 2012. **144**(2): p. 459-466.

338. Mohamed, S.A., et al., *Novel missense mutations (p.T596M and p.P1797H) in NOTCH1 in patients with bicuspid aortic valve.* Biochemical and Biophysical Research Communications, 2006. **345**(4): p. 1460-1465.

339. Rowe, V.L., et al., *Vascular smooth muscle cell apoptosis in aneurysmal, occlusive, and normal human aortas.* Journal of Vascular Surgery, 2000. **31**(3): p. 567-576.

340. Jakanani, G.C. and W. Adair, *Frequency of variations in aortic arch anatomy depicted on multidetector CT.* Clinical Radiology, 2010. **65**(6): p. 481-487.

341. Okamoto, R.J., et al., *The influence of mechanical properties on wall stress and distensibility of the dilated ascending aorta.* Journal of Thoracic and Cardiovascular Surgery, 2003. **126**(3): p. 842-850.

342. López-Candales, A., et al., *Decreased vascular smooth muscle cell density in medial degeneration of human abdominal aortic aneurysms.* American Journal of Pathology, 1997. **150**(3): p. 993-1007.

343. Nataatmadja, M., et al., *Abnormal extracellular matrix protein transport associated with increased apoptosis of vascular smooth muscle cells in Marfan syndrome and bicuspid aortic valve thoracic aortic aneurysm.* Circulation, 2003. **108**(10 SUPPL.): p. II329-II334.

344. Mohamed, S.A., et al., *Elevation of matrix metalloproteinases in different areas of ascending aortic aneurysms in patients with bicuspid and tricuspid aortic valves.* The Scientific World Journal, 2012. **2012**.

345. Koullias, G.J., et al., *Tissue microarray detection of matrix metalloproteinases, in diseased tricuspid and bicuspid aortic valves with or without pathology of the ascending aorta.* European Journal of Cardio-thoracic Surgery, 2004. **26**(6): p. 1098-1103.

346. Bia, D., et al., *Cryopreservation procedure does not modify human carotid homografts mechanical properties: an isobaric and dynamic analysis.* Cell and Tissue Banking, 2006. **7**: p. 183–194.

347. Sacks, M.S., *A method for planar biaxial mechanical testing that includes in-plane shear.* J Biomech Eng, 1999. **121**(5): p. 551-5.

348. Vande Geest, J.P., M.S. Sacks, and D.A. Vorp, *The effects of aneurysm on the biaxial mechanical behavior of human abdominal aorta.* Journal of Biomechanics, 2006. **39**(7): p. 1324-1334.

349. Yuan, S.M. and H. Jing, *Cystic medial necrosis: Pathological findings and clinical implications.* Necrose cística da média: Manifestações patológicas com implicações clínicas, 2011. **26**(1): p. 107-115.

350. Tadros, T.M., M.D. Klein, and O.M. Shapira, *Ascending aortic dilatation associated with bicuspid aortic valve. Pathophysiology, molecular biology, and clinical implications.* Circulation, 2009. **119**(6): p. 880-890.

351. Agozzino, L., et al., *Ascending aorta dilatation in aortic valve disease: Morphological analysis of medial changes.* Heart and Vessels, 2006. **21**(4): p. 213-220.

352. Schmid, F.X., et al., *Structural and biomolecular changes in aorta and pulmonary trunk of patients with aortic aneurysm and valve disease: implications for the Ross procedure.* European journal of cardio-thoracic surgery : official journal of the European Association for Cardio-thoracic Surgery, 2004. **25**(5): p. 748-53.

353. De Sa, M., et al., *Histologic abnormalities of the ascending aorta and pulmonary trunk in patients with bicuspid aortic valve disease: Clinical relevance to the Ross procedure.* Journal of Thoracic and Cardiovascular Surgery, 1999. **118**(4): p. 588-596.

354. Choudhury, N., et al., *Local mechanical and structural properties of healthy and diseased human ascending aorta tissue.* Cardiovascular Pathology, 2009. **18**(2): p. 83-91.

355. Carmo, M., et al., *Alteration of elastin, collagen and their cross-links in abdominal aortic aneurysms.* European Journal of Vascular and Endovascular Surgery, 2002. **23**(6): p. 543-549.

356. Malone, C.D., et al., *Bovine aortic arch: A novel association with thoracic aortic dilation.* Clinical Radiology, 2012. **67**(1): p. 28-31.

357. Deyl, Z., et al., *Collagen and elastin synthesis in the aorta of spontaneously hypertensive rats.* Blood Vessels, 1987. **24**(6): p. 313-20.

358. Wolinsky, H., *Response of the rat aortic media to hypertension. Morphological and chemical studies.* Circulation Research, 1970. **26**: p. 507-522.

359. Hu, J.J., S. Baek, and J.D. Humphrey, *Stress–strain behavior of the passive basilar artery in normotension and hypertension.* Journal of Biomechanics, 2007. **40**: p. 2559–2563.

360. Matsumoto, T. and K. Hayashi, *Stress and strain distribution in hypertensive and normotensive rat aorta considering residual strain.* J Biomech Eng, 1996. **118**(1): p. 62-73.

361. Antonini-Canterin, F., et al., *Symptomatic aortic stenosis: Does systemic hypertension play an additional role?* Hypertension, 2003. **41**(6): p. 1268-1272.

362. Pasta, S., et al., *Effect of aneurysm on the mechanical dissection properties of the human ascending thoracic aorta.* Journal of Thoracic and Cardiovascular Surgery, 2012. **143**(2): p. 460-467.

363. Carson, M.W. and M.R. Roach, *The strength of the aortic media and its role in the propagation of aortic dissection.* Journal of Biomechanics, 1990. **23**(6): p. 579-588.

364. Hirst, A.E., Jr. and V.J. Johns, Jr., *Experimental dissection of media of aorta by pressure. Its relation to spontaneous dissecting aneurysm.* Circ Res, 1962. **10**: p. 897-903.

365. CDC. *National Center for Injury Prevention and Control, WISQARS Leading Causes of Death Reports, 1999 - 2007*. 2007 [cited 2011 April 27].

366. Wang, Y., et al., *Gene expression signature in peripheral blood detects thoracic aortic aneurysm.* PLoS ONE, 2007. **2**(10).

367. Svensson, L.G., et al., *Relationship of aortic cross-sectional area to height ratio and the risk of aortic dissection in patients with bicuspid aortic valves.* J Thorac Cardiovasc Surg, 2003. **126**(3): p. 892-893.

368. Kirklin, J. and B. Barrat-Boyes, eds. Cardiac Surgery. 1993.

369. Richens, D., et al., *The mechanism of injury in blunt traumatic rupture of the aorta.* European Journal of Cardio-thoracic Surgery, 2002. **21**(2): p. 288-293.

370. Hatzaras, I., et al., *Weight Lifting and Aortic Dissection: More Evidence for a Connection.* Cardiology, 2007. **107**(2): p. 103-106.

371. Elefteriades, J.A., *Beating a sudden killer.* Scientific American, 2005(293): p. 64-71.

372. Pape, L.A., et al., *Aortic Diameter â‰¥5.5 cm Is Not a Good Predictor of Type A Aortic Dissection.* Circulation, 2007. **116**(10): p. 1120-1127.

373. La Canna, G., et al., *Progression Rate of Ascending Aortic Dilation in Patients With Normally Functioning Bicuspid and Tricuspid Aortic Valves.* The American Journal of Cardiology, 2006. **98**(2): p. 249-253.

374. Davies, R.R., et al., *Natural History of Ascending Aortic Aneurysms in the Setting of an Unreplaced Bicuspid Aortic Valve.* The Annals of Thoracic Surgery, 2007. **83**(4): p. 1338-1344.

375. Edwards, W.D., D.S. Leaf, and J.E. Edwards, *Dissecting aortic aneurysm associated with congenital bicuspid aortic valve.* Circulation, 1978. **57**(5): p. 1022-5.

376. Gore, I., *Dissecting aneurysms of the aorta in persons under forty years of age.* AMA Arch Pathol, 1953. **55**: p. 1-13.

377. Gundiah, N., et al., *Significant material property differences between the porcine ascending aorta and aortic sinuses.* The Journal of heart valve disease, 2008. **17**(6): p. 606-613.

378. Sokolis, D., E. Kritharis, and D. Iliopoulos, *Effect of layer heterogeneity on the biomechanical properties of ascending thoracic aortic aneurysms.* Medical and Biological Engineering and Computing, 2012: p. 1-11.